Via Array Modeling for Application in Fast, Energy-Efficient Digital Systems

Vom Promotionsausschuss der
Technischen Universität Hamburg-Harburg
zur Erlangung des akademischen Grades
Doktor-Ingenieur (Dr.-Ing.)
genehmigte Dissertation

von
Sebastian Müller

aus
Hamburg

2014

1. Gutachter:
Prof. Dr. sc. techn. Christian Schuster

2. Gutachter:
Prof. Dr.-Ing. Stefan Dickmann

Vorsitzende des Promotionsverfahrens:
Prof. Dr. Sibylle Schupp

Tag der mündlichen Prüfung: 31.10.2014

URN: urn:nbn:de:gbv:830-tubdok-13130

Summary

This thesis studies the application of so-called "physics-based" via models for an efficient modeling of dense via arrays in multilayer PCBs. Physics-based via models are based on a division of the multilayer PCB in separate cavities, and on a further division of each cavity into different subdomains. Each subdomain is represented by a separate sub-block in the physics-based model. The network parameters of the sub-blocks can be calculated using analytical formulas, leading to a large reduction in simulation times in comparison to full wave solutions. The network parameters of the sub-blocks are combined to obtain the model of the complete multilayer PCB.

The thesis reviews different approaches that can be used to calculate sub-blocks of the physics-based via model and evaluates them with regard to their impact on the modeling accuracy. In particular, the application of an improved local field model is identified as a suitable way to improve the model accuracy for the simulation of via arrays, especially at frequencies above 20 GHz. Additionally, effects related to higher order radial waveguide modes — which are neglected in the physics-based approach — are investigated with the goal to find general limitations for the accuracy of the physics-based model for dense via arrays. The applicability of the model within the observed limitations is confirmed by comparison to full wave results and hardware measurements.

Also improvements with regard to the model efficiency are studied. Based an efficient combination of calculation methods and network parameters for the model evaluation and additional optimizations, a total acceleration factor of about 26 in comparison to a previous implementation of the physics-based via model is achieved. This acceleration makes it possible to study very large via arrays in multilayer PCBs in a reasonable time, and to carry out fast design explorations on a single PC for smaller via arrays in multilayer PCBs containing a few 100 vias. The efficient model is applied in the thesis to study several physical effects related to PCB links and via arrays, including a study of crosstalk behavior for an array consisting of 10,000 vias.

Finally, a systematic approach for the evaluation of link design alternatives is proposed. The presented approach for a systematic design evaluation integrates the advantages of the efficient physics-based via model in a larger concept. The approach takes into account both signal integrity and energy efficiency, and allows a quantitative comparison between different designs in terms of the total link input power through an application of identical constraints. In contrast to previous approaches for design evaluations, it takes into account the impact of design changes on the complete system, allowing a fair comparison of different alternatives. An application of the approach to evaluate four design alternatives resulting from two fundamental design decisions shows differences of up to 17 % in the required link input power due to different choices for the signal to ground via ratio.

Acknowledgment

This thesis is the result of my time as a research assistant at the Institute of Electromagnetic Theory (Institut für Theoretische Elektrotechnik, TET) at Hamburg University of Technology (Technische Universität Hamburg-Harburg, TUHH). The main part of the work was carried out during the three-year project "Via Array Design in Multilayer Substrates for Application in Fast, Energy and Material Efficient Digital Systems". I would like to acknowledge the project funding provided by the German Research Foundation (Deutsche Forschungsgemeinschaft, DFG). Furthermore, I would like to thank those people without whose contributions and support this work would not have been possible:

First of all, I want to express my sincere gratitude Prof. Christian Schuster, head of the Institute of Electromagnetic Theory and supervisor of this thesis, for the chance to work on a highly interesting and relevant topic, and for the excellent guidance and constant feedback and advice during this work. His expertise, enthusiasm and dedication have set a great example to me.

I am also grateful to Prof. Stefan Dickmann for his willingness to be the coexaminer of this work as well as for his careful review of this thesis, and to Prof. Sibylle Schupp as the president of the doctoral committee.

I would like to thank all my colleagues at the Institute of Electromagnetic Theory for the wonderful time and great teamwork. I am deeply indebted to my former colleague, Prof. Renato Rimolo-Donadio, for teaching me about the topic of via modeling, and for the great advice, tremendous support, and continuing cooperation throughout the years. I would like to thank him as well as Dr. Heinz-D. Brüns for many helpful discussions and for the careful review of several publications that were written during my time at the institute. Furthermore, I would like to express my gratitude to Dr. Xiaomin Duan, Dr. Miroslav Kotzev, Andreas Hardock, Fabian Happ, and Torsten Reuschel for the fruitful cooperation and their valuable feedback and contributions on several research topics. Special thanks goes to Dr. Kotzev for the large amount of time that he invested in teaching me about high frequency measurements on PCBs. In addition to the aforementioned colleagues, I would also like to thank David Dahl, Jan Preibisch, and Alexander Vogt for proof-reading parts of this thesis.

This work greatly benefited from the cooperation with several people at the IBM T. J. Watson Research Center, Yorktown Heights, NY, USA. Particularly, I would like to thank

Dr. Young H. Kwark, Dr. Xiaoxiong Gu, and Christian Baks, for the constant cooperation and their contributions to the via model accuracy study as well as many other topics. During my four-month stay at IBM, I also learned a lot from the advice of Dr. Timothy Chainer, Dr. Lei Shan, and Dr. Duixian Liu.

I also benefited from the regular exchange with Prof. Yaojiang Zhang and Prof. Jun Fan at the Missouri University of Science and Technology. In particular, I would like to thank Prof. Zhang for his helpfulness on the via model accuracy study and for the provision of multiple scattering results.

At the Georgia Institute of Technology, I would like to thank Prof. Madhavan Swaminathan and all members of the Mixed Signal Design Group - especially Dr. Jae Y. Choi - for the great and productive stay that I had in 2010.

Above all, I would like to thank my family: My parents, Birgit and Bodo, for their unconditional love and support, and for allowing me to always follow my interests. My brothers, Jan Hendrik and Tobias, who are always there for me. My parents-in-law, Juying and Defu, for caring for me like for their own son. And, last and foremost, my wife Qin, for her endless love, and for all her support and understanding during the writing of this thesis. Qin, this thesis is for you.

Contents

List of Acronyms and Symbols

Acronyms

ACA	Adaptive Cross Approximation
BER	Bit Error Rate
BGA	Ball Grid Array
CEI	Common Electrical I/O
CIM	Contour Integral Method
CPU	Central Processing Unit
CRM	Cavity Resonator Method
DUT	Device Under Test
FDTD	Finite-Differences Time-Domain
FEM	Finite Element Method
FEXT	Far-End Crosstalk
FIT	Finite Integration Technique
GMS	Generalized Multiple Scattering approach
IC	Integrated Circuit
M-FDM	Multilayered Finite Difference Method
M-FEM	Multilayered Finite Element Method
MoM	Method of Moments
MPI	Message Passing Interface
NEXT	Near-End Crosstalk
NRZ	Non-Return-to-Zero
OIF	Optical Internetworking Forum
PCB	Printed Circuit Board
PCI Express	Peripheral Component Interconnect Express
PMC	Perfect Magnetic Conductor
PML	Perfectly Matched Layer
RPL	Recessed Probe Launch
RWM	Radial Waveguide Method
Rx	Receiver
SOLT	Short Open Load Through

TEM	Transverse Electromagnetic
TE^z	Transverse Electric (with respect to z)
TL	Transmission Line
TLM	Transmission Line Matrix method
TM^z	Transverse Magnetic (with respect to z)
Tx	Transmitter
UI	Unit Interval
VNA	Vector Network Analyzer

Symbols

a	Incident field coefficient
C^{b}	Via barrel-to-plane capacitance
d	Separation (via-to-via or via-to-trace)
E	Electric field
η	Wave impedance
f	Frequency
$\tilde{F}$	Single-bit Fourier transform
ε	Permittivity
μ	Permeability
h	Thickness of the dielectric layer (cavity height)
$H_\alpha^{(2)}$	Hankel function of second kind and order α
j	Imaginary unit
J_α	Bessel function of order α
k	Wave number – or
k	Modal decomposition factor
k_{rl}	Radial wave number
l	Mode number with respect to z-variation
n	Mode number with respect to φ-variation
P	Input power
P_{XX}	Power spectral density
ρ	Via position
r_{ap}	Antipad radius
r_{p}	Pad radius
r_{v}	Via radius

σ	Conductivity
t	Reference plane thickness
tc	Stripline thickness
$\tan(\delta)$	Dielectric loss tangent
T	T-matrix coefficient
T_b	Bit period
V_R	Receiver voltage
V_T	Transmitter voltage
w	Exciting field coefficient
ω	Angular Frequency
Z_in	Input impedance
Y^pp	Parallel plate admittance
Z^pp	Parallel plate impedance
Z_R	Receiver termination
Z_T	Transmitter termination

Units

$1\,\mathrm{inch} \approx 25{,}4\,\mathrm{mm}$
$1\,\mathrm{mil} = 0.001\ \mathrm{inch} \approx 0.0254\,\mathrm{mm}$

1 Introduction

The main goal of the work described in this thesis is the fast and accurate modeling of via arrays on printed circuit boards (PCBs), with an application of the models to a systematic comparison of different via array design alternatives for PCB links. This introduction shall give a motivation for the modeling of via arrays as a crucial part of high speed digital links. Additionally, challenges with regard to signal integrity and energy efficiency are briefly introduced as major concerns for high speed link design. Afterwards, the contributions made in this work are specified, and the content of the following chapters is outlined. Finally, an overview of the publications made during the work on this thesis is provided.

1.1 High Speed Digital Links

High speed links are an essential part of modern digital systems. They provide the connection between different integrated circuits (ICs) such as central processing units (CPUs), memory chips, and peripheral components. The schematic of a typical high-speed link setup is shown in Fig. 1.1(a). The link consists of a transmitter (Tx) in the first chip, which prepares and transmits the data, a receiver in the second chip, which receives the data and prepares it for further processing, and the interconnect, which constitutes the physical transmission channel. An example of an interconnect structure is shown in Fig. 1.1(b). Two ICs acting as transmitter and receiver are connected to a PCB by packages and sockets. Inside the PCB, arrays of vertical interconnects (vias) provide the connection to striplines on different routing layers, which bridge the horizontal distance between the ICs. Packages, sockets and the PCB together form the interconnect, which will typically show a complex frequency dependent behavior for signal transmission, reflection, and crosstalk (unwanted coupling between different lines).

Traditionally, research and development efforts for digital systems have focused on the IC design, i.e. on the internal logic and on transmitter and receiver circuits, with interconnect design being a minor concern. However, due to continuous improvement and downscaling of the underlying semiconductor technology, interconnect bandwidth has become a major bottleneck for modern digital systems [1, 2]. The need for an improved interconnect design was first encountered – and is still most relevant – for large server and data center systems, where backplane links transmit high amounts of data over comparatively long distances. In addition, high performance, multi-core systems are increasingly employed also in small scale digital systems such as personal computers or even mobile devices. The related requirements on interconnect bandwidth – especially for the communication between multiple CPUs and off-chip memory – extend the importance of interconnect design for high speed links to a wide range of practical systems [3].

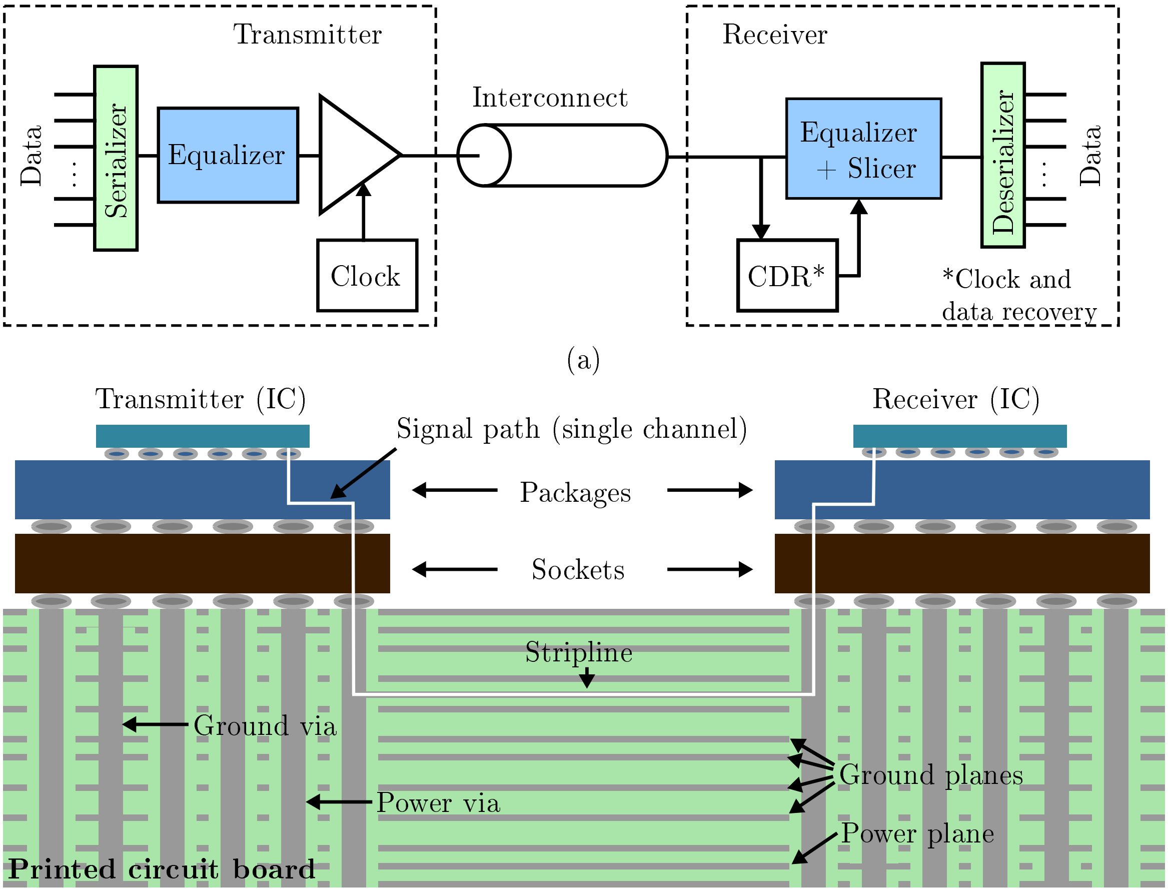

(a)

(b)

Figure 1.1: (a) Schematic of a high speed digital link. The link consists of a transmitter which prepares and transmits the data, the interconnect itself, and the receiver, which receives the data and prepares it for further processing (Figure from [4]). (b) Examplary high speed link structure. Two ICs acting as transmitter and receiver are mounted on a PCB. The space transition between small IC dimensions and larger PCB dimensions is provided by packages mounted on sockets, which can be connected to the board e.g. using ball grid arrays (BGAs). Inside the PCB, via arrays provide the connection to the striplines routed on different signal layers (Figure from [5]).

1.2 Via Arrays as a Part of High Speed Links

Via arrays constitute an important part of high speed links. As described in the previous section, signal vias provide the connection between components mounted on top of the PCB and striplines routed on the inner signal layers of the PCB. Typically, the vias under an IC are arranged in a regular pattern to form an array. In addition to signal vias, via arrays contain power vias and ground vias. Power vias are connected to the corresponding power planes in the PCB stackup, and provide the supply voltages for the ICs. Ground vias are connected to all ground planes in the stackup. They provide a return path for signal currents, and can mitigate crosstalk between signal vias. Via arrays not only appear under ICs, but also as connector footprints where daughtercards are connected to a backplane. This means that for the communication between two ICs on different daughtercards, six via array transitions occur in a single link.

Practical via arrays can consist of up to several thousand regularly arranged vias. A top view of a large via array is shown in Fig. 1.2(a). The cross section of four vias in Fig. 1.2(b) shows how the ground vias are connected to the reference planes, while the signal vias traverse the ground planes through antipads. The reference planes of the PCB form cavities which support the propagation of radial waveguide modes excited by the via currents. The wave propagation, which will be treated in more detail in Section 3.1, can lead to crosstalk between vias even for large via separations [6]. While the methods described in this thesis allow the modeling of the PCB as a whole – including vias, striplines, and power and ground planes in different configurations – the focus of the work is on the modeling of via arrays. This focus is chosen for two reasons: From a modeling point of view, via arrays constitute the most challenging part of the link. The simulation of several thousand vias requires the application of very efficient modeling approaches, while a high model accuracy is required to accurately take into account the interaction between the closely spaced vias provided by radial waveguide modes. From an application point of view, via arrays are of high interest since they provide a large design space. Design decisions for via arrays include the via pitch, the arrangement of signal, power and ground vias, the signal to ground via ratio, and the assignment of signals to different routing layers. The impact of all these decisions can only be fully evaluated in a global context, which takes into account the resulting changes for all channels in a link. For this reason, efficient models, which allow to accurately model complete links including large via arrays, can be an important tool to explore different designs in order to find improved solutions.

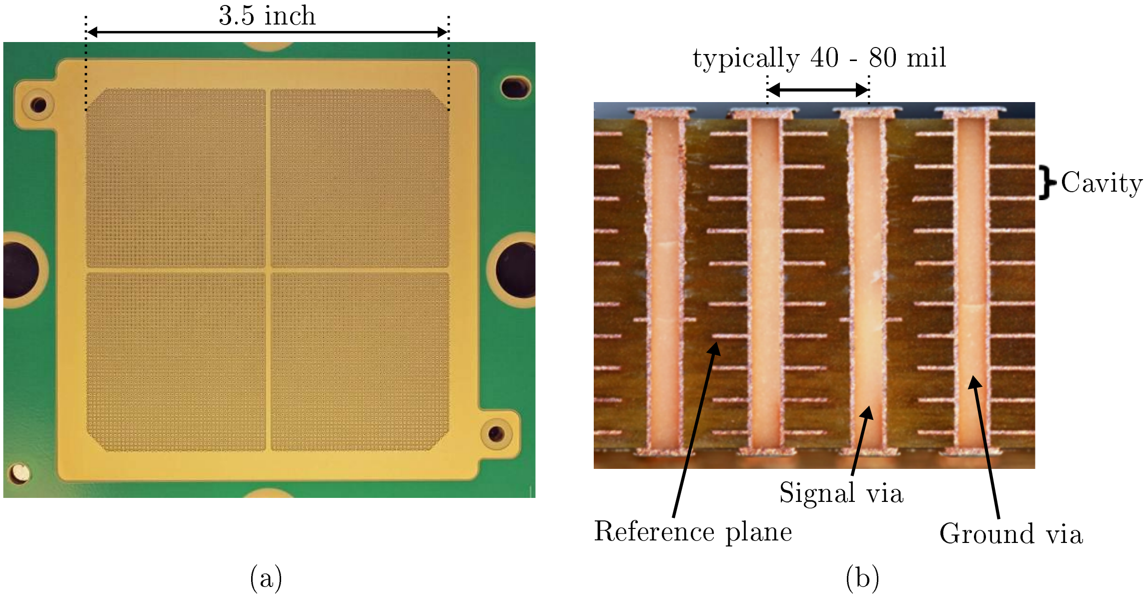

Figure 1.2: Pictures of a large land grid array footprint (Figures adapted from [7,8]). (a) Top view of the via array consisting of about 3000 vias with 40 mil pitch. (b) Cross section of four vias inside the array. Signal vias are traversing the ground planes through antipads (circular cutouts), while ground vias are connected to the planes.

1.3 Signal Integrity and Energy Efficiency Challenges

Typically, signal integrity is the main concern during the design of high speed links. In simple terms, signal integrity ensures that every signal arrives at the receiver in a state that allows it to be further processed in the intended way—normally meaning that logical ones and zeros are detected correctly. Several effects of the physical interconnect are detrimental to signal integrity: For the stripline part of the link, lossy dielectric substrates can lead to a severe signal attenuation. At the via transitions, impedance mismatches between vias and striplines lead to reflections, and stub resonances are caused by the via portions below the connected striplines. Additionally, the crosstalk between vias due to the propagation of radial waveguide modes further impairs the signals. Guaranteeing signal integrity for high speed links remains a challenging task due to the steady increase of the targeted data rates, which is shown for two exemplary standards in Fig. 1.3. The spectral content of signals increases with the data rate, which typically leads to higher losses and an increased crosstalk. A solution that is currently followed to reduce the detrimental impact of stripline losses lies in the development and application of low loss dielectric materials [9]. As indicated in the previous section, the via array parts of the link offer a large additional design space. They require considerable analysis effort, but also offer the potential for design improvements in

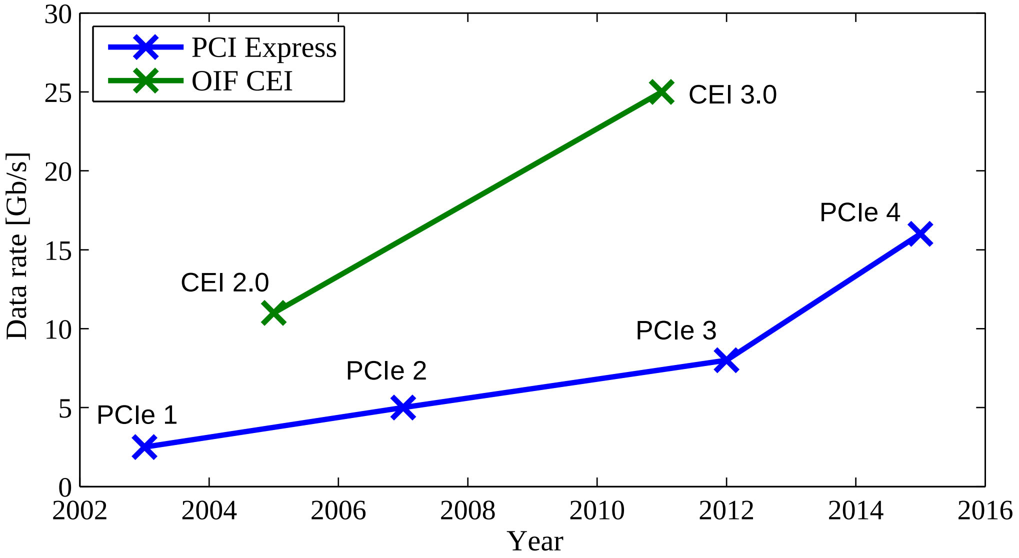

Figure 1.3: Example for the increase of data rates over recent years: Data rates specified by the Peripheral Component Interconnect Express (PCI Express or PCIe) standard [10, 11], and by the Optical Internetworking Forum (OIF) Common Electrical I/O (CEI) electrical and jitter interoperability agreements [12, 13]. In the case of the OIF CEI, which mainly targets high speed backplane and chip to chip interconnects, a data rate of 25 Gb/s (and even 28 Gb/s) is already part of the specification.

order to keep up with the challenges posed by increasing data rates.

A second aspect that has recently gained more attention is the energy efficiency of digital systems. Due to the development towards an IT-based industry which relies on the processing and storage of large amounts of data, gains in energy efficiency do not currently keep pace with the growth of installed resources. From an economic point of view, additional efforts towards the development of energy-efficient systems gain importance since the energy cost for the operation of servers have reached the same order of magnitude as the initial acquisition cost [14]. Also from an environmental point of view, the development of highly energy efficient solutions becomes more and more relevant due to the increasing environmental impact of installed IT systems: It is estimated that the energy consumption of servers and data centers in the US has more than doubled in the period from 2000 to 2006 [15]. The impact of information and communication technology can be illustrated by comparison to the aviation industry, which caused comparable global CO_2 emissions in 2008 [16].

In the past, much effort with regard to improved energy efficiency has been spent on the IC design, and in particular on power reduction for the internal logic. I/O links, which consume about 20-30 % of the total system power [9], provide chances for additional energy efficiency improvements. Optical interconnects are currently investigated as one option to improve energy efficiency by overcoming drawbacks related to classical copper interconnects. Optical links are state of the art for longer connections, ranging from internet backbone links down to rack level connections in data centers. For the PCB domain, however, considerable improvements with regard to production cost and integration have to be made before optical interconnects become a viable alternative. For this reason, improvements for classical copper interconnects provide the most direct way towards higher energy efficiency. This changes the goal of high-speed link design, and adds complexity to the analysis: The design target is not only to meet signal integrity requirements, but to do so in the most energy efficient way.

1.4 Content and Organization of this Work

In this work, the application of so-called "physics-based" via models for an efficient modeling of dense via arrays is proposed. Different approaches that can be used to calculate sub-blocks of the physics-based via model are reviewed and evaluated with regard to their impact on modeling accuracy. Additionally, effects which pose general limitations on the accuracy of the physics-based model for dense via arrays are investigated. Based on the findings, it is specified within which limitations with regard to the model geometry the physics-based via model can provide accurate results. The applicability of the model within these limitations is confirmed by comparison to full-wave results and measurements. Furthermore, it is studied how different choices of calculation methods and network parameters impact the efficiency of the physics-based via model for the simulation of large numbers of vias. With the results, an efficient algorithm for the model evaluation is proposed, and possible trade-offs between modeling accuracy and model efficiency are pointed out. The model is applied to study several physical effects related to PCB links and via arrays, including a study of crosstalk behavior for an array consisting of 10,000 vias. Finally, a systematic approach for the evaluation of link design alternatives is proposed. The approach combines the efficient physics-based via model with a time domain evaluation. The approach takes into account both signal integrity and energy efficiency, and allows a quantitative comparison between different designs in terms of the total link input power under identical constraints. The remaining chapters of this thesis are organized as follows:

Chapter 2 gives a short overview of the existing approaches to via modeling. The approaches are grouped into four categories, and compared in terms of their advantages and disadvantages. Based on the comparison, the application of physics-based via models for the modeling of dense via arrays is motivated.

Chapter 3 treats the physics-based via model in more detail. Starting from the physical background, the construction of the model from sub-blocks is described. For each sub-block, different calculation methods are described, which are evaluated with regard to their accuracy and efficiency in later chapters.

In **Chapter 4**, it is analyzed how different calculation methods for the sub-blocks of the physics-based via model change the modeling accuracy. Additionally, the impact of effects not included in the physics-based model is studied to determine the general limitations of the modeling approach for via arrays. The study is carried out using alternative modeling approaches including full-wave simulations. Together with the following efficiency study, the findings allow to choose an appropriate version of the physics-based via model for the modeling task.

Chapter 5 studies the numerical efficiency of the modeling approach. The efficiency is determined by the choice of calculation methods for the sub-blocks and by the choice of network parameters for the sub-block combination. Based on the findings, an efficient algorithm for the model evaluation is proposed, and trade-offs between modeling accuracy and modeling efficiency are pointed out. Together with the previous accuracy study, the results allow an adequate choice of the via model depending on the model geometry, the required accuracy, and the required simulation speed.

In **Chapter 6**, modeling results are compared to measurements. The comparison demonstrates that within the limitations found during the accuracy study, results obtained with the physics-based via model show a good agreement not only to other simulation results but also to measuremed results for practical via array structures.

In **Chapter 7**, the model is applied to study specific aspects related to signal integrity on PCBs. The chapter demonstrates the application of the physics-based model with several examples and at the same time provides insights about important design aspects, leading the way to the systematic analysis in the following chapter.

Chapter 8 presents a general approach for the design of PCB links that is based on the physics-based via model in combination with a time domain evaluation. The approach takes into account both signal integrity and energy efficiency and allows a quantitative comparison of different design alternatives.

1.5 Project Report, Conference and Journal Contributions

The main part of the work described in this thesis has been carried out during the project "Via Array Design in Multilayer Substrates for Application in Fast, Energy and Material Efficient Digital Systems" (original title: "Via-Arrays in Mehrlagensubstraten für den Einsatz in schnellen, energie- und ressourcensparenden digitalen Systemen"), which was funded by the German Research Foundation (DFG) for three years. The most important results of the project are summarized in the report to the German Research Foundation.

During the course of the project, preliminary results were presented at conferences [4,17–24]. An erratum to [4] was published in [25]). Journal papers have been published [7,26] or submitted [5] on three major aspects of the work: the accuracy of physics-based via models for dense via arrays [7], the efficiency of physics-based via models for large via constellations [26], and the application of the models in a systematic study of energy efficiency for PCB links [5]. A correction to [26] was provided in [27]. Some contributions to conference publications on related topics have been made in [8, 9, 28–34]. The results presented in the listed publications constitute a major part of this thesis. Additionally, results from students' theses [35–38] have contributed to this work as indicated at the corresponding points throughout this thesis.

2 Approaches to Via Modeling

For the modeling of vias in PCBs, several different approaches can be found in the literature. The model complexities range from simple static equivalent circuits for the analysis of a via transition through a single reference plane to numerical full-wave solutions that allow for the analysis of arbitrary geometries. Different modeling approaches differ in their accuracy, in the range of geometries that can be simulated, and in the involved computational effort. Typically, higher capabilities with regard to the first two aspects are related to a higher computational effort in terms of computation time and memory requirement. In this chapter, a short overview of different via modeling scenarios is given, and the main terms and definitions with regard to the via geometry are introduced. Subsequently, the existing approaches for via modeling are described and grouped into four categories. At the end of the chapter, a separate section deals with the applicability of the different model categories to the simulation of via arrays based on the respective advantages and disadvantages.

2.1 Via Modeling Scenarios

Via modeling approaches can be applied to different scenarios. A very simple scenario is shown in Fig. 2.1(a): a single via is crossing a single reference plane of a PCB. In this scenario, the via model has to predict the impact of the via on the signal transmission and reflection. In more complex cases, vias are crossing a PCB cavity formed by two reference planes (see Fig. 2.1(b)), or multiple cavities of a multilayer PCB (see Fig. 2.1(c)). In these cases, radial waveguide modes inside the cavity have an impact on the signal transmission as well as on the interaction between vias. In this thesis, scenarios with multiple cavities are studied, as they are encountered for high speed links in multilayer PCBs. The multilayer results are typically assembled from the simulation results for single cavities. In this sense, the scenario of vias crossing a single cavity constitutes the main building block of the simulation.

For a single via crossing a single cavity, important terms are given in Fig. 2.2. The via itself consists of the via barrel and – potentially – pads on the signal or reference layers. The via traverses the reference planes through antipads, which are circular cutouts in the metal planes. Fig. 2.2 also introduces the main parameters that are used to describe the via geometry and defines the coordinate system employed in this thesis.

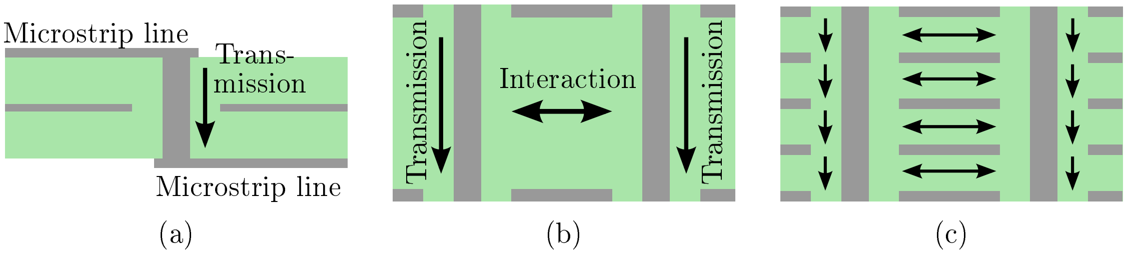

(a) (b) (c)

Figure 2.1: Different scenarios for via modeling. (a) Single via crossing a single reference plane. The excitation is typically provided by microstrip lines connected to the via. In this scenario, the goal is an accurate modeling of the signal transmission. (b) Vias crossing a single cavity formed by two reference planes. The excitation can be provided by microstrip lines or by components mounted on top of the PCB (not shown in the figure). The parallel-plate modes inside the cavity have an impact on the signal transmission as well as on the interaction (the crosstalk) between different vias. (c) Vias crossing multiple cavities. This is the scenario relevant for modeling via arrays in multilayer PCBs. In each cavity, an impact of parallel-plate modes on the signal transmission and on the interaction between vias exists.

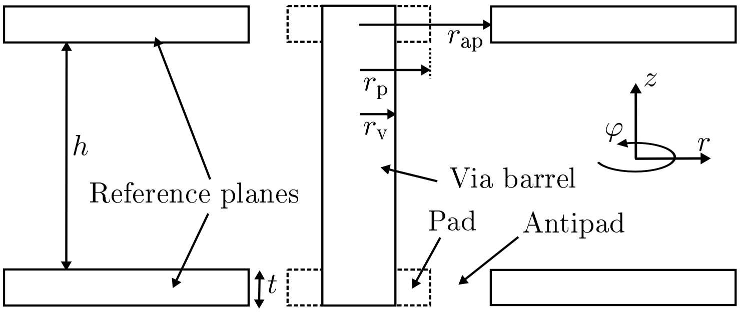

Figure 2.2: Schematic of a via crossing a single cavity with definitions of the different geometry parameters: via radius r_{v}, pad radius r_{p}, antipad radius r_{ap}, plane thickness t, and dielectric thickness h. The shown coordinate system is common for via modeling problems, and is employed throughout this thesis. It should be noted that most of the numerical examples studied in this thesis do not include pads in the simulation. Pads at the top and bottom via ends are, however, contained in the measured test structures.

2.2 Overview of Existing Approaches

Different via modeling approaches exist which can handle one or more of the modeling scenarios described in Section 2.1. This section gives an overview of the main approaches, grouping them into four categories and describing their applicability to the different modeling scenarios. The section is building upon previous overviews and categorizations which have been given in [39–41].

2.2.1 Quasi-Static Equivalent Circuit Models

Simple equivalent circuit models for via transitions can be found in the literature that are composed of lumped elements calculated under a quasi-static assumption. Typically, the models use a pi-equivalent circuit as shown in Fig. 2.3(a). Early investigations have focused on the modeling of a via transition through a single reference plane (see Fig. 2.1(a)). In this scenario, the via barrel is represented by its partial inductance and by its capacitance against the reference plane, which is split into an upper and a lower part. In some cases, an additional element for the via barrel resistance is included. Numerical approaches have been used in [42] to calculate capacitance and inductance values, in [43, 44] to calculate capacitance values only, and in [45] to calculate inductance values only. It should be noted that the equivalent circuit has also been applied to other configurations such as a via connecting two signal layers between two reference planes [46] or above a reference plane [47] (omitting one of the two capacitances in the latter case). In [48], the capacitance calculation in [43] was extended to a via crossing a cavity formed by two reference planes. In this case, the pi-equivalent circuit represents the via behavior inside the cavity, with the via barrel capacitances against bottom side of the upper plane and top side of the lower plane. In [49], capacitance and inductance values for a cavity were calculated, and the concatenation of single cavity models was used to obtain a model for a multilayer via setup as shown in Fig. 2.1(c). In [50], mutual capacitances and inductances between vias were added to the approach in [49] to simulate multiple vias inside a multilayer PCB. It shall be mentioned that in addition to the described numerical evaluations, also analytical formulas for capacitance and inductance values (including mutual via inductances) exist in the literature (see [51, ch. 5.5]). However, the analytical formulas only give approximate values, which are less accurate than the solutions obtained numerically.

Simple quasi-static equivalent circuit models exhibit two main limitations. First, the models typically represent only a single via. A coupling to other vias is not taken into account. This limitation is to some extent overcome by the inclusion of mutual capacitances and inductances in [50], which in this sense represents a step towards the physics-based via models discussed in the following section. Second, the quasi-static elements provide an acceptable approximation only up to a certain frequency limit. This is especially true for vias crossing one or several cavities formed by the reference planes of the PCB, since the quasi-static elements cannot represent the waveguide behavior of the parallel planes. The validity of quasi-static models up to a few GHz has been demonstrated in [49, 50] for a well defined return current path through adjacent vias. If the impact of the parallel planes is increased (e.g. if a larger portion of the return current is flowing as a displacement current

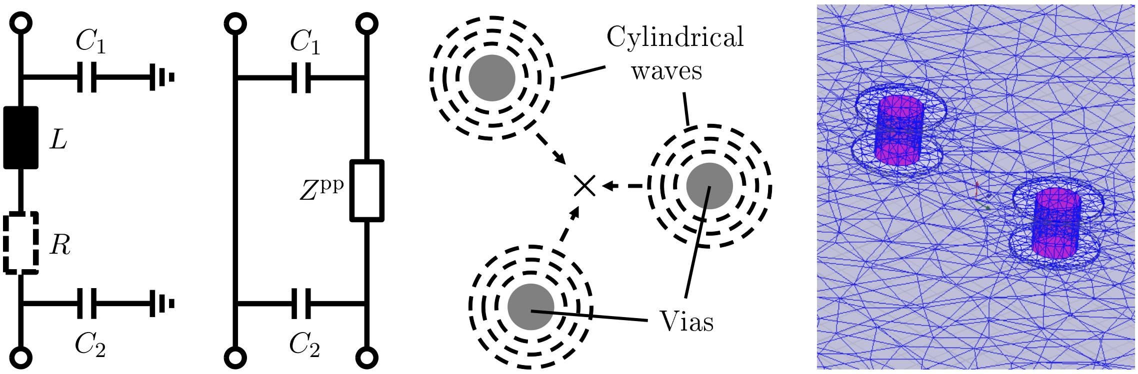

(a) (b) (c) (d)

Figure 2.3: Different approaches to via modeling. (a) Quasi-static equivalent circuit for a via transition through a single reference plane or for a via crossing a cavity formed by two reference planes. (b) Physics-based via model, taking into account the impact of the reference planes on the return current path through the parallel-plate impedance Z^{pp}. (c) Multiple scattering approach. The via modeling problem is formulated in terms of multiple scattering of cylindrical waves, with the via barrels acting as scatterers. (d) Simulation with a general purpose full-wave solver, requiring a discretization of the simulated structure. The discretization obtained with a commercial tool [52] is shown for two vias in a single cavity.

between the planes), the frequency range for which quasi-static models are valid is further reduced.

2.2.2 Physics-Based Via Models

In a second category of models, the two critical limitations of the quasi-static equivalent circuit models for vias that cross a PCB cavity are resolved by replacing the via inductance with the parallel-plate impedance Z^{pp}, see Fig. 2.3(b). In this work, this category of models will be referred to as "physics-based" via models. The term "physics-based" was used in several papers [40, 53–57] which suggested the integration of the parallel-plate impedance into an equivalent circuit to obtain a model that accurately represents the physical via behavior. The frequency dependent parallel-plate impedance takes into account the waveguide behavior of the complete cavity crossed by the via. In Fig. 2.3(b), it is placed in the right branch of the equivalent circuit to represent the fact that it describes the return current path rather than the partial inductance of the via barrel. The via barrel itself is often represented by a short circuit in the model, since its resistance and partial inductance are several orders of magnitude smaller than the parallel-plate impedance. Coupling between vias inside a cavity can be included in the physics-based via model by extending the parallel-plate impedance to an impedance matrix which includes self and coupling impedances of the via locations in the cavity. Although the physics-based model for multiple vias is sometimes also represented in an equivalent circuit fashion, calculations are more conveniently carried out based on network parameter matrices [58–61].

The parallel-plate impedance required for physics-based via models can be calculated from analytical formulas for infinite reference planes [62,63] and rectangular [63–65] or triangular [64, 66] cavities. For more complex geometries, special numerical approaches for planar structures can be employed. These approaches include the contour integral method (CIM) [64], which has been applied to PCB modeling e.g. in [41, 67, 68], or the transmission line matrix method (TLM) [69], which has been employed e.g. in [70]. For the capacitances between via barrel and reference planes, static solutions obtained from numerical solvers were used in early publications. Later, analytical formulas were derived [71, 72] that take into account the frequency dependent behavior of the capacitances. The capacitances can also be replaced by more complex models for the local field behavior [73]. A modeling of this type was applied to via problems already in [74, 75]. A combination of a more complex local field model with the parallel-plate impedance was suggested in [76]. Physics-based via models are typically set up for vias crossing a single cavity. Models for multilayer PCBs can be obtained through a combination of single cavity results, which can e.g. be carried out using segmentation methods [77].

2.2.3 Multiple Scattering Approaches

As a third category of methods, multiple scattering approaches can be applied to via modeling problems. The general form of multiple scattering solutions is given by the so-called Foldy-Lax equations for multiple scattering of waves [78–80]. In general terms, the Foldy-Lax equations state that for scattering problems, the total wave quantity at each point in space is a superposition of the incident wave and all scattered waves. With a known incident wave and known scattering behavior at all scattering bodies, the Foldy-Lax equations allow setting up systems of linear equations to calculate the wave quantities at the positions of the scatterers. When applied to the modeling of vias in a PCB cavity in [81, 82], the Foldy-Lax equations are formulated in terms of cylindrical waves, which are the eigenmodes of the radial waveguide formed by the cavity. The incident waves result from the fields in the via antipads, which are related to a certain excitation voltage. The via barrels are acting as scatterers, as indicated in Fig. 2.3(c). The solution of the multiple scattering equations results in the field coefficients at the via locations, from which the via currents can be calculated. In a final step, the admittance parameter matrix for the cavity can be obtained from the ratios between via currents and excitation voltages. A detailed description of a multiple scattering approach for via modeling is given in Appendix A.

In theory, multiple scattering approaches can provide an exact full-wave solution for the simulation of multiple vias inside a PCB cavity with infinite planes. In practice, the accuracy is limited since only a finite number of radial waveguide modes can be taken into account. Nevertheless, since the applied scattering formulation is well adapted to the special geometry of the via modeling problem, it can provide an accuracy comparable to general purpose full-wave solvers with reduced computational effort. In recent years, multiple scattering approaches have been extended for several practical application scenarios. The simulation of layered dielectric substrates has been treated in [83]. Through numerical calculation of the exciting fields, arbitrary shapes of pads and antipads [84] and shared antipads [85] can be taken into account. Furthermore, multiple scattering approaches for finite reference planes have been formulated in [86, 87]. Like the physics-based via model, multiple scattering approaches provide the solution for a single cavity. For multilayer PCBs, a combination of single cavity results has to be carried out, for which the same methods as for the physics-based model can be used.

2.2.4 General Purpose Full-Wave Approaches

Obviously, general purpose full-wave approaches can also be applied to via modeling problems. In contrast to the previously described methods, general purpose full-wave approaches work with a discretization of the structure, as shown in Fig. 2.3(d) for the discretization of two vias in a single cavity obtained with a commercial tool [52]. A main advantage of full-wave solvers lies in their high flexibility with regard to the modeled structures. Arbitrary shapes of vias, pads and ground pads can be taken into account as well as arbitrarily shaped splits and gaps in reference planes. Very accurate simulation results can be obtained as long as a sufficiently fine discretization of the modeled geometry is used. Due to the confined geometry of PCB modeling problems, volume based methods such as the finite element method (FEM) [88], the finite-difference time-domain (FDTD) method [89,90], or the finite integration technique (FIT) [91] are well suited if only the internal structures of the PCB have to be modeled. Surface based methods such as the method of moments (MoM) [92] are useful if also radiation and interaction with external structures have to be taken into account. A combination of CIM and MoM to handle both internal and external structures efficiently has been proposed in [93]. To exploit the layered structure of PCBs, also adapted full-wave approaches such as the multilayered finite difference method (M-FDM) [94] and the multilayered finite element method (M-FEM) [95] have been developed.

2.3 Applicability to Via Array Modeling

Due to their different advantages and disadvantages described in the previous section, not all via modeling approaches are applicable to via arrays in the context of high-speed digital links. Quasi-static equivalent circuit models are typically not suited for the analysis of via arrays due to their limitation to a single via and one or two reference planes. Even if the approach is extended to multiple vias in a multilayer PCB as described in [49, 50], the approach is inherently limited with regard to the coupling between distant vias and with regard to the covered frequency range due to the omission of the parallel-plate impedance. For this reason, quasi-static models are not applied in this thesis.

General purpose full-wave methods, in contrast, can provide very accurate results. Furthermore, they can be applied to all geometries occurring in single- or multilayer PCBs. However, as previously indicated, this accuracy and flexibility come at a high computational cost. The simulation of large via arrays with 1000 or more vias is not possible with general purpose full-wave methods due to their high memory demand. Even for comparatively small structures with less than 100 vias, the simulation of a few 100 frequency points takes several days, which is too long for practical design processes. For this reason, full-wave methods are not promising for via array simulations even in light of an expected further development of the methods and of the available computational resources. Nevertheless, general purpose full-wave solvers are a valuable tool for model validation. In this thesis, commercial full-wave solvers are used to validate modeling results for structures consisting of up to 64 vias.

With the previous considerations, physics-based via models and multiple scattering methods remain as candidates for the modeling of PCBs containing large via arrays. In general, both methods are well suited for this modeling task. Typically, multiple scattering approaches provide higher accuracy, with the specific accuracy and efficiency depending on the number of radial waveguide modes that are taken into account in the calculation. On the other hand, physics-based via models, which take into account only one mode for the calculation of the parallel-plate impedance (see Section 3.2.1), provide a higher modeling efficiency. In this thesis, the focus is on the application of physics-based via models to via array modeling. An argument for the selection of the more efficient modeling approach may be made in light of previous investigations: even with the physics-based model, a calculation time of more than two hours was observed for the simulation of 1000 vias in a single cavity with 100 frequency points in [1], p. 105. Considering the demand for short simulation times in practical design processes, it makes sense to choose the most efficient model and investigate possible further improvements with regard to accuracy and efficiency. However, this decision means that some general limitations with regard to the modeling accuracy have to be expected. Multiple scattering methods are applied in this thesis for model validation. Additionally, they are used for the study of some physical effects, since they provide a way to study the relevance of different radial waveguide modes separately.

2.4 Summary and Discussion

An overview of via modeling approaches falling into four main categories has been given in this chapter. Models in the category of quasi-static equivalent circuits are not suitable for the simulation of via arrays due to their limited accuracy. General purpose full-wave solvers provide a high accuracy, but can be applied only to a limited number of vias due to their high computational cost. Two model categories are in general well suited for the modeling of via arrays: physics-based via models and multiple scattering approaches. In this thesis, physics-based via models are applied to the simulation of large via arrays. In comparison to multiple scattering approaches, physics-based models provide a higher modeling efficiency, which is important for practical design processes. At the same time, the higher efficiency means that some limitations with regard to the modeling accuracy have to be expected.

3 Construction of the Physics-Based Via Model

As a foundation for the following studies, a more detailed description of the physics-based model is provided in this chapter. In the first part of the chapter, a general description of the physical behavior of vias inside a PCB cavity is given, and the connection to the block diagram of the physics-based model is pointed out. In the second part, the sub-blocks of the physics-based model are explained. For each sub-block, at least two alternative approaches to calculate the corresponding network parameters are described as a basis for the following studies of model accuracy in Chapter 4 and model efficiency in Chapter 5. In the third part of the chapter, the combination of the model sub-blocks to form the cavity models and then to form the complete multilayer PCB model is described. Finally, a short summary of a modal decomposition approach is given that allows for the inclusion of traces in the physics-based via model, which is important for the analysis of practical links.

3.1 Physical Behavior of Vias

In this section, the physical behavior of vias inside a PCB cavity is described in terms of the eigenmodes of the radial waveguide. First, the radial waveguide modes excited in the cavity by vertical via currents are described and classified according to their central properties for the via model. In a second step, a subdivision of the cavity model into different field regions based on the predominant waveguide modes is carried out, and a corresponding circuit block diagram is presented.

3.1.1 Radial Waveguide Modes in a PCB Cavity

The basic geometry of a PCB cavity is of a comparably simple nature: cylindrical vias are enclosed between parallel reference planes. This geometry lends itself to an analysis of the electromagnetic fields inside the cavity in terms of radial waveguide modes. In principle, two types of radial waveguide modes exist: Transverse Electric (TE^z) and Transverse Magnetic (TM^z) modes. However, vertical via currents only excite TM^z modes, which are related to a vertical magnetic vector potential. A general description of TM^z modes in the radial waveguide is given in [96, ch. 9.4]. Here, only the z-component of the electric field (the component orthogonal to the reference planes) is shown, which is sufficient to illustrate the main properties of the TM^z modes. The E^z component of the TM^z mode in cylindrical coordinates is given as [96, ch. 9.4]

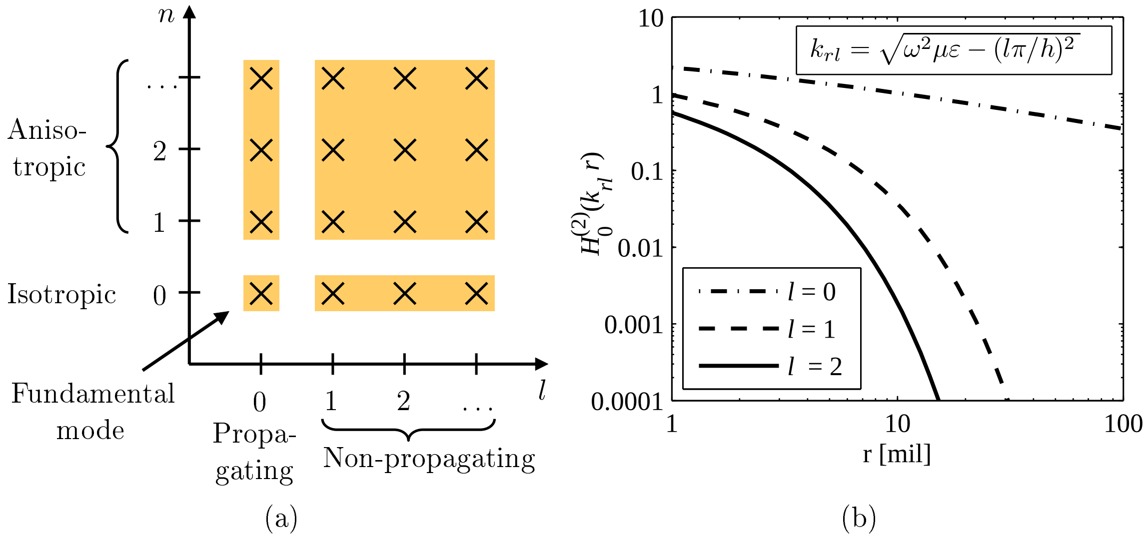

Figure 3.1: Radial waveguide modes inside a PCB cavity. (a) Classification of modes with different mode numbers according to their properties. (b) Plot showing the attenuation due to the Hankel function in (3.1) with increasing distance r to the via barrel for $\{l = 0, 1, 2\}$, $h = 12\,\text{mil}$, $\mu = \mu_0$ and $\varepsilon = 3.8 \cdot \varepsilon_0$ at $f = 50\,\text{GHz}$ (Figure adapted from [7]).

$$E^z_{ln}(r, \varphi, z) = -\mathrm{j}B_{ln}\frac{k^2_{rl}}{\omega\mu\varepsilon}H^{(2)}_n(k_{rl}r)\cos(n\varphi)\cos\left(\frac{l\pi}{h}z\right), \tag{3.1}$$

with the radial wavenumber

$$k_{rl} = \sqrt{\omega^2\mu\varepsilon - (l\pi/h)^2}. \tag{3.2}$$

In (3.1) and (3.2), $\omega = 2\pi f$ is the angular frequency, ε and μ are the permittivity and permeability of the dielectric medium, h is the thickness of the dielectric substrate (equal to the separation between upper and lower reference plane) and l and n give the mode order with respect to variations in z-direction and in φ-direction (angular direction). In (3.1), $H^{(2)}_n$ is the Hankel function of second kind and order n, and B_{ln} is the constant weight factor of the corresponding mode. For $n > 0$, the TM^z_{ln} modes become anisotropic due to the $\cos(n\varphi)$ factor. For $l > 0$ (which introduces a field variation in z-direction), the TM^z_{ln} modes have a cutoff frequency which can be calculated by setting the radial wavenumber given in (3.2) equal to zero. For dielectric thicknesses and material parameters encountered in typical PCBs, all modes with $l \geq 1$ are cut off in the frequency range of interest for signal integrity investigations. In the case of $l = 1$, $h = 20\,\text{mil}$, $\mu = \mu_0$ and $\varepsilon = 3.8 \cdot \varepsilon_0$, for example, the cutoff frequency is about 150 GHz. This leads to the classification of TM^z modes shown in Fig. 3.1(a). The fundamental mode of the radial waveguide is the

TM_{00}^{z} mode, which is isotropic and propagating. For $n \geq 1$, the modes are anisotropic, whereas for $l \geq 1$, they do not propagate. The attenuation of the propagating and the first two non-propagating modes with an increasing distance to the via barrel is illustrated in Fig. 3.1(b).

3.1.2 Subdivision of the Cavity

As already mentioned in Chapter 2, the physics-based via model is based on the simulation of coupled vias in a single cavity. Starting from the relevant types of waveguide modes, the cavity can be partitioned into different domains. To illustrate these domains, a vector plot of the electric field is shown in Fig. 3.2(a) for the cross section through two vias in a single cavity. At Port 1, the structure is excited by the transverse electromagnetic (TEM) mode of the short coaxial waveguide formed by the via and the reference plane. The excitation can originate either from an external source - such as a connected microstrip line - or from an adjacent cavity. Inside the cavity, a mode conversion between coaxial waveguide mode and radial waveguide modes occurs. In the vicinity of the via, both propagating and non-propagating radial waveguide modes exist. The superposition leads to the observed field pattern with field lines starting on the via barrel and ending on the reference planes. In some distance from the via barrels, all non-propagating modes are attenuated so far that only the propagating modes are relevant. The propagating modes are characterized by electric field vectors which are orthogonal to the reference planes and independent of the z-coordinate. The observed field behavior leads to a partitioning of the cavity into three different domains as shown in Fig. 3.2(b): coaxial waveguide regions formed by vias and antipads, local field regions around the vias inside the cavity, and the propagating field region between the local field regions.

The "physical" partitioning of the cavity can directly be translated into an equivalent circuit block diagram as shown in Fig. 3.2(c) for the case of two vias. Each domain in the physical cavity is represented by an equivalent circuit or a network parameter block. The propagating field model provides the interaction between different vias, while each via is represented by a local field model with connected antipad models. The equivalent circuit is modular in the sense that the calculation methods for different blocks can be chosen independently of each other. In the following section, at least two approaches for the calculation of each network parameter block are presented in detail.

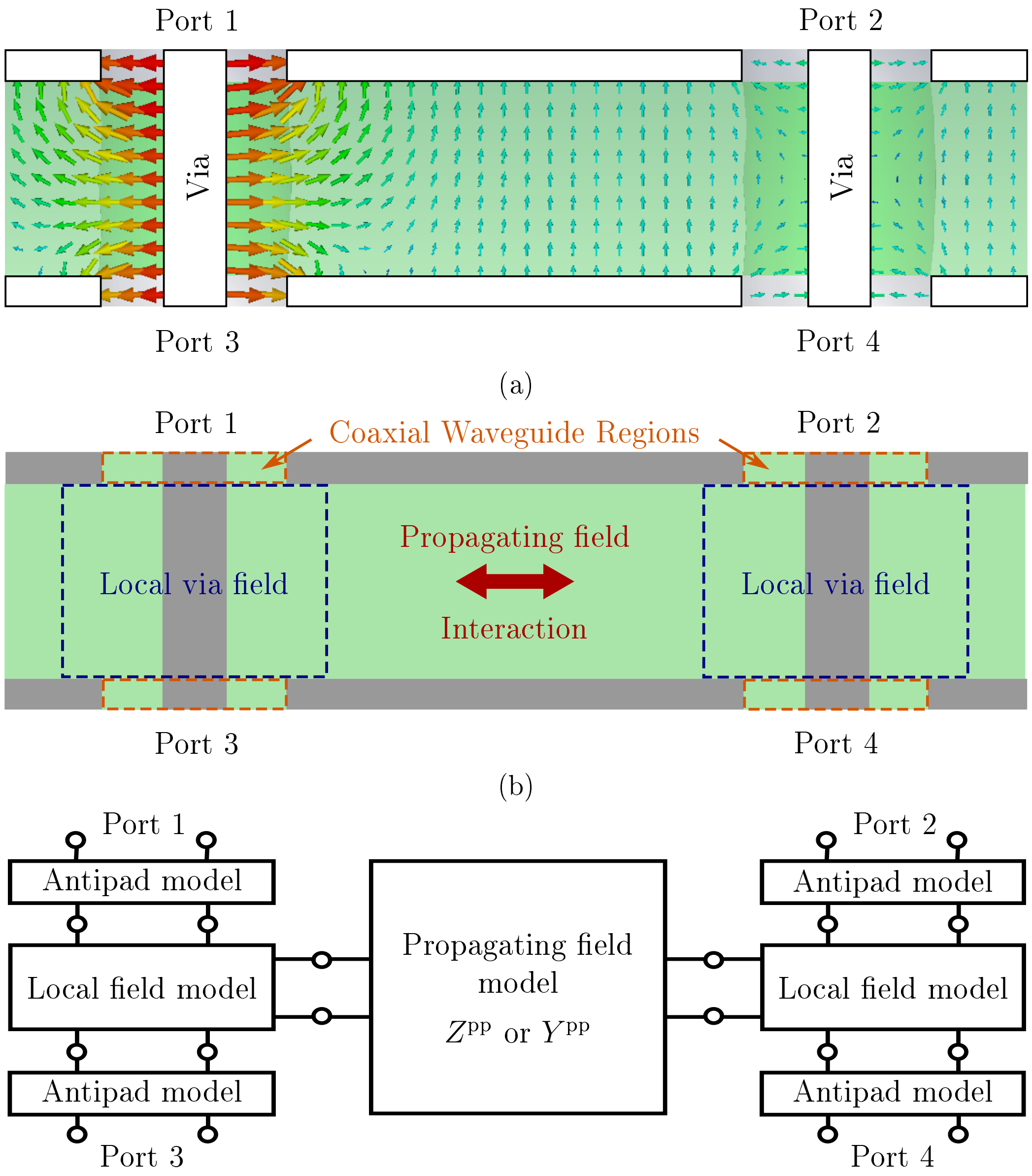

(a)

(b)

(c)

Figure 3.2: Partitioning of the PCB cavity. (a) Vector plot of the electric field in the cross section of a cavity with two vias for excitation with the coaxial TEM mode at port 1, obtained with a full-wave solver [97]. Close to the vias, the electric field distribution results from a superposition of the fundamental mode and non-propagating modes. In a larger distance to the vias, the fundamental mode is predominant, leading to a constant electric field oriented in z-direction. (b) Based on the predominant waveguide modes, the cavity can be partitioned into local via field regions and the propagating field region. Additionally, short coaxial waveguide regions exist in the via antipads (Figure adapted from [26]). (c) Equivalent circuit block diagram corresponding to the physical partitioning of the cavity. Each block can be represented by a network parameter description, so that the calculation methods for different blocks can be selected independently (Figure adapted from [26]).

3.2 Subdomain Modeling Approaches

In this section, different modeling approaches for the calculation of the sub-blocks of the physics-based via model in Fig. 3.2(c) are described. The description is based on the comprehensive overview of calculation methods for the physics-based model given in [1,59]. Additional approaches which can be found in the literature are included in the discussion, so that for each sub-block, at least two alternative approaches are discussed. The additional approaches take into account effects that were neglected in earlier implementations of the physics-based model, potentially providing more accurate modeling results.

3.2.1 Propagating Field Model

In this thesis, the propagating field model is typically calculated assuming infinite reference planes—which is equivalent to a perfectly matched layer (PML) boundary condition. Infinite reference planes are a good approximation for real PCB structures if reflections from the board edges can be neglected. This is the case for large PCBs with lossy dielectric substrates, or if signal vias are sufficiently shielded from the edges by ground vias [98]. For design studies of a general type, the assumption of infinite reference planes has the advantage that the fundamental behavior of structures can be studied, without an additional impact of the cavity resonances. A calculation of the propagating field model in case of infinite planes can be carried out using the radial waveguide method (RWM) as described in [1] based on [62, 63]. The formulation is derived for the fundamental radial waveguide mode and gives the following values for the self and transfer impedances:

$$Z_{ij}^{\mathrm{pp}}(f) = \frac{\mathrm{j}\eta h}{2\pi r_{\mathrm{v}} H_1^{(2)}(k r_{\mathrm{v}})} \cdot H_0^{(2)}(k r_{ij}), \tag{3.3}$$

where $\eta = \sqrt{\mu/\varepsilon}$ is the wave impedance and $k = \omega\sqrt{\mu\varepsilon}$ is the wavenumber, r_{v} is the radius of via i, and r_{ij} is the center to center via separation (with $r_{ij} = r_{\mathrm{v}}$ for the evaluation of the self impedance). To take into account conductor and dielectric losses in the calculation of the propagating field model, a complex radial wavenumber can be used as described e.g. in [1, 59] based on [64, ch. 2.2.1]. It should be noted that the formulation in (3.3) is extended by an additional Bessel function in the transfer impedance term in [98, 99] to include the radius of the second via. However, the results of the extended formulation are very similar to the results of the original formulation for typical PCB geometries [1].

An alternative formulation to calculate the parallel-plate impedance for infinite planes was derived in [8] based on the CIM with circular ports for isotropic excitations [99]. In the CIM based formulation, the parallel-plate impedance matrix is calculated from two matrices $\overline{\overline{U}}$ and $\overline{\overline{H}}$ as [8]

$$\overline{\overline{Z}}^{\mathrm{pp}} = \overline{\overline{U}}^{-1}\overline{\overline{H}}, \tag{3.4}$$

where

$$U_{ij} = \frac{k\pi r_{\mathrm{v},j}}{\mathrm{j}} \cdot \begin{cases} J_0(kr_{\mathrm{v},i})J_1(kr_{\mathrm{v},j})H_0^{(2)}(kr_{ij}), & (i \neq j) \\ J_0(kr_{\mathrm{v},i})H_1^{(2)}(kr_{\mathrm{v},i}), & (i = j) \end{cases} \tag{3.5}$$

and

$$H_{ij} = \frac{k\eta h}{2} \cdot \begin{cases} J_0(kr_{\mathrm{v},i})J_1(kr_{\mathrm{v},j})H_0^{(2)}(kr_{ij}), & (i \neq j) \\ J_0(kr_{\mathrm{v},i})H_0^{(2)}(kr_{\mathrm{v},i}), & (i = j) \end{cases}, \tag{3.6}$$

with the Bessel functions J_0 and J_1 of order 0 and 1. In contrast to the radial waveguide method, which neglects the presence of other vias in the calculation of self- and transfer impedances, the CIM based formulation takes into account backscattering from all vias inside the analyzed cavity, which may lead to more accurate modeling results. It shall however be pointed out that neither of the described propagating field models takes into account the impact of non-propagating modes or anisotropic modes on the interaction between vias. For this reason, the accuracy study carried out in Chapter 4 addresses three points with respect to the propagating field model: a comparison of the two described models, an evaluation of the impact of neglected non-propagating modes, and an evaluation of the impact of neglected anisotropic modes.

As mentioned in Section 2.2.2, approaches exist that take into account the impact of finite planes. A short overview of references related to these approaches is given here, since evaluations for finite planes are included in Chapter 5 and Chapter 7 of this thesis. In the case of finite reference planes, the edges of the cavity act in good approximation as perfect magnetic conductor (PMC) or "open" boundaries, which lead to a reflection of the radial waveguide modes. In case of a rectangular cavity, the parallel-plate impedance can be obtained in two ways. In the radial waveguide method, reflections from the edges of the cavity can be taken into account using image layers [63, 100]. Alternatively, the cavity resonator method (CRM) [64, 65] directly takes into account the boundary conditions at the cavity edges in the solution of the 2D Helmholtz equation, which leads to a double infinite sum of cavity modes for the parallel-plate impedance. Several works have proposed ways to reduce the numerical effort for the CRM, see e.g. [101, 102]. In [100], a hybrid method combining RWM with image layers and CRM was proposed to further reduce the numerical effort. For more complicated plane shapes, segmentation methods [103, 104] or numerical methods for planar structures [41, 67, 68, 70] as mentioned in Section 2.2.2 may be applied to calculate the parallel-plate impedance at the cost of a higher numerical effort.

3.2.2 Local Field Model

To model the impact of higher order modes (more specifically non-propagating, isotropic modes) at the via locations, the via barrel-to-plane capacitance is used in the physics-based via model as described in [1, 59]. The formula for the barrel-to-plane capacitance is given in [71] as

$$C^{\mathrm{b}} = \frac{8\pi\varepsilon}{h \cdot \ln(r_{\mathrm{ap}}/r_{\mathrm{v}})} \sum_{l=1,3,5,\ldots}^{L} \frac{H_0^{(2)}(k_{rl}r_{\mathrm{ap}}) - H_0^{(2)}(k_{rl}r_{\mathrm{v}})}{k_n^2 H_0^{(2)}(k_{rl}r_{\mathrm{v}})}. \tag{3.7}$$

In comparison to the parallel-plate impedance, (3.7) additionally depends on the antipad radius r_{ap}. The utilization of the barrel-to-plane capacitance corresponds to physical intuition, and its inclusion in the physics-based model has provided accurate results e.g. in [58, 59] for the simulation of distributed vias. However, the capacitance model does not fully include the effects of mode conversion between coaxial waveguide modes and radial waveguide modes taking place in the vicinity of the via. Equivalent circuit models that contain more elements for a more accurate representation of the mode conversion can be found in the literature. In [73], the equivalent circuit in Fig. 3.3(a) was derived for the coaxial waveguide to radial waveguide junction. Although the work was carried out in an antenna context, it can readily be applied to via modeling, as already pointed out in [59]. In [76], the model shown in Fig. 3.3(b) was derived specifically in a via modeling context.

Here, the model in Fig. 3.3(a) is analyzed in more detail. In the following, the model will be referred to as "Williamson model" after the author of [73]. In the following, the different model elements are evaluated for typical geometry and material parameters: $r_{\mathrm{v}} = 5\,\mathrm{mil}$, $r_{\mathrm{ap}} = 15\,\mathrm{mil}$, $h = 10\,\mathrm{mil}$, and $\varepsilon_r = 3.8$. The Williamson model contains two elements - $\mathrm{j}B_{\mathrm{a}}$ and $\mathrm{j}B_{\mathrm{c}}$ - in parallel to the via ports (Port 1 and Port 2). These elements behave like capacitances. Their values are close to the via barrel-to-plane capacitances calculated according to (3.7). However, with increasing frequency, some deviation becomes notable as shown in Fig. 3.4(a). Furthermore, the formulations used in (3.7) and in [73] show a different convergence behavior. While the evaluation of the via barrel-to-plane capacitance requires about 50 modes (see convergence behavior for the first modes in Fig. 3.4(b)), the values for $\mathrm{j}B_{\mathrm{a}}$ and $\mathrm{j}B_{\mathrm{c}}$ converge after less than 5 modes. A more important difference to the simple capacitance model lies in the three additional elements which are present in the Williamson model: an ideal transformer with ratio R, and the admittances $\mathrm{j}B_{\mathrm{b}}$ and $\mathrm{j}B_3$, which behave like a positive and a negative inductance, respectively. For frequencies up to about 10 GHz, the transformer ratio R is close to 1, and $\mathrm{j}B_{\mathrm{b}}$ and $\mathrm{j}B_3$ have magnitudes

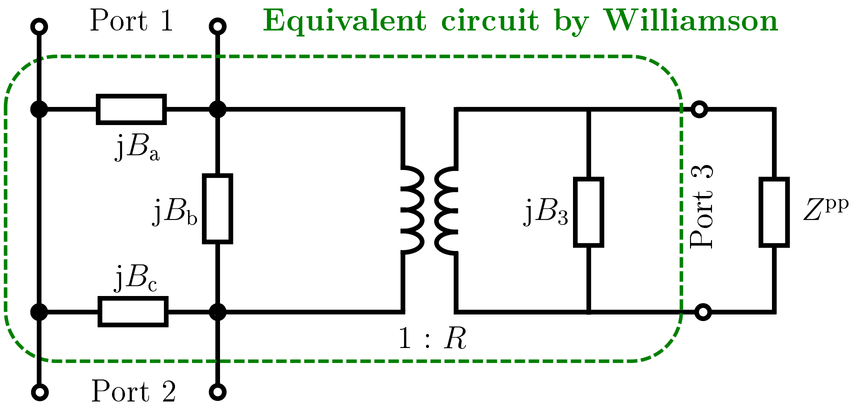

(a)

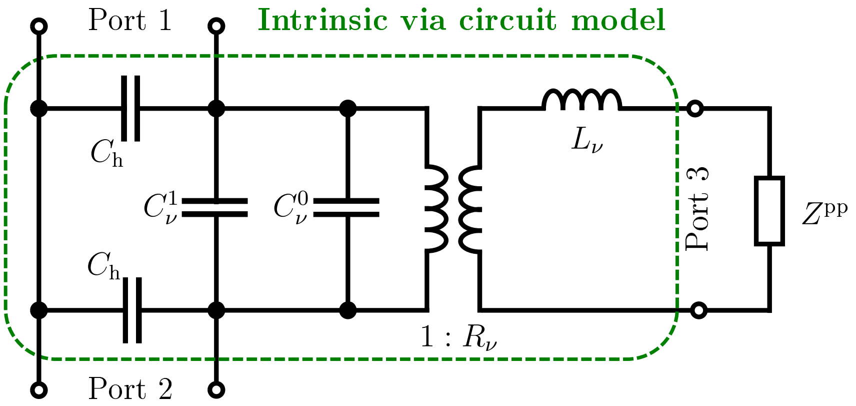

(b)

Figure 3.3: Alternative local field models with additional elements for a more accurate representation of the mode conversion taking place in the vicinity of the via. (a) Model for a coaxial to radial waveguide junction suggested in [73] - in the following referred to as "Williamson model" (Figure from [7]). (b) So-called intrinsic via model suggested in [76] (Figure from [7]). In comparison to the Williamson model, a different topology with frequency dependent capacitances and inductances is chosen. C_ν^1 takes negative values. In the numerical evaluation, the two models lead to very similar (but not identical) results.

similar to each other, so that they cancel out, which explains why the simple capacitances used in earlier implementations of the physics-based model are a very good approximation in this frequency range. With higher frequencies, the transformer ratio increases as shown in Fig. 3.5(a). At 50 GHz, the transformer modifies the parallel-plate impedance by a few percent. The magnitudes of $\mathrm{j}B_\mathrm{b}$ and $\mathrm{j}B_3/R^2$ become different at about 30 GHz, as shown in Fig. 3.5(b). The elements lead to an impedance Z^par in parallel to the parallel-plate impedance. Since the value of Z^par decreases with frequency (see Fig. 3.5(c)) while the value of Z^pp increases (see Fig. 3.5(d)), Z^par leads to an increasing modification of the parallel-plate impedance as seen from the via ports. At 40 GHz, Z^par modifies the value

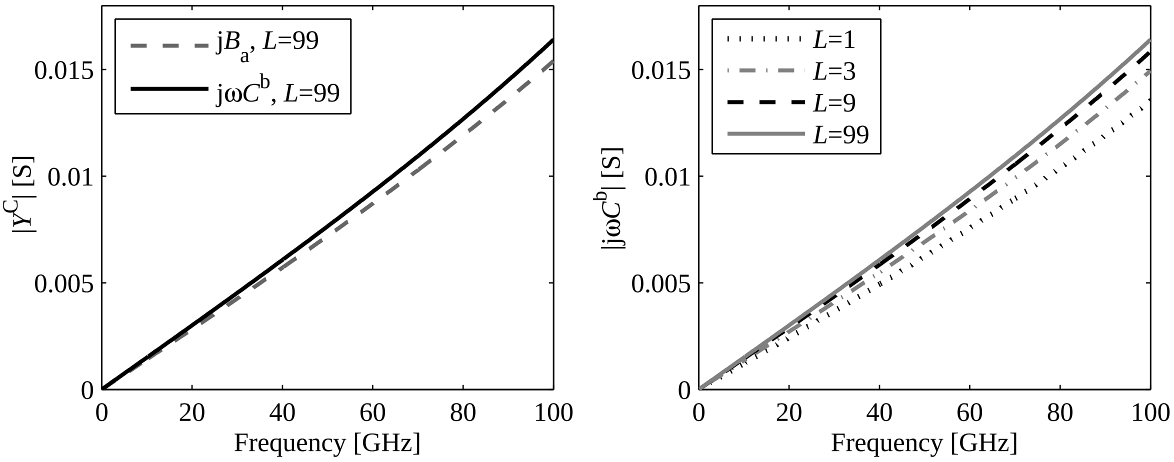

(a) (b)

Figure 3.4: (a) Comparison of the frequency dependent admittance $\mathrm{j}B_\mathrm{a}$ in the Williamson model (see Fig. 3.3(a)) and the admittance $\mathrm{j}\omega C^\mathrm{b}$ of the via barrel-to-plane capacitance in (3.7) for $r_\mathrm{v} = 5\,\mathrm{mil}$, $r_\mathrm{ap} = 15\,\mathrm{mil}$, $h = 10\,\mathrm{mil}$, and $\varepsilon_r = 3.8$. The comparison shows that the admittance $\mathrm{j}B_\mathrm{a}$ in the Williamson model behaves essentially like the via barrel-to-plane capacitance. However, an increasing deviation exists in the higher GHz range (about 6 % at 40 GHz). (b) Convergence behavior of the frequency dependent admittance $\mathrm{j}\omega C^\mathrm{b}$ calculated from the via barrel-to-plane capacitance. About 50 modes have to be taken into account to obtain a good approximation of the infinite sum in (3.7). In contrast, the calculation of $\mathrm{j}B_\mathrm{a}$ requires less than five modes for a good approximation.

of $Z^\mathrm{pp} \cdot R^2$ by about 15 %. The impact of the Williamson model and the intrinsic via model with their additional elements on the simulation results in comparison to the simple capacitance model will be investigated in detail for several via structures in the accuracy study in Chapter 4.

3.2.3 Coaxial Field Model

The previously presented propagating field models and local field models assume an excitation by the TEM mode of the coaxial waveguide. The coaxial field region itself can be modeled using either only a coaxial capacitance or a short transmission line (TL) segment. The coaxial capacitance, which is employed in the model in [59], can be calculated from the per unit length capacitance of the coaxial waveguide [105, ch. 3.1],

$$C'_\mathrm{coax} = \frac{2\pi\varepsilon}{\ln(r_\mathrm{ap}/r_\mathrm{v})}, \tag{3.8}$$

by multiplication with the reference plane thickness t (or $t/2$ for inner planes, if a coaxial

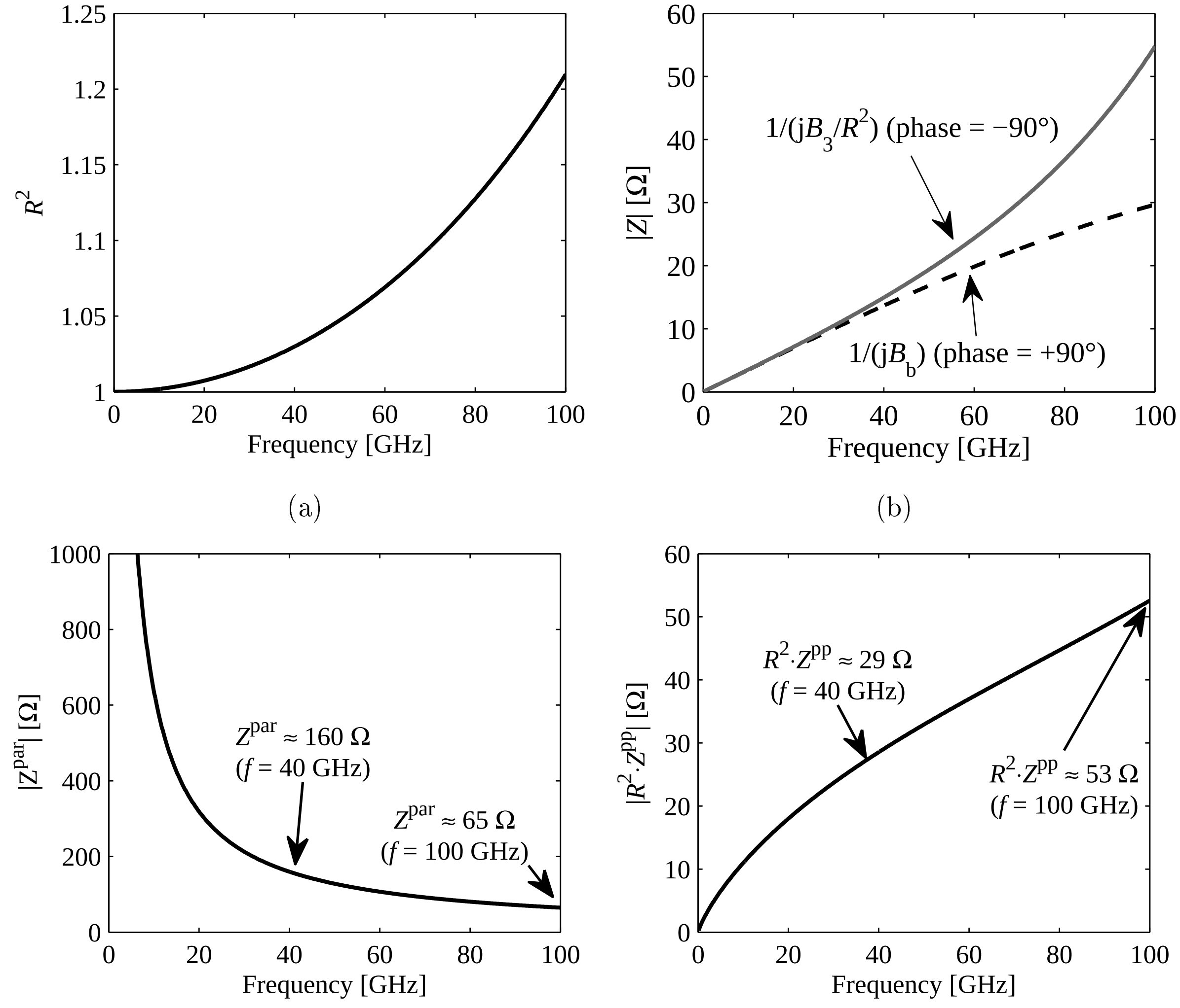

(a) (b)

(c) (d)

Figure 3.5: Evaluation of the additional elements contained in the Williamson model for $r_\mathrm{v} = 5\,\mathrm{mil}$, $r_\mathrm{ap} = 15\,\mathrm{mil}$, $h = 10\,\mathrm{mil}$, and $\varepsilon_r = 3.8$. (a) Plot showing the square of the transformer ratio R. The impact of the transformer in the equivalent circuit increases with frequency. At 50 GHz, it leads to a modification of the parallel-plate impedance Z^pp by about 5 %. (b) In addition to the transformer, the Williamson model contains two further elements in parallel to Z^pp: B_b and B_3, with the latter one placed behind the transformer. The plot compares the resulting impedances of the two elements. (c) The parallel elements can be summarized to a single impedance $Z^{par} = 1/(\mathrm{j}B_\mathrm{b} + \mathrm{j}B_3/R^2)$ in parallel to Z^pp. In the lower GHz range, the similar values and opposite phases of $\mathrm{j}B_\mathrm{b}$ and $\mathrm{j}B_3/R^2$ lead to a high impedance that does not considerably modify the parallel-plate impedance. In the higher GHz range, in contrast, Z^par and Z^pp are in the same order of magnitude, as demonstrated by the plot of Z^pp (modified by the transformer) in (d) for a single via and infinite reference planes.

field model with half the plane thickness is assigned to each of the two adjacent cavities). The transmission line model, which correctly takes into account the phase shift of the signal due to its propagation through the metal layers of the PCB, additionally requires the per unit length inductance of the coaxial waveguide [105, ch. 3.1]

$$L'_{\mathrm{coax}} = \frac{\mu}{2\pi} \cdot \ln(r_{\mathrm{ap}}/r_{\mathrm{v}}). \tag{3.9}$$

With the values for per unit length capacitance and per unit length inductance, the two-port network parameters of the LC transmission line model can be calculated.

3.3 Combination of Partial Results

After the selected models for the different subdomains have been evaluated for the studied structure, the obtained partial results have to be combined to obtain the overall solution. The combination of results can be divided into two parts: the combination of the subdomain results for a single cavity, and the combination of single cavity network parameters to obtain the final network parameters of the complete structure.

3.3.1 Combination of Cavity Subdomains

Before the different subdomain models can be combined, the propagating field model has to be expanded to represent upper and lower via ports as described in [59]. In Y-parameters, the expansion is a simple matrix operation:

$$\overline{\overline{Y}}^{\mathrm{pp}}_{\mathrm{exp}} = \begin{bmatrix} \overline{\overline{Y}}^{\mathrm{pp}} & -\overline{\overline{Y}}^{\mathrm{pp}} \\ -\overline{\overline{Y}}^{\mathrm{pp}} & \overline{\overline{Y}}^{\mathrm{pp}} \end{bmatrix}. \tag{3.10}$$

After the matrix expansion, the local field models can be included to obtain the admittance matrix $\overline{\overline{Y}}^{\mathrm{cav}}$, which represents the via behavior inside the cavity. If the via barrel-to-plane capacitance is used as a local field model, the inclusion is a simple addition of the corresponding admittances to the diagonal terms of the expanded propagating field matrix $\overline{\overline{Y}}^{\mathrm{pp}}_{\mathrm{exp}}$:

$$Y^{\mathrm{cav}}_{ij} = \begin{cases} Y^{\mathrm{pp}}_{\mathrm{exp},ij} + \mathrm{j}\omega C^{\mathrm{b}}_{i}, & (i = j) \\ Y^{\mathrm{pp}}_{\mathrm{exp},ij}, & (i \neq j) \end{cases}. \tag{3.11}$$

In case of a more complex local field model, all entries of $\overline{\overline{Y}}^{\mathrm{pp}}_{\mathrm{exp}}$ are modified. If the Williamson model is used as a local field model for a cavity with N vias, it can be combined with the expanded propagating field matrix $\overline{\overline{Y}}^{\mathrm{pp}}_{\mathrm{exp}}$ in the following way:

$$Y^{\mathrm{cav}}_{ij} = \begin{cases} \mathrm{j}B_{\mathrm{a}} + \mathrm{j}B_{\mathrm{b}} + \dfrac{1}{R_i R_j}(\mathrm{j}B_3 + Y^{\mathrm{pp}}_{\mathrm{exp},ij}), & (i = j) \\ \mathrm{j}B_{\mathrm{b}} + \dfrac{1}{R_i R_j}(\mathrm{j}B_3 + Y^{\mathrm{pp}}_{\mathrm{exp},ij}), & (i = j + N \text{ or } i + N = j) \; . \\ \dfrac{1}{R_i R_j} Y^{\mathrm{pp}}_{\mathrm{exp},ij}, & (\text{else}) \end{cases} \tag{3.12}$$

After the inclusion of the local field model, the coaxial field model has to be combined with the cavity model. If simple capacitances are used as coaxial field models, they can be added to $\overline{\overline{Y}}^{\mathrm{cav}}$ similar to the addition of the via barrel-to-plane capacitances in (3.11). If transmission line segments are used as coaxial field models, a simple addition is not possible. Instead, segmentation methods [77] have to be applied to connect the transmission line segments to the ports of $\overline{\overline{Y}}^{\mathrm{cav}}$. Segmentation methods are described in detail for the combination of single cavity results in Section 3.3.2.

3.3.2 Combination of Single Cavity Results

To combine the network parameter blocks of two adjacent cavities with connected internal ports as shown in Fig. 3.6, methods are used which enforce a continuity of voltages and currents at the connected ports. In general, two alternatives exist for the combination of the network parameter blocks: a multiplication in ABCD-parameters as described in [58], or the application of so-called segmentation methods [77] as described in [1,59], which can be carried out in S-parameters, Y-parameters, and Z-parameters. With both approaches, two network parameter blocks are combined, eliminating the internal ports from the matrices. The single cavity results for a multilayer stackup can thus be combined using a stepwise procedure. For the combination of an upper S-parameter block $S_a = \begin{bmatrix} S_{p^a p^a} & S_{p^a q} \\ S_{q p^a} & S_{qq} \end{bmatrix}$ and a lower S-parameter block $S_b = \begin{bmatrix} S_{p^b p^b} & S_{p^b r} \\ S_{r p^b} & S_{rr} \end{bmatrix}$ with p^a top side ports, p^b bottom side ports, and $q = r$ connected ports, the segmentation is described by [77, ch. 3.2.1]

$$S_{ab} = S_{pp} + S_{pq} \cdot (I - S_{rr} S_{qq})^{-1} \cdot (S_{rp} + S_{rr} S_{qp}) + S_{pr} \cdot (I - S_{qq} S_{rr})^{-1} \cdot (S_{qp} + S_{qq} S_{rp}) \; , \tag{3.13}$$

with $S_{pp} = \begin{bmatrix} S_{p^a p^a} & 0 \\ 0 & S_{p^b p^b} \end{bmatrix}$, $S_{pq} = \begin{pmatrix} S_{p^a q} \\ 0 \end{pmatrix}$, $S_{pr} = \begin{pmatrix} 0 \\ S_{p^b r} \end{pmatrix}$, $S_{qp} = (S_{pq})^T$, $S_{rp} = (S_{pr})^T$, and the identity matrix I. For the combination of two Y-parameter blocks Y_a and Y_b, the segmentation is described by [77, ch. 3.2.3]

$$Y_{ab} = Y_{pp} - (Y_{pq} + Y_{pr}) \cdot (Y_{qq} + Y_{rr})^{-1} \cdot (Y_{rp} + Y_{qp}) \; , \tag{3.14}$$

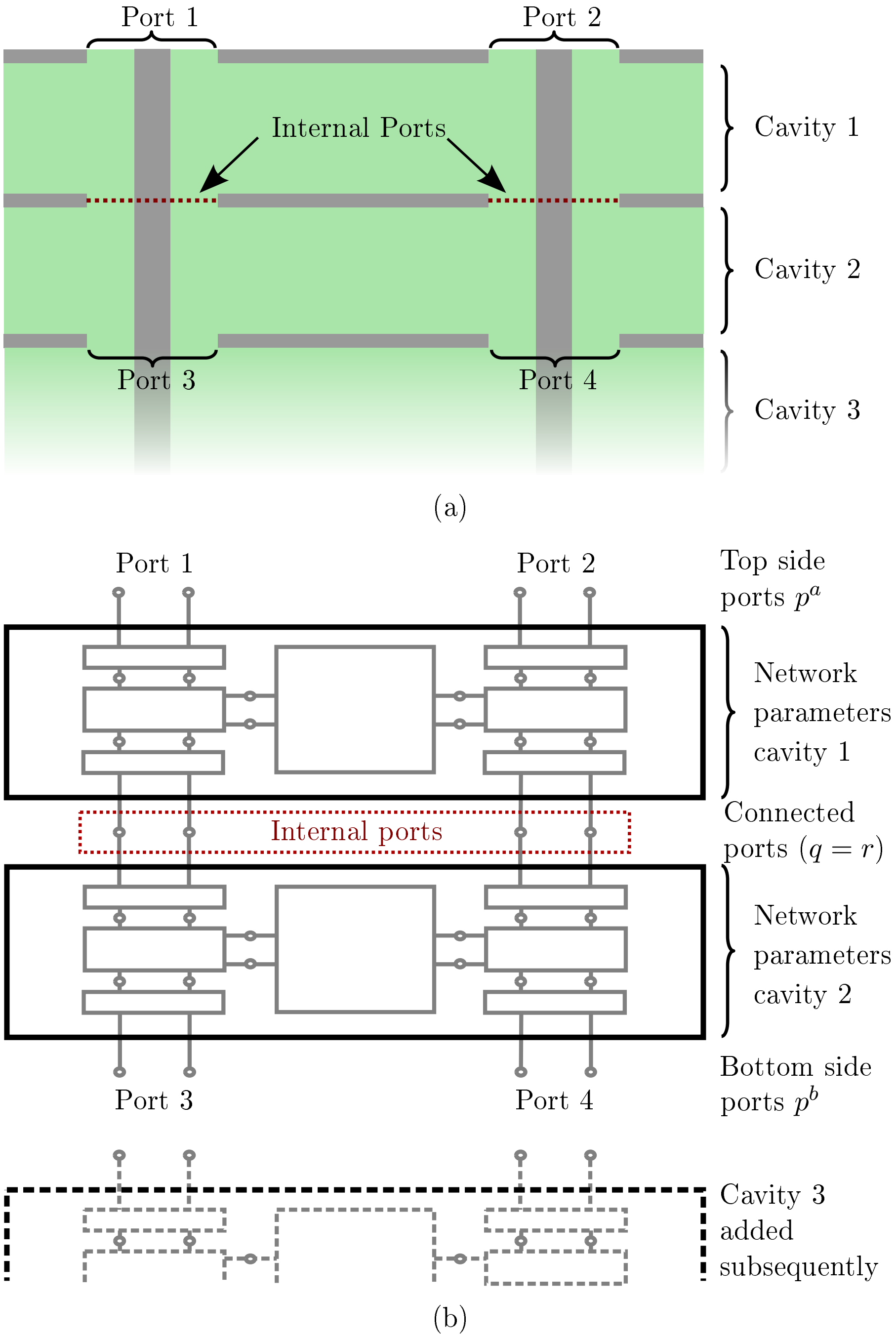

(a)

(b)

Figure 3.6: Combination of single cavity results for a multilayer PCB. (a) Combination of the first two cavities. The internal ports (which are shared by the two cavities) are connected, so that the lower ports of the second cavity become the lower ports of the combined structure. Further cavities are added in subsequent steps. (b) Combination shown in the form of network parameter blocks. At the internal ports, voltage and current continuity is enforced during the calculation of the combined network parameter block (Figure adapted from [26]).

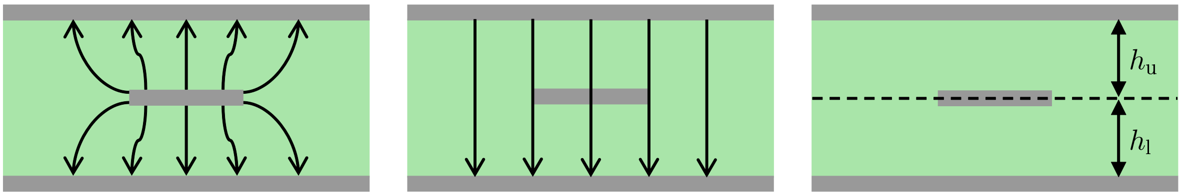

(a) (b) (c)

Figure 3.7: Modal decomposition approach for the inclusion of striplines in the physics-based via model. (a) Schematic representation of the stripline mode indicating the electric field lines between trace and reference planes. (b) Schematic representation of the parallel-plate mode indicating the electric field lines between upper and lower reference plane. (c) Definition of h_u and h_l for the calculation of the factor k.

with submatrix definitions similar to the S-parameter case. The formulation for a segmentation in Z-parameters, which is also possible, can be found in [77, ch. 3.2.2].

3.4 Inclusion of Striplines into Via Modeling Approaches

So far, the described models are concerned only with the calculation of via models. For a modeling of realistic link structures as described in Section 1.1, also striplines that provide the connection between signal vias in the different arrays have to be included in the modeling. An efficient approach for the inclusion of striplines has been presented in [106]. Based on the assumption that the stripline mode indicated in Fig. 3.7(a) and the parallel-plate mode indicated in Fig. 3.7(b) are coupled only at the via locations, the stripline models can first be calculated separately and then be included via a model decomposition approach [107, ch. 7.2.1]. The approach is suitable for methods which explicitly calculate the parallel-plate admittance matrix for the via structure, as it is the case for both physics-based via models and multiple scattering approaches. Given the expanded parallel-plate admittance matrix, the admittance parameters $\overline{\overline{Y}}^{\mathrm{tl}}$ of the striplines can be included as [59]

$$\overline{\overline{Y}}^{\mathrm{c}} = \begin{bmatrix} \overline{\overline{Y}}^{\mathrm{pp}} & -\overline{\overline{Y}}^{\mathrm{pp}} \\ -\overline{\overline{Y}}^{\mathrm{pp}} & \overline{\overline{Y}}^{\mathrm{pp}} \end{bmatrix} + \begin{bmatrix} k^2\overline{\overline{Y}}^{\mathrm{tl}} & (-k^2-k)\overline{\overline{Y}}^{\mathrm{tl}} \\ (-k^2-k)\overline{\overline{Y}}^{\mathrm{tl}} & (k^2+2k+1)\overline{\overline{Y}}^{\mathrm{tl}} \end{bmatrix}. \tag{3.15}$$

Besides the two matrices $\overline{\overline{Y}}^{\mathrm{pp}}_{\mathrm{exp}}$ and $\overline{\overline{Y}}^{\mathrm{tl}}$, the combination only requires the factor k, which describes the ratio between stripline return current in the upper reference plane and stripline return current in the lower reference plane. Assuming an infinitely thin trace, k can be calculated from upper and lower dielectric thickness as specified in Fig. 3.7(c): $k = h_\mathrm{l}/(h_\mathrm{l}+h_\mathrm{u})$. Numerical investigations show that the formula gives accurate values for practical trace geometries [108, ch. 7]. In the modal decomposition approach, the inclusion of striplines does not lead to additional ports, but rather to a modification of entries in the parallel-plate admittance matrix. Further steps, such as the addition of local field models, can be carried out in the same manner as before (it should be mentioned, however, that the accuracy of the local field model may be reduced at the point of the stripline connection, since the presence of a stripline is not taken into account in the local field model derivation). The network parameters of the stripline required for the combined model can be obtained from suitable simulations or measurements. In this work, network parameters for striplines are obtained from analytical formulas [109] for single-ended lines and from numerical simulations based on a 2D-MoM formulation [107, ch. 6.3.1] for differential and coupled lines. Since the inclusion of striplines does not fundamentally change the via model calculation, the accuracy of via and stripline models can largely be studied independently of each other. For this reason, the accuracy study in Chapter 4 first focuses on vias without striplines. Effects that may impact the accuracy of combined via and stripline models are investigated in Section 4.5.

3.5 Summary and Discussion

The physics-based via model can be applied to simulate vias and striplines in multilayer PCBs. The model can be represented in form of a block diagram which corresponds to the different field regions inside a PCB cavity. For all sub-blocks of the model, network parameters can be calculated from analytical formulas. The sub-blocks are then combined to obtain network parameter descriptions of all cavities. Subsequently, the single cavity results are combined to obtain the solution for the complete multilayer PCB. Stripline models can be included in the calculation through a modal decomposition approach.

For each sub-block of the physics-based via model, a simpler calculation method and a more complex method which takes into account additional effects have been described in this chapter. The impact of the different calculation methods and of neglected aspects on the modeling accuracy is studied in Chapter 4, where also effects that limit the accuracy of the modal decomposition approach for the combination of via and stripline models are investigated. The impact of the different calculation methods on the modeling efficiency is studied in Chapter 5.

4 Accuracy of the Modeling Approach

In this chapter, the accuracy of physics-based via and stripline models is analyzed. The impact of the alternative calculation methods for the model sub-blocks on the model accuracy is investigated, in particular with regard to modeling of dense via arrays on PCBs. The goal of this investigation is to find improvements to the model that increase the accuracy for relevant cases as far as possible without suffering loss of efficiency. Additionally, limitations of the modeling accuracy due to effects that are not taken into account by the physics-based model are studied. Here, the aim is to determine which cases cannot be handled with sufficient accuracy and therefore need to be addressed by multiple scattering approaches or full-wave methods, which provide accurate results for a larger range of scenarios at the cost of an increased computational effort. The accuracy study starts with an analysis of simple cases. Afterwards, the studied structures are extended first to via arrays in a single cavity and then to via arrays in a multilayer PCB. Finally, effects related to the inclusion of striplines are investigated. The study of the modeling accuracy is not only an end to itself, but also a preparation for the application of the physics-based models to the study of PCB designs carried out in Chapters 7 and 8 - ensuring that the studied design scenarios can be handled with a sufficient accuracy.

4.1 Simulation of a Single Via

While the main focus of this work is on the modeling of large via arrays, the accuracy study first looks at simple cases, beginning in this section with the simplest possible case of a single via. The advantage of the study of very simple cases is that it allows to distinguish the impact of different effects on the model accuracy more clearly. Effects that play a role for very simple geometries can be expected to have an impact also in the case of more complex structures. First, the impact of the different propagating field models and local field models on the accuracy of the calculated transmission and reflection is studied for a single via in a single cavity. Subsequently, the impact of an anisotropic excitation on the transmission along a single via is studied.

4.1.1 Accuracy of the Propagating Field Model

A comparison of the parallel plate impedance formulations in (3.3) and (3.4) shows that for the case of a single via, both lead to the same result. This is plausible, since the difference

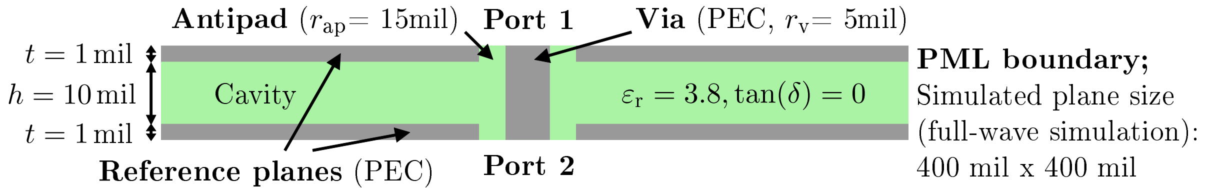

Figure 4.1: Test structure to study the accuracy of different local field models for the single via case. Simulations have been carried out with the specified material and geometry parameters, varying a single geometry parameter at a time to determine its impact on the local field model accuracy (Figure from [7]).

between the two formulations lies in the consideration of backscattering from other vias in (3.4), which does not exist in the single via case. Due to the absence of further vias, the structure is furthermore rotationally symmetric, so that no anisotropic modes will exist unless there is an anisotropic excitation. It can be concluded that given an isotropic excitation, both discussed propagating field models are in fact accurate for a single via in the sense that they do not neglect any major effects. Therefore, the accuracy of the physics-based model primarily depends on the local field model.

4.1.2 Accuracy of the Local Field Model

To determine the accuracy of different local field models for the simulation of a single via, several simulations of the test structure depicted in Fig. 4.1 were carried out with variations of different geometry parameters. For the dimensions and material parameters specified in Fig. 4.1, a comparison of the results for the transmission obtained with different local field models shows a good agreement between all modeling approaches and the reference result obtained with a commercial full-wave solver [97] up to about 15 GHz in Fig. 4.2(a). At higher frequencies, the result obtained with the via barrel-to-plane capacitance as local field model shows an increasing deviation from the full-wave result. Also the results obtained with the alternative local field models described in Section 3.2.2 - the Williamson model [73] and the intrinsic via model [76] - start to deviate, however, the deviation is considerably smaller. It should be mentioned that although only the results for the transmission are shown, the stated observations apply to the results for the reflection in a similar way.

The variation of the geometry parameters shows that the agreement between physics-based via model and full-wave solution improves if the via radius is increased or the antipad radius is decreased. The parameter with the largest impact is the dielectric thickness h of the cavity. With an increasing dielectric thickness, the accuracy of the via barrel-to-plane capacitance as a local field model becomes severely deteriorated. The comparison of results for the transmission in Fig. 4.2(b) for the case of $h = 30\,\mathrm{mil}$ (all other dimensions

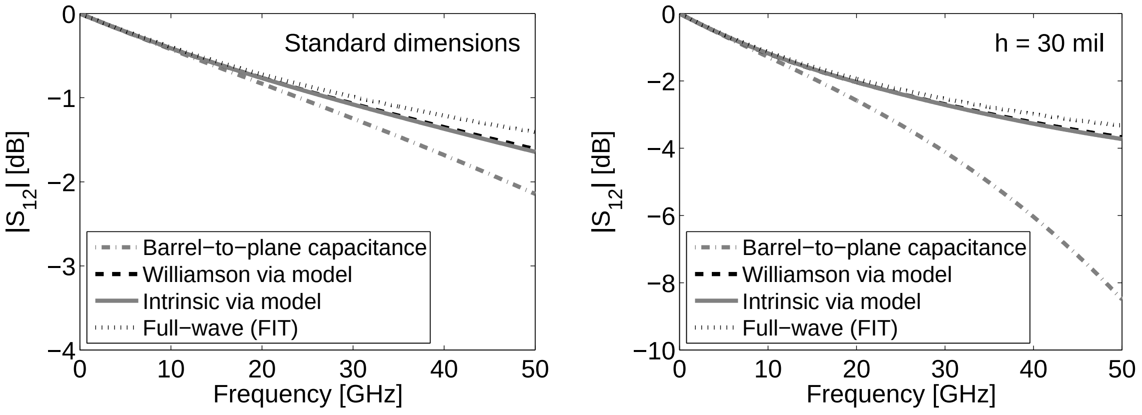

(a) (b)

Figure 4.2: Comparison of results for the transmission along a single via in a single cavity obtained with different local field models. Results for the intrinsic via model were provided by Dr. Yaojiang Zhang, Missouri University of Science and Technology. (a) Results for the test structure with standard dimensions as specified in Fig. 4.1. Up to about 15 GHz, all models are in good agreement. At higher frequencies, the physics-based via model shows the largest deviations from the full-wave result used as a reference (Figure from [7]). (b) Results for the test structure in Fig. 4.1 with $h = 30\,\mathrm{mil}$. The larger dielectric thickness leads to a more severe deviation of the physics-based via model above 15 GHz (Figure from [7]).

as specified in Fig. 4.1), which is at the upper end of dielectric thicknesses encountered in practical applications, shows a deviation of more than 4 dB between full-wave solution and physics-based model at 50 GHz. For the same structure, the reflection shows a deviation of almost 6 dB at 50 GHz. The impact of the three named parameters - via radius, antipad radius, and cavity height - can be summarized in the observation that the via barrel-to-plane capacitance leads to acceptable results if the local field region around the via, in which the conversion between coaxial waveguide modes and radial waveguide modes takes place, is sufficiently small. Even in those cases, the more complex local field models lead to some improvement in the accuracy of the obtained results for frequencies above about 10 to 15 GHz. In case of an increased size of the region of mode conversion in radial or vertical direction, the more complex local field models can considerably improve the agreement to full-wave results.

4.1.3 Impact of Anisotropic Modes

Even though anisotropic modes will not be created inside the cavity in case of a single via with infinite reference planes due to the rotational symmetry of the structure, anisotropic modes may be excited by the external signal entering the cavity. To investigate the excitation and the behavior of anisotropic modes in case of a single via, the structure shown

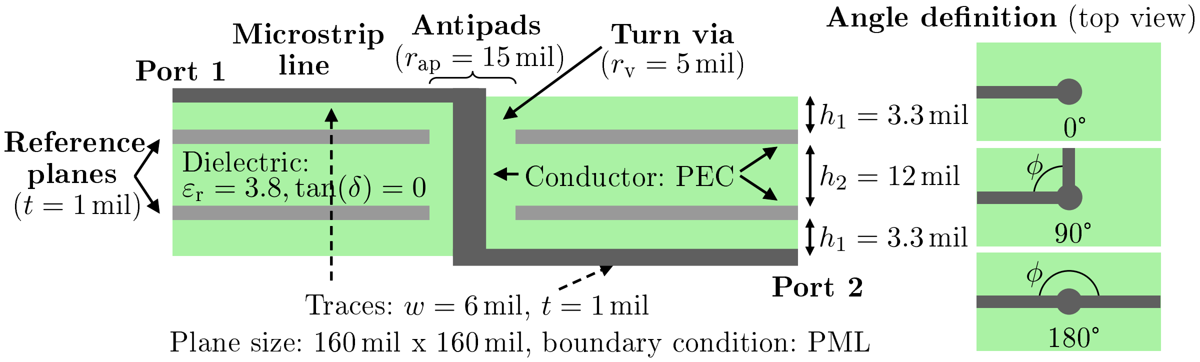

Figure 4.3: Test structure to investigate the impact of anisotropic modes for a single via (Figure adapted from [7,19]). Two microstrip lines provide the excitation of the via, leading to a non-uniform current distribution as shown in Fig. 4.4(a). To study the impact of anisotropic modes on the network parameters of the structure, simulation results for the three shown microstrip connection angles are compared in Fig. 4.4(b).

in Fig. 4.3 is investigated: two microstrip lines at the top and bottom of a PCB are connected by a signal via that traverses a single cavity. As shown in Fig. 4.4(a), the current distribution is not uniform in this case. At the upper microstrip line, the larger part of the current flows at the bottom side of the trace, which is closer to the reference plane than the top side of the trace. When the current reaches the via, it has to redistribute to reach the upper side of the bottom microstrip line, leading to a non-uniform current distribution on the via barrel. To investigate the impact of the non-uniform current distribution on the transmission through the via, the angle between the connecting microstrip lines is varied from 0° to 180° as illustrated in Fig. 4.3. The experiment is adapted from the study carried out in [111], where a large impact of the microstrip connection angle on the S-parameters of the transmission was found for a via crossing a single metal plane. The results of simulations with a commercial FEM solver [110] are plotted in Fig. 4.4(b). A notable deviation between the different cases exists only for frequencies higher than 30 GHz. The impact of the connection angle is much smaller than for the single reference plane setup studied in [111]. When the stackup is extended to 3 cavities (adding 2 inner cavities to the PCB, each of thickness $h_2 = 12\,\mathrm{mil}$), only a very small deviation between the three cases exists up to 50 GHz. The results show that the impact of anisotropic modes on the transmission quickly decreases with an increasing number of cavities in the PCB stackup. Two effects contribute to this behavior: First, the via length increases, offering the current a longer distance to redistribute between upper and lower via end. Second, with a larger number of cavities, the via traverses more reference planes through coaxial antipad sections. While isotropic and anisotropic radial waveguide modes show the same propagation behavior inside the cavity, only the (isotropic) TEM mode is propagating in the coaxial waveguide at the frequencies of interest, while all anisotropic modes are attenuated. The observed results

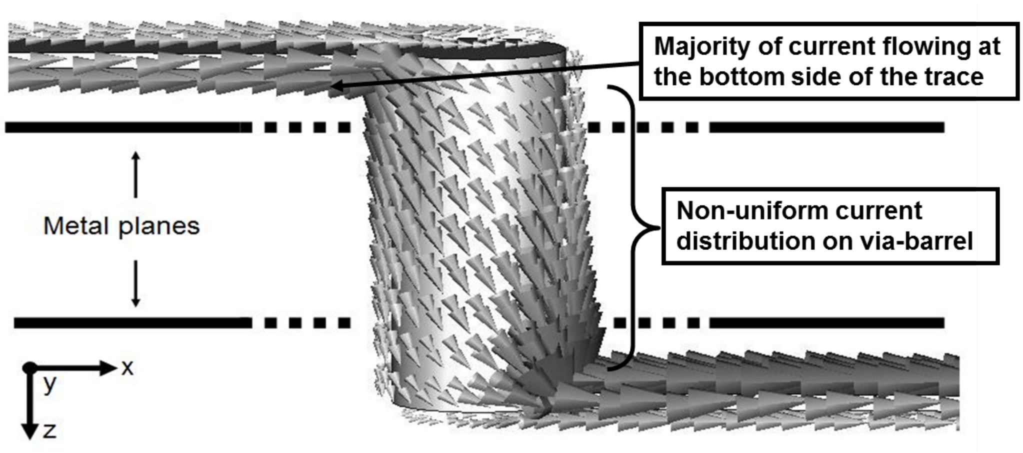

(a)

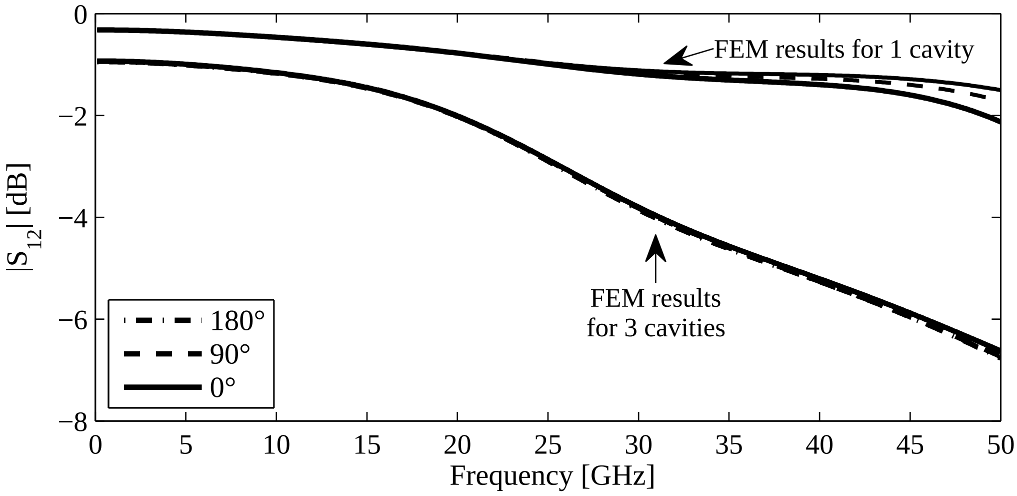

(b)

Figure 4.4: Impact of an anisotropic excitation by a microstrip line. (a) Current distribution around the via for a single-cavity stackup. The anisotropic excitation by the microstrip current leads to a non-uniform current distribution around the via inside the cavity (Figure adapted from [19]). (b) Comparison of full-wave (FEM [110]) results for the transmission for different microstrip connection angles. For a single-cavity stackup, an impact of the connection angle on the S-parameters can be observed above 30 GHz. If the stackup is extended to 3 cavities, only a very small deviation exists up to 50 GHz (Figure adapted from [7]).

suggest that for multilayer PCBs, the physics-based via model can be used to simulate the network parameters of the internal structure even in the case of anisotropic excitations.

4.2 Simulation of Two Vias

The simulation of two vias in a single cavity is studied here as the simplest case that includes coupling between vias. As already indicated in Section 3.1.2, three major concerns exist with regard to the simulation of coupled vias: the impact of the applied propagating and local field models on the modeling accuracy, the relevance of non-propagating modes, and the relevance of anisotropic modes. The three aspects are investigated in the following.

4.2.1 Impact of Propagating and Local Field Models

To study the impact of the different propagating and local field models on the modeling accuracy for the coupling between vias, a test structure with two vias in a single cavity is investigated. The modeling accuracy is studied for different via separations d, while all other geometry and material parameters have the values specified in Fig. 4.5. Note that a very small antipad radius has been chosen, so that the vias can be brought closely together without an antipad overlap. For a via separation of $d = 40\,\mathrm{mil}$, the far-end crosstalk between the vias shows a deviation between physics-based model using the RWM and the via barrel-to-plane capacitance and a full-wave simulation for frequencies above about 15 GHz, see Fig. 4.6(a). Replacing the via barrel-to-plane capacitance by the Williamson model shows that the deviation is caused by the already observed inaccuracy of the capacitance as a local field model at higher frequencies. The CIM as a more accurate propagating field model, in contrast, does not lead to a notable improvement of the modeling accuracy in comparison to the RWM. In case of a very small via separation of $d = 12.2\,\mathrm{mil}$ (with only 0.2 mil of the reference plane remaining between the two antipads), a substantially larger deviation between physics-based model using RWM and via barrel-to-plane capacitance and full-wave result is observed. The deviation can only to a small part be decreased by

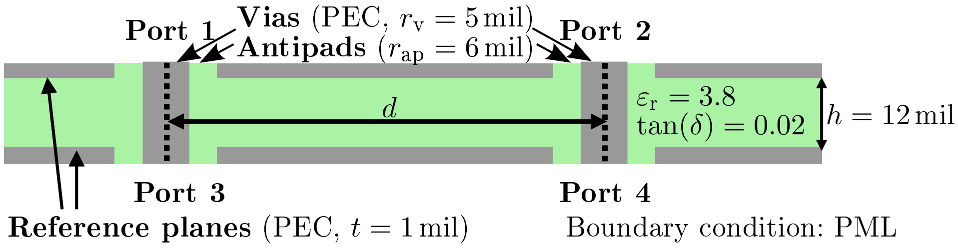

Figure 4.5: Test structure to investigate the accuracy of different modeling approaches for the coupling between two vias depending on the via separation d. For the simulations, the antipad radius has been chosen smaller than feasible in practical PCB structures in order to study very small via separations without an antipad overlap (Figure from [7]).

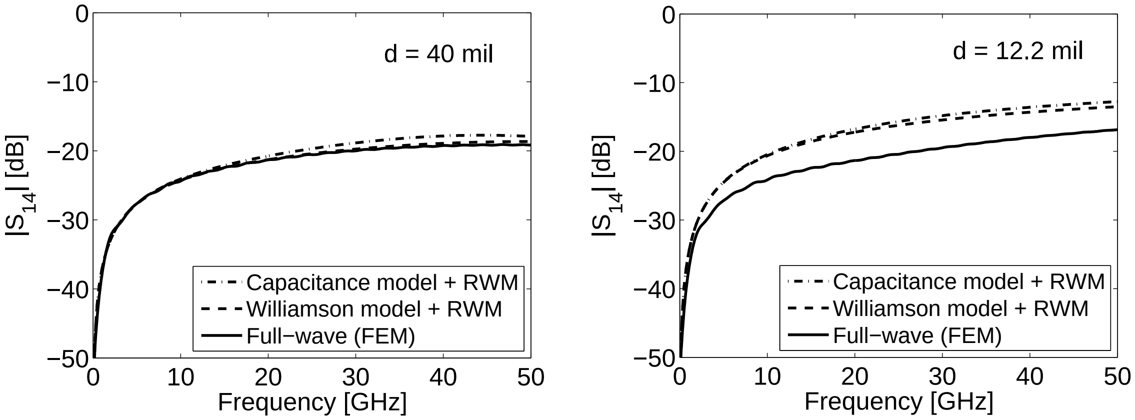

(a) (b)

Figure 4.6: Comparison of results for the far-end crosstalk obtained with different local field models. (a) Results for the test structure in Fig. 4.5 with a via separation of $d = 40\,\text{mil}$. Already the via barrel-to-plane capacitance leads to a good agreement with the reference solution obtained from a full-wave (FEM) solver [110]. A deviation of about 1 dB occurring at higher frequencies can be further reduced with the Williamson model (Figure from [7]). (b) Results for the test structure in Fig. 4.5 with a via separation of $d = 12.2\,\text{mil}$, leading to a distance of only 2.2 mil between the surfaces of the via barrels. The physics-based via model starts to deviate from the full-wave solution already in the low GHz range. Only a small part of the deviation is avoided with the Williamson model (Figure from [7]).

an improved local field model, and is not notably reduced by an improved propagating field model. Two possible explanations for the larger deviation in case of a smaller via separation exist: a coupling provided by non-propagating modes, or an increased impact of anisotropic modes - both could be caused by the small via separation. The respective impacts are investigated in the following two subsections.

4.2.2 Via Coupling Provided by Non-Propagating Modes

The coupling between closely spaced vias due to non-propagating modes has been investigated in [23]. The analysis was carried out based on a simple implementation of a multiple scattering approach, including isotropic modes only. Since the different isotropic modes are decoupled (see Appendix A), the multiple scattering approach leads to a separate admittance matrix for each mode. The total admittance matrix of the system is the sum of the fundamental mode admittance matrix (which corresponds to the parallel plate admittance in the physics-based via model) and all higher order (non-propagating) mode admittance matrices [23]:

$$[Y] = [Y]_{l=0} + \left[\sum_{l=1}^{\infty} [Y]_l \right]. \tag{4.1}$$

For a via separation of $d = 40\,\mathrm{mil}$, the first row of the admittance matrix due to non-propagating modes takes the following characteristic form:

$$\left[\sum_{l=1}^{\infty} [Y]_l \right]_{1,i} \approx \left[\begin{array}{cccc} (Y_c + Y_p) & 0 & -Y_p & 0 \end{array} \right], \tag{4.2}$$

with the ports numbered according to Fig. 4.5. The non-propagating modes lead to a coupling admittance Y_c between via barrel and reference planes, as reflected in the via barrel-to-plane capacitances C^b in (3.11) or the corresponding element $\mathrm{j}B_\mathrm{a}$ of the Williamson model in (3.12). Furthermore, for each via, an additional coupling admittance Y_p between upper and lower port exists. This coupling admittance can be interpreted as the combined effect of the elements in parallel to the parallel plate admittance in the Williamson model. It is neglected in the physics-based via model if only the via barrel-to-plane capacitance is used to model the local fields. Entries which would indicate a coupling between vias due to non-propagating modes are much smaller than the corresponding entries resulting from the fundamental mode, and can be approximated as zero.

For a via separation of $d = 12.2\,\mathrm{mil}$, the characteristic form of the first row of the admittance matrix related to non-propagating modes changes:

$$\left[\sum_{l=1}^{\infty} [Y]_l \right]_{1,i} \approx \left[\begin{array}{cccc} \left(\tilde{Y}_c + Y_{12} + \tilde{Y}_p + Y_{14}\right) & -Y_{12} & -\tilde{Y}_p & -Y_{14} \end{array} \right]. \tag{4.3}$$

The coupling between the vias due to non-propagating modes can no longer be neglected for the smaller via separation, which is reflected in to non-zero entries Y_{12} and Y_{14}. An inspection of the two admittance values shows that the coupling can be described by effective coupling capacitances with $Y_{12} = \mathrm{j}\omega C_{12}$ and $Y_{14} = \mathrm{j}\omega C_{14}$. It should be noted that the effective coupling capacitances are not identical with the static capacitance between the via barrels. In particular, near and far end coupling capacitances inside a cavity have different values, as shown in Fig. 4.7(a) for a via separation of $d = 12.2\,\mathrm{mil}$. Similar to the via barrel-to-plane capacitance, the effective coupling capacitances show a slight frequency dependency. It is noteworthy that if via coupling due to non-propagating modes exists, also the capacitance between via barrel and referenc plane is changed. Fig. 4.7(b) compares the via barrel-to-plane capacitance calculated from (3.7) for a single via to the capacitance value calculated from Y_c in (4.2) for $d = 40\,\mathrm{mil}$. The two values are almost identical.

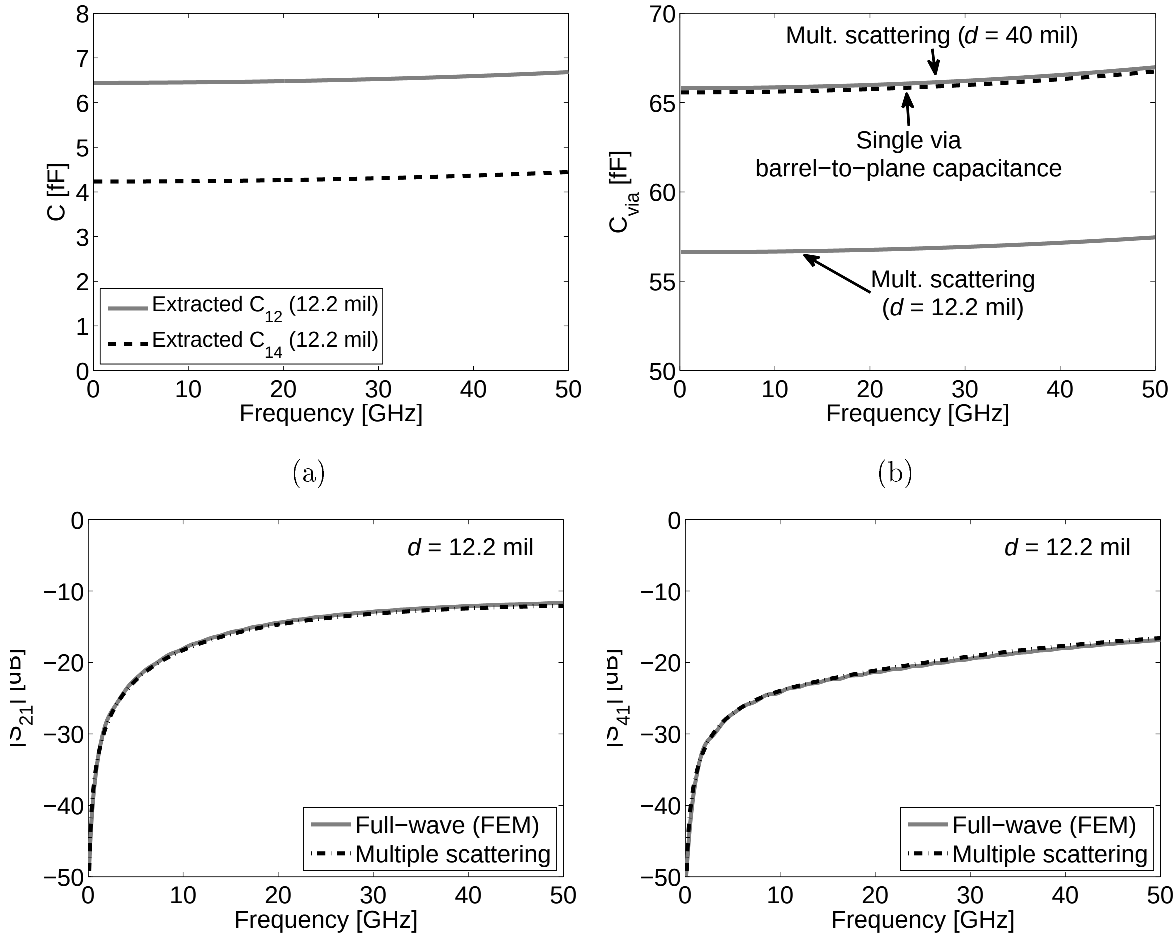

(a) (b)

(c) (d)

Figure 4.7: Impact of non-propagating modes on the coupling between very closely spaced vias (all Figures from [23]). (a) Frequency dependent behavior of the effective coupling capacitances for a via separation of $d = 12.2\,\mathrm{mil}$. In the higher GHz range, the effective coupling capacitances show a slight frequency dependendy similar to the via barrel-to-plane capacitance. (b) Capacitance between via barrel and reference plane. For a via separation of $d = 40\,\mathrm{mil}$, the capacitance value obtained from the multiple scattering approach is in good agreement with the value calculated based on (3.7). For a smaller via separation of $d = 12.2\,\mathrm{mil}$, the value obtained from the multiple scattering approach is smaller due to additional field lines ending on the second via instead of the reference planes. (c) Near-end crosstalk for a via separation $d = 12.2\,\mathrm{mil}$. The effective coupling capacitances, which are taken into account by the multiple scattering approach, considerably improve the agreement to the full-wave solution [112] in comparison to the results obtained with the physics-based via model without effective coupling capacitances (compare Fig. 4.6(b)). (d) Comparison for the far-end crosstalk. Also here, the effective coupling capacitances included in the multiple scattering approach lead to a good agreement to the full-wave solution.

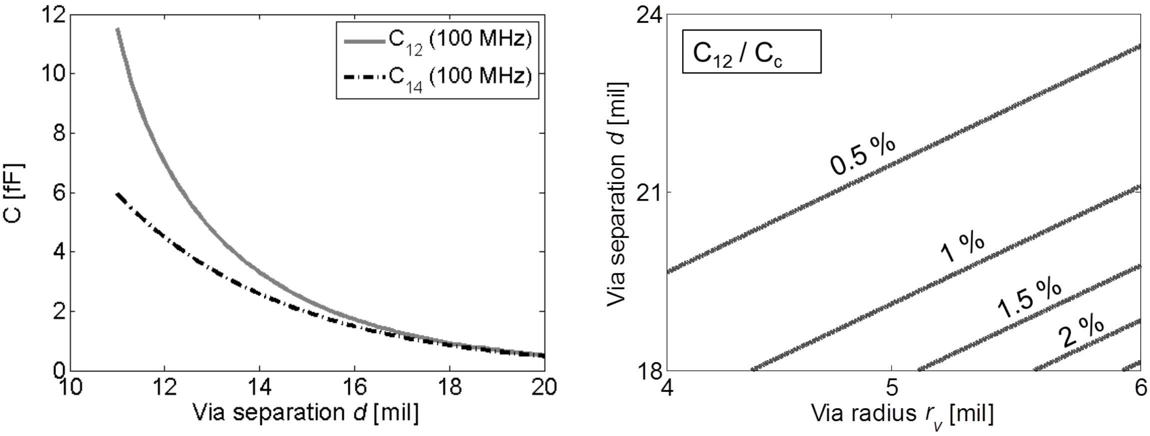

(a) (b)

Figure 4.8: Distance dependency of the coupling between vias due to non-propagating modes. (a) Effective coupling capacitances between the two vias in Fig. 4.5 plotted over the via separation d for a frequency of 100 MHz (Figure from [23]). (b) Contour plot showing lines of a constant ratio between the effective coupling capacitance C_{12} and the via barrel to plane capacitance C_c (Figure from [23]).

For a via separation of $d = 12.2\,\text{mil}$, in contrast, the capacitance between via barrel and reference plane calculated from $\tilde{Y}_c$ in (4.3) is considerably lower due to the increased portion of electric field lines ending on the adjacent via barrel.

Taking the effective coupling capacitances into account – as it is done by the multiple scattering solution – can considerably improve the agreement to full-wave simulations for near-end crosstalk (Fig. 4.7(c)) and far-end crosstalk (Fig. 4.7(d)) between closely spaced vias. However, due to the strongly distant dependent behavior of the coupling capacitances shown in Fig. 4.8(a), a relevant impact occurs only for very small via separations. The ratio between the effective near-end coupling capacitance C_{12} and the capacitance C_c between via barrel and reference plane is shown in Fig. 4.8(b) depending on via radius and via separation (assuming an antipad radius 1 mil larger than the via radius and other geometry and material parameters as specified in Fig. 4.5). Typically, the impact of a coupling due to non-propagating modes on the S-parameters for near- and far-end crosstalk can be neglected as long as the capacitance ratio is less than 1 %, which is equivalent to a via separation of less than 30 mil for the studied structure.

A structure for which coupling provided by non-propagating modes may in fact become relevant is given by a differential via pair with a very small via separation. For the case of two vias, analytical formulas for the effective coupling capacitances as well as for the modified capacitance between via barrel and reference plane can be obtained by explicitly solving the 2×2 equation system of the multiple scattering approach. The obtained admittance values can directly be added to the corresponding entries of the parallel plane admittance. However, it should be noted that the basic multiple scattering approach assumes separate antipads. A multiple scattering approach using a numerical calculation of surface charges for vias in shared antipads can be found in [85].

4.2.3 Impact of Anisotropic Modes

To study the impact of anisotropic modes in the case of two vias, the via constellation from Fig. 4.5 is analyzed using the contour integral method with discretized circular ports. The evaluation does not take into account non-propagating modes. For this reason, all results are shown for a via separation of $d = 40\,\mathrm{mil}$, for which an analysis based on propagating modes is sufficient as shown in Section 4.2.2. Similar to full-wave approaches, the contour integral method allows to evaluate the fields inside the cavity. In Fig. 4.9(a), the electric field distribution around the circumference of the first via is shown at different frequencies for an isotropic excitation at the second via with a 1 mA uniform current. Already at 10 GHz, an impact of the first anisotropic mode can be observed. At 60 GHz, the variation of the electric field strength indicates the impact of even higher anisotropic modes. To investigate the impact of higher order modes in a more quantitative way, the electric field distribution is written as a Fourier series of azimuthal modes [19]:

$$\hat{E}_z(\varphi) = \sum_{n=-\infty}^{\infty} \tilde{E}_n \cdot e^{\mathrm{j}n\varphi} \approx \sum_{n=-N}^{N} \tilde{E}_n \cdot e^{\mathrm{j}n\varphi}. \tag{4.4}$$

A numerical approximation for the complex Fourier coefficient $\tilde{E}_n$ representing the n^{th} azimuthal mode on the circumference of the via can be calculated from the electric field strengths at the N different line segments of the discretized circular ports [19]:

$$\tilde{E}_n = \frac{1}{2\pi} \int_0^{2\pi} \hat{E}_z(\varphi) e^{-\mathrm{j}n\varphi} \mathrm{d}\varphi \approx \sum_{k=0}^{N-1} \hat{E}_z(k) \cdot e^{-\mathrm{j}n \cdot 2\pi k/N}. \tag{4.5}$$

For an evaluation with $N = 32$ line segments, the Fourier coefficients obtained at different frequencies are shown in Fig. 4.9(b). The results confirm that already at 10 GHz, energy is coupled to the first anisotropic mode if a via is excited by a neighboring via. Furthermore, the energy coupled to anisotropic modes increases with frequency. At 60 GHz, even the second and third anisotropic mode start to play a role.

The results found here seem to be contradictory to the S-parameter comparisons in Fig. 4.6(a), Fig. 4.7(c), and Fig. 4.7(d), which show that a simulation with only isotropic modes is suf-

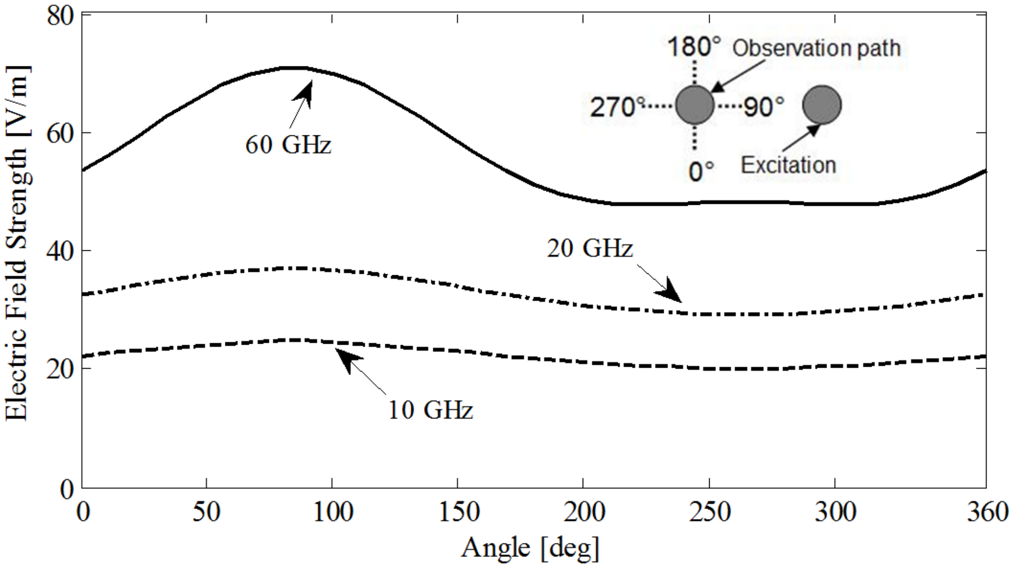

(a)

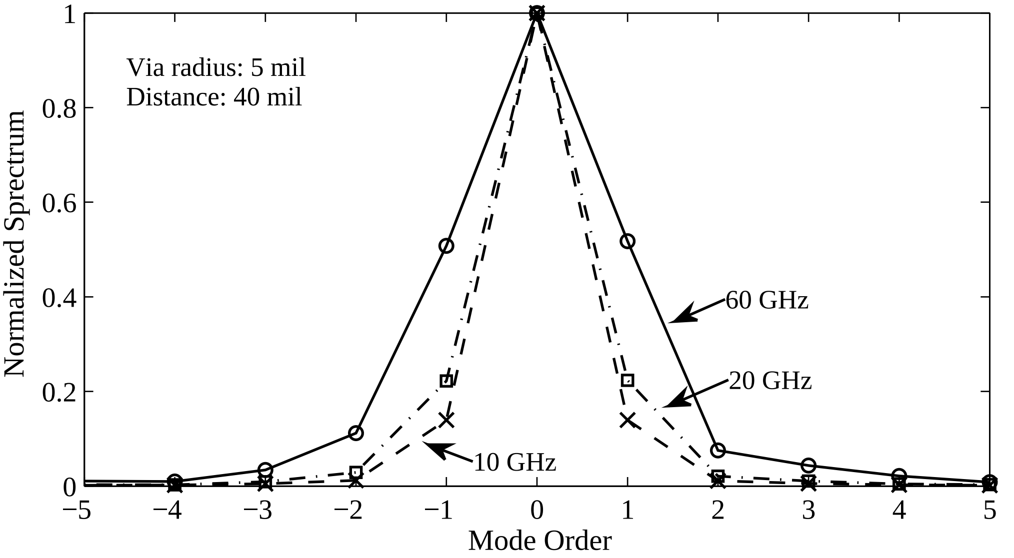

(b)

Figure 4.9: Anisotropic modes in case of two vias with isotropic excitation. (a) Magnitude of the electric field strength observed at the circumference of via 1 (left via) for an isotropic excitation at via 2 (right via). Already at 10 GHz, an anisotropic field distribution related to the impact of the first higher order mode can be observed. At 60 GHz, also higher anisotropic modes have an impact (Figure adapted from [19]). (b) Amplitude spectrum of the electric field strength indicating the energy coupled into the different anisotropic modes. All coefficients are normalized to the coefficient of the fundamental (isotropic) mode (Figure adapted from [19]).

ficient to obtain a good agreement with full-wave results for 40 mil and even for 12.2 mil via separation. A possible explanation is that for structures with only two vias, the fundamental mode coupling is not substantially changed by the presence of anisotropic modes. Since the network parameters in the physics-based model as well as in multiple scattering approaches are calculated from integral voltage and current definitions which take into account isotropic modes only, the impact of existing anisotropic modes cannot be seen directly in the network parameters. However, the existence of anisotropic modes already for two vias indicates that their impact should be studied thoroughly in the following accuracy study for via arrays.

4.3 Single Cavity Simulation of Via Arrays

After basic limitations of the physics-based via model with regard to reflection, transmission and coupling have already been discussed in the preceding sections, the accuracy of the physics-based model is now studied for the application to via arrays. Due to the dense arrangement of multiple vias in close proximity, additional effects may impact the accuracy for the simulation of via arrays that do not occur or are not relevant in the case of one or a few vias. In this section, detailed investigations on the modeling accuracy are carried out for an 8×8 via array with the via arrangement, geometry and material parameters, and port numbering as shown in Fig. 4.10. Investigations are carried out for via pitches of 80 mil and 40 mil, which can be encountered in practical PCB designs. For each via pitch, two aspects are investigated: the impact of different propagating and local field models on the accuracy of the physics-based via model and the impact of anisotropic modes on the simulation results. To study the impact of anisotropic modes, results from a multiple scattering approach are used.

4.3.1 Detailed Study for 80 mil Pitch

To determine the impact of the different propagating and local field models on the accuracy of the physics-based via model, three combinations of sub-models are compared: the RWM together with the via barrel-to-plane capacitance, the RWM with the Williamson model as an improved local field model, and the CIM with the Williamson model as a combination of improved propagating and local field models. A Comparison of the three models to a reference full-wave solution is shown in Fig. 4.11(a) for the transmission between via ports 5 and 2 as defined in Fig. 4.10(a). Already the combination of RWM and via barrel-to-plane capacitance shows a good agreement to the full-wave solution, with somewhat larger deviations at the resonance frequencies and in the frequency range above 40 GHz. The improved local field model leads to an even better agreement with the full-wave solution.

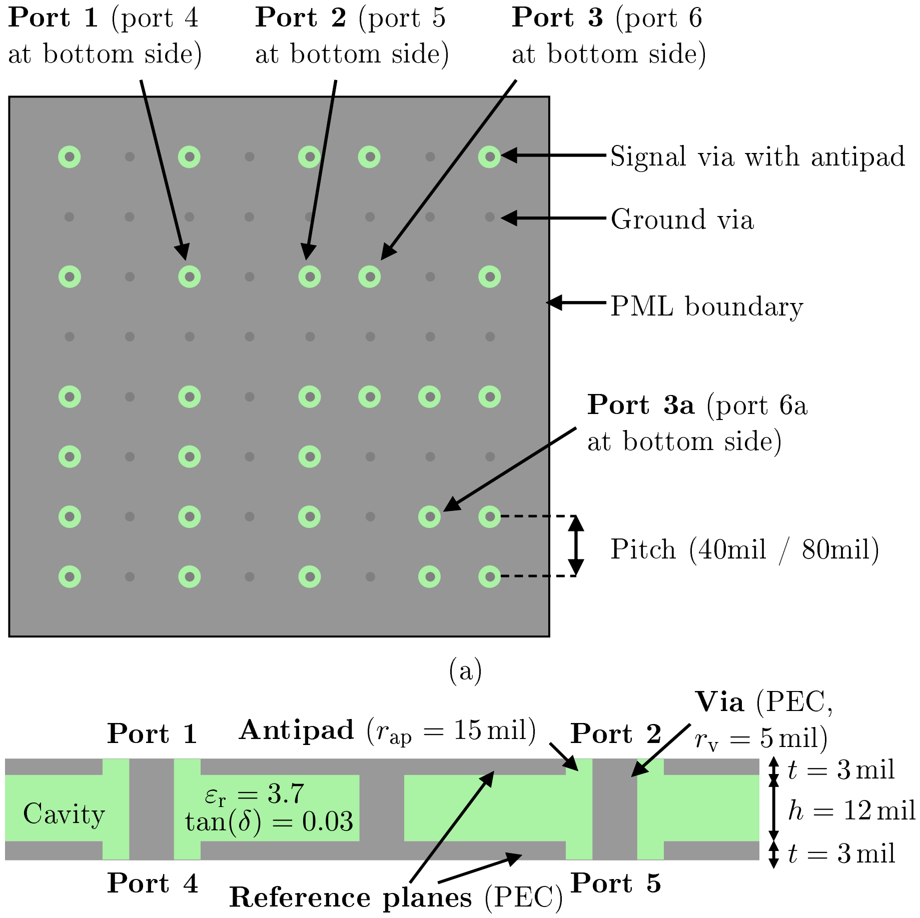

(a)

(b)

Figure 4.10: 8x8 via array for the comparison of different modeling approaches. (a) Top view of the via arrangement with definition of ports 1 to 6. Signal vias without ports are open (Figure adapted from [7]). (b) Cross section of the cavity showing two signal vias with port definitions and a ground via (Figure from [7]).

The improved propagating field model does not substantially change the agreement. To further study the impact of anisotropic modes, the most accurate version of the physics-based via model (CIM + Williamson model), which takes into account only isotropic modes, is compared to multiple scattering results obtained with a generalized multiple scattering approach (GMS) [87] for $M = 0$ and $M = 1$. All GMS results used in this thesis were provided by Dr. Yaojiang Zhang, Missouri University of Science and Technology. The comparison in Fig. 4.11(b) shows a good agreement between all curves. The inclusion of the first anisotropic mode in the multiple scattering approach does not improve the agreement with the full-wave solution. Similar results are obtained for the reflection and for the crosstalk between vias. It can be concluded that a consideration of anisotropic modes is not necessary to obtain accurate simulation results in the case of 80 mil pitch.

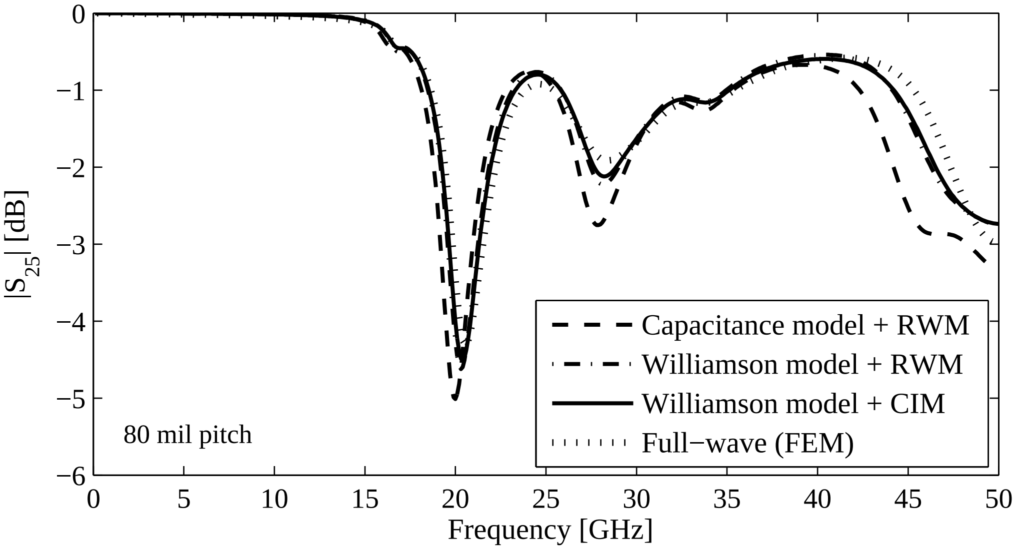

(a)

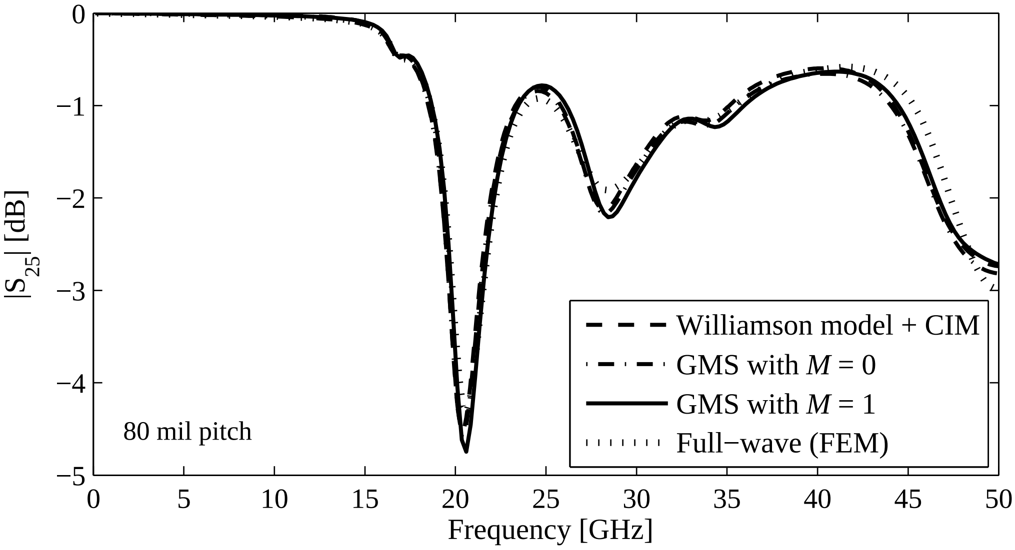

(b)

Figure 4.11: Comparison of the transmission between ports 2 and 5 in Fig. 4.10, calculated with different modeling approaches for 80 mil pitch. (a) Comparison of different versions of the physics-based via model to a full-wave (FEM) solution (Figure from [7]). The original model shows the largest deviations at resonance frequencies, but may still be considered a good approximation up to 40 GHz. The Williamson model leads to an improved agreement at the resonances and above 40 GHz. (b) Comparison to multiple scattering solutions calculated with $n = 0$ and $n = 1$ (Figure from [7]). For the test case with 80 mil pitch, the impact of anisotropic modes can be neglected up to at least 50 GHz.

4.3.2 Detailed Study for 40 mil Pitch

The comparison carried out in the previous subsection is now repeated for a via array with 40 mil pitch. The comparison between the different versions of the physics-based via model and the reference full-wave solution for the transmission between via ports 5 and 2 is shown in Fig. 4.12(a). Up to about 35 GHz, the curves show a good agreement due to the lack of resonances in the transmission. At higher frequencies, however, the combination of RWG and via barrel-to-plane capacitance shows a considerable shift of the resonance to lower frequencies in comparison to the full-wave solution. The resulting deviation is much larger than all deviations observed in the 80 mil case. Applying the Williamson via as the local field model gives a considerable improvement, but is not sufficient to obtain a good agreement to the full-wave result. Applying the CIM leads to a further improvement, showing that for 40 mil pitch, backscattering from other vias does in fact have an impact on the propagating field behavior. As described in [8], the application of the CIM can also resolve passivity problems that were observed for the RWM in case of 40 mil pitch. However, a considerable deviation to full-wave results exists even for the most accurate version of the physics-based via model. The comparison to multiple scattering results in Fig. 4.12(b) shows that in the case of 40 mil pitch, also an impact of anisotropic modes on the simulation results can be observed. The inclusion of the first anisotropic mode further reduces the frequency shift in comparison to the full-wave result, although it is not sufficient to obtain a complete agreement. Since for the transmission, the impact of anisotropic modes can only be observed at high frequencies, additional curves are included for reflection and crosstalk, which show deviations already at lower frequencies. For the reflection at via port 2 in Fig. 4.13(a), the inclusion of the first anisotropic mode improves the agreement to the full-wave result only at higher frequencies. At lower frequency, the simulation without anisotropic modes shows a better agreement to the full-wave solution. The reason for this behavior is uncertain, and may be related to a general sensitivity of the reflection to small impacts that will be discussed in Section 6.2. For the near-end crosstalk between ports 1 and 2 in Fig. 4.13(b), in contrast, the result calculated including the first anisotropic mode provides a better agreement to the full-wave solution over the entire frequency range. This demonstrates that at least for the crosstalk, an impact of anisotropic modes can be observed already in the low GHz range in the case of 40 mil pitch.

4.3.3 Possible Extension to Anisotropic Modes

The preceding results demonstrate that for via arrays with a small pitch, anisotropic modes have a considerable impact on the network parameters. For the physics-based via model, this means that below a certain via pitch, the propagating field model has to be extended to include anisotropic modes in order to provide accurate results. The limit with regard

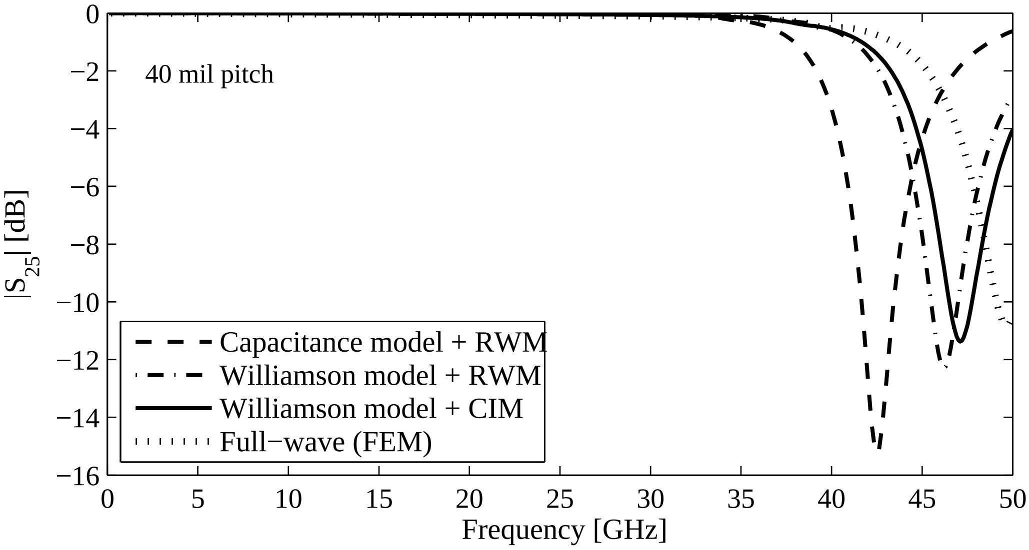

(a)

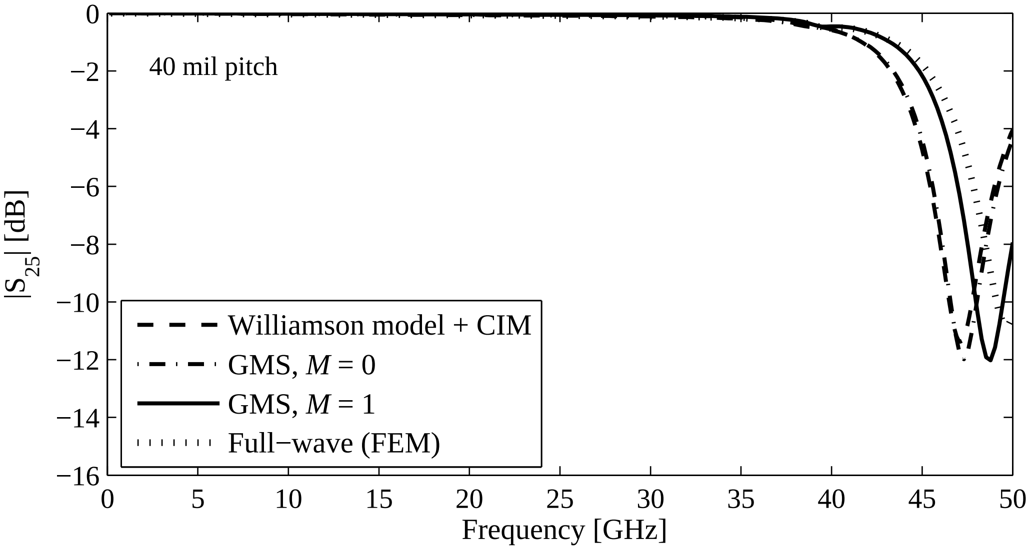

(b)

Figure 4.12: Comparison of the transmission between ports 2 and 5 in Fig. 4.10, calculated with different modeling approaches for 40 mil pitch. (a) Comparison of the original physics-based via model and improved versions to a full-wave (FEM) solution (Figure from [7]). Although both the improved local field model and the improved propagating field model lead to improvements in the modeling result, a considerable deviation to the full-wave result remains. (b) Comparison to multiple scattering results, showing that taking the first higher order mode into account shifts the resonant frequency further towards the full-wave result (Figure from [7]).

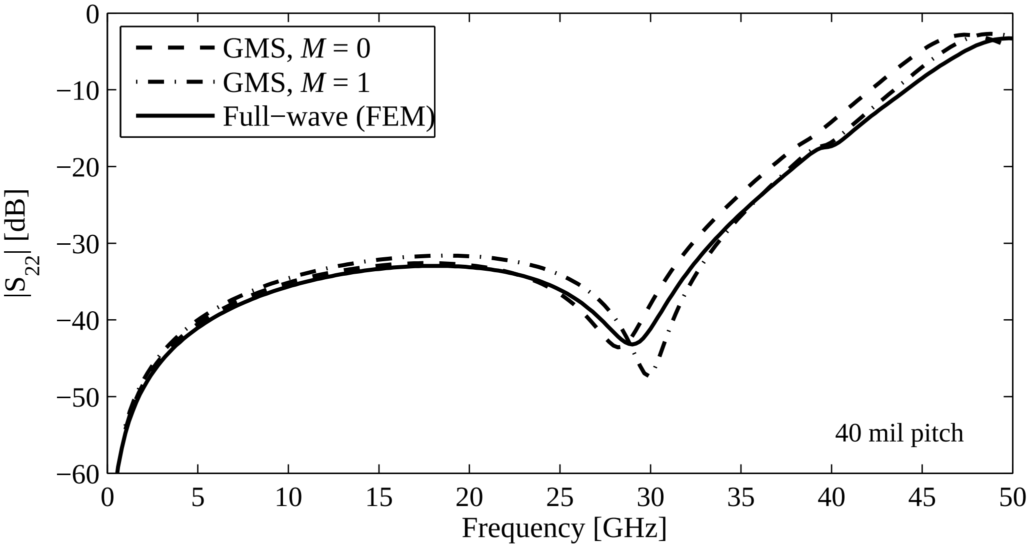

(a)

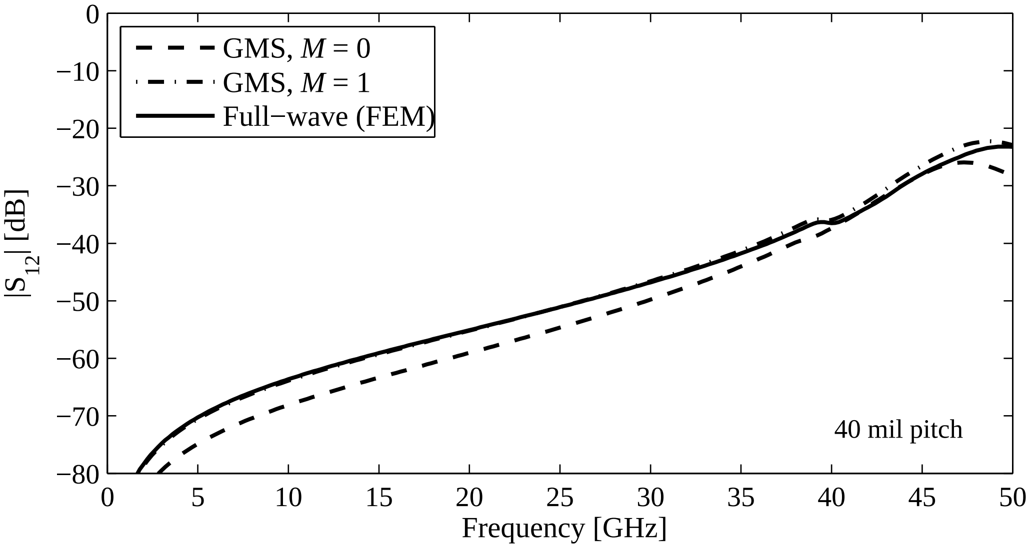

(b)

Figure 4.13: Impact of anisotropic modes on the reflection at port 2 and the near-end crosstalk between port 2 and port 1 in Fig. 4.10 for 40 mil pitch. (a) For the reflection, the isotropic simulation leads to a better agreement with to the full-wave solution up to the first resonance frequency around 29 GHz. The inclusion of the first anisotropic mode improves the agreement only at higher frequencies (Figure adapted from [7]). (b) For the near-end crosstalk, in contrast, the inclusion of the first anisotropic mode improves the agreement to the full-wave solution over the complete frequency range, leading to a considerable improvement already in the low GHz range (Figure adapted from [7]).

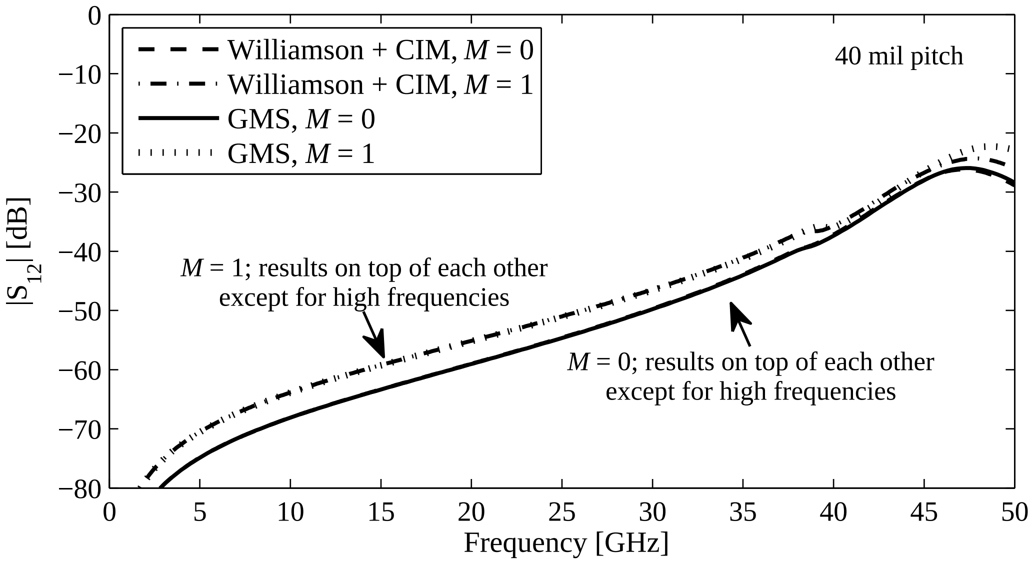

Figure 4.14: Comparison between results from the multiple scattering approach and from the contour integral method with anisotropic modes on circular ports. The results from the contour integral method with short circuited anisotropic modes for inclusion in the physics-based via model were provided by Dr. Xiaomin Duan at the Institute of Electromagnetic Theory, TUHH. The comparison for the near-end crosstalk between port 2 and port 1 as defined in Fig. 4.10 shows that using the CIM with anisotropic modes as the propagating field model, the physics-based via model can provide an accuracy similar to that of a multiple scattering approach for a via pitch of 40 mil.

to the via pitch will be investigated more closely for multilayer via arrays in Section 4.4.3). Two options exist for the extension of the physics-based via model: As previously described, multiple scattering approaches can take into account anisotropic modes. By carrying out a simulation that takes into account only propagating modes (the fundamental mode and anisotropic propagating modes up to a certain mode number), a parallel-plate admittance matrix Y^{pp} is obtained that includes the impact of anisotropic modes and can without further modification be employed as propagating field model in the physics-based via model. As a second option, the CIM was recently extended to include anisotropic modes [113]. Different than multiple scattering approaches, the contour integral method provides an explicit impedance matrix for the interaction between all modes on all ports. For the inclusion in the physics-based via model, the entries related to anisotropic modes have to be eliminated from the matrix. If the elimination is carried out in Y-parameters matrix - which corresponds to a short-circuiting of the anisotropic modes - an inclusion of the reduced Y^{pp} matrix in the physics-based via model leads to a good agreement with the multiple scattering solution, as shown in Fig. 4.14 for the near-end crosstalk between ports 1 and 2 for the case of 40 mil pitch. Although further investigations are necessary to determine which termination of anisotropic modes is correct from a physical point of view, it can be concluded that in principle, methods exist that can handle the impact of anisotropic modes as long as it is confined to a single cavity.

In this thesis, an extension of the physics-based via model to include anisotropic modes is not further studied. The application examples in Chapter 7 and Chapter 8 take this into account by using test structures with 80 mil via pitch, for which a sufficient accuracy of the propagating field model can be obtained with the conventional RWM or CIM formulations as previously discussed.

4.4 Multilayer Simulations of Via Arrays

The accuracy study of the physics-based via model is now extended from the simulation of a single cavity to the simulation of multilayer PCBs. To obtain the multilayer result, the network parameter matrices of the single cavities are combined. As described in Section 3.3.2, segmentation methods or a multiplication in ABCD parameters can be used to carry out the combination. Since the multiplication in ABCD parameters cannot be used for all structures (problems arise if cavities have different numbers of top and bottom ports e.g. due to power vias), typically segmentation methods are applied. The segmentation can be carried out in different network parameter forms (S-, Y-, and Z-parameters). For the examples in this thesis, no notable impact of the network parameter form has been observed. In this section, three points are addressed. First, a detailed accuracy study is carried out for a multilayer via array with 80 mil pitch. The aim is to confirm the good accuracy of the physics-based model observed for a single cavity in case of 80 mil pitch for a multilayer scenario—also with a view to the application examples in Chapter 7 and Chapter 8. Subsequently, the impact of the coaxial field model on the modeling accuracy in a multilayer scenario is studied. Finally, a variation of the via pitch is carried out to more precisely determine the lower limit for the via pitch up to which the physics-based via model can provide sufficiently accurate results.

4.4.1 Validation of Multilayer Results for 80 mil pitch

To study the accuracy of the physics-based via model in a multilayer PCB scenario, the stackup of the via array in Fig. 4.10(a) with 80 mil pitch is extended from a single cavity to the multilayer configuration illustrated in Fig. 4.15. Simulation results obtained with the physics-based via model are compared to results obtained with a commercial full-wave solver. Results for the transmission between via ports 2 and 5 are shown in Fig. 4.16(a). Although the behavior of the transmission in the multilayer case becomes more complex than in the single-cavity case due to additional resonances, the physics-based via model

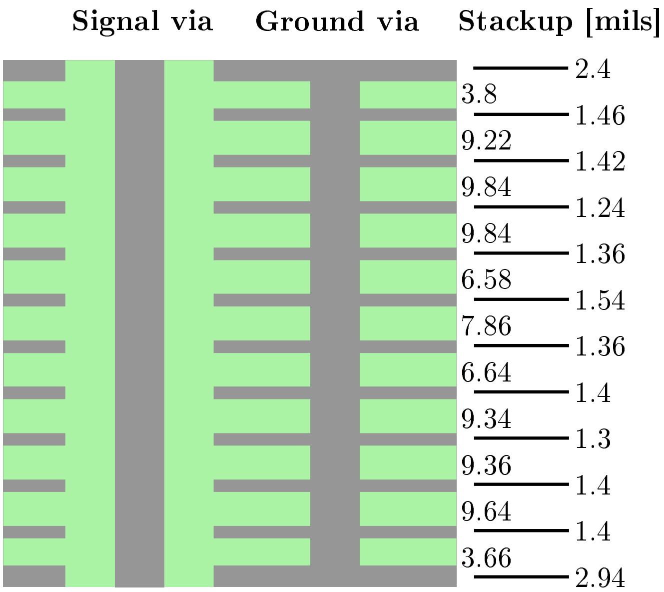

Figure 4.15: Multilayer PCB stackup for the via array structure shown in Fig. 4.10(a) to study the agreement between physics-based via model and full-wave results in the multilayer case. Thicknesses of metal and dielectric layers are specified in mil. All reference planes are assigned to ground (i.e., ground vias are connected to all reference planes), and no striplines exist in the test structure (Figure adapted from [7]).

shows a good agreement to the full-wave result over the entire frequency range up to 50 GHz. All characteristics of the full-wave result are captured by the physics-based model, and deviations between the two curves with regard to magnitude are below 2 dB except for a deviation related to a frequency shift of about 0.3 GHz around 15 GHz. A good agreement between physics-based via model and full-wave solution can also be observed for the reflection at via port 2 shown in Fig. 4.16(b). Results for the crosstalk between vias 1 and 2 (which are separated by an intermediate ground via) are shown in Fig. 4.17(a) for the near-end crosstalk and in Fig. 4.17(a) for the far-end crosstalk. In both cases, a good agreement between physics-based via model and full-wave result can be observed. For the near-end crosstalk, some larger deviations exist above 40 GHz, while the deviation for the far-end crosstalk is small over the entire frequency range up to 50 GHz. A good agreement between physics-based via model and full-wave simulation exists not only with regard to the magnitude, but also with regard to the phase of the simulated S-parameters. As an example, the results for the phase of the transmission between via ports 2 and 5 is shown in Fig. C.1 in Appendix C. The appendix also shows additional comparisons for the magnitude of the crosstalk between two directly adjacent vias in Fig. C.2 and two vias in a larger distance from each other in Fig. C.3. For a larger distance between the vias, some deviations between physics-based via model and full-wave result can be observed already at lower frequencies. However, also in this case, the physics-based model provides a good approximation in the frequency range up to 50 GHz in the overall view.

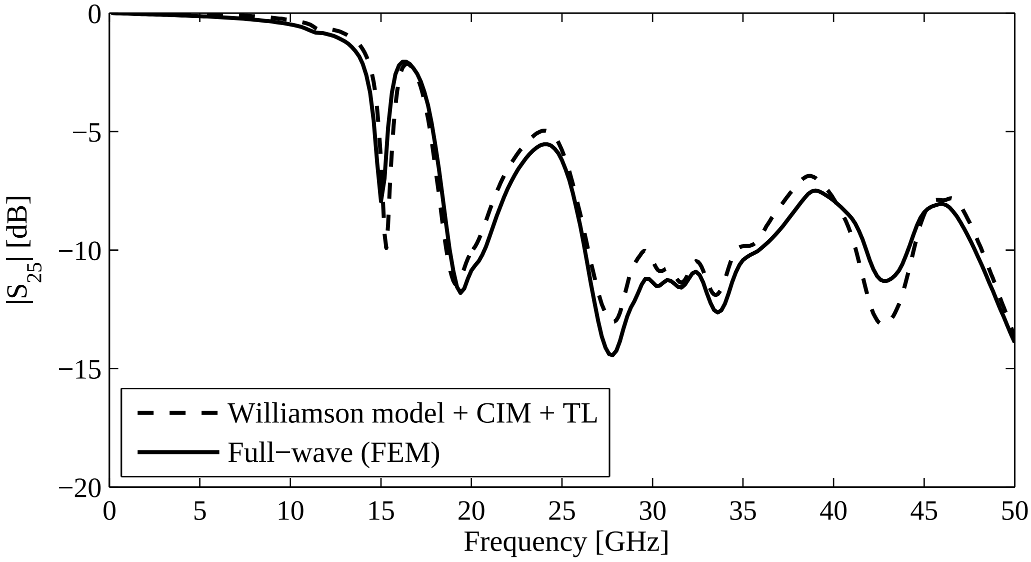

(a)

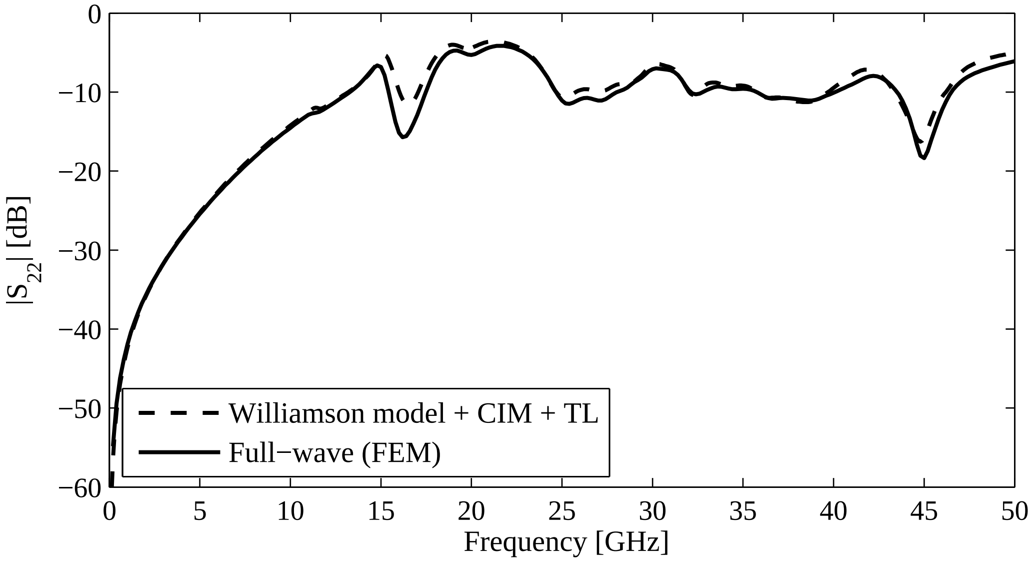

(b)

Figure 4.16: Comparison between results obtained with the improved physics-based via model and a full-wave solution for the via array in Fig. 4.10 with 80 mil pitch and the multilayer stackup in Fig. 4.15. (a) Transmission between via ports 2 and 5 (Figure adapted from [7]). (b) Reflection at via port 2 (Figure adapted from [7]). Although differences in magnitude exist at the resonance frequencies, the physics-based via model provides a good approximation of the full-wave result for both transmission and reflection up to 50 GHz.

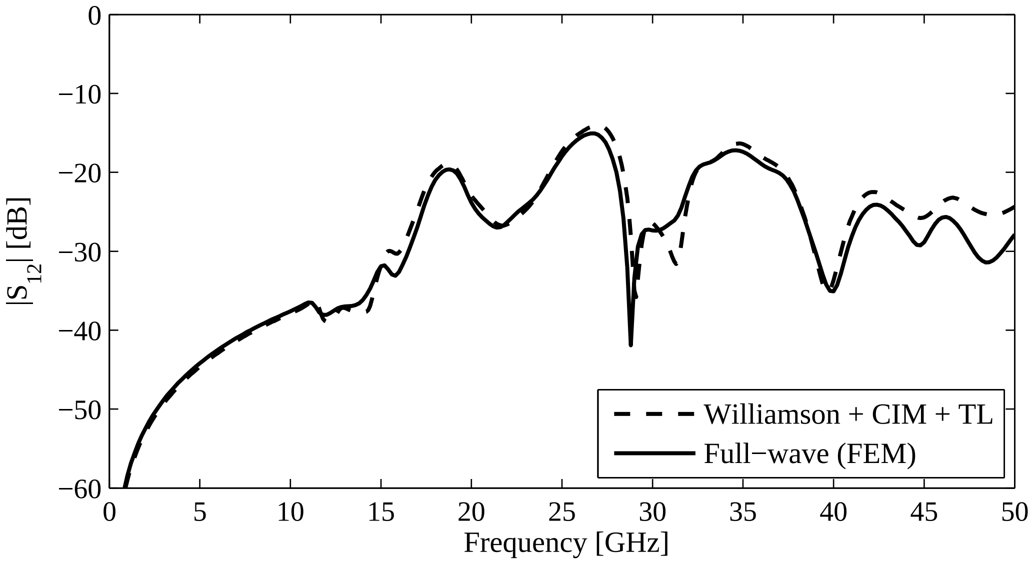

(a)

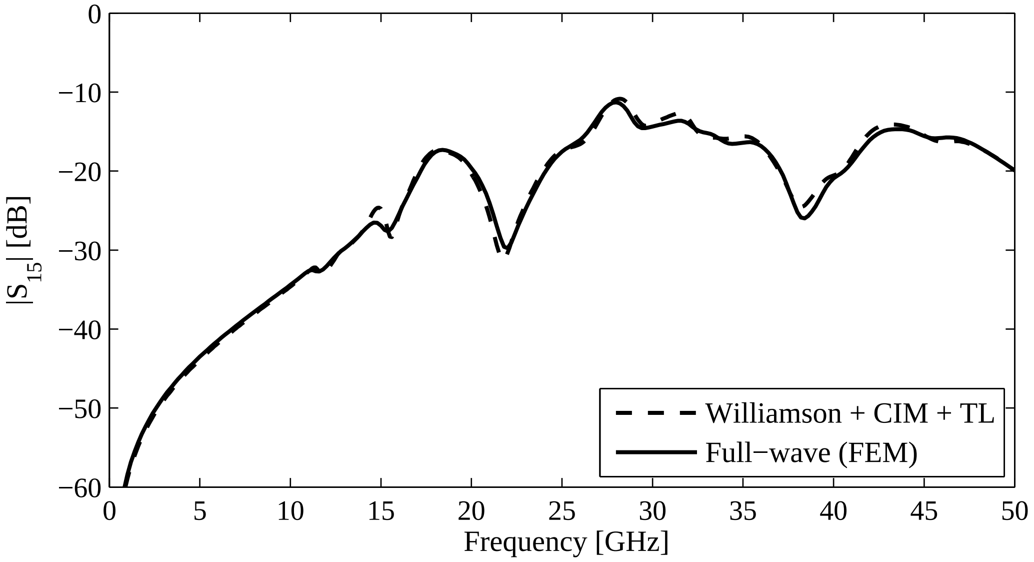

(b)

Figure 4.17: Comparison between results obtained with the improved physics-based via model and a full-wave solution for the via array in Fig. 4.10 with 80 mil pitch and the multilayer stackup in Fig. 4.15. (a) Near-end crosstalk between via ports 1 and 2 (Figure adapted from [7]). (b) Far-end crosstalk between via ports 1 and 5 (Figure adapted from [7]). A good agreement between physics-based via model and full-wave result can be obtained for both near- and far-end crosstalk. In the near-end crosstalk, some larger deviations can be observed for frequencies above 40 GHz.

4.4.2 Impact of the Coaxial Field Model

As described in Section 3.2.3, two alternatives exist for the modeling of the coaxial field regions between vias and antipads: a representation using only the coaxial capacitance, or a more accurate representation using a short LC transmission line model. The previously shown results have been obtained with the more accurate transmission line model. Here, the impact of a change to the simpler capacitance model on the accuracy of the physics-based via model is studied. For this purpose, the plots of the transmission between via ports 2 and 5 and the reflection at via port 2 from Fig. 4.16 are extended with an additional curve calculated with the coaxial capacitance as coaxial field model. For the transmission in Fig. 4.18(a), the coaxial capacitance increases the deviation to the full-wave result at some resonances. A more systematic deviation can be observed in the phase of the transmission, which is shown in Fig. C.4(a) in Appendix C. At frequencies above 30 GHz, the capacitance model leads to a deviation of about 15° in comparison to the TL model. An evaluation of the phase of the transmission between via ports 2 and 5 for a reduced stackup containing only the three center cavities of the original 11 cavity stackup shows a phase deviation between capacitance model and TL model of less than 5°, see Fig. C.4(b). The results can be explained with the phase shift due to the signal transmission through the coaxial antipad regions, which is not correctly taken into account by the capacitance model. The impact of this inaccurate modeling increases with an increasing cumulated thickness of the reference layers in the stackup. Nevertheless, even if the capacitance is used as a coaxial field model, the physics-based via model provides a good approximation for the transmission with regard to magnitude and phase. Similar observations can be made with regard to the crosstalk. The strongest impact of the antipad model can be seen for the reflection in Fig. 4.18(b). Since, in comparison to the TL model, the capacitance model changes the input impedance of the via as seen from the port, it leads to deviations in the reflection, especially in the lower frequency range up to 10 GHz. Nevertheless, the characteristics of the full-wave result are still captured. All in all, the obtained results show that also with the capacitance as a coaxial field model, the physics-based via model provides a good approximation of full-wave results. The TL model improves the modeling accuracy mostly with regard to the reflection - especially at lower frequencies - and with regard to the phase of the transmission - especially for a large cumulated thickness of the reference layers.

4.4.3 Impact of the Via Pitch

As observed in Section 4.3.2 for a single cavity, the accuracy of the physics-based via model is not sufficient for the simulation of via arrays with 40 mil pitch. The reason is that the physics-based model neglects anisotropic modes, which play a role for the interaction between vias in very dense arrays. Through a variation of the via pitch, the lower limit up

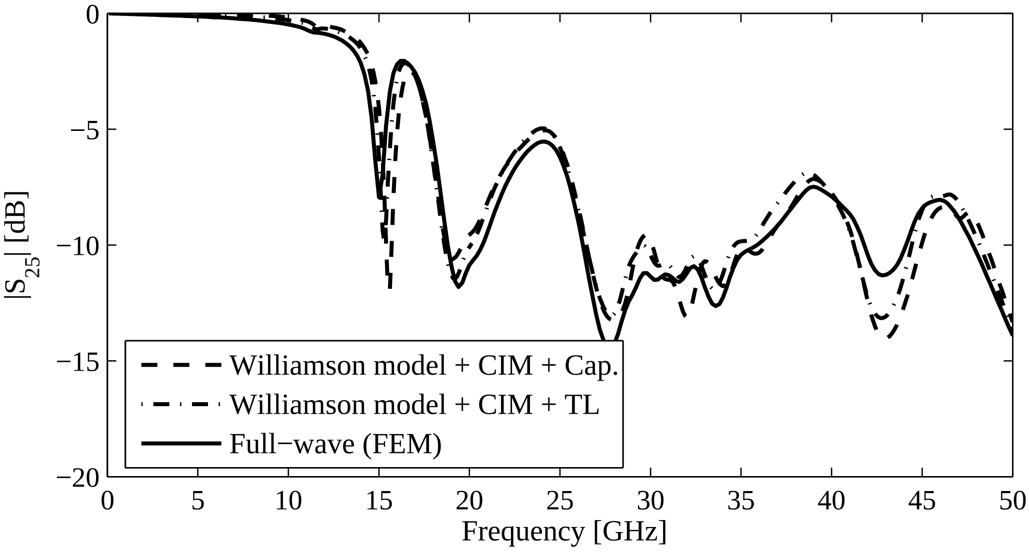

(a)

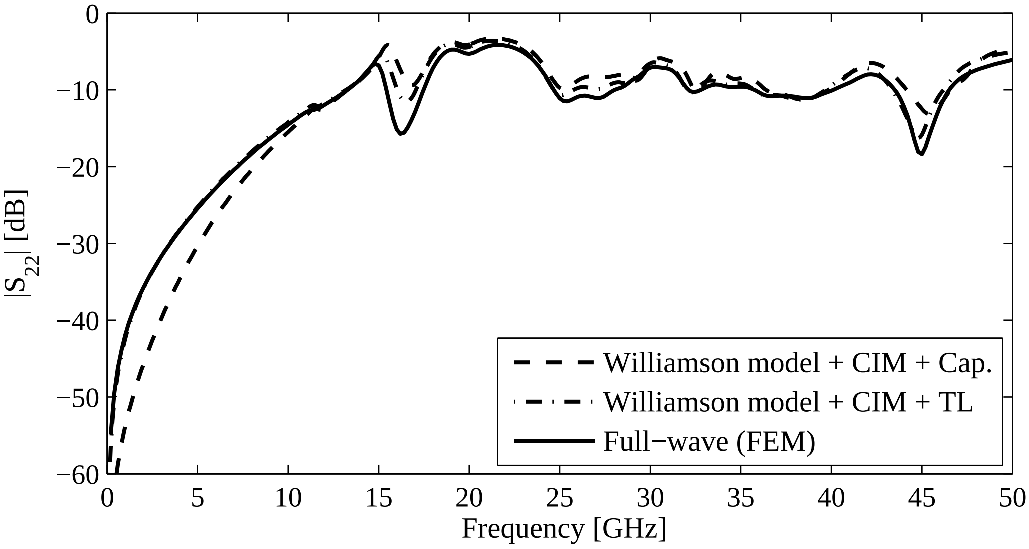

(b)

Figure 4.18: Comparison of reflection and transmission for a via inside the multilayer via array with the top view in Fig. 4.10(a) and the cross section in Fig. 4.15, calculated using either capacitances only or coaxial transmission lines as antipad models. (a) Comparison for the transmission. While the transmission line model generally leads to an improved agreement, the improvements are comparatively small, and exist only at some frequency ranges (Figure adapted from [7]). (b) Comparison for the reflection, showing the strongest impact of the antipad model. In the frequency range up to 10 GHz, the transmission line model clearly improves the agreement to full-wave results (Figure adapted from [7]).

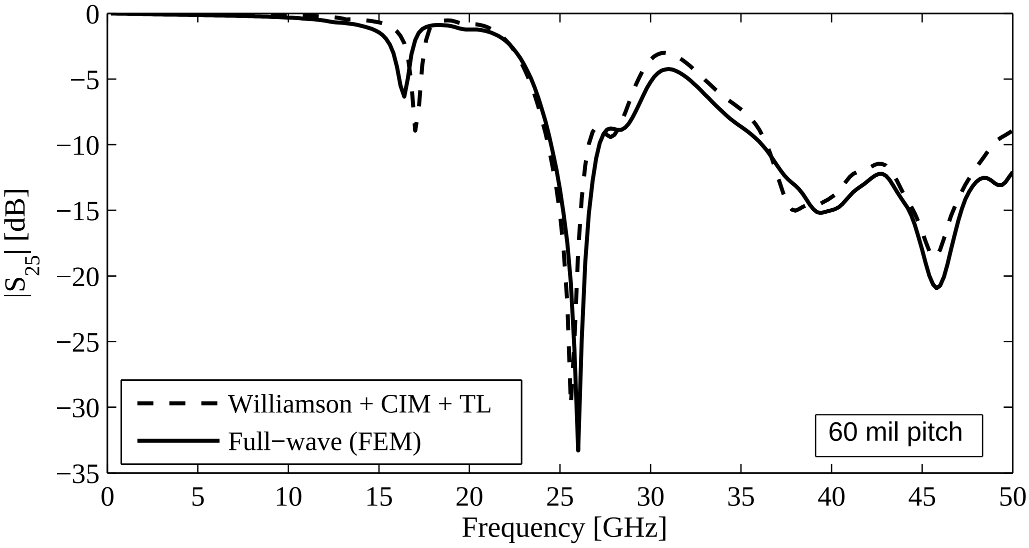

(a)

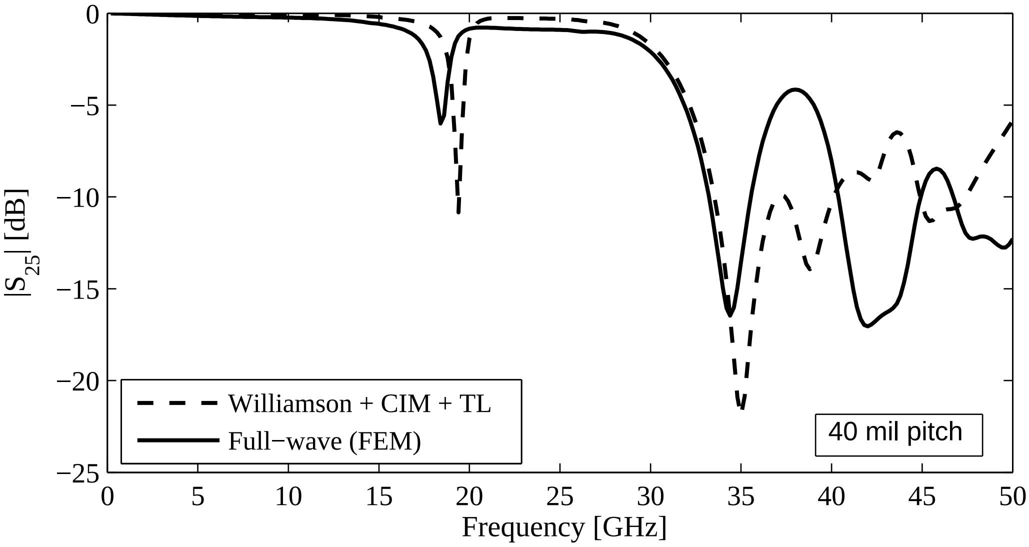

(b)

Figure 4.19: Impact of the via pitch on the accuracy of the physics-based via model for the simulation of the transmission between via ports 2 and 5 for the via array in Fig. 4.10 with the multilayer stackup in Fig. 4.15. (a) Simulation results for 60 mil via pitch. A considerable frequency deviation of 0.6 GHz can be observed already at the first resonance of the transmission. Nevertheless, the physics-based via model provides a good overall approximation of the full-wave solution. (b) Simulation results for 40 mil pitch. The frequency shift at the first resonance is increased to 0.8 GHz. Above 35 GHz, the physics-based via model does not capture the characteristic features of the transmission.

to which the physics-based via model can still provide accurate results is investigated here more closely for the multilayer scenario. The transmission between via ports 2 and 5 is shown in Fig. 4.19 for the two cases of 60 mil pitch and 40 mil pitch. The results for 60 mil in Fig. 4.19(a) show that although a frequency shift of 0.6 GHz exists for the first resonance, the physics-based via model still provides a good overall approximation of the full-wave result in the frequency range up to 50 GHz. This is confirmed by the result for the near-end crosstalk between via ports 1 and 2, which are shown in Fig. C.5(a) in Appendix C. Also for 50 mil pitch, a fair overall agreement can still be observed, although the deviations increase in comparison to the case of 60 mil pitch (as an example, the transmission is shown in Fig. C.6(a) in Appendix C). For 40 mil pitch, the frequency shift of the first resonance of the transmission in Fig. 4.19(a) is 0.8 GHz, and the physics-based via model captures the characteristic features of the full-wave result only up to about 35 GHz. The results for the near-end crosstalk between ports 1 and 2 in (see Fig. C.5(b) in Appendix C) show deviations between physics-based via model and full-wave result over the entire frequency range - similar to the single cavity evaluation in Fig. 4.13(b). In conclusion, the results indicate that a limit for the accuracy of the physics-based via model lies between 60 mil and 40 mil pitch. Accurate results can be expected for pitch sizes of 60 mil or more. It shall be mentioned in this context that for the simulation of power vias, additional challenges have been observed in comparison to the simulation of signal vias. A brief description of the modeling accuracy for power vias is given in Appendix D. However, also in presence of power vias, no reduction in the accuracy of the physics-based via model for the interaction between signal vias has been observed.

4.5 Accuracy of Combined Via and Stripline Models

So far, the accuracy study has focused on via arrays without striplines. As described in Section 3.4, stripline models can be included in the physics-based via model through a modal decomposition approach. This approach assumes that a coupling between stripline mode and parallel plane mode occurs only at the via location. In this case, the cavity model - including all vias but no striplines - and the stripline model can be calculated independently from each other. A combination of the two models is then carried out by combining the Y-parameter matrices as described in (3.15). If this modal decomposition approach is used for the inclusion of striplines, two possible sources for inaccuracies exist: First, inaccurate stripline models (e.g. resulting from approximations made in a numerical calculation) will necessarily lead to inaccuracies in the combined model. Second, the approach cannot lead to accurate results if a direct interaction between striplines and adjacent vias occurs. The analysis in this section will focus on the second aspect, assuming that it is generally possible to obtain sufficiently accurate models for striplines. Accuracy studies for stripline model calculations with the 2D-solver employed in the context of this work can be found in [37, 108].

A direct interaction between striplines and adjacent vias has to be expected in case of small separations. So far, the interaction has been mostly studied with regard to guard via rows in the literature [114–118]. Guard vias are ground vias that are used with the purpose of shielding neighboring traces from each other. As shown in [114–116], if traces are placed too close to guard via fences, the vias can provide a coupling that increases the crosstalk between the traces rather than reducing it. The goal of the following analysis is to study the nature of the interaction for signal vias, and to determine an approximate limit for the separation between stripline and via above which direct interaction can be neglected. Two main effects leading to interaction can be distinguished for signal vias: On the one hand, a local field coupling between via barrel and the signal conductor of the stripline will occur. On the other hand, the antipads of the via will act as discontinuities in the return current path of the stripline [119]. To investigate these effects, different full-wave simulations have been carried out for a simple configuration with only one via and one trace as shown in Fig. 4.20. The cross section in Fig. 4.20(a) and the top view in Fig. 4.20(b) show the general setup of the structure, including the material parameters. The port numbering is included in the full-wave setup in Fig. 4.20(c). The standard geometry parameters, which were used for all simulations unless otherwise specified, are defined in Table 4.1.

First, the coupling between via and stripline has been investigated for different via trace separations d. The coupling is shown in Fig. 4.21(a) in terms of S-parameters for the crosstalk between via port 1 and stripline port 3. A time domain evaluation shows that the coupling is of capacitive nature. This corresponds to physical intuition, since no inductive coupling is expected due to the orthogonality of the conductors. It is shown in [36] that an equivalent circuit model using a simple lumped capacitance between via barrel and stripline conductor is sufficient to reproduce the observed crosstalk behavior. The values of the lumped capacitance for different via trace separations can be extracted from the full-wave results. Results are shown in Fig. 4.21(a) for two different relative permittivities of the dielectric substrate. The stripline widths w have been adjusted, so that the characteristic impedance of the stripline is approximately $50\,\Omega$ in both cases. An empirical formula for the coupling capacitance was proposed based on extracted capacitance values in [36]:

$$C_{\mathrm{coup}}(d) = A \cdot \ln(B/d). \tag{4.6}$$

In addition to the via trace separation d, the formula contains the constants A and B, which depend on the material and geometry parameters of the structure. A least squares fit of

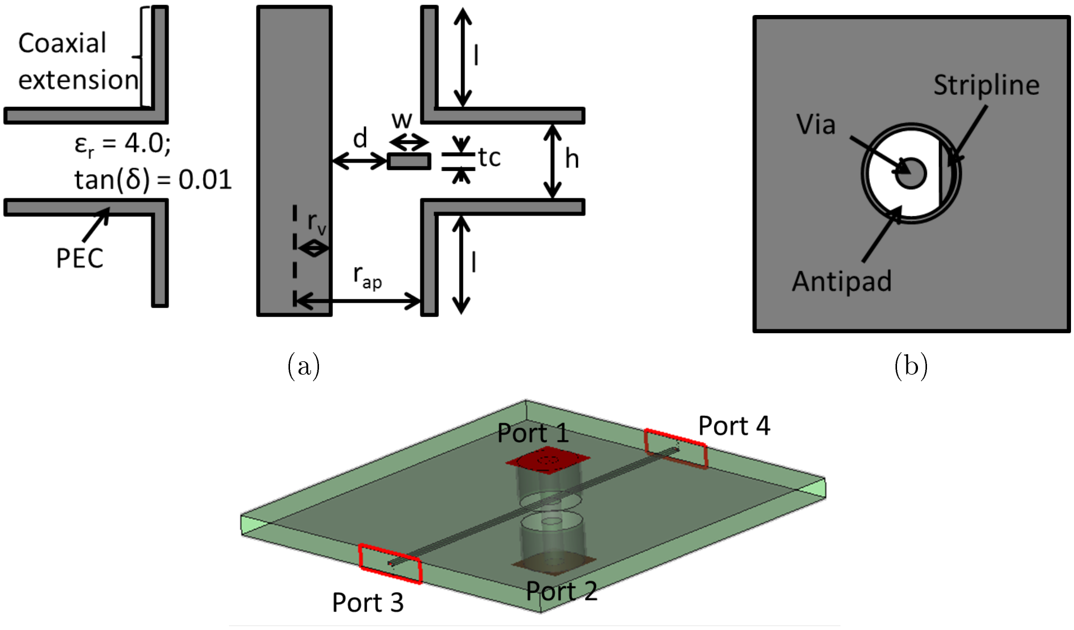

(a) (b)

(c)

Figure 4.20: Test structure to investigate the proximity effects between vias and striplines (all Figures from [34]). (a) Cross section of the investigated structure including geometry and material parameter definitions. (b) Top view of the investigated structure. (c) Model setup in a commercial FIT solver [97], including the port definitions.

(4.6) to the extracted capacitance values gives values of $A_1 = 17.0\,\mathrm{fF}$ and $B_1 = 14.0\,\mathrm{mil}$ for $\varepsilon_{\mathrm{r}1} = 4.3$, and $A_2 = 14.2\,\mathrm{fF}$ and $B_2 = 13.9\,\mathrm{mil}$ for $\varepsilon_{\mathrm{r}2} = 3.5$. The fitted curves are plotted in Fig. 4.21(b) together with the static capacitance between via barrel and stripline conductor obtained with a commercial solver [120]. Apart from via trace separations smaller than 2 mil, which will not be encountered in practical structures, the static capacitance values show a good agreement to values extracted from full-wave simulations, which indicates that the static capacitance is suitable do describe the observed coupling effect.

The capacitance between a stripline and a via in close proximity does not only imply a coupling, but also leads to a local change of the characteristic impedance of the stripline. As mentioned before, an additional impact results from the antipads of the via, which constitute a discontinuity in the return path of the stripline current. Together, the two

Table 4.1
Standard parameter definitions for the test structure in Fig. 4.20

Parameter	h	r_{v}	r_{ap}	w	tc	l	d
Dimension [mil]	10	5	15	4	1	20	2.5

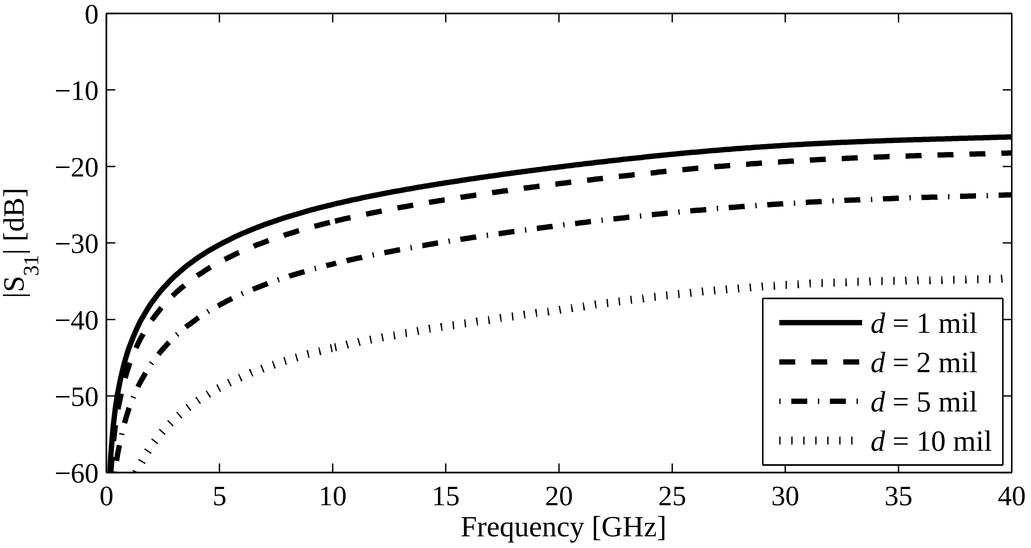

(a)

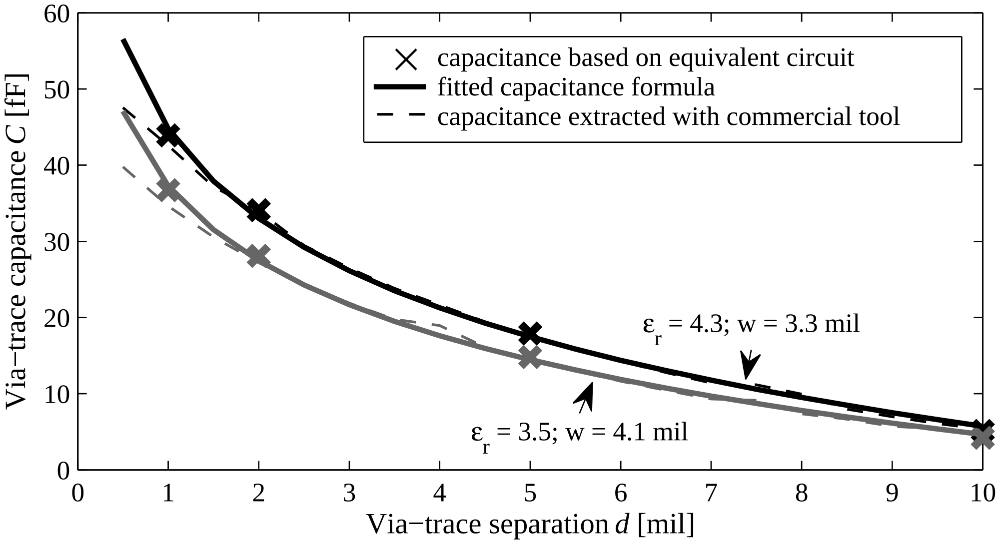

(b)

Figure 4.21: Study of capacitive coupling between via and stripline. (a) Crosstalk between via and stripline port depending on the via to trace separation. The results show the increasing coupling between via and stripline for a decreasing separation (Figure from [34]). (b) Values for the coupling capacitance extracted from full-wave simulations with an equivalent circuit compared to static capacitance values extracted with a commercial tool [120]. Except for very small via separations below 2 mil, the values show a good agreement. This indicates that the coupling between vias and striplines in close proximity can in good approximation be modeled by the static capacitance (Figure from [34]).

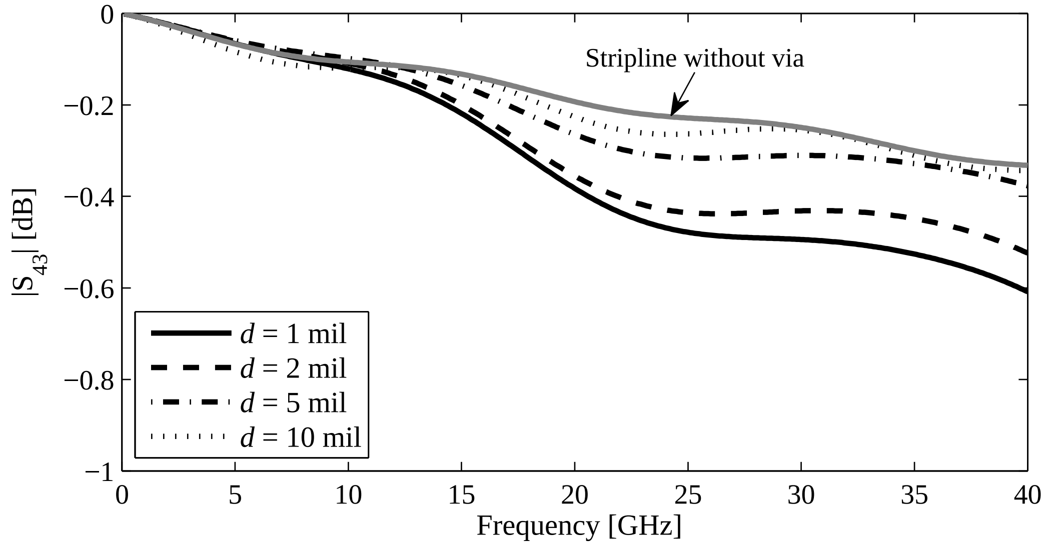

(a)

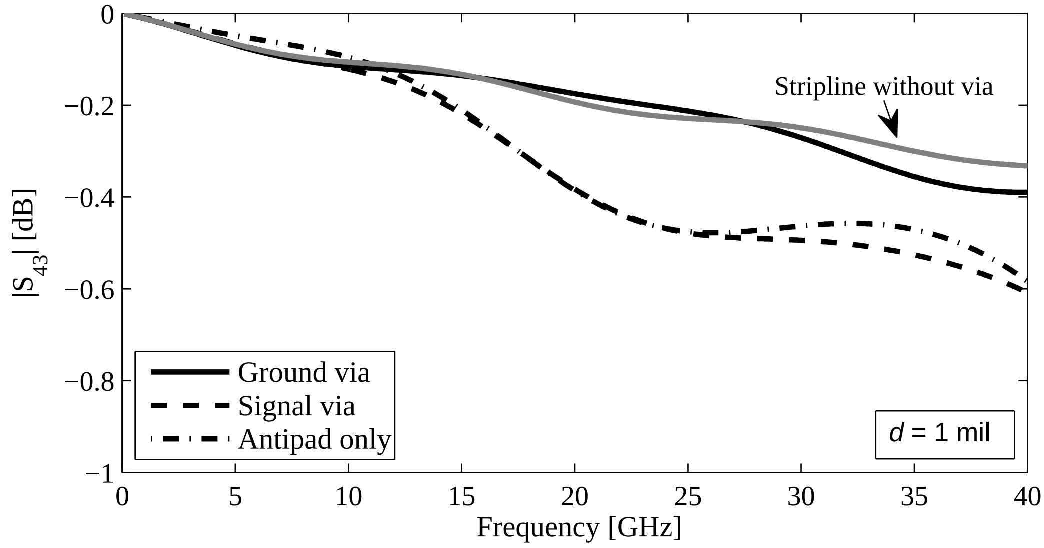

(b)

Figure 4.22: Impact of a via in close proximity on the stripline transmission. (a) With decreasing separation between via and trace, an increasing detrimental impact on the stripline transmission exists. (Figure from [34]) (b) Comparison of the different detrimental impacts of a via in close proximity. Compared are a ground via, a signal via, and circular cutouts in the reference planes representing antipads without a signal via. The results show that the impact of the capacitive coupling to the ground via on the transmission is small, while the impact of the discontinuity represented by the antipad is almost as large as the impact of the signal via (Figure from [34]).

effects impact the stripline transmission. Their combined impact is shown in Fig. 4.22(a) for different via trace separations. While for small separations of 1 mil or 2 mil, a clear deviation of the transmission from the behavior without a via can be observed, only a small deviation remains for a separation of 10 mil. In Fig. 4.22(b), an attempt is made to separate the impacts of the two effects. For a small via trace separation of 1 mil, the stripline transmission is shown for three structures adjacent to the stripline: a signal via, a ground via, and antipads without via. The antipads without via are modeled as cutouts with radius r_{ap} in the reference planes, terminated with a PMC boundary condition. The largest deviation from the transmission without adjacent via can be observed in the signal via scenario. However, with antipads only, the resulting deviation is almost as large. In contrast, the ground via leads only to a small change in the stripline transmission. The results indicate that for the stripline transmission, the impact of the discontinuities represented by the antipad is much larger than the impact of the capacitance to signal or ground vias. A further investigation with a stripline routed between two rows of signal vias in [34] shows that a relevant impact on the stripline transmission typically occurs if the stripline shows an antipad overlap, giving a clear lower limit for the separation up to which proximity effects can be neglected. It should be mentioned that in case of a periodic arrangement of vias, relevant effects may occur even for larger separations between vias and striplines due to a positive interference between originally weak effects. In conclusion, the model decomposition approach used in the physics-based via model is only valid for a sufficient separation between vias and traces. For the routing of striplines through via arrays, a sufficient separation will typically be given for 80 mil pitch, while striplines are already close to the antipads in case of 40 mil pitch.

4.6 Summary and Discussion

The analysis carried out in this chapter shows that all sub-blocks of the physics-based via model have an impact on the modeling accuracy. For the antipad region, a transmission line model leads to more accurate modeling results, in particular for the reflection. For the local via fields, a more complex model such as the Williamson model leads to more accurate results than the simple capacitance model. The local field model becomes relevant for large values of the dielectric thickness as well as for the simulation of via arrays. For the propagating field model, the accuracy depends mainly on the via pitch. For 80 mil pitch, simple models are sufficient. In case of 40 mil pitch, an inclusion of anisotropic modes will be necessary to obtain accurate results. At least for the simulation of a single cavity, a solution can be provided by multiple scattering approaches as well as by an inclusion of the CIM with anisotropic modes in the physics-based via model. For the design studies in

Chapter 7 and Chapter 8 of this thesis, examples with 80 mil pitch are chosen to ensure the reliability of the employed modeling results. For this pitch size, proximity effects between vias and striplines can be neglected, so that also the inclusion of striplines via a model decomposition approach provides accurate results.

5 Numerical Efficiency of the Modeling Approach

In this chapter, the numerical effort for the simulation of PCBs with the physics-based via model is analyzed in detail. In the first part of the chapter, an analysis of calculation times is carried out for the different parts of the algorithm, and an efficient algorithm based on a suitable combination of calculation methods and network parameters for the model evaluation is described. For the efficient algorithm, the overall calculation time is discussed for different numbers of vias and for stackups related to different modeling complexities. In the second part of the chapter, a parallelization of the code and an exploitation of structural regularity in via arrays are described as possible additional measures for a further reduction of calculation times. Finally, an application of the efficient algorithm to model a very large via array is briefly compared to other simulations of large via constellations described in the literature, and the acceleration achieved in comparison to a previous implementation of the physics-based via model is evaluated for a test case that was documented in [1].

5.1 Analysis of Calculation Times

The computational effort for the simulation of a test structure with the physics-based via model depends on two main factors: the specific combination of calculation methods and network parameters for the simulation and the complexity of the investigated test structure. The numerical efficiency of the algorithm strongly depends on the calculation methods selected for the different sub-blocks of the physics-based model (as described in Section 3.2, alternative approaches exist for each sub-block). Furthermore, an analysis of the numerical efficiency has to take into account that the combination of the sub-block models may require network parameter conversions, which are numerically expensive as well. Possible calculation paths - resulting from specific choices of subdomain models and the associated network parameter conversions - are described in Section 5.1.1. The different possible paths are evaluated and compared with regard to their numerical complexity in Section 5.1.2. For the impact of the test structure on the computational effort, the main factor is the number of vias to be simulated. The impact of the number of vias on the calculation time is included in the evaluation in Section 5.1.2. The number of cavities to be simulated has a simple linear impact on calculation times. However, other factors such as the signal-to-ground ratio – the ratio between signal vias and ground vias – or the presence of mixed reference planes have a considerable impact on the computational effort. For example, the presence of mixed reference planes increases the numerical and organizational effort for the algorithm, as shown in Section 5.1.3.

5.1.1 Overview of Alternative Calculation Paths

The alternative calculation paths shown in Fig. 5.1 arise from the different methods available to calculate the network parameters for the subdomains of the physics-based via model and to combine the single cavity results, and from the required network parameter conversions. Network parameter conversions are necessary since some steps can be carried out with a reasonable effort only in a certain network parameter form. This is for example the case for the matrix expansion of the propagating field model, which is a very simple operation in Y-parameters, and for the following inclusion of the local field models, which only requires additions and - possibly - scalar multiplications in Y-parameters. The numerical effort for the individual paths - including the impact of network parameter conversions where necessary - is evaluated in the following subsection. All evaluations are carried out for the calculation of a single frequency point on an AMD Opteron™ 6140 processor (2.6 GHz clock frequency), using Fortran implementations of the necessary calculation steps.

5.1.2 Selection of Fast Calculation Methods

As shown in Fig. 5.1, the calculation of the propagating field model requires several steps: the calculation of Y^{pp} or Z^{pp}, the elimination of ground via entries from the matrix, the conversion to Y-parameters (in the case of Z^{pp}), and the matrix expansion to include upper and lower ports in the calculation. In this section, three alternative methods for the Z^{pp} calculation are taken into account: the RWM and CIM as described in Section 3.2.1 for the calculation for infinite planes, and the CRM in the numerically efficient single summation formulation [101] for the calculation for rectangular finite planes. In their basic formulation, all three methods calculate the parallel plane impedance Z^{pp}, which requires a subsequent conversion from Z- to Y-parameters for the following matrix expansion. Although the matrix reduction for ground vias can be carried out in a very simple way (by eliminating the corresponding rows and columns from the matrix) in Y-parameters, the calculation time can be decreased by eliminating the ground vias already in Z-parameters using the Schur's complement as described in [58, 59], so that the matrix size is reduced already before the conversion to Y-parameters is carried out. An alternative calculation path arises since for the CIM formulation, a simple rearrangement of the formula is possible to directly obtain the parallel plate admittance as $\overline{\overline{Y}}^{\mathrm{pp}} = \overline{\overline{H}}^{-1}\overline{\overline{U}}$ without increasing the numerical effort. In this case, ground vias can simply be reduced from the Y-matrix, and no parameter conversion is necessary. The calculation times of the Z^{pp} or Y^{pp} calculation and – where required – the subsequent parameter conversion are shown depending on the number of

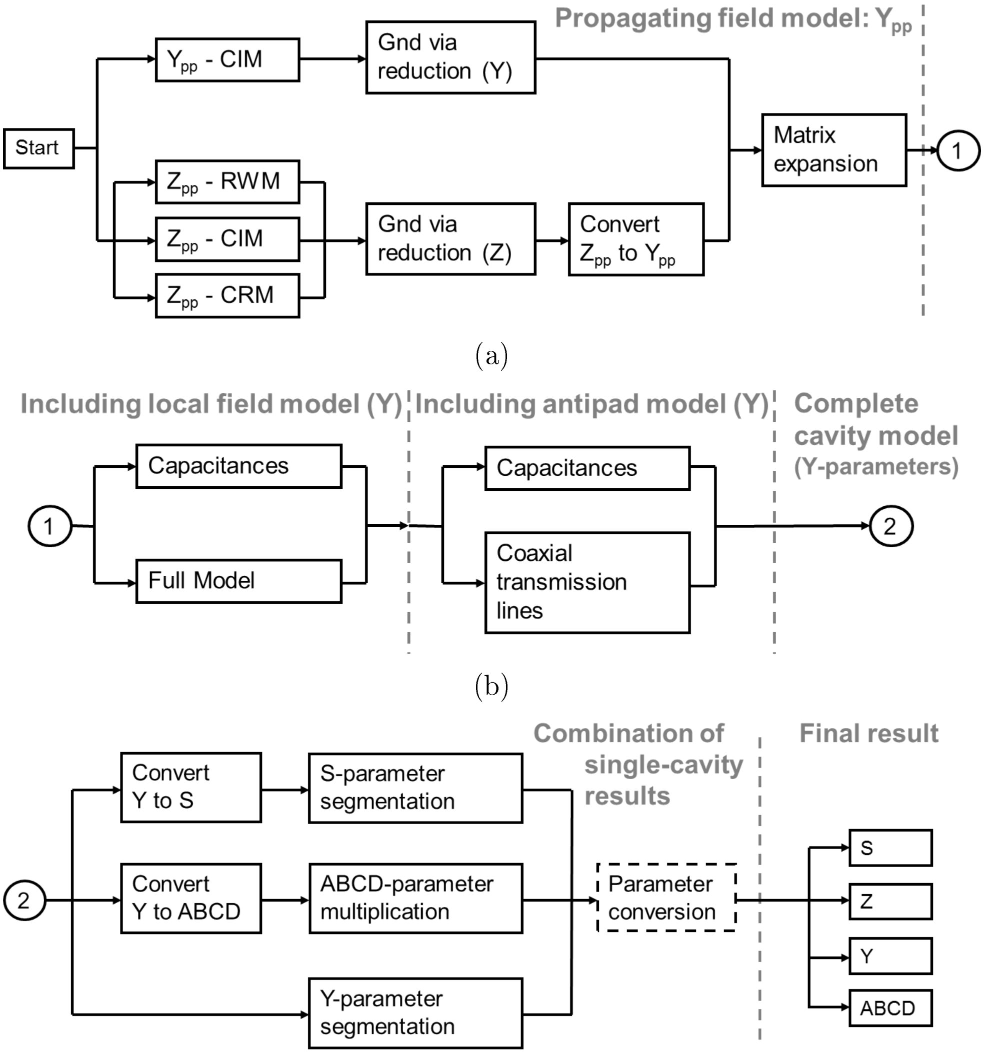

(a)

(b)

(c)

Figure 5.1: Flow diagram showing the different possible paths for the network parameter calculation with the physics-based via model, consisting of (a) the calculations for the propagating field model, (b) the inclusion of local field models and antipad models, and (c) the combination of single-cavity results (all Figures from [26]).

vias in Fig. 5.2(a). It should be noted that, for the shown evaluation, no ground vias are present in the test structure, which represents the worst case with regard to the numerical effort.

To assess the impact of the number of vias on the calculation times in a more systematic way, the obtained curves are fitted to the formula

$$t(n) = a \cdot n^3 + b \cdot n^2, \tag{5.1}$$

with the calculation time t, the number of vias n, and the coefficients a and b. The coefficient a represents the portion of operations with cubic complexity, such as matrix multiplications and inversions. The coefficient b represents the portion of operations with quadratic complexity, which is mainly determined by the matrix setup for the calculation of the propagating field model. To illustrate the information contained in the coefficients for the different methods included in Fig. 5.2(a), a detailed interpretation is carried out here for the example of the propagating field model. A comparison of the coefficient a shows that the portion of cubic operations for RWM and CRM is similar. Both methods do only require one matrix inversion, which occurs during the parameter conversion from Z^{pp} to Y^{pp}. The portion of quadratic operations described by the coefficient b, in contrast, is considerably higher for the CRM. This can be attributed to the higher numerical effort for the matrix setup, which requires the evaluation of an infinite sum (which can be truncated only after about 100 terms depending on plane size, port location, and frequency). For the CIM formulation (in Z-parameters or Y-parameters), the portion of quadratic operations is - in a rough approximation - twice as large as for the RWM, since the two matrices $\overline{\overline{H}}$ and $\overline{\overline{U}}$ have to be set up. For the CIM in Y-parameters, one matrix inversion and one matrix multiplication are required, leading to a being about twice as large as for the RWM. For the CIM in Z-parameters, an additional matrix inversion is required for the conversion to Y-parameters, making a about three times as large as in the case of the RWG. In summary, the RWM provides the fastest Y^{pp} calculation. If the CIM formulation has to be used due to its higher accuracy for certain cases as described in Chapter 4, the direct calculation of Y-parameters should be used, which will roughly double the time for the Y^{pp} calculation in comparison to the RWM. If a finite board size has to be taken into account, an application of the CRM will further increase the calculation time. Although the asymptotic behavior of the CRM for increasing via numbers – as described by the coefficient a – is similar to that of the RWM, the calculation time for the CRM is still several times larger even for the simulation of 10,000 vias due to the numerically expensive matrix setup. Especially for applications where a finite board size has to be taken into account, it is therefore worthwhile to investigate methods for an acceleration of the matrix setup. A possible approach will be briefly described in the outlook in Section 5.4 at the end of this chapter.

For the calculation of the local field model, two alternative approaches as described in Section 3.2.2 are considered here: the via barrel-to-plane capacitance, and the Williamson model as an example for an extended local field model. The numerical effort for each local field model is caused by the setup of the model itself, which requires the calculation of the different model elements, and by the combination with the propagating field model. For test structures consisting of more than a few vias, the computational effort for the setup of the local field model can be neglected for both the capacitance model and the Williamson model, since it grows only linearly with the number of vias. For typical PCB designs, the effort is reduced even further, since only one or a few different via diameters exist per cavity. The local field model calculation has to be carried out only once per diameter, since it does not depend on the via location. Also the numerical effort for the combination of local field model and propagating field model can be neglected in comparison to the effort of the propagating field calculation for large via constellations. From (3.11), it can be seen that the capacitance model requires only one addition for each main diagonal entry of the expanded Y^{pp} matrix, leading to complexity of $\mathcal{O}(n)$. The Williamson model requires a scalar multiplication for each entry of the expanded Y^{pp} matrix and additions for each entry on the main diagonal and two further diagonals as shown by (3.12), which leads to a complexity of $\mathcal{O}(n^2)$. Since both modeling approaches lead to very short calculation times, no extra plot is shown for the local field model. In summary, the numerical effort for both setup and inclusion of the local field models can be neglected in comparison to the effort of the propagating field model calculation, which is of complexity $\mathcal{O}(n^3)$. This also means that the Williamson model, which was found to improve the modeling accuracy in Chapter 4, can be used for all simulations without a notable increase in computation time.

For the antipad model, two alternatives are compared as described in Section 3.2.3: a model using only the coaxial capacitance, and an LC transmission line model. For the model setup, both approaches behave similar to the local field model: the numerical effort grows only linearly with the number of vias, and is further reduced when only a few via diameters exist in the modeled PCB, so that the antipad model has to be calculated only a few times. With regard to the combination with propagating and local field model, however, the two calculation approaches show a fundamentally different numerical complexity. If the simple capacitance model is used, it can directly be added using only one addition for each main diagonal entry of the expanded Y^{pp} matrix (similar to the addition of the via barrel to plane capacitance used as a local field model), again leading to a negligible computational effort of complexity $\mathcal{O}(n)$. For a simulation using transmission line models, a two-port network parameter block is created for the antipad model that has to be combined with the Y^{pp} matrix using segmentation methods. This leads to a cubic complexity with high computation times as shown in Fig. 5.2(b). The choice of the antipad model therefore constitutes a trade-off between numerical efficiency and physical accuracy. Although the coaxial transmission line models the impact of the antipad fields more accurately, the more efficient capacitance model may in many cases be sufficient to obtain a good approximation of the network parameters of the test structure (see Section 4.4.2).

After the inclusion of local field model and antipad model, a model of the complete cavity

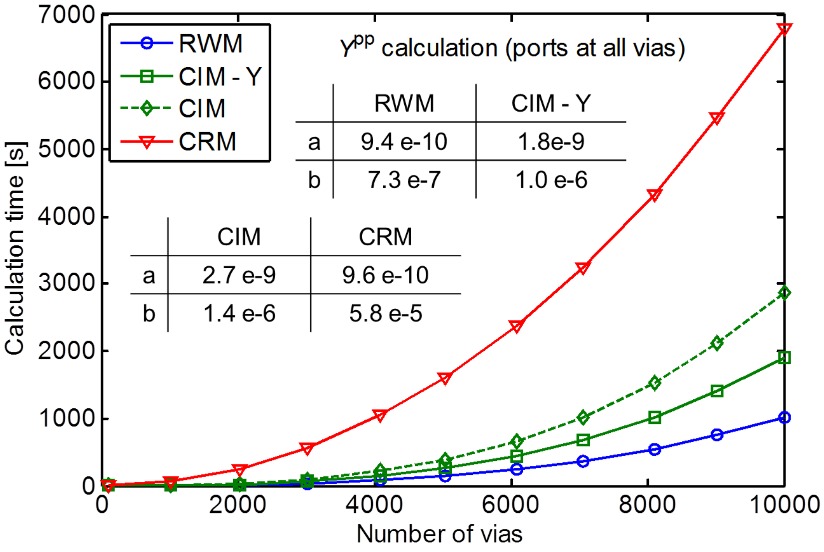

(a)

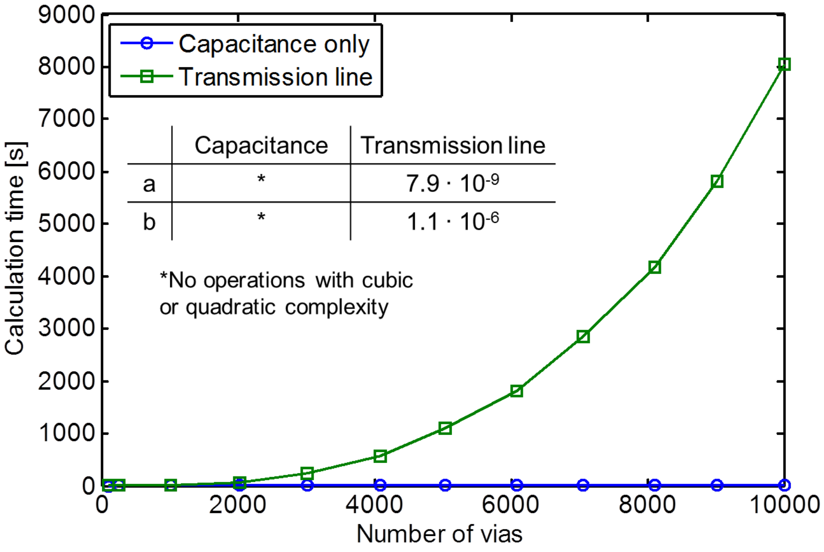

(b)

Figure 5.2: Calculation time depending on the number of vias for the individual blocks of the equivalent circuit model. Processor: AMD Opteron™ 6140, 2.6 GHz. (a) Calculation time with different modeling approaches for the parallel plate admittance. The evaluation assumes that all vias are signal vias, so that no entries can be eliminated from the Z^{pp} matrix before the inversion to Y^{pp} (Figure from [26]). (b) Calculation time for the antipad model, including the combination with propagating field and local field model. The transmission line model requires a segmentation for the combination with propagating field and local field model, leading to the observed large calculation times. (Figure from [26]).

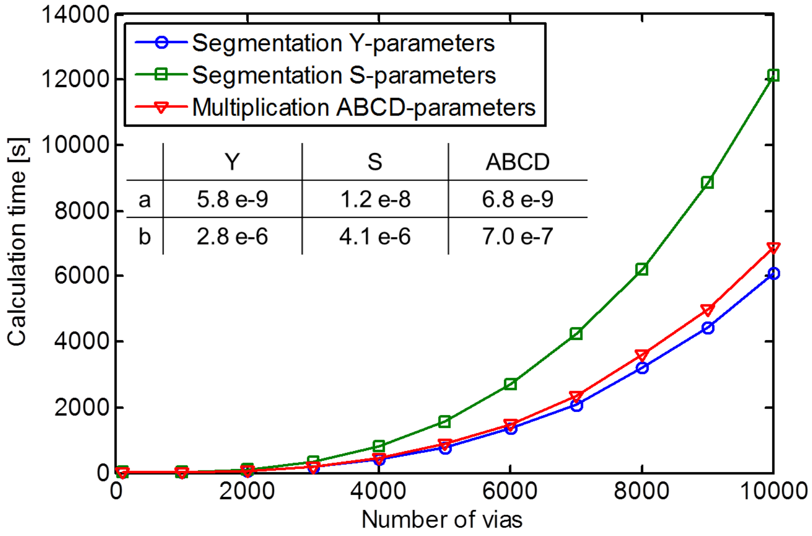

	Y	S	ABCD
a	5.8 e-9	1.2 e-8	6.8 e-9
b	2.8 e-6	4.1 e-6	7.0 e-7

Figure 5.3: Calculation time depending on the number of vias for the combination of the network parameters of two cavities. Processor: AMD Opteron™ 6140, 2.6 GHz. Even though the plot does not include the additional calculation times for network parameter conversions, the most efficient combination of single cavity results is achieved in Y-parameters (Figure from [26]).

exists in Y-parameters. To obtain the final result, the results for the single cavities have to be combined as described in Section 3.3.2. Possible ways are a segmentation in S-parameters or a multiplication in ABCD-parameters - both requiring a previous network parameter conversion - or a segmentation in Y-parameters, which can be carried out directly. All approaches contain operations with cubic complexity. However, different combinations of these operations lead to different calculation times. The calculation times depending on the number of vias are shown in Fig. 5.3 without the additional effort for the network parameter conversions. Even though parameter conversions are not included, the segmentation in Y-parameters is the most efficient approach. The segmentation in S-parameters takes about twice as long. This can be explained directly from the segmentation formulas (3.13) and (3.14), where the segmentation in S-parameters requires a higher number of operations with cubic complexity, and is also reflected in the value of the coefficient a in Fig. 5.3. Even the combination in ABCD-parameters, which requires no matrix inversion and only one matrix multiplication, leads to a longer calculation time than the segmentation in Y-parameters, which requires one inversion and two multiplications. The reason is that the segmentation operates only on submatrices instead of the full matrix. Due to the cubic complexity of the multiplication, the lower matrix size more than compensates for the higher number of operations. In conclusion, the segmentation in Y-parameters is the preferable method for the combination of single cavity results. It has not only the shortest calculation time in itself, but also fits best into the general calculation flow, without requiring additional network parameter conversions. It should be noted that a lower numerical stability of the segmentation in Y-parameters in comparison to the segmentation in S-parameters was reported in [59]. However, no instability of the segmentation in Y-parameters was observed for the examples in this thesis.

5.1.3 Overall Calculation Times with a Fast Algorithm

In this subsection, the overall calculation times for the simulations of different test structures are analyzed. For this analysis, a fast algorithm is selected from the different possible calculation paths in Fig. 5.1 based on the previous investigations: The propagating field model is calculated from the RWM, the Williamson model is used for the local field region, and the capacitance model for the coaxial field region. The combination of single cavity results is carried out in Y-parameters. As previously described, the application of the RWM for the propagating field calculation and the capacitance model for the coaxial field will somewhat reduce the accuracy of the modeling approach as a cost for the high model efficiency. However, as shown by the investigations in Section 4.4, the methods can in general provide sufficiently accurate results for test structures with 80 mil pitch.

As previously mentioned, the calculation time for the simulation of a test structure does not only depend on the number of vias, but also on the number of cavities and other properties of the test structure which increase the numerical or organizational effort for the algorithm. To demonstrate this, three test cases with different stackups as shown in Fig. 5.4 are evaluated with regard to their impact on calculation times. The stackup in Fig. 5.4(a) has 8 identical cavities, so that the cavity model has to be calculated only once. All reference planes are assigned to ground. In contrast to the worst case evaluation in Section 5.1.2, ground vias are included in the structure, which is a more realistic scenario. A signal-to-ground via ratio of 1:1 is used. In the stackup in Fig. 5.4(b), four of the reference planes are assigned to power, so that all cavities are bounded by mixed reference planes (one power and one ground plane). Half of the ground vias are replaced by power vias, leading to a signal:power:ground ratio of 2:1:1. In the third stackup, two power planes are in the system, again with a signal:power:ground ratio of 2:1:1. In contrast to the previous cases, all cavities have individual thicknesses. While the propagating field models could still be obtained from a single calculation in the lossless case – where the entries of Z^{pp} are proportional to the cavity thickness – an accurate consideration of losses requires an individual evaluation of the propagating field model for each cavity.

For the first stackup, for which the cavity model has to be calculated only once, the evaluation in Fig. 5.5(a) shows that the segmentation requires more than 80% of the calculation time, and that the percentage increases with the number of vias. The remaining

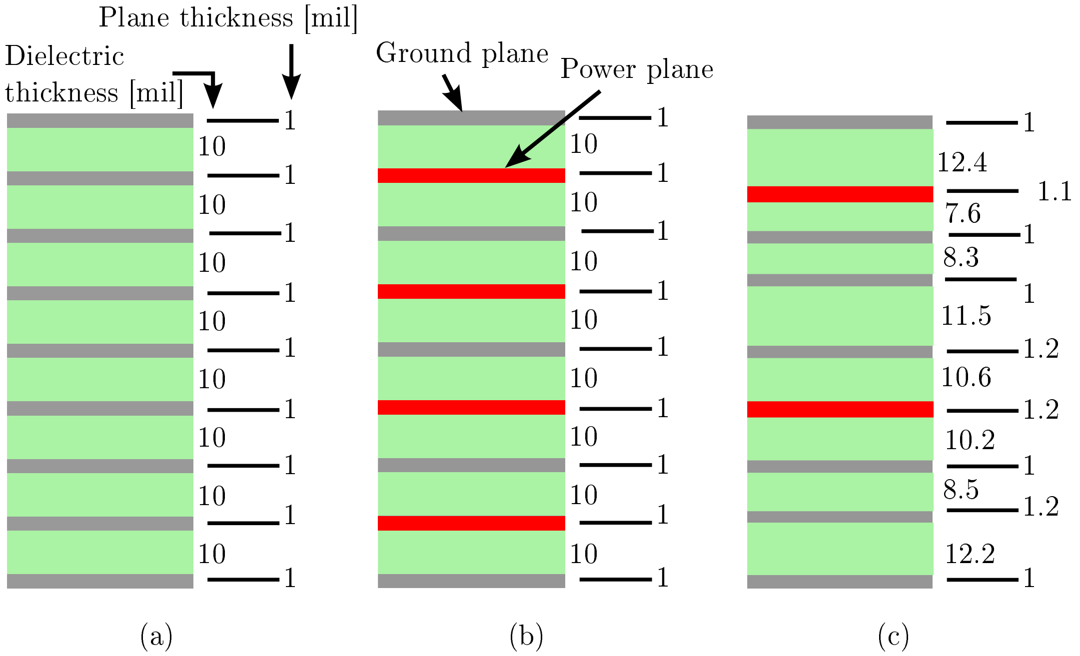

Figure 5.4: Stackups to evaluate the calculation times for structures of different complexity. (a) Simple stackup. (b) Stackup with four power planes (leading to mixed reference planes for each cavity). (c) Stackup with two power planes and different cavity thicknesses (all Figures adapted from [26]).

calculation time is mainly required for the Y^{pp} calculation. The boundary layer calculation, which contains the calculation and addition of the antipad models, makes up only a small part of the numerical effort. For the second stackup, this is changed due to the mixed reference planes in the stackup. Since power and ground vias are connected only to either the top or the bottom plane – not to both – the ground via reduction for the Z^{pp} matrix using the Schur's complement cannot be carried out. Instead, short circuited ports of ground and power vias can only be eliminated from the Y^{pp} matrix after the matrix expansion has been carried out. The ports are eliminated individually during the boundary layer organization, which is reflected in the high percentage of calculation time needed for the boundary layers in Fig. 5.5(b). Also the absolute calculation time required for the segmentation increases, since more ports have to be connected between the cavities. Together, this leads to a considerable increase of more than a factor of 4 in the calculation time in comparison to the first stackup. The third stackup is the most realistic scenario (although practical stackups typically show more symmetry): only a smaller part of the reference planes is assigned as power, but an individual calculation of each cavity model is necessary. This leads to a larger percentage of the calculation time being required for the Y^{pp} calculation, as shown in Fig. 5.5(c). The overall calculation time is reduced in comparison to the second case, but still considerably higher than in the first case.

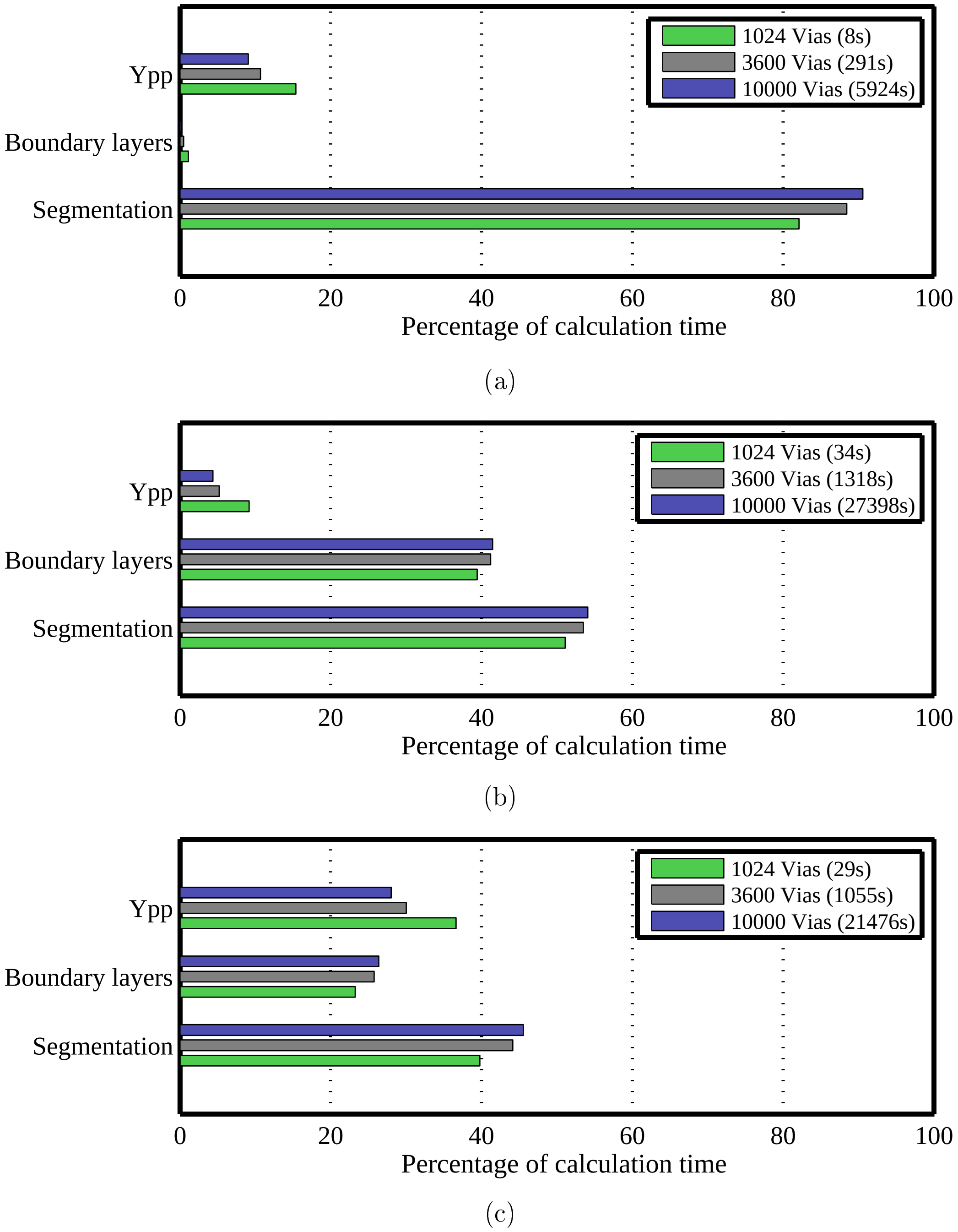

Figure 5.5: Comparison of calculation times for the stackups shown in Fig. 5.4. Calculation times for a single frequency point are shown for different numbers of vias and a signal-to-ground ratio of 1:1. Processor: AMD Opteron™ 6140, 2.6 GHz (all Figures from [26])). (a) Calculation times for the simple stackup. (b) Calculation times for the stackup with 4 power planes (mixed reference planes for each cavity). (c) Stackup with two power planes and different cavity thicknesses, requiring an individual Y^{pp} calculation for each cavity.

5.2 Additional Acceleration of the Algorithm

Apart from the selection of fast calculation methods, a further acceleration of the algorithm is desirable. In this section, two possible directions are investigated: an exploitation of the structural regularity in via arrays, and a parallelization of the numerical code.

A square $n \times n$ via array contains only $\frac{n(n+1)}{2} - 1$ different distances between vias due to the regular arrangement of vias [26, 35]. This can be exploited in the calculation of the parallel plate impedance matrix Z^{pp}. A prerequisite is that the entries for coupling impedances in Z^{pp} only depend on the via separation. This is the case if the calculation is carried out for infinite planes, so that there is no dependence on the position relative to board edges, and the same port geometry can be assumed for all vias. If only one via array has to be simulated, all required coupling impedances are contained in the first row of the Z^{pp} matrix. The rest of the matrix can then be filled using this information, reducing the numerical complexity of the matrix setup to $\mathcal{O}(n)$. Also an acceleration of further calculation steps may be achieved e.g. by using an efficient algorithm for the matrix inversion [121]. However, the introduction of additional vias outside the regular structure of the array - or, as an equally relevant case, a second via array - would destroy the regular form of the Z^{pp} matrix, although most distances between vias would still occur several times. In this case, additional information - or data processing linking vias to certain arrays - is required to decide which sub-blocks of the Z^{pp} matrix can still be set up in an efficient way. A simpler solution can be obtained by using a lookup table that links via separations to the corresponding Z^{pp} entries. A lookup table can be applied to arbitrary structures, and will accelerate the calculation if a sufficient regularity in the structure (leading to a repetition of via separations) exists. For a 50 x 50 Via array, a lookup table can accelerate the Z^{pp} calculation by a factor of about 10 as described in [26, 35].

A parallelization of the Fortran implementation of the physics-based via model was carried out in [35] using the message passing interface (MPI) [122]. Two approaches for the parallelization were compared. First, a parallel calculation of different frequency points was implemented. The parallelization over frequency points can be achieved in a simple way, since the calculations for different frequency points are independent from each other. For a 64 x 64 via array, a computation with the implemented parallel code on 2 processors lead to a speedup of almost 2, while a computation on 8 processors leads to a speedup of about 6. The comparatively large speedup is achieved since the independent calculations for different frequency points do not require any communication between processors. As a second approach, a parallelization of matrix inversions and matrix multiplications - as critical operations with a complexity of $\mathcal{O}(n^3)$ - was carried out for the calculation of individual frequency points. The parallel matrix multiplication was implemented based on [123], while routines from the ScaLAPACK library [124] were used for the parallel matrix inversion. With this approach, the implemented parallel code achieved a speedup of about 1.8 for the simulation of a 64 x 64 via array on 2 processors , while a computation on 8 processors leads to a speedup of about 3. Two main reasons contribute to the lower speedup. First, with the parallelization of matrix inversions and matrix multiplications, only a smaller part of the code is parallelized. A larger part remains that has to be carried out sequentially, setting a limit on the achievable speedup. Second, the parallel matrix inversion requires communication between the different processors, which increases the required calculation time. In spite of the lower speedup, the application of the code with parallelized matrix inversions and multiplications can make sense in certain cases. For the calculation of very large via constellations, for example, the memory may be too small to hold the data for several frequency points at the same time. Furthermore, algorithms for the interpolation of results in the frequency domain may require a subsequent calculation of individual frequency points. In both cases, the parallelization of matrix inversions and multiplications allows a parallel computation even for a single frequency point.

5.3 Application and Assessment of the Efficient Code

The efficient code for the physics-based via model has been applied to the modeling of a very large via array consisting of 10,000 vias in a multilayer PCB with eight cavities in [26]. The obtained results for the crosstalk between vias are discussed in Section 7.3. Previous simulations of very large via constellations that can be found in the literature are typically restricted to a single cavity. A multiple scattering approach was applied to the modeling of 2447 vias in [125]. An iterative solution of a multiple scattering problem for a few ports using a preconditioned sparse-matrix canonical grid method was discussed in [126] for up to 20,000 vias. In [61], the simulation of 3025 vias using a physics-based via model was demonstrated. The application of a physics-based via model to simulate a larger number of vias in a PCB with multiple cavities was demonstrated in [61] for up to 900 vias. To the knowledge of the author, the complete simulation of several thousand vias in a multilayer PCB was addressed in [26] for the first time.

The simulation of 10,000 vias in eight cavities in [26] took about 40 minutes per frequency point with the parallelization of matrix multiplications and inversions on 16 AMD Opteron™ 6140 processors (2.6 GHz clock frequency) and without exploitation of structural regularity. Since no reference calculation times are available for the simulation of very large via constellations, the acceleration achieved in comparison to a previous implementation of the physics-based via model is evaluated for a smaller test structure. For the simulation of 100 vias and 100 frequency points in a multilayer PCB with 12 cavities, the simulation time is reduced from 16 min 45 s as reported in [1], p. 106, to about 38 s on a single processor. This corresponds to an acceleration factor of about 26, of which a factor of about three [1] can be attributed to porting the code from Matlab to Fortran, which was carried out as a student work. With the achieved acceleration, a simulation of very large via constellations within a reasonable time becomes possible in the first place. For smaller arrays consisting of a few 100 vias, simulation times are reduced so far that a fast design exploration becomes possible.

5.4 Summary and Discussion

The evaluation of the numerical complexity of sub paths in the physics-based via model carried out in this section shows how fast calculation methods can be combined for an efficient model evaluation. While for the local field model, accurate methods can be used without compromising efficiency, the parallel plate impedance and the antipad model require a trade-off between accuracy and efficiency. For these model components, it has to be decided based on the test structure, the available simulation time and the required accuracy if fast (but less accurate) models can be employed. In many cases, a somewhat reduced accuracy may be acceptable. In the application of pre-layout design analysis and optimization, for example, it may be desirable to obtain fast characterizations of several different design scenarios. At the same time, a proper representation of changes in the network parameters caused by design modifications may be sufficient for the analysis, while there is no need for the highest possible modeling accuracy. This is even more true in the light of manufacturing tolerances with regard to geometry and material parameters, which introduce an uncertainty on the simulation results that may be in the same order of magnitude as the inaccuracies introduced by the fast calculation methods (the impact of manufacturing tolerances is to some extent investigated in Section 6.3.4).

For finite reference planes, the calculation of the parallel plate impedance takes several times longer than for infinite reference planes due to the large matrix setup time. An acceleration of the matrix setup may be possible with the adaptive cross approximation (ACA) [127], which provides a low rank approximation of a matrix based on the calculation of only a few rows and columns. The ACA should be well suited for the analysis of via arrays due to the regularity inherent in the via array structure. An additional advantage of the ACA is that the resulting low rank approximation can be used to accelerate further calculation steps using e.g. an arithmetic based on hierarchical matrices (H-matrices, [128, 129]). Such an acceleration is interesting also in case of infinite reference planes. However, future investigations have to show how far the calculation steps of the physics-based via model can be accelerated without losing too much accuracy in the final result.

6 Comparison to Measurements

In addition to the numerical validation in Section 4.4, the results obtained with the implemented physics-based via model are compared to hardware measurements in this chapter. The purpose of this comparison is to investigate the applicability of the modeling approach to via arrays on real manufactured PCBs. Measurements have been carried out for via arrays without and with connected striplines to confirm the validity of the modeling approach for both scenarios. In addition to the model validation, the repeatability of measurements and the impact of deviations between specifications and the manufactured test structure with regard to geometry and material parameters are discussed at the end of this chapter.

6.1 Measurements on PCBs

In comparison to simulations, measurements show several disadvantages such as the need for expensive equipment, time-consuming and costly prototype production, and a sensitivity of results to disturbances and calibration errors. Furthermore, measurements offer a low flexibility for the evaluation of design alternatives due to the long waiting time between test board design and actual measurements on the manufactured hardware. Nevertheless, hardware measurements are a well-established step in the development and testing of PCBs. Measurements are the only way to confirm that the network parameters of manufactured prototypes actually conform to the intended behavior. For some cases, an additional advantage of measurements is that they take into account the impact of the complete structure, which may be too big or too complex to simulate as a whole.

The feasibility of hardware measurements for dense via arrays on PCBs using a vector network analyzer (VNA) and microprobes is demonstrated in [130,131]. Also a comparison of different calibration approaches is carried out in [130,131], including the application of custom-made calibration standards on a multilayer PCB. All measurements shown in this chapter were carried out using a 12-port VNA (Agilent E8364C [132]), in a frequency range of 10 MHz - 50 GHz. High frequency microprobes were connected to the VNA using measurement cables [133] suitable for the frequency range up to 50 GHz. For all measurements, microprobes with one signal tip and one ground tip with 225 µm pitch (Picoprobe model 40A-GS- and SG-225µm-DS-style [134]) were used. A Short-Open-Load-Through (SOLT) calibration [135] up to the probe tips was carried out on calibration substrate (CS-14 [134]) obtained from the probe vendor. In comparison to calibration standards on the PCB itself, the use of a calibration substrate has some disadvantages. Inaccuracies in the calibration may occur due to the deviating parasitic properties of the probe access to the calibration substrate and the PCB, and due to the possible need for a probe reorientation between calibration and measurement. Nevertheless, the calibration on CS-14 substrate was chosen to avoid the disadvantages of custom-made calibration standards, which lie in the high design effort and in the uncertain properties of custom-made standards due to PCB manufacturing tolerances.

6.2 Via Array without Traces

A first series of measurements has been carried out by Dr. Miroslav Kotzev at the Institute of Electromagnetic Theory, TUHH, for the 8×8 via array that was already used for the numerical accuracy study in Section 4.4. No striplines are connected to the vias, so that the analysis focuses on the via model alone (excluding the stripline models as a potential source of modeling inaccuracies). Schematics were shown for the top view of the via arrangement in Fig. 4.10(a) and for the cross section of the test board in Fig. 4.15. The measured via array has a pitch of 80 mil; a photo of the manufactured test structure can be seen in Fig. 6.1(a). For the measurement, the test board was placed vertically, so that vias could be probed from top and bottom as depicted in Fig. 6.1(b). All measurements were carried out with four ports, allowing the measurement of transmission, reflection, near- and far-end crosstalk of two vias.

Results for the transmission and reflection of via 2 (ports 2 and 5 as defined in Fig. 4.10(a)) are shown in Fig. 6.2. For comparison, results from a more efficient version of the physics-based model (using the Williamson model for the local fields, the RWG for the propagating field and the capacitance model for the coaxial fields) are shown together with the results from a more accurate version of the physics-based model (using the Williamson model for the local fields, the CIM for the propagating field and the transmission line model for the coaxial fields). For the transmission, the comparison of the physics-based via model to the measured S-parameters in Fig. 6.2(a) shows larger deviations than the comparison to full-wave results in Section 4.4.1. This can - at least in part - be explained by deviations between the geometry and material parameters of simulated and measured structure. While the full-wave simulation uses the same parameter values as the physics-based model, the parameters of the manufactured test structure are impacted by tolerances of the production process, which are in the range of $\pm 10\,\%$. The possible impact of these tolerances is further evaluated in Section 6.3.4. It should be noted that additional factors contribute to the deviations between physics-based model and measured results. First, the test board contains additional test structures, which were not included in the simulation. Second,

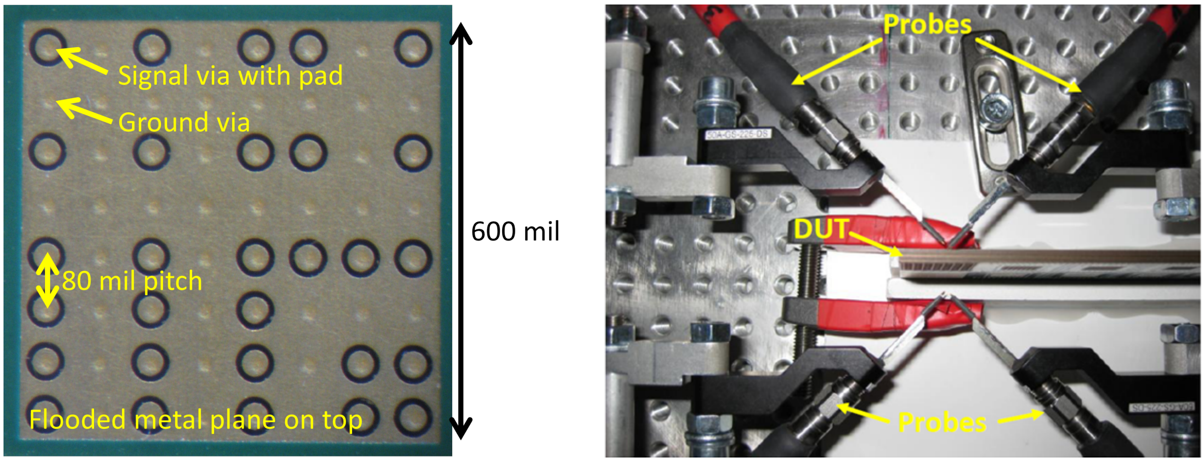

(a)

(b)

Figure 6.1: (a) Photo of the manufactured test via array. The via pitch is 80 mil. On top and bottom, 600 mil × 600 mil flooded planes are used for probe access, while the inner metal layers extend over the complete board size (21.8 in × 16.8 in). The stackup of the test board, which was already used for the simulations in Section 4.4, is shown in Fig. 4.15. (b) Microprobe setup for the measurement. The device under test (DUT) was placed vertically. This allows 4-port measurements with two vias each being probed at top and bottom for a measurement of transmission, reflection, near- and far-end crosstalk (Figure from [7]).

the calibration on substrate does not eliminate all errors from the measured results. This becomes obvious in the comparison between measured and simulated reflection. The deviation between the results can be reduced by de-embedding a parasitic inductance from the measured S-parameters. For the additional curve in Fig. 6.2(b), an inductance value of 100 pH has been chosen as an approximate value for the employed microprobe type based on previous investigations [136]. A comparison between simulated and measured results for the crosstalk is shown in Fig. 6.3. In contrast to the reflection, transmission and crosstalk are not substantially changed by the de-embedded inductance, so that only the original measured results are shown. Although the comparison to measurements shows larger deviations than the comparison to full-wave results, the physics-based via model provides an acceptable approximation of the measured results in the frequency range up to 50 GHz.

It is noteworthy that due to the impact of manufacturing tolerances on the measured S-parameters, the application of a more accurate version of the physics-based via model - or even of computationally very expensive full-wave approaches - does not necessarily improve the agreement to the measured results in comparison to the most efficient version of the physics-based model. For the results compared in Fig. 6.2 and Fig. 6.3, the deviation between the two versions of the physics-based model over wide frequency ranges is smaller or in the same order of magnitude as the deviation to the measured results. Some exceptions

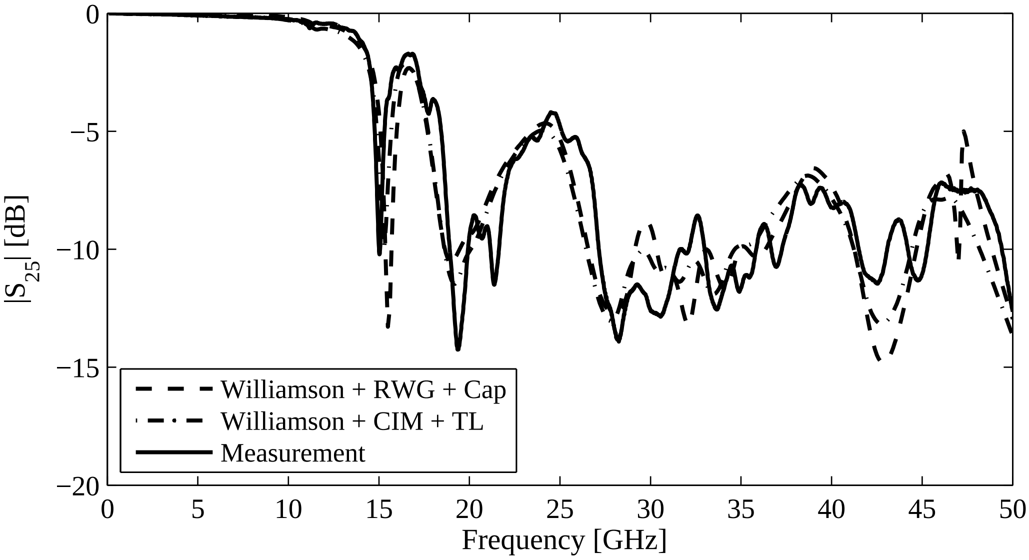

(a)

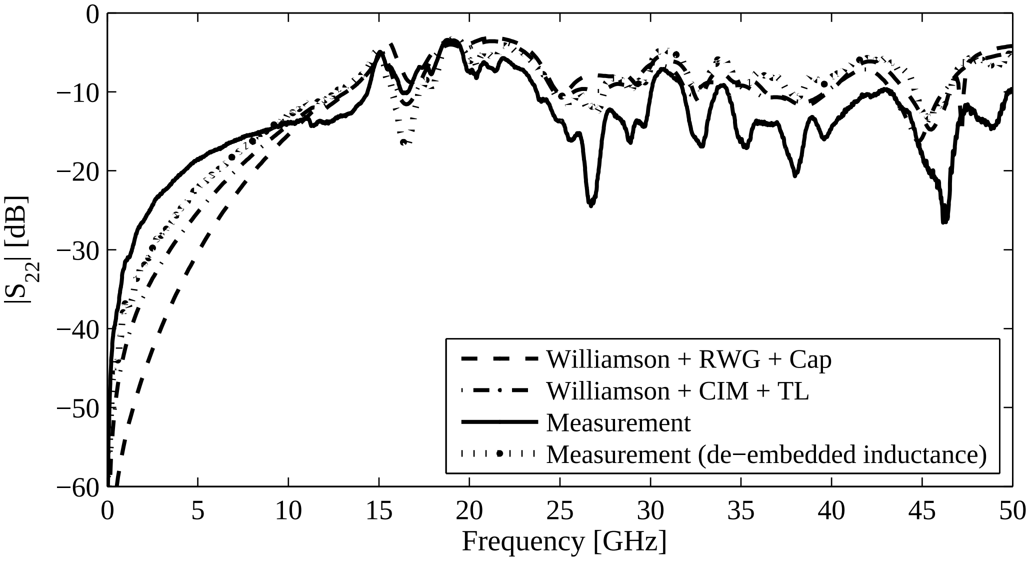

(b)

Figure 6.2: Comparison of a more efficient (Williamson + RWG + Cap) and a more accurate (Williamson + CIM + TL) version of the physics-based via model to measured results obtained by Dr. Miroslav Kotzev, TUHH. (a) Transmission between via ports 2 and 5 as defined in Fig. 4.10(a) (Figure adapted from [7]). (b) Reflection at via port 2 as defined in Fig. 4.10 (Figure adapted from [7]). After de-embedding a parasitic inductance of 100 pH from the measured reflection, both versions of the physics-based via model provide an acceptable approximation of transmission and reflection for frequencies up to 50 GHz. Larger deviations for the more efficient version of the physics-based model exist for some resonances and antiresonances in the transmission above 30 GHz, and for the reflection up to 10 GHz.

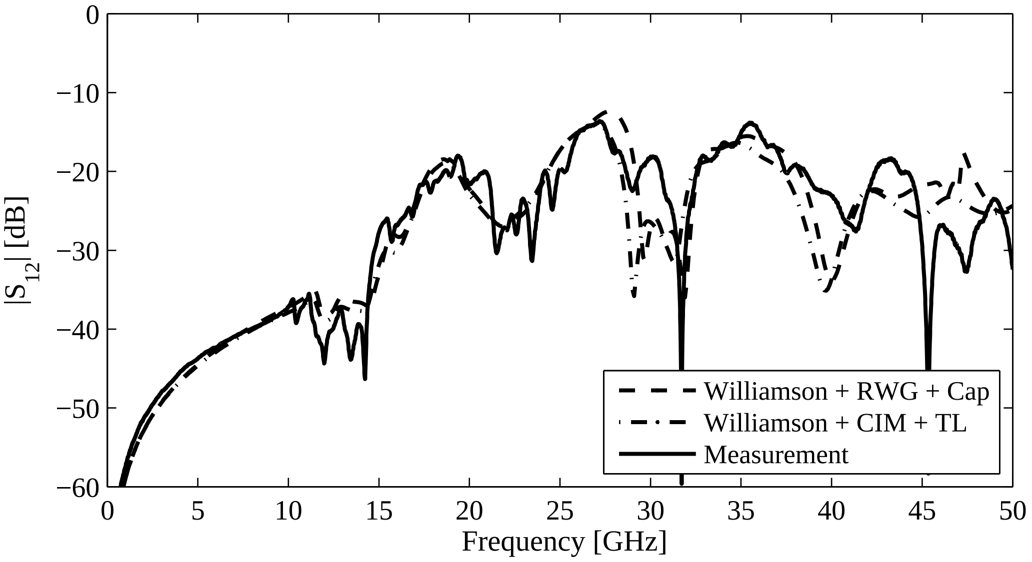

(a)

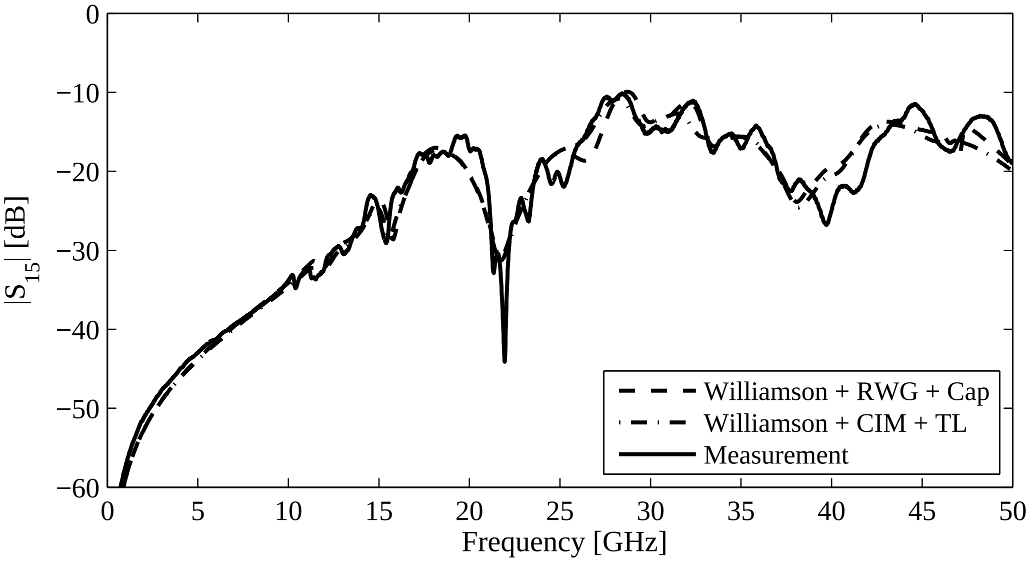

(b)

Figure 6.3: Comparison of a more efficient (Williamson + RWG + Cap) and a more accurate (Williamson + CIM + TL) version of the physics-based via model to measured results obtained by Dr. Miroslav Kotzev, TUHH. (a) Near-end crosstalk between via ports 1 and 2 as defined in Fig. 4.10(a) (Figure adapted from [7]). (b) Far-end crosstalk between via ports 1 and 5 as defined in Fig. 4.10 (Figure adapted from [7]). For the crosstalk, both versions of the physics-based via model provide an acceptable approximation of the measured results for frequencies up to 50 GHz. The deviation between the two versions of the physics-based via model is smaller than the deviation to measurement results.

exist in the transmission for some resonances and antiresonances starting from 30 GHz, and in the reflection for the frequency range up to 10 GHz, where the more accurate version of the physics-based via model leads to a better approximation of the measured S-parameters. Nevertheless, it will often make sense to use the most efficient version of the physics-based via model for a fast assessment of different design variations, since inaccuracies related to the model are within the range of uncertainty related to the manufactured hardware. This option should especially be taken into account for investigations on large structures, for which the calculation time is critical.

6.3 Via Arrays with Traces

To validate the physics-based via model for via arrays with connecting striplines in multilayer PCBs, a test board with four different via array test structures has been designed. The four via array designs have been chosen with a view to the design evaluations in Chapter 8, and reflect different signaling schemes and different signal-to-ground ratios.

Here, exemplary results are discussed for the first test structure, which is shown in Fig. 6.4. The measured via array contains 10×10 vias with a pitch of 80 mil. Signal and ground vias are placed alternately, leading to a signal-to-ground via ratio of 1:1. Striplines of 400 mil length are routed on three different signal layers. Outside the via array, the striplines end in hybrid launches, which allow both a probing at the top via surface and a measurement using a recessed probe launch (RPL) [137]. The measurement from top has the advantage that it does not require any additional preparation of the structure. Furthermore, it allows a more direct comparison to the physics-based via model, as will be discussed later. The measurement with a recessed probe launch requires additional preparation, but allows a more direct physical interpretation of the measured results, since the results do not contain the impact of an additional access via. The hybrid launches are numbered from L1 to L34 as shown in the top view in Fig. 6.4(a). Signal vias inside the array are assigned the same number as the connected launch via, leading to a numbering from V1 to V34 (not shown in the figure). The detailed stripline geometry is shown in Fig. 6.4(b), the stackup with the factor k (see Section 3.4) required for the inclusion of the stripline models in the physics-based via model is shown in Fig. 6.4(c). The complete test array is surrounded by a ground via cage with 23 ground vias per row and 80 mil via pitch. The purpose of the ground via cage is to provide a shielding against other structures on the test board. In this way, a comparable setup of simulated and measured structure can be achieved without modeling the complete board.

It shall be mentioned that in real PCB links, traces typically span several inches of distance between two different via arrays. The comparatively small stripline length in the measured

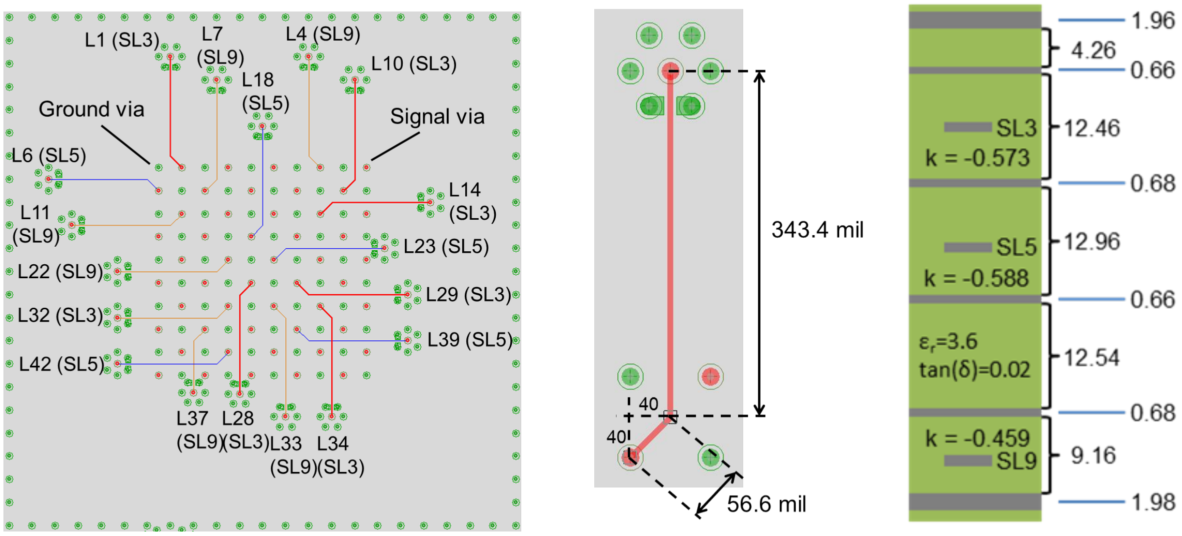

(a) (b) (c)

Figure 6.4: Schematic representation of the measured test structure. (a) Top view showing the via arrangement and the striplines routed on the different signal layers, including the numbering of the launch vias and the routing layer of the corresponding stripline (Figure adapted from [24]). Signal vias inside the array are assigned the same number as the connected launch via (i.e., launch via L1 is connected to signal via V1 inside the array). (b) Detailed dimensions of the stripline geometry. All striplines have the same geometry with 400 mil total length, except for a shorter line ending in launch L37. (c) Stackup of the test board with thicknesses specified in mil based on a cross section measurement (Figure adapted from [24]). The stackup includes the values of the factor k used for the inclusion of the stripline models in the physics-based via model. Since traces were not included in the measured cross sections, the values for k are based on the nominal stackup.

test structures has been chosen for two reasons: First, the limited space on the test board does not allow for long stripline sections. Second, the behavior of homogeneous stripline sections is well understood. With regard to the modeling accuracy, the transition between via model and stripline model can be expected to be the most critical aspect. For the study of this aspect, the comparatively short stripline sections in the test structures are expected to be sufficient.

6.3.1 Measurement Results without Recessed Probe Launches

Four-port measurements without recessed probe launches have been carried out for vias at different positions inside the array and connected to striplines on different routing layers. For comparison, simulations with the physics-based via model have been carried out using the Williamson model for the local field regions, the CIM for the propagating field and the transmission line model for the antipad regions. The required network parameters for the striplines have been obtained analytically, assuming a characteristic impedance of 52 Ω. A comparison of different simulation results shows that a value larger than the target characteristic impedance of 50 Ω leads to a better agreement with measured results for the reflection. The value of 52 Ω is chosen based on an expected deviation of a few Ω for the manufactured structure. A via radius of 4 mil and an antipad radius of 14 mil are assumed based on nominal values. Pads on top and bottom of the manufactured structures are taken into account through an additional capacitance in the physics-based model. The capacitance value is set to 20 fF based on a value of 23.9 fF extracted with a commercial solver [120] for a pad radius of 8 mil.

As an example, results for a measurement of vias V29 and V34 are shown with the corresponding simulation results (see Fig. 6.4(b) for the positions of the vias and the connected launches L29 and L34). For both vias, the striplines providing the connection to the respective launch vias are routed on SL3, leading to comparatively long via stubs below the connection to the stripline. The transmission between signal via V29 inside the array and launch via L29 is shown in Fig. 6.5(a). Both measurement and simulation show the impact of reflections from the surrounding ground cage - especially around 15 GHz - and the resonances related to the via stubs. In spite of the differences in magnitude and the frequency shift of the resonance around 22 GHz, the physics-based model provides a good approximation of the measured result, including all characteristic features. It should be mentioned that for some of the measured vias, the simulation results show larger frequency shifts of the resonances as well as larger deviations at higher frequencies. However, the shown example gives an impression of the agreement between measured and simulated results that can be expected. The reflection at the launch via L29 is shown in (Fig. 6.5(b)). Also here, it should be mentioned that for some of the measured vias, the simulation results show larger deviations - especially in case of a lower magnitude of the reflection. The crosstalk is shown between launch via L29 and via V34 inside the array in (Fig. 6.6(a)), and between launch via L29 and launch via L34 in (Fig. 6.6(b)). Although the shown cases include one and two stripline transmissions, respectively, a good agreement between measurement and simulation can be observed. In summary, the simulation with the physics-based model gives a good approximation of measured results also for structures containing traces. This is especially true when taking into account that - as previously described - some portion of the deviation may result from measurement and calibration errors as well as geometry and material parameter deviations between simulated structure and fabricated test board. Additional results for vias connected to striplines routed on the lowest routing layer (SL9) are shown in Fig. E.1, Fig. E.2 and Fig. E.3 in Appendix E.

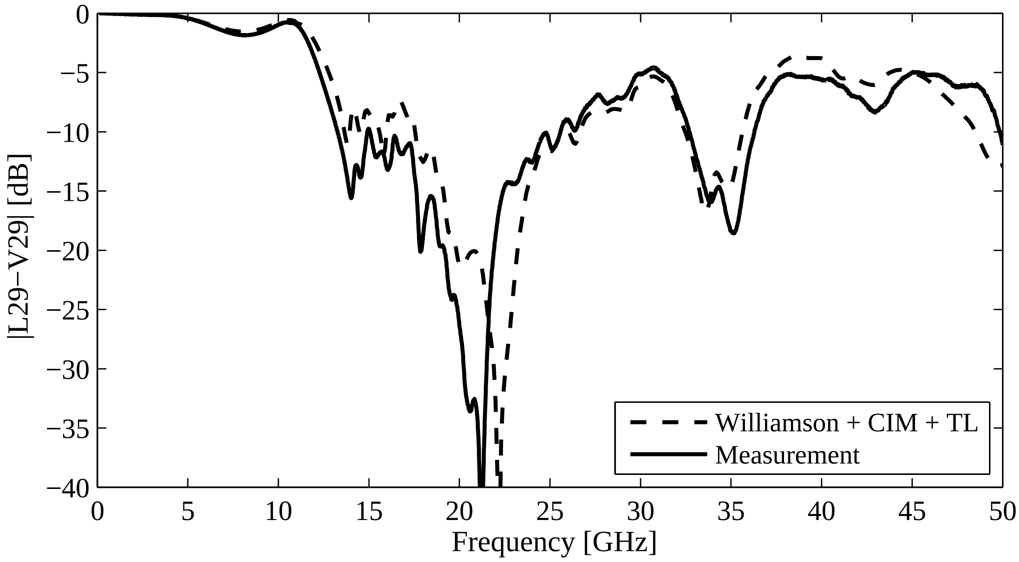

(a)

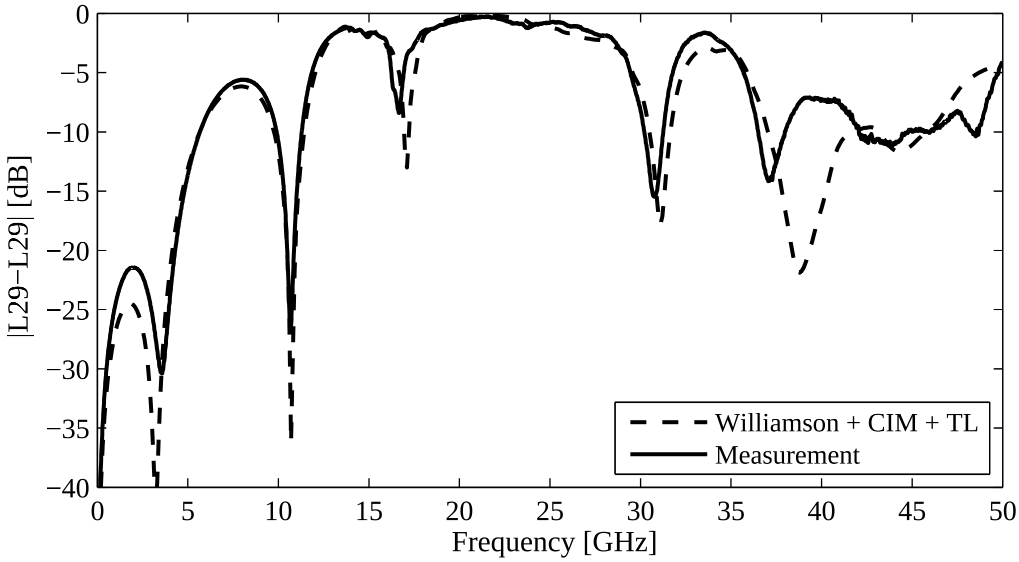

(b)

Figure 6.5: Comparison between physics-based model and measurement for transmission and reflection. (a) Transmission between signal via V29 and launch via L29. (b) Reflection at launch via L29. It should be noted that for some of the measured vias, larger deviations between simulation and measurement are observed for both transmission and reflection. However, the shown plots give an impression of the agreement that can be expected between simulated and measured results.

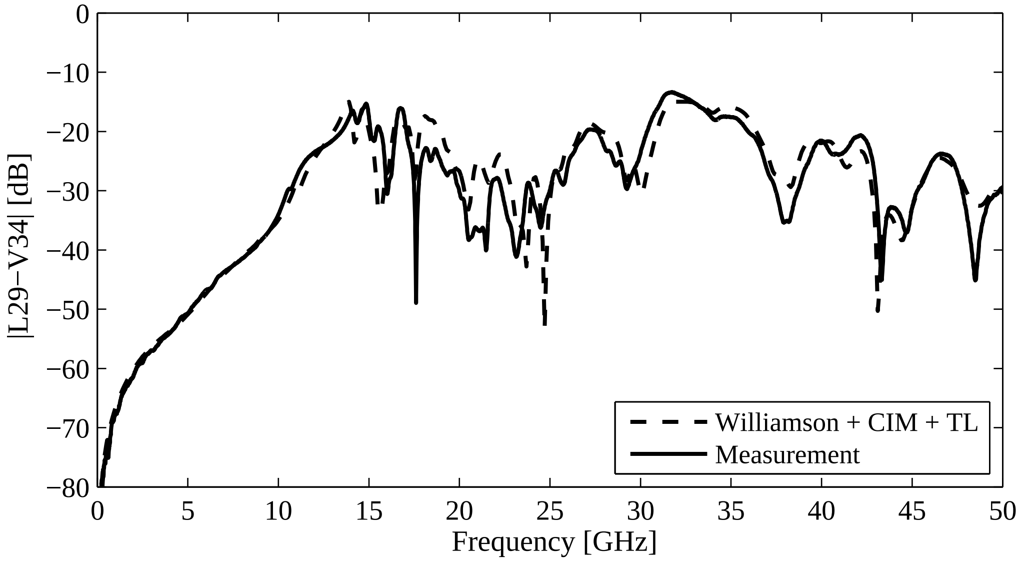

(a)

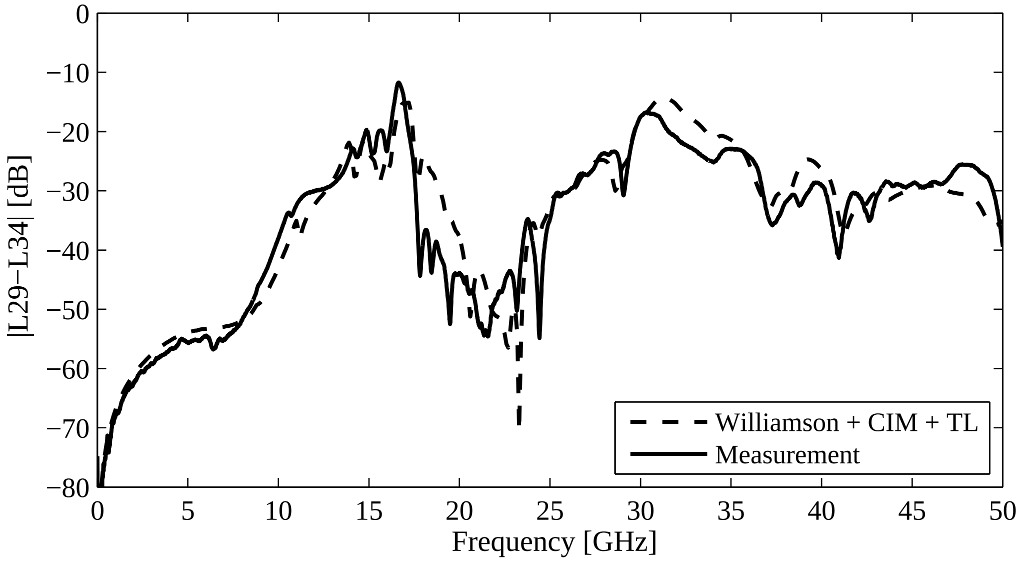

(b)

Figure 6.6: Comparison between physics-based model and measurement for the crosstalk. (a) Crosstalk between via V34 inside the array and launch via L29 (including the impact of one stripline transmission). (b) Crosstalk between launch via L34 and launch via L29 (including the impact of two stripline transmissions). Although some deviations exist, the physics-based via model provides a good approximation of the measured results for the crosstalk.

6.3.2 Measurement Results with Recessed Probe Launch

The use of RPLs for PCB measurements is suggested in [137], and further studied in [136, 138, 139]. The idea of the RPL is to measure network parameters directly at a certain point of a stripline, without an impact of an additional access via on the measured results. For this purpose, ground pads are included in the manufactured PCB on both sides of the stripline. Ground vias provide the connection between the ground pads and the ground planes of the PCB. If the material above the stripline is milled away as shown in Fig. 6.7(a), a direct measurement can be carried out with the signal tip placed on the stripline and the ground tip placed on one of the ground pads. For the test structures analyzed in this section, hybrid probe launches were used, which allow a measurement using an access via as well as an RPL measurement. For the RPL measurement, the access via is separated from the stripline in an additional milling step, as visible in the additional milling edge at the end of the stripline trace in Fig. 6.7(a). An advantage of the RPL is that it allows to use measured results for the analysis of a single via transition. Additionally, as described in [137], vias measured with RPLs can be concatenated with measured or simulated stripline models of arbitrary length, allowing a flexible use of the measured network parameters that is not restricted to a specific link length. The probe setup for a four-port measurement with RPLs is shown in Fig. 6.7(b): Vias inside the array are probed on the top pads, while RPLs are used for the launches outside the array.

As a drawback with regard to the validation of the physics-based via model, measurements carried out with RPLs cannot be accurately represented in the current model implementation. An accurate representation would require stripline ports in combination with an adequate approximation of the launch parasitics, which are influenced by parameters such as the size of the milled cavity, the length of the stripline stub, and the exact position of the probe tip [138, 139]. Currently, however, ports in the implemented physics-based model can only be placed at vias. For the following comparison, a short blind via without local field model is used as an approximate model for the RPL, and it is studied whether this model is suitable for the simulation of test structures that contain RPLs. For the comparison between measurement and simulation, the same vias as in Section 6.3.1 are chosen. All material and geometry parameters are identical with exception of the stripline length, which is reduced by 35 mil to account for the section of the stripline which has been removed during the RPL preparation. A comparison between the measured results for the transmission between via V29 inside the array and launch L29 outside the array in Fig. 6.5(a) (without RPLs) and in Fig. 6.8(a) clearly shows the impact of the removed access vias. At the same time, Fig. 6.8(a) shows that for the transmission, the approximation of the RPL with a short blind via provides acceptable results, leading to an agreement

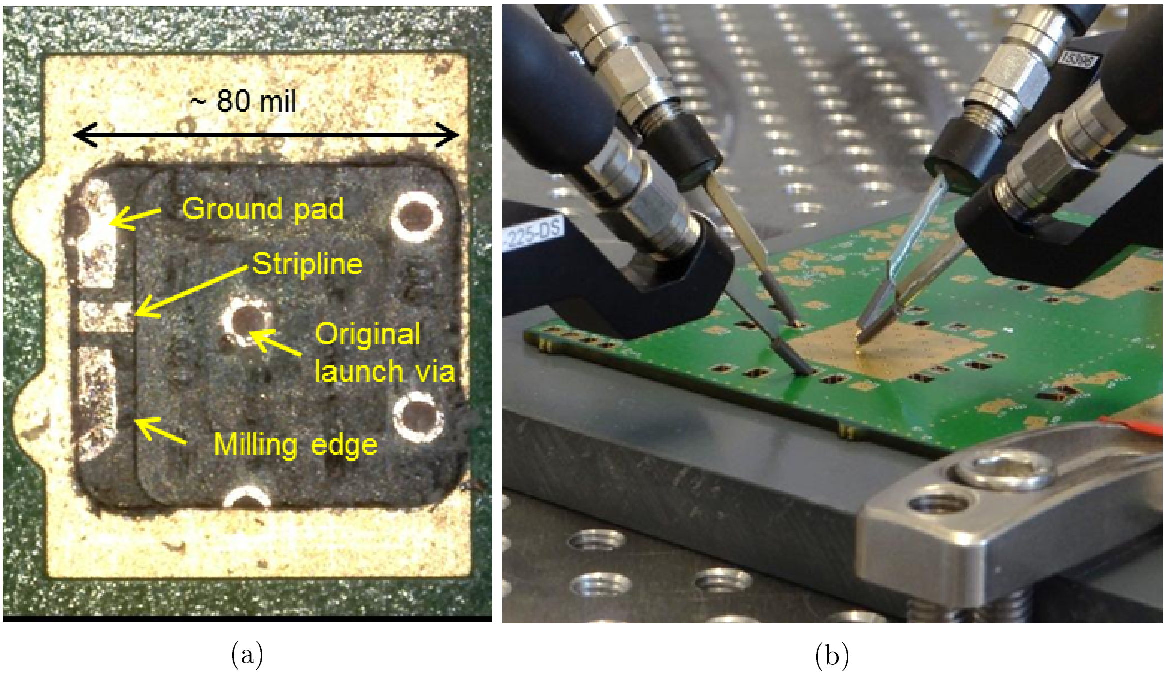

(a) (b)

Figure 6.7: (a) Detailed view of a recessed probe launch. The signal tip of the probe can be placed directly on the stripline, while the ground tip is placed on one of the two ground pads. (b) Probe setup for a four-port measurement with RPLs to determine transmission, reflection and crosstalk. For vias inside the via array, the probes are placed on the top pads, while RPLs are used at the stripline ends outside the array (Figure from [24]).

between simulation result and measurement that is in the same range as for cases without RPL. The same is true for the crosstalk, which is not shown here. For the reflection, in contrast, the approximation of the RPL with a short blind via reduces the agreement between measurement and simulation in comparison to cases without RPL. Even more than the reflection at the launch itself, the reflection at the via inside the array is concerned, as shown for the example of via V29 in (Fig. 6.8(b)).

6.3.3 Measurement Repeatability

To test the repeatability of the measured results shown in this chapter, measurements were repeated for some of the vias on the test structures. Fig. 6.9 shows the comparison of two measurements of the transmission between via V22 and launch via L22 carried out on the same test board with two different calibrations and several months apart from each other. Furthermore, the measurements were carried out by two different persons, with the first measurement carried out by Dr. Miroslav Kotzev at the Institute of Electromagnetic Theory, TUHH. Although some differences between the measured curves exist, a good general agreement can be observed. Particularly, the characteristic features are reflected

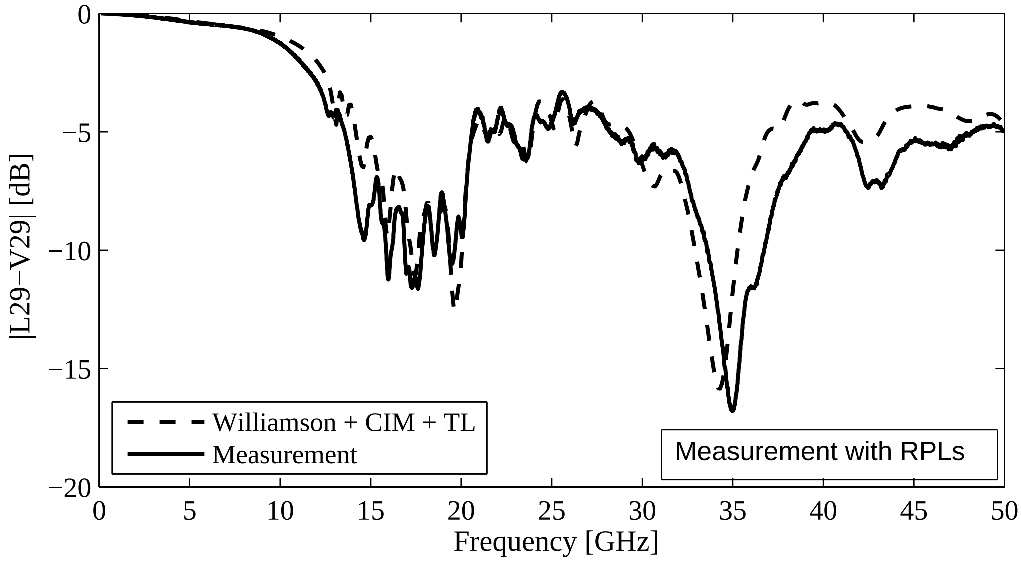

(a)

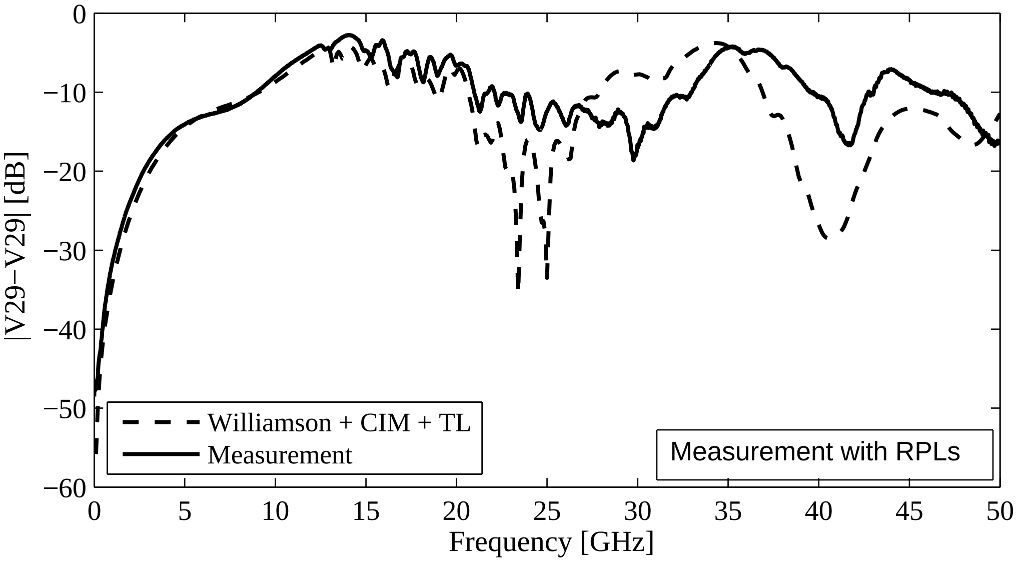

(b)

Figure 6.8: Comparison between physics-based model and measurement for transmission and reflection measured with RPLs. (a) Transmission between signal via V29 and launch via L29. (b) Reflection at via V29 inside the array. While the physics-based model can provide a good approximation of the transmission also for cases with RPLs, the accuracy of the simulated reflection is reduced by the insufficient launch model.

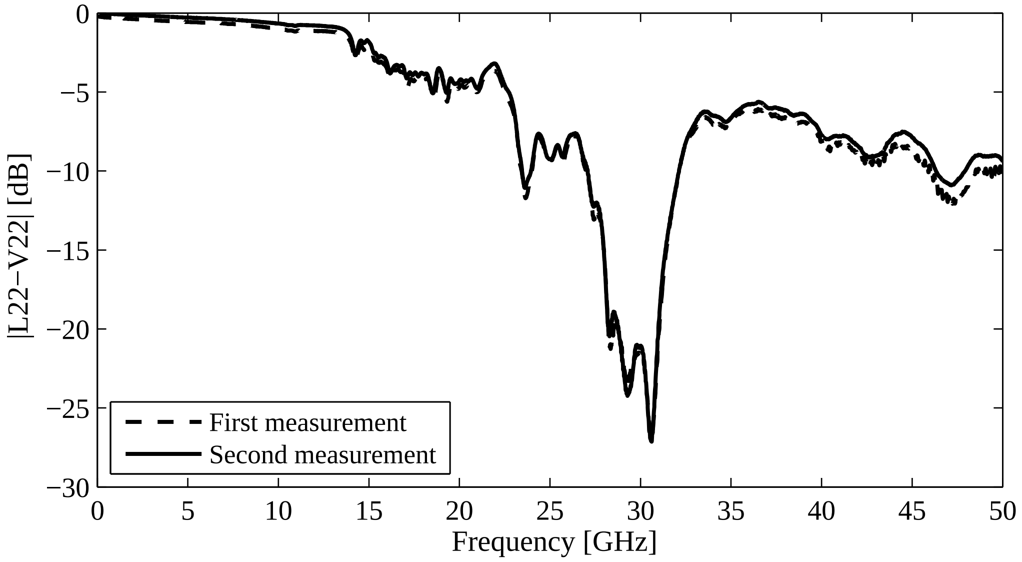

Figure 6.9: Comparison of two measured results for the transmission between via V22 and launch via L22. Both measurement results were obtained for the same test board, but with different calibrations and several months apart from each other. The first measurement was carried out by Dr. Miroslav Kotzev at the Institute of Electromagnetic Theory, TUHH. Although some deviations between the curves exist, a good general agreement can be observed, especially with regard to the characteristic features of the curves.

in both curves. A similar agreement between the two measurements could be observed for reflection and crosstalk. It can be concluded that an impact of random variations between the two measurements - such as differences in the probe placement during the calibration or during the measurement - is comparatively small. However, it should be noted that systematic measurement errors may still exist.

6.3.4 Impact of Variations in Geometry Parameters

As previously mentioned, manufacturing tolerances with regard to geometry and material parameters may be a cause for deviations between measured and simulated results. In general, all geometry parameters such as via, pad, and antipad radii as well as the stripline dimensions may be subject to variations. On the studied test board, pad radii ranging from 8 mil to 9.5 mil and antipad radii ranging from 14 mil to 15.3 mil were measured for the test structure in Fig. 6.4(a). Via radii and stripline dimensions could not be measured without destruction of the test structure. However, the characteristic impedance resulting from the trace dimensions can be expected to vary by up to 10 % according to the specifications of the PCB vendor. Here, the impact of the observed variation in the pad radius and of a 10 % variation in the characteristic trace impedance of the traces on the simulated transmission

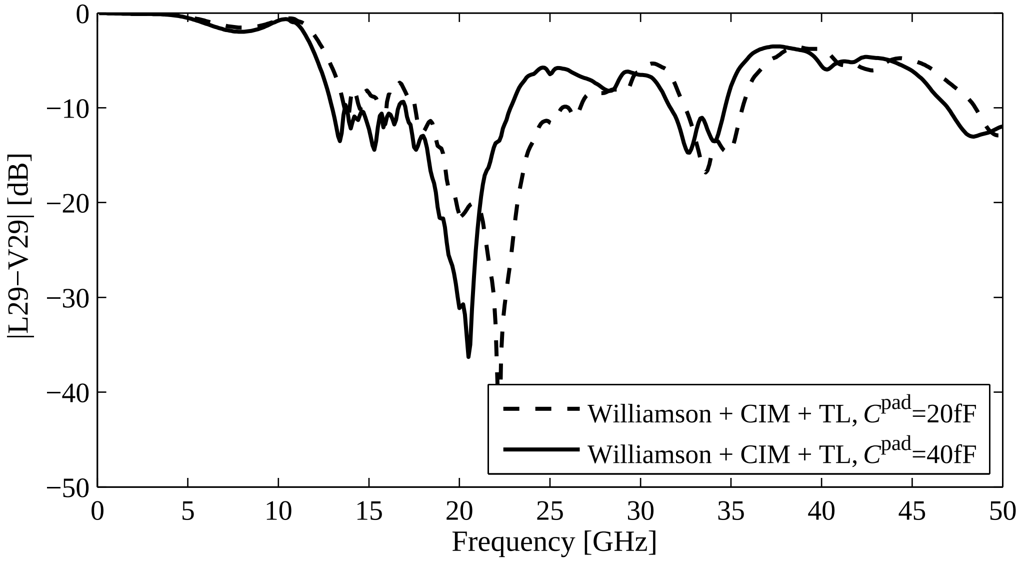

(a)

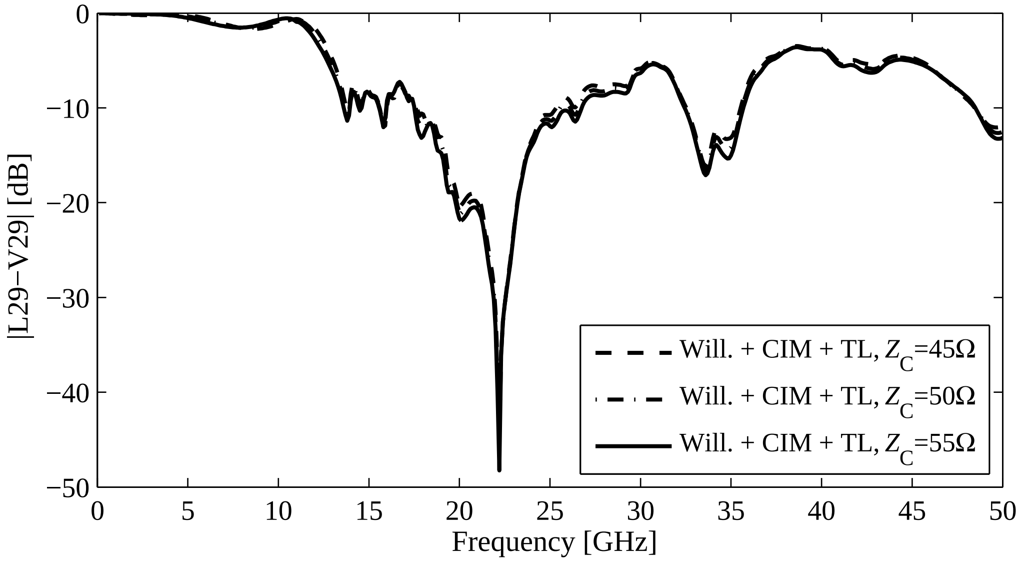

(b)

Figure 6.10: Impact of geometry parameter variations on the simulated transmission for the studied test structure. (a) Impact of an increase of the additional pad capacitance included in the model. The increase from 20 fF to 40 fF roughly corresponds to an increase of the pad radius from 8 mil to 9.5 mil. A considerable frequency shift due to the changed pad capacitance can be observed. (b) Impact of a change in the characteristic impedance within the typical range of ±10 % around the target impedance of 50 Ω. In comparison to the impact of the pad capacitance, the impact of the characteristic impedance is small for the studied range.

between via V29 and launch L29 are shown as examples for a possible impact of geometry parameter variations. An increase of the pad radius from 8 mil to 9.5 mil increases the pad impedance from roughly 20 fF to roughly 40 fF. A substantial frequency shift between the simulated transmission for these two capacitance values can be observed in Fig. 6.10(a). In contrast, the impact of the characteristic impedance on the transmission is small for the studied test structure, at least for the impedance range of $45\,\Omega$ to $55\,\Omega$ as shown in Fig. 6.10(b).

6.4 Summary and Discussion

The comparison carried out in this chapter demonstrates that the physics-based model can provide a good approximation of measured results for transmission, reflection and crosstalk in the frequency range up to 50 GHz for a via pitch of 80 mil. Good results can be obtained for structures without traces as well as for structures that include traces. The measured results show a good repeatability between different measurements carried out with different calibrations. Nevertheless, uncertainties with regard to the exact geometry and material parameters of the manufactured test structure exist due to manufacturing tolerances. These uncertainties may provide an argument for the application of the most efficient version of the physics-based via model for a fast design exploration. The related deviations from more accurate models are - with a few exceptions - smaller than or in the same order of magnitude as the deviations between modeling and measurement results.

An extension of the physics-based via model would be desirable with regard to the modeling of recessed probe launches. While RPLs are not necessary for the measurement of complete links, they are interesting for design investigations since they allow the measurement of a single via transition. While a sufficient approximation of measurements with RPLs can be achieved with the current physics-based model for transmission and crosstalk, the presence of RPLs leads to an increased deviation between model and measurement for the reflection.

7 Signal Integrity Evaluations for PCB Links

In the previous chapters, the focus has been on the accuracy and efficiency of physics-based models, especially when applied to model via arrays. As far as simulation results for test structures were shown, they were studied mostly with regard to the accuracy of the simulation approach and less with regard to their implications for signal integrity. In this chapter, the focus is shifted towards a true signal integrity analysis.

As described in Section 1.3, signal integrity in PCB links remains a challenging task. Steadily increasing data rates - leading to higher spectral contents of signals - aggravate issues such as transmission loss and crosstalk. Aspects of the design may become critical which have not been a major concern at lower data rates. In this context, the physics-based model can be useful in two ways. First, it allows a fast evaluation of specific designs and the detection of possible issues at an early stage of the design phase - before prototypes are manufactured or more time and resource consuming full-wave simulations are set up. Second, the efficiency of the physics-based model also allows for in-depth analyses of specific signal integrity issues. Many variations of a structure can be simulated in a short time, providing information about the relevant parameters and possibly allowing conclusions about the underlying physical effects. In this chapter, the physics-based via model is applied to study three signal integrity issues that may occur in PCB links. The size of the studied examples is increased from a few vias over a small via array to a very large via array. The first issue is the impact of mixed reference planes on transmission, crosstalk, and mode conversion in PCB links, which is studied for isolated links with only a few vias in Section 7.1. The second issue is the impact of the routing layer on the signal transmission. The test structure for the study in Section 7.2 is a 10×10 via array, and the study takes into account the impact of the position inside the array. Third, the behavior of crosstalk is studied for a 100×100 via array in Section 7.3. For the analysis, it is in general assumed that the models provide accurate results based on the validation in Chapter 4. Additional validation is only shown where new aspects are introduced.

The signal integrity issues studied in this chapter do not represent the most important or critical issues, let alone a complete coverage of signal integrity on PCBs. Rather, they serve the purpose of demonstrating the application of the physics-based model to some exemplary aspects.

7.1 Impact of Mixed Reference Planes

In a multilayer PCB, the metal layers in the stackup typically serve as reference planes for striplines routed in the different cavities. While most of the planes are connected to ground, it is necessary in practical designs that some of the planes are connected to the supply voltages of the integrated circuits mounted on the board (i.e., to potentials different from ground). These reference planes are commonly referred to as power planes. For the striplines inside the PCB, this can lead to scenarios with mixed reference planes, meaning that the two reference planes of a stripline do not have the same potential. The stripline mode itself should not be affected in these scenarios - power planes are physically identical to ground planes as long as they are continuous (without splits or gaps). At the ends of the stripline, however, a discontinuity occurs for the portion of the return current which is flowing in the power plane. The current is forced to return as a displacement current, since no conductive path exists between power and ground planes. In this section, the impact of this effect related to mixed reference planes is investigated. The analysis that is carried out demonstrates the application of the model to small PCB coupons. The finite board size is taken into account by using a PMC boundary condition in the parallel plate impedance calculation. The increased numerical effort caused by the PMC boundary condition (see Section 5.1.2) does not pose a problem here due to the small number of vias studied.

7.1.1 Physical Effects for a Simple Test Structure

The effects of mixed reference planes are first demonstrated for the simple test structure in Fig. 7.1: in a PCB with two cavities, two signal vias are connected by a 0.5 in stripline in the upper cavity. A finite board size of 1 in × 0.5 in is assumed. Both vias are excited from top, using coaxial port extensions of 30 mil length. For full-wave simulations carried out for validation purposes, the coaxial extensions guarantee a sufficient separation between the excitation port and the via and stripline discontinuity in the first cavity (see [1], p.75). The impact of mixed reference planes will be shown by a comparison of the signal transmission between the via ports for different plane assignments. To simplify the description of different scenarios for the test structures used in this section, the reference plane assignment will be indicated from top to bottom of the PCB using the abbreviation "G" for a plane assigned to ground and "P" for a plane assigned to power. The cases studied here are GGG (all planes connected to ground) and GPG (inner reference plane assigned to power). The ground planes are connected by the four ground vias indicated in Fig. 7.1(a), while the power plane is floating (see the schematics in Fig. 7.1(b) for the via connectivity). As a worst case reference, a constellation without ground vias is simulated. In this case, only the

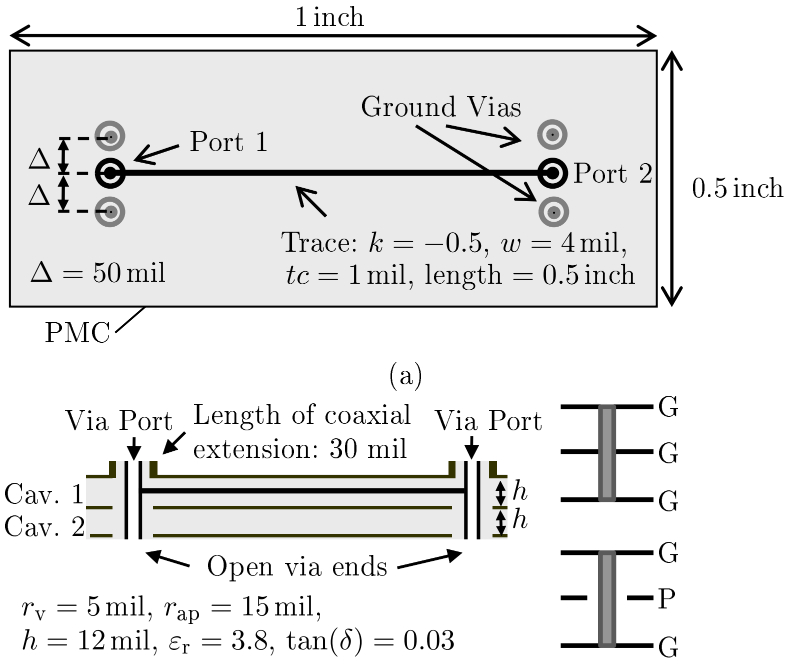

(a)

(b)

Figure 7.1: Simple test structure to show the effects of mixed reference planes. (a) Top view: two vias are connected by a single-ended line of 0.5 in length. Ground vias are placed on both sides of the signal vias. A finite board size of 1 in × 0.5 in is assumed for the simulation with a PMC boundary condition at the board edges (Figure from [18]). (b) Stackup: Two cavities are formed by the three reference planes of the test structure. The stripline is routed in the upper cavity. Coaxial extensions are used to excite the vias from top, while the lower via ends are open. The schematics on the right show the connectivity of the ground vias: In the GGG configuration, the ground vias are connected to all reference planes. In the GPG configuration, the inner reference plane is not connected (Figure from [18]).

top plane is assigned to ground, while both lower planes are floating. Simulation results for the transmission between port 1 and port 2 are shown in Fig. 7.2. It has to be mentioned that the extensive validation of the physics-based via model in Chapter 4 was carried out for infinite reference planes, while the test structures studied in this section have a finite size. For a validation specifically for the case of finite reference planes, the results obtained with the physics-based model in Fig. 7.2(a) are compared to results obtained with a commercial FEM solver [140] in Fig. 7.2(b). Although some differences exist with regard to the magnitudes of the resonant valleys, both approaches show a good general agreement. An extensive validation of the physics-based model for test structures of finite size - including a scenario with mixed reference planes - can be found e.g. in [59].

The obtained results show that for the simple test structure, the effect of mixed reference

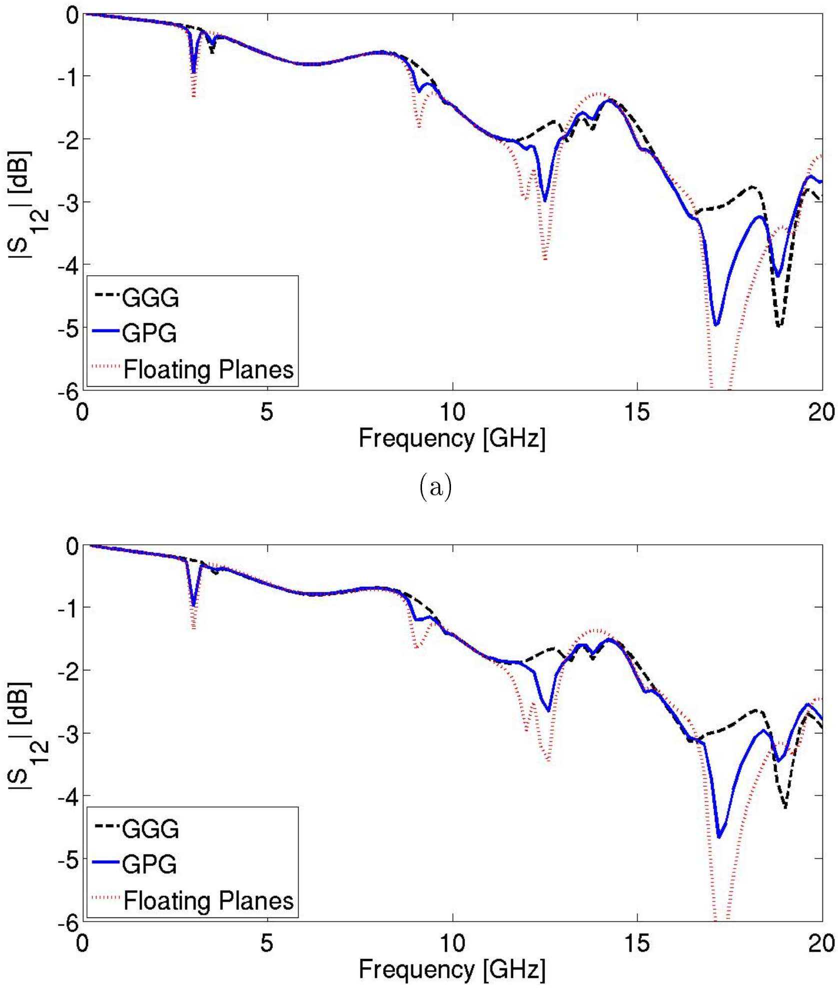

(a)

(b)

Figure 7.2: Comparison of the transmission S_{12} with all planes assigned to ground, with the center plane assigned as power plane, and with all planes floating. Results are shown for simulations with (a) the physics-based via model using the via barrel-to-plane capacitance and the CRM (Figure from [18]), and (b) a commercial FEM solver [140] (Figure from [18]). Although some differences exist with regard to the magnitudes of the resonant valleys, both approaches show a good general agreement, and the relevant effects of mixed reference planes on the transmission can be observed in both plots.

planes is of a narrow-band nature. A clear impact of the plane configuration can be seen at resonance frequencies of the structure, while no impact at all exists over broad frequency ranges between the resonances. Where an impact occurs, as expected the configuration without ground vias constitutes the worst case (lowest transmission). The GPG configuration is better, but still shows large resonant valleys. With the GGG configuration, some large resonant valleys can be completely avoided. Only above 13 GHz, some additional resonances are introduced by the ground vias, which are avoided in the case of floating planes. Except for special cases such as a clock signal operated exactly at the frequency of a resonance introduced by the ground vias, the GGG configuration will clearly provide the best signal transmission. In Fig. 7.3(a), the effect of mixed reference planes in the test structure is shown from the perspective of relative power loss. The power which is lost in the interconnect (being neither reflected nor transmitted) is calculated from the S-parameters as $P_{\text{loss}} = 1 - S_{11}^2 - S_{21}^2$ for the GGG and GPG configuration and plotted over frequency. For comparison, the power loss of a stripline with identical geometry and material parameters, but without the impact of the connected vias is shown. In the frequency range up to 10 GHz, both reference plane configurations behave widely similar, showing a loss close to the baseline provided by the the stripline loss. At the frequency of 3.02 GHz, however, the GPG configuration shows a resonance leading to a power loss of 18 %, while the power loss for the GGG configuration, which does not show the corresponding resonance, is only 4 %. The electric field plots in Fig. 7.3(b) show that in the configuration with mixed reference planes, the lost energy is coupled into the first resonant mode of the parallel planes, which can be calculated analytically (see e.g. [96, ch. 8.3.2]) to occur at 3.03 GHz for the studied structure. After being coupled into the resonant mode, the energy is dissipated in the cavity, leading to the observed power loss.

7.1.2 Effects on Single-Ended and Differential Links

Here, the effect of mixed reference planes is studied for the slightly more complex test structure in Fig. 7.4. The size of the test board is now 4 in × 1 in, and the board contains 5 reference planes forming 4 cavities. Two striplines in the third cavity form two single-ended links. The stripline geometry and the material parameters remain the same as for the first test structure (see Fig. 7.1). Four variations of the reference plane assignment are compared: GGGGG (all planes connected by the ground vias), GGPGG (one of the stripline reference planes assigned to power), GGPPG (both stripline reference planes assigned to power), and floating planes (test structure without ground vias). The remaining cases are not shown here, since the assignments of the second and fifth reference plane did not have a relevant impact on the simulation results. The transmission for one of the links is shown in Fig. 7.5(a). As for the first test structure, configurations with mixed reference planes have a detrimental effect on the transmission at the resonance frequencies of the structure. Due to the larger dimensions of the simulated coupon, more resonances occur and the effect appears to be more broadband, especially in the frequency range above 10 GHz. While the floating plane configuration again constitutes the worst case, also the configuration with two power planes shows some additional losses. In contrast, the configuration with only one power plane seems to be generally closer to the configuration with all planes connected to ground than observed in the first test case. Also in the near-end crosstalk in Fig. 7.5(b),

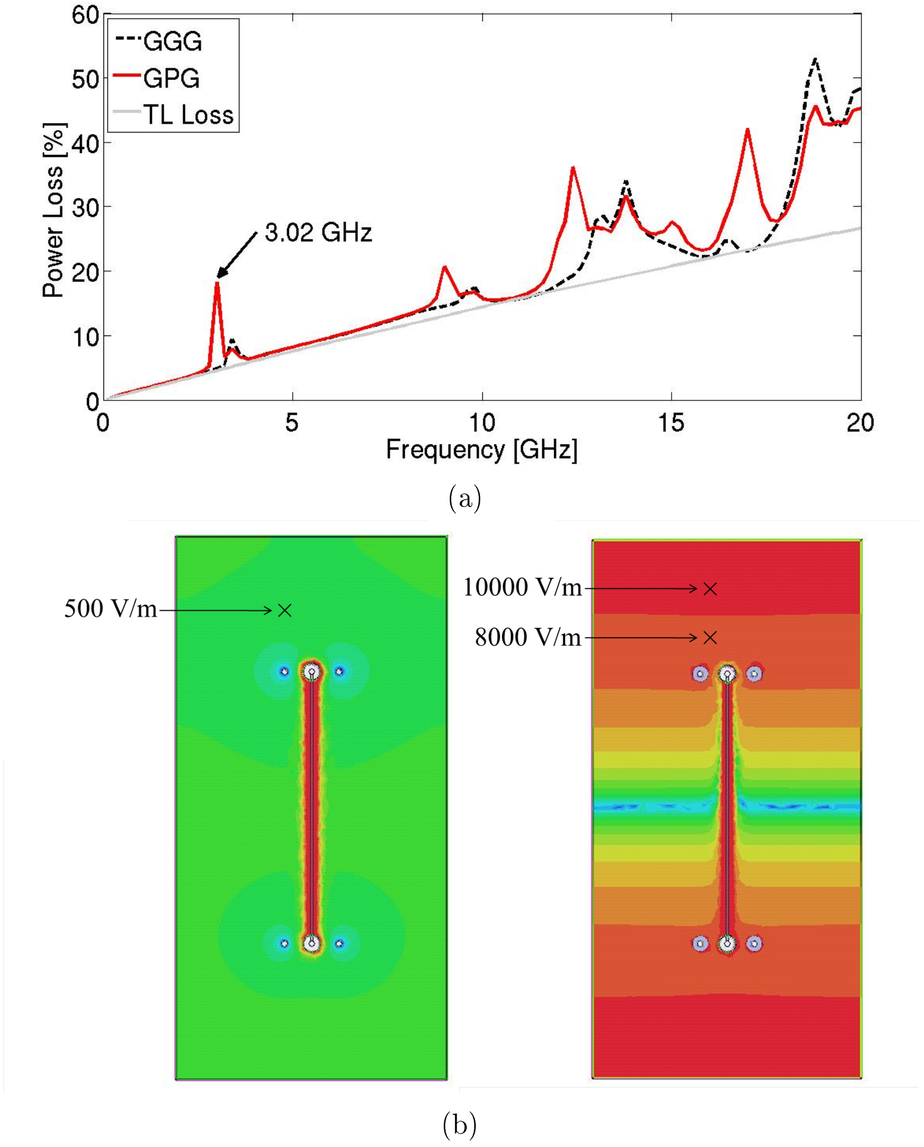

Figure 7.3: Energy coupled into the cavity for different reference plane configurations. (a) Power loss in per cent of the total energy inserted into the via port, calculated from the S-parameters obtained with the physics-based via model. At certain frequencies, the GPG configuration shows a much higher power loss than the GGG configuration. The power loss of a simple stripline (without vias) is shown as a baseline for comparison (Figure from [18]). (b) Electric field distribution in the upper cavity for the GGG configuration (left) and the GPG configuration (right) at 3 GHz, simulated with a commercial FEM solver [140]. In the GPG configuration, energy is coupled into the resonant mode of the cavity. This can be explained by the discontinuity in the return current path seen by the portion of the signal current returning in the power plane. Since the ground vias do not provide a conductive return path for this part of the current, it is forced to return to the ground plane as a displacement current, coupling into the resonant mode (Figure from [18]).

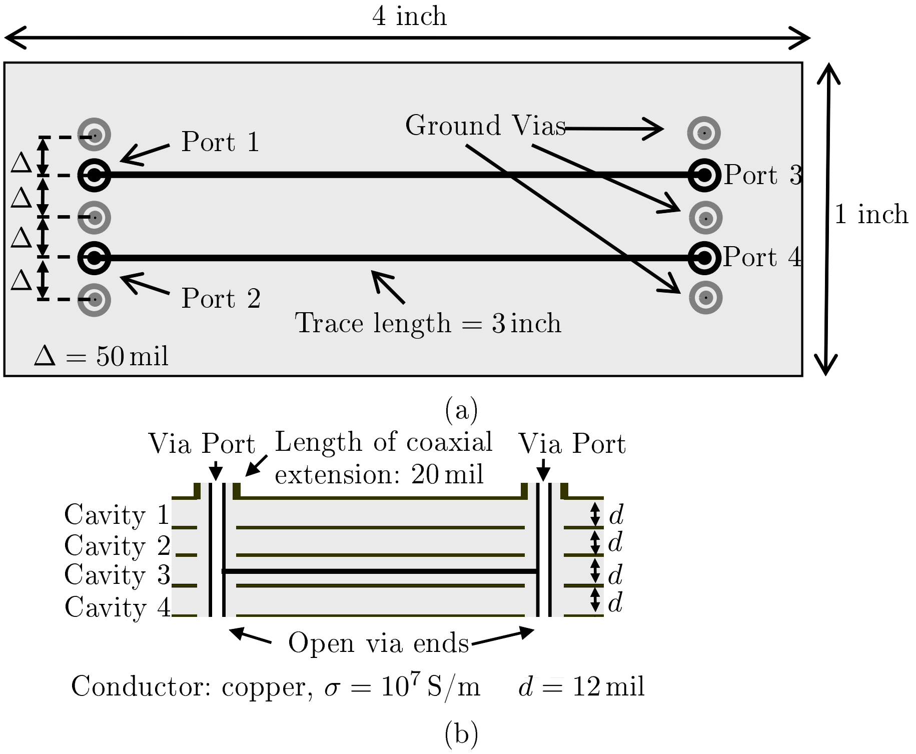

Figure 7.4: Larger test structure with 4 cavities to investigate the impact of mixed reference planes on signal transmission and crosstalk. (a) Top view: Four signal vias are connected by two single-ended striplines. A finite board size of 4 in × 1 in is assumed for the simulation. Stripline geometry and material parameters are identical to the definition in Fig. 7.1 (Figure from [18]). (b) Stackup: The striplines are routed in the third cavity. To investigate the impact of mixed reference planes, either one or both of the reference planes adjacent to the third cavity can be assigned to power (Figure from [18]).

differences between the four configurations can be seen. At low frequencies, the difference is more than 10 dB between the different alternatives. Furthermore, the effect appears comparatively broadband, indicating that the impact on the crosstalk may be more relevant than the impact on the transmission. Up to about 8 GHz, the GGPPG configuration leads to a considerably higher crosstalk than the GGGGG configuration. Above 8 GHz, differences between the alternative stackups are less pronounced - only the configuration without ground vias can still clearly be identified as the worst case.

In addition to the single-ended configuration in Fig. 7.4, a similar test structure has been studied with the single-ended striplines replaced by differential striplines (see [18] for the exact geometry definition). Also for this test structure, the stackup with 5 reference planes as shown in Fig. 7.4(b) has been employed. The simulation results for the differential transmission and crosstalk confirm that an impact of mixed reference planes also exists for

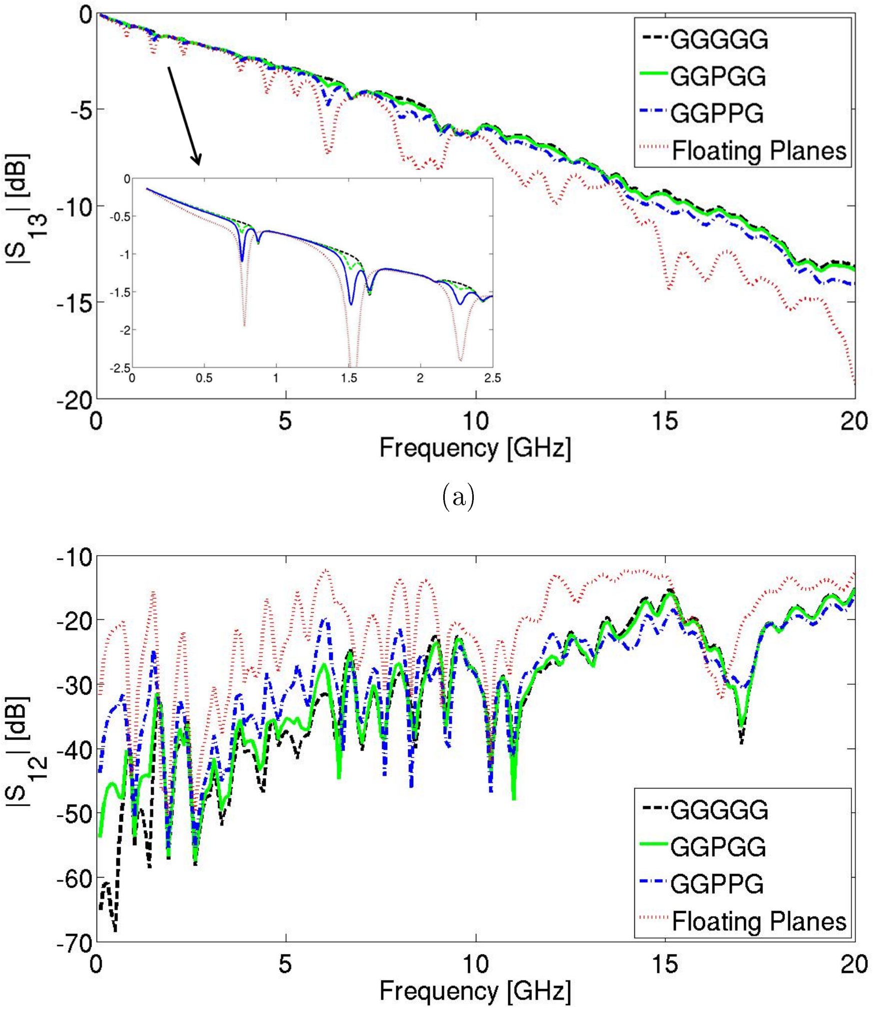

(a)

(b)

Figure 7.5: Results for the larger test structure with 4 cavities. All results were obtained with the physics-based via model (local field model: via barrel to plane capacitance; propagating field model: CRM). (a) Transmission. Similar to the first test case, a detrimental effect of mixed reference planes can be seen at the resonance frequencies of the test structure. Due to the larger dimensions of the test structure, more resonances occur, and the effect appears more broadband. The configuration with one power plane (GGPGG) clearly leads to a better transmission than the configuration with two power planes (GGPPG) (Figure from [18]). (b) Near-end crosstalk between the two lines in Fig. 7.4(a). At low frequencies, more than 10 dB difference exist between the crosstalk levels of each different plane configuration. Up to about 8 GHz, the GGPPG configuration leads to a considerably higher crosstalk than the GGPGG configuration (Figure from [18]).

differential links, and is not fundamentally different from the impact for single-ended cases. In the differential case, an additional aspect worth studying is the mode conversion between differential and common mode transmission. The mode conversion mainly occurs due to the asymmetric environment seen by each of the differential via pairs due to different distances to the board edges. The simulation results show that mixed reference planes have a considerable impact also on the mode conversion. Although at low frequencies, the impact on the mode conversion is smaller than for the crosstalk, the impact on the mode conversion extends to higher frequencies, showing a considerable effect up to 14 GHz.

7.2 Impact of the Routing Layer

Besides the assignment of reference planes studied in the previous section, also the routing layer has an impact on the signal transmitted over an interconnect. Similar to the reference plane assignment, the routing layer does not affect the stripline mode itself: The transmission along the stripline will show an identical behavior on different routing layers provided that all layers use an identical stripline design. However, the signal transmission over an interconnect is also influenced by the behavior of the access vias, which is strongly dependent on the routing layer. Two main effects exist: First, the part of the access vias above the routing layer represents a discontinuity in the signal path. It can cause reflections as well as a coupling of energy into the parallel plate modes of the traversed PCB cavities. Second, the part of the access via below the routing layer acts as an open stub. Reflections from the open end of the via stub can superpose the intended signal, leading to a destructive interference at certain frequencies. Furthermore, a coupling into the parallel plate modes of the traversed cavities can occur also for the stub portion of the via. Typically, the via stub has a larger impact on the signal transmission than the upper part of the access via. The detrimental impact of via stubs on high speed signal transmission has been studied in [141] in the frequency domain and in [142–144] in frequency and time domain. In principle, the via stub effect can be minimized by backdrilling (eliminating the largest part of the via stub by drilling into the bottom side of the PCB) or through an equalization of the signal that compensates for the impact of the stub. However, these measures lead to an increase in manufacturing or operating cost of the PCB.

In this section, the impact of the routing layer on signal transmission is studied both without and with backdrilling of via stubs. In contrast to the studies in [141–144], which focus on single interconnects, the impact of the routing layer is studied here for vias inside arrays under full consideration of the surrounding vias. This allows to compare the impact of the routing layer to the impact of the via position inside the array. Knowledge about the impact of the routing layer on signal transmission may allow an optimized assignment of signals to different routing layers, improving the overall signal integrity and reducing or eliminating the need for costly measures such as backdrilling or equalization.

7.2.1 Impact in the Frequency Domain

The investigation in this section is carried out using measured and simulated results for the 10×10 via array test structure in Fig. 6.4, for which a comparison between measurements and results obtained with the physics-based via model was already carried out in Section 6.3. The signal vias inside the array are connected to striplines on three different routing layers (see Fig. 6.4(a)). The detailed stripline geometry is shown in Fig. 6.4(b), the stackup including the different routing layers in Fig. 6.4(c). Measurements with RPLs (see Section 6.3.2) are used here. In this way, the impact of a single via transition inside the array can be evaluated, without the impact of an additional access via.

In Fig. 7.6, measurement results are used to compare the impact of the via position inside the array to the impact of the routing layer of the connected stripline. Fig. 7.6(a) shows the transmission over striplines routed on the highest signal layer (SL3) in the PCB for three vias at different positions inside the via array. While the position in the array has an impact on the detailed characteristics of the curves, the general characteristics look very similar: all curves show the resonances caused by the via stub and the impact of reflections from the ground via cage. In contrast, the comparison of three vias routed on different layers in Fig. 7.6(b) shows a clear impact of the routing layer. While the transmission shows a similar behavior on all layers for frequencies up to about 8 GHz, the impact of the via stub becomes visible at higher frequencies. Between 8 GHz and 18 GHz, the worst transmission can be observed at the highest routing layer - SL3 - while the best transmission exists at the lowest routing layer - SL9. At frequencies above 18 GHz, the transmission shows a more complex behavior due to higher stub resonances and additional effects.

7.2.2 Impact in the Time Domain

While the measurement results in Fig. 7.6 show that a substantial impact of the routing layer exists, it is difficult to assess the consequences for signal integrity directly from the S-parameters. For this reason, time domain evaluations are carried out to further investigate the impact of the routing layer at different data rates. The resulting eye diagrams for via 29 (highest routing layer) and via 32 (lowest routing layer) are shown in Fig. 7.7. At a data rate of 5 Gb/s, the impact of the routing layer is very small, and both eyes are almost fully open (see Fig. 7.7(a) and Fig. 7.7(b)). At 15 Gb/s, an impact of the routing layer on the shape of the eye diagram can already be seen in Fig. 7.7(c) and Fig. 7.7(d). However, the maximum vertical eye opening is still similar for both diagrams. At 25 Gb/s, a large impact of the routing layer exists (see Fig. 7.7(e) and Fig. 7.7(f)). For the signal routed

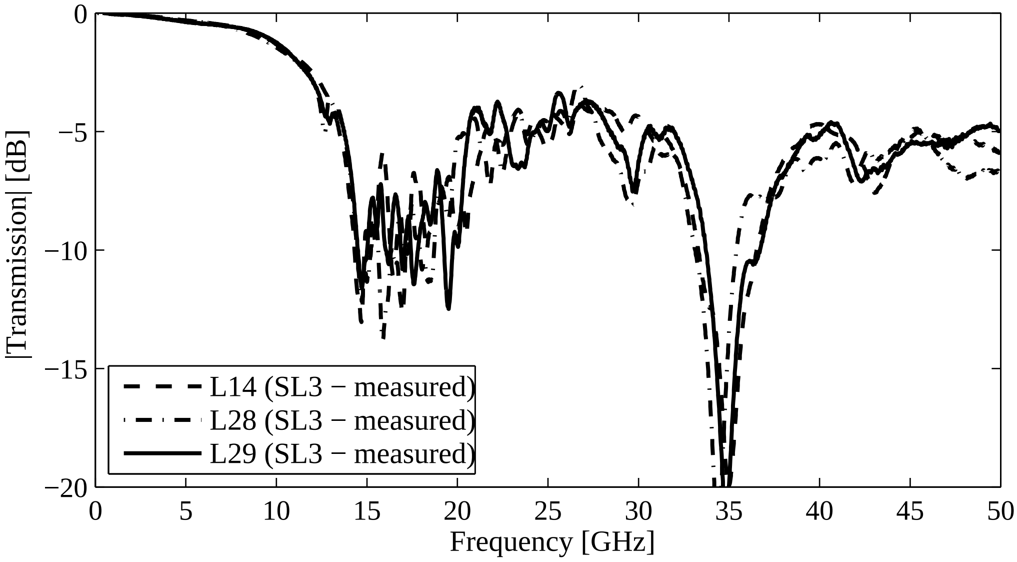

(a)

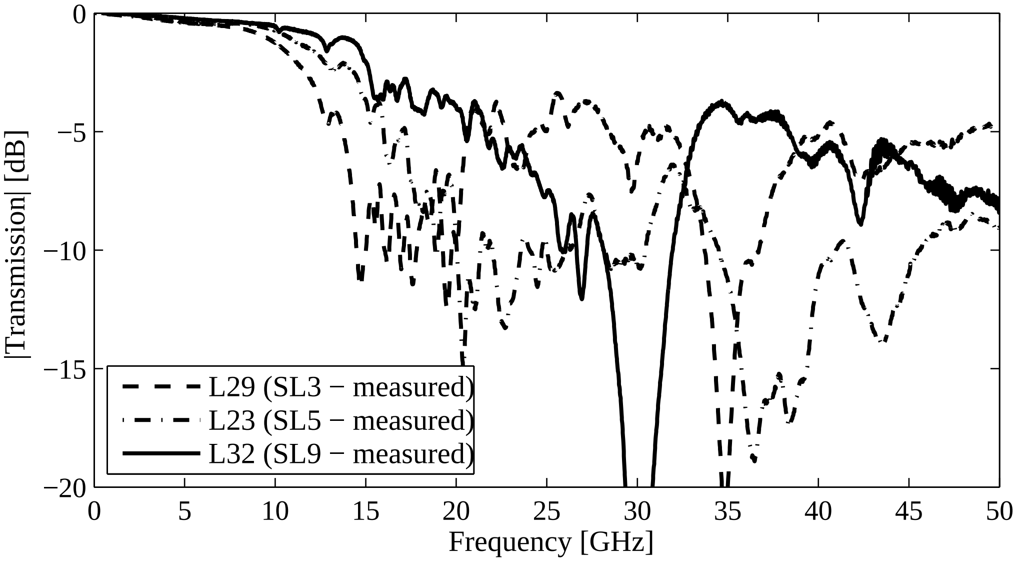

(b)

Figure 7.6: Comparison between measured S-parameters for the transmission for different vias. (a) Comparison for vias connected to the same routing layer at different positions of the array. Although the curves show some differences, the general behavior is the same (Figure adapted from [24]). (b) Comparison for vias connected to different routing layers. The curves show much larger deviations, demonstrating the large impact of the routing layer on the signal transmission (Figure adapted from [24]).

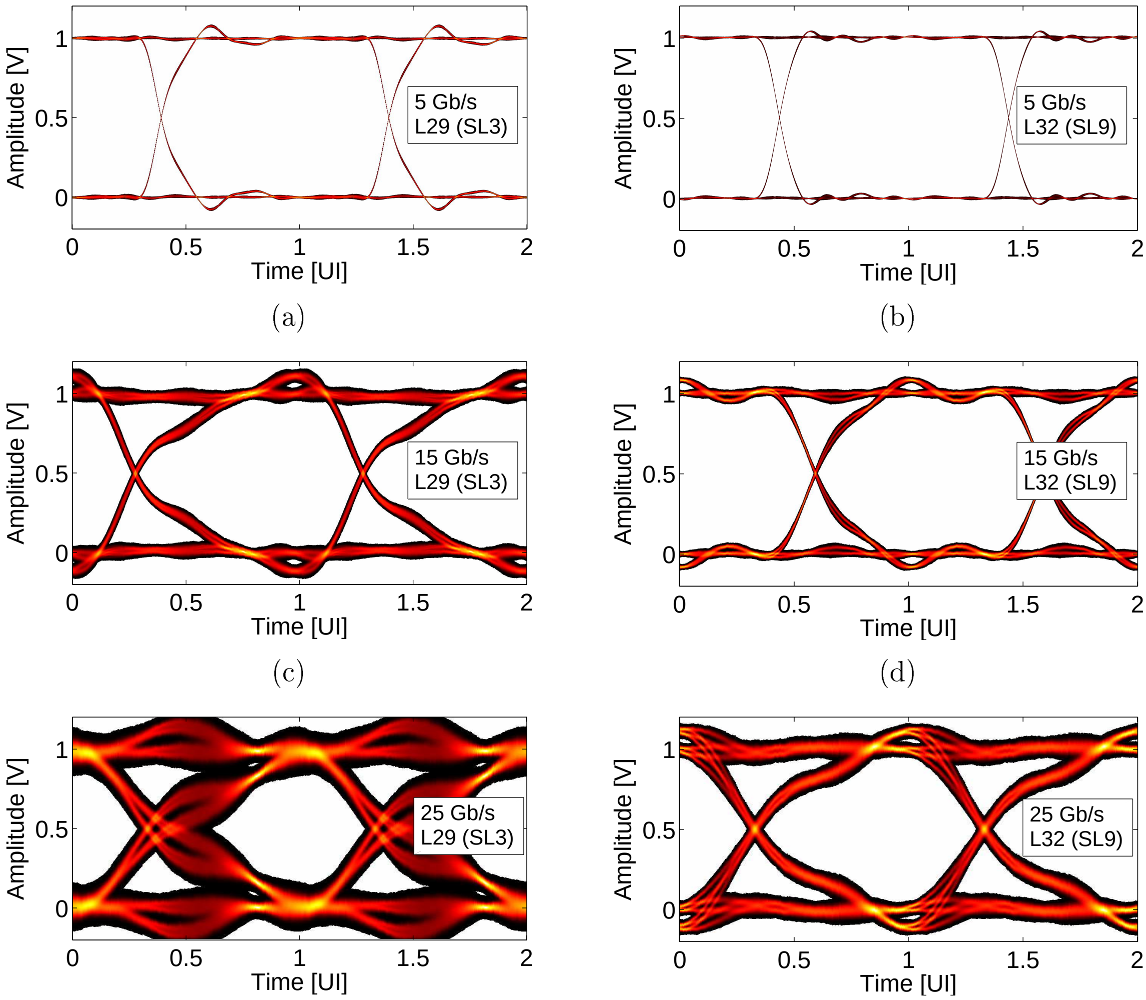

(a) (b)

(c) (d)

(e) (f)

Figure 7.7: Impact of the routing layer on the eye diagram (measured results, all Figures adapted from [24]). Eye diagrams at 5 Gb/s are compared for (a) via 29 at signal layer 3 and (b) via 32 at signal layer 9. Both eyes are virtually fully open, and no relevant impact of the routing layer can be seen. At 15 Gb/s, different shapes of the eye diagram can already be seen for (c) via 29 and (d) via 32. At 25 Gb/s, the eye diagrams of (e) via 29 and (f) via 32 both show an impact of the via stub. A considerable difference between the different routing layers exists, with a smaller eye opening at the higher routing layer.

on SL3, the eye opening is considerably smaller due to the longer via stub.

To summarize the impact of different via locations and routing layers on the signal in time domain, the vertical eye opening is used as a figure of merit for the comparison of different cases. In Fig. 7.8, the vertical eye openings are plotted over the data rate. Four vias routed on SL3 are compared to 6 vias routed on SL9. For data rates up to 15 Gb/s,

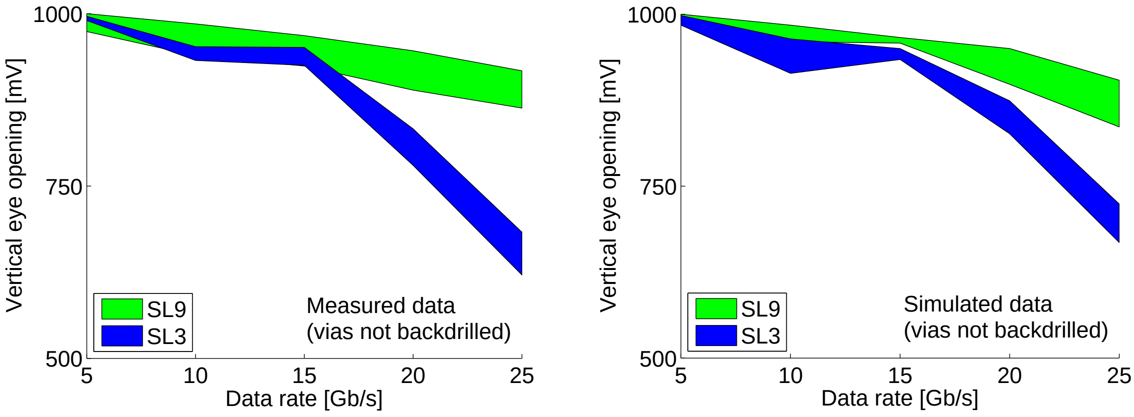

(a) (b)

Figure 7.8: Vertical eye openings depending on the data rate, shown for (a) measured S-parameters (Figure adapted from [24]) and (b) simulated S-parameters (Figure adapted from [24]).

the impact of the position inside the via array is still in a similar order of magnitude as the impact of the routing layer. For data rates of 20 Gb/s and 25 Gb/s, however, the impact of the routing layer clearly dominates. A comparison between the evaluation based on measurements in Fig. 7.8(a) and the evaluation based on Fig. 7.8(b) shows that both lead to similar conclusions. This allows to employ the physics-based model to study additional cases, which were not included in the measured structure. In [24], for example, the impact of backdrilling the vias on SL3 was investigated using the physics-based model, which allowed a quick evaluation of the impact without actually having to backdrill the vias on the test vehicle. The results in [24] show that after backdrilling, the signals routed on SL3 actually perform better than the signals routed on SL9 for all evaluated data rates from 5 Gb/s up to 25 Gb/s. The difference between the routing layers can be attributed to the shorter via length for signals routed at SL3. Although the difference between the layers is smaller with backdrilled vias than with via stubs, it can amount to more than 10 % at 25 Gb/s. The physics-based via model is also used to carry out an additional evaluation of differential links in [24]. The example shows that the general tendencies observed in the single-ended case can also be found in the differential case. However, the impact of via stubs is smaller than in the single-ended case.

7.3 Crosstalk Study for Large Via Arrays

So far, the physics-based via model has been applied to problems that could be analyzed on a smaller scale. In this section, the crosstalk behavior in large via arrays is studied, which

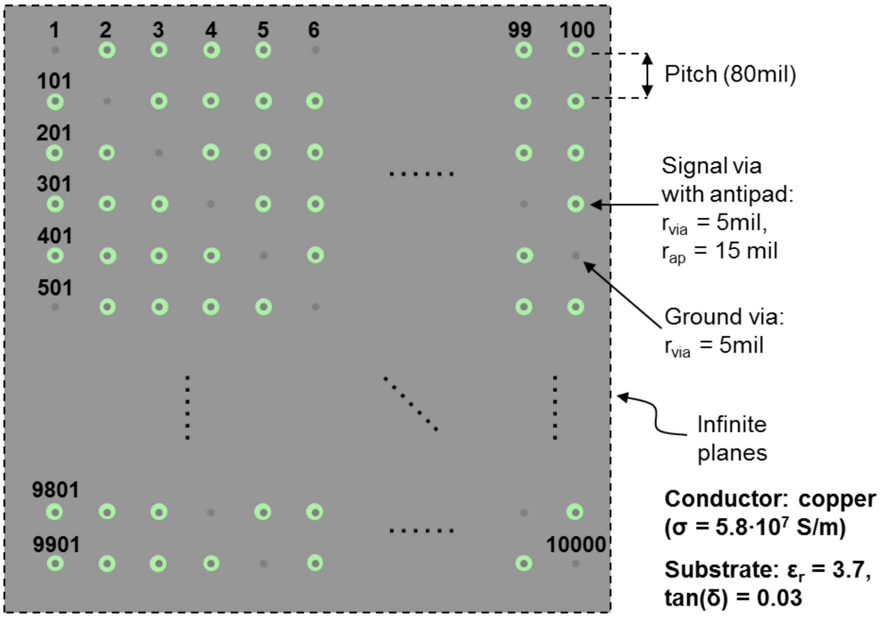

Vias for the crosstalk study (center area of the board)

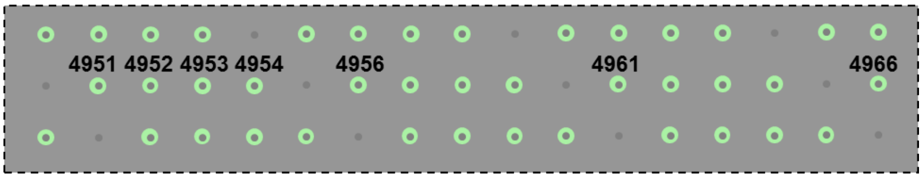

Figure 7.9: Top view of the 100 x 100 via array employed for the crosstalk study. The near-end crosstalk between signal vias is evaluated along the two main diagonals of the array and along the shown horizontal row at the center of the via array (Figure from [26]).

requires a full modeling of the complete arrays. The crosstalk behavior is first analyzed for a 100 × 100 via array as shown in Fig. 7.9. The signal to ground via ratio is 4:1, and the ground vias are arranged regularly along diagonals in the array. The stackup has the configuration shown in Fig. 5.4(a). The complete simulation of the structure with the physics-based via model allows to evaluate the crosstalk behavior for the entire array. Here, results for the near-end crosstalk to a via at the center of the array (via 4951) are shown. The evaluation of vias at the center of the array is of interest since it may be assumed that they see the highest overall crosstalk. In Fig. 7.10(a), the near-end crosstalk to via 4951 is evaluated for vias along the two main diagonals of the via array. Results are shown for the 10th vias along the two diagonals and for the 49th vias along the two diagonals as seen from the center via. The crosstalk to the 10th vias along the diagonals amounts to about -60 dB. The crosstalk to the 49th vias, which are at the outer edge of the via array, amounts to up to -80 dB. The results for the crosstalk to these outer vias should only be seen as an approximation of the real crosstalk behavior due to the low crosstalk levels and

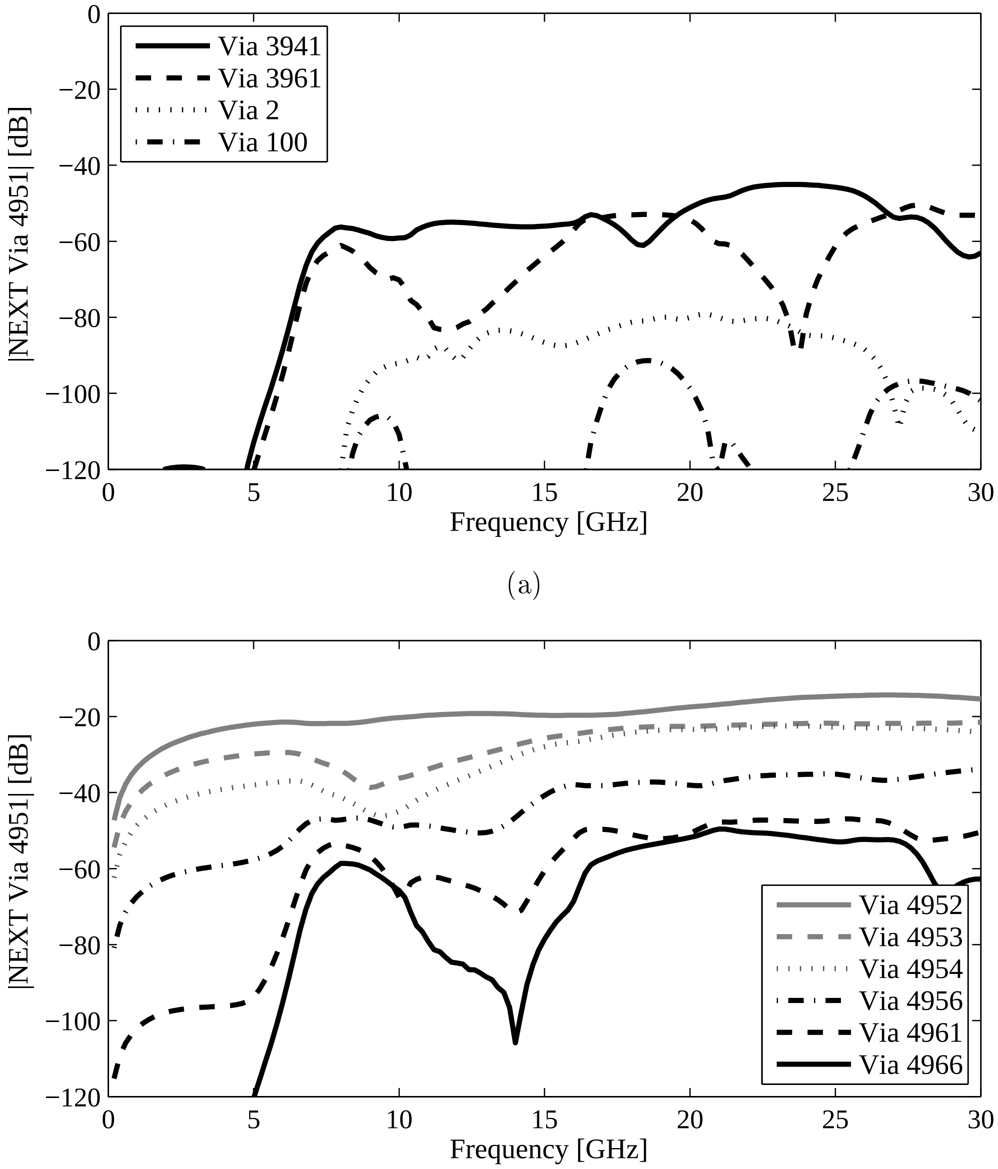

(a)

(b)

Figure 7.10: Evaluation of near-end crosstalk (NEXT) for the 100 x 100 via array shown in Fig. 7.9. (a) Crosstalk to via 4951 (at the center of the array) is evaluated for two vias in a distance of 10 vias along the diagonals (vias 3941 and 3961), and two vias in a distance of 49 vias along the diagonals (vias 2 and 100 at the upper edge of the array). The curves show the dependency of the crosstalk on the distance between vias as well as on the direction of the diagonal (Figure from [26]). (b) Crosstalk to via 5951 along the horizontal row shown in Fig. 7.9. The curves show that the crosstalk behavior depends on the distance between vias as well as on the intermediate ground vias (Figure from [26]).

the large number of intermediate vias. Nevertheless, the results show interesting properties of the crosstalk such as the directional behavior which is introduced by the ground via diagonals: Over wide frequency ranges, the crosstalk "along" the ground via diagonals is considerably higher than the crosstalk "orthogonal" to the ground via diagonals. A second evaluation of the near-end crosstalk to via 4951 at the center of the array is carried out along the horizontal via row in Fig. 7.9. The crosstalk from the different vias along the row is shown in Fig. 7.10(b). Similar to the evaluation along the diagonal, the evaluation along the row shows the considerable impact of the ground vias on the crosstalk behavior. While the crosstalk levels generally decrease with distance, the decrease is not proportional to distance. Vias 4953 and 4954, for example, almost show the same crosstalk to via 4951 at higher frequencies. Via 4956 in contrast, which is separated from via 4951 by an additional ground via, exhibits a much lower crosstalk.

Besides the distance between vias and the arrangement of signal and ground vias, additional factors exist which have an impact on the crosstalk between vias. The impact of some of these factors is discussed here. For the corresponding simulations, the 100×100 array has been reduced to a 40×40 array to achieve shorter simulation times. Via arrangement and stackup dimensions remain the same as before. As a first variation, mixed reference planes are introduced by assigning every second reference plane in the stackup to power. For adjacent vias, only a small impact of the change can be observed in the crosstalk level. For the crosstalk to the 15th via along a row, in contrast, a considerable increase in the crosstalk level in case of mixed reference planes can be observed as shown in Fig. 7.11(a). The increase can be explained by a reduced shielding efficiency of intermediate ground vias in the case of mixed reference planes. The observation that the impact of mixed reference planes on the crosstalk occurs only for distant vias underlines the importance of an efficient simulation method that can provide results for large via constellations. To study the impact of the dielectric loss tangent on the crosstalk behavior, the simulation for mixed reference planes is repeated with a reduced loss tangent of $\tan(\delta) = 0.01$ (in comparison to the original loss tangent of $\tan(\delta) = 0.03$). Although an increase in the crosstalk can be observed in case of the lower loss tangent, the effect is comparatively small even for distant vias, as shown in Fig. 7.11(a). This result is encouraging with regard to the application of low loss dielectrics, which are currently investigated as an option to reduce stripline losses for high-speed links as mentioned in Section 1.3. The finding indicates that low loss dielectrics do not lead to a severe increase of crosstalk problems.

With additional simulations for the 40×40 via array, the impact of the applied via terminations on the crosstalk behavior is studied. Three different configurations are compared which can be encountered in the analysis of via arrays. For S-parameter simulations which investigate the interaction between vias (such as the crosstalk analysis in this section),

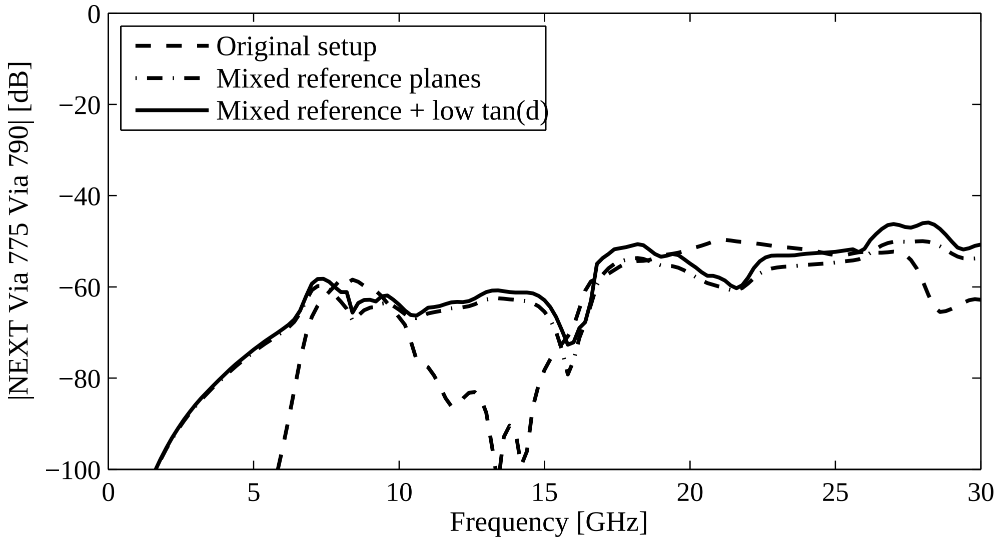

(a)

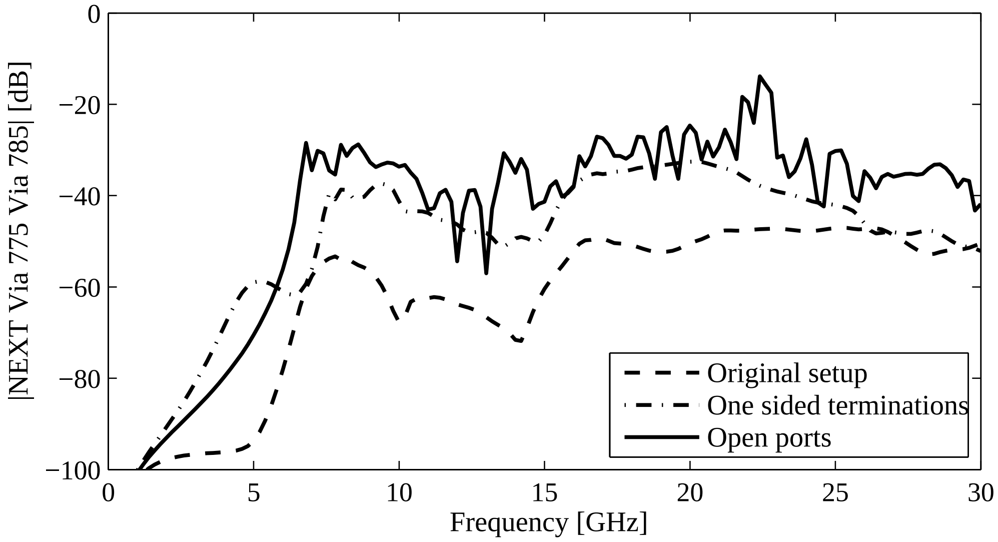

(b)

Figure 7.11: Evaluation of different impacts on the near-end crosstalk (NEXT) for a 40 x 40 via array. (a) Evaluation of mixed reference planes and a reduced tan(δ) on the crosstalk between vias in 15 vias separation. (b) Effects of the via termination on the crosstalk between vias in 10 vias separation.

ports which correspond to 50 Ω terminations are placed at top and bottom of all vias. In the case of a practical link structure, typically only the upper via ends are terminated (through a connection to the surface mounted components), while the lower via ends are open. Finally, in the case of microprobe measurements, only the probed via ends are typically terminated, while all other via ends are open. The near-end crosstalk to the 10th via along a row is compared for the three different termination scenarios in Fig. 7.11(b). The lowest crosstalk level exists if upper and lower via ends are terminated. The removal of lower via terminations leads to a considerable increase in the crosstalk level. If also the upper via terminations are removed, a further increase of the crosstalk level can be observed together with a resonant behavior introduced by the completely unterminated vias. It shall be mentioned that for vias in a smaller distance from each other, the impact of via terminations on the crosstalk level is more complicated, and frequency ranges may exist where the crosstalk level is in fact lower in the unterminated case.

7.4 Summary and Discussion

The examples in this section have applied the physics-based via model (in combination with measurement results) to study three different signal integrity aspects: The effects of mixed reference planes, the impact of the routing layer on the signal transmission, and the crosstalk behavior in large via arrays. The study of mixed reference planes is carried out for small PCB coupons, taking into account the finite size of the reference planes. It shows that the mixed reference planes lead to a coupling of signal energy into the resonant modes of the PCB cavities. The energy is lost for the signal transmission and either dissipated or coupled to other vias in the cavity (increasing crosstalk). In the differential case, mixed reference planes also increase the differential to common mode conversion. A considerable impact of the routing layer on the signal transmission can be observed for data rates of 20 Gb/s. The main detrimental impact for the transmission results from open via stubs, which makes a transmission on the lowest routing layer (related to the shortest via stubs) favorable. In case of backdrilled via stubs, the highest routing layer becomes favorable due to the shorter access vias. The crosstalk study for large via arrays demonstrates - among other observations - the considerable impact of the ground via arrangement on the crosstalk behavior. At the same time, a limitation of the signal integrity evaluation in terms of S-parameters becomes obvious: each S-parameter curve only represents the crosstalk between two vias. Typically, however, design changes impact all vias in an array (and all of them in a different way), so that a global evaluation is required for a meaningful comparison of different design alternatives. A step towards such a global approach is proposed in the next chapter.

8 Systematic Comparison of Link Design Alternatives

This chapter presents an approach to a systematic, energy-aware comparison of link designs. The first part of the chapter describes the advantages of such an approach, and gives an overview of related existing works. In the second part of the chapter, the approach is described in detail. The proposed evaluation takes into account signal integrity as well as energy efficiency, and makes different designs comparable by applying identical constraints to several key design properties. At the end of the evaluation, each design alternative is characterized by its input power requirement, which serves as a single figure of merit for a quantitative comparison. To illustrate the approach, it is applied to evaluate the energy efficiency of four fundamental link design alternatives in the third part of this chapter.

8.1 Motivation for a Systematic, Energy-Aware Analysis

As pointed out in Chapter 1, demands on PCB links are steadily rising with regard to both signal integrity and energy efficiency. For a design process, this means that the aim is not only to meet signal integrity requirements, but also to provide the highest possible energy efficiency.

The examples given in Chapter 7 have already demonstrated that physics-based via and trace models can be applied to study the behavior of PCB structures as well as the impact of design changes on signal integrity. However, the evaluations were comparatively simple, since each of them focused on a specific design aspect. An assessment was carried out mostly through comparison of S-parameter curves. Although this is an approach commonly followed in the literature, a more systematic analysis is desirable for several reasons, as described in the following. First, due to the complexity of S-parameters of real systems, a comparison of S-parameter curves typically has to be of a qualitative nature. While the amount of information contained in the S-parameter description may be desirable for an in-depth analysis of certain aspects, a comparison of multiple design alternatives can be drastically simplified through a restriction to only one or a few meaningful figures of merit. Second, in a realistic PCB link, a design decision will concern not only one S-parameter curve (i.e. transmission of a certain channel or crosstalk between two points), but transmission and crosstalk properties for several or all channels in the link. For this reason, a meaningful evaluation has to take into account all channels in the link simultaneously, and allow for a decision whether an improvement at one point is worth the deterioration at another. Third, signal integrity is not the only link design goal. Additional important objectives are a high data rate, a small space requirement, and a high energy efficiency. This means that in the analysis, a step back has to be taken from assessing the S-parameters of an interconnect toward a combined assessment of the different design objectives, including the energy efficiency of the system.

In the past, several approaches have been presented that aimed at an optimization of energy efficiency for link structures. Most of these works focus on on-chip links, and employ only simple interconnect models [145–148] (e.g. lumped [145] or distributed [146] RC models). These models are sufficient in the on-chip domain, but cannot handle the complexity of off-chip interconnects. Furthermore, the works focus on an optimization of transmitter and receiver circuits rather than on an optimization of the interconnect itself. An exception is the work in [149], which includes an optimization of interconnects for on-chip links based on RLGC models. For off-chip links, the focus of existing works is again on an optimization of transmitter and receiver designs and parameters. In [150], such an optimization is carried out based on measured network parameters of a PCB interconnect. Simple transmission line models are employed to find the most energy-efficient trade-off between transmitter output power and receiver amplification in [151] and the optimal data rate leading to the minimum energy per transferred bit in [152–154]. Many works study the impact of off-chip interconnect design on signal integrity - some of them aiming at a systematic assessment of the overall impact of design parameters. In [155], for example, the achievable aggregate data rate is used as a figure of merit to find the optimal number of signal layers for a PCB. However, to the knowledge of the author, no works exist that systematically study the impact of off-chip interconnect design on the energy-efficiency of a link, which is one main goal of the approach proposed in Section 8.2.

8.2 Proposed Approach for a Systematic Comparison

The proposed approach is based on the network parameter description of the PCB link, which can be obtained from the physics-based via and trace models. In contrast to the signal integrity evaluations in Chapter 7, additional steps toward a quantitative analysis are introduced here. In the following, a general overview of the approach is given, followed by a more detailed description of the methods and assumptions chosen for the different steps of the evaluation.

8.2.1 General Overview

An important goal of the proposed approach is to simultaneously take into account the different objectives of link design. For the analysis in this work, we identify four objectives as most important (as already listed in Section 8.1): a good signal integrity, a high aggregate data rate, a small space requirement, and a high energy efficiency. By representing the quality of signal integrity by the bit error rate and the energy efficiency by the aggregate link input power, we obtain – together with aggregate data rate and space requirement – four figures of merit for the analysis. The chosen quantities have the advantage of being integral values in the sense that each of them summarizes the corresponding properties of the complete link in a single number, which simplifies the comparison between different designs. For the practical evaluation, the problem is now further simplified by assuming three of the four values of the objective functions to be given. For the bit error rate and the aggregate data rate of the link, this is a realistic assumption, since both values will typically be defined at the beginning of the link design process. In contrast, the space requirement of the link can in general be variable in a PCB design optimization. For the sake of simplicity, it is assumed here that the allowed space requirement is fixed at an early design stage as well. This leaves the link input power as the only remaining objective function, which has to be minimized under the constraints given by the values for bit error rate, aggregate data rate and space requirement of the link.

The evaluation of the link input power for a certain link design follows the approach outlined in Fig. 8.1. For a given link design (which has to satisfy the constraint with regard to the space requirement), the S-parameter description of the link is calculated. Based on the S-parameters, time domain simulations are carried out to calculate the receiver eye openings for all channels of the link at the specified bit error rate (similar to the time domain analysis already carried out in Section 7.2). The eye diagram of a channel takes into account crosstalk from all other channels in the link. The single channel data rate, for which the eye diagrams are calculated, is the required aggregate link data rate divided by the number of channels in the link. After a time domain simulation of the complete link has been carried out, the worst case channel (smallest vertical eye opening) is found. If the vertical eye opening of the worst case channel is smaller than the target eye opening, the requirement for the bit error rate is not met. In this case the input voltage swing of the link has to be increased. If the vertical eye opening is larger than the target eye opening, the bit error rate is lower than required. This means that the input voltage swing can be reduced. In the presented approach, two assumptions are made with regard to the input voltage swing: first, the voltage swing is assumed to be continuously variable (similar to the analyses in [150–152]). Second, it is assumed that all channels are operated with the same input voltage swing, which means that an adjustment of the worst case channel impacts all channels in the link. With the adjusted input voltage swing, the simulation of the worst case channel is repeated (as before, the impact of crosstalk from all other channels in the link is included). After the target eye opening has been met, the corresponding input

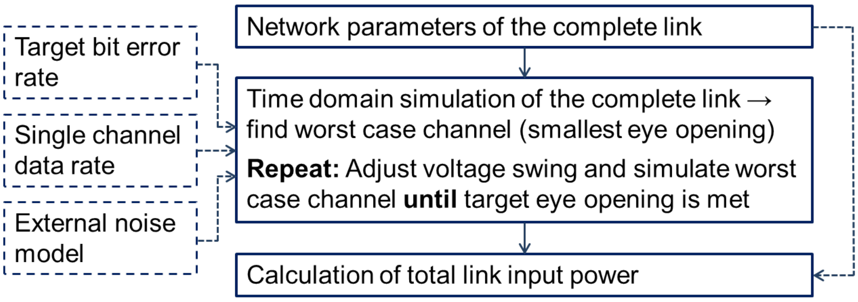

Figure 8.1: Link optimization scheme consisting of three steps: network parameter calculation, time domain evaluation, and input power calculation. Input parameters to the time domain evaluation are the target bit error rate, the single channel data rate, and an optional model for the impact of external noise (Figure adapted from [5]).

voltage swing is used to calculate the input power of the link. The input power is the figure of merit that is employed for the comparison of different design alternatives. In the following, methods and assumptions used in the three steps of the design evaluation are described in more detail.

8.2.2 Network Parameter Calculation

The presented approach for a systematic comparison requires the availability of a network parameter description of the complete link. In general, the network parameters can be obtained in any suitable way—by any simulation approach or even by measurement. Here, the physics-based via and trace models are employed for the calculation. The advantage of the physics-based model lies in its computational efficiency, which allows to carry out fast analyses of parameter variations for smaller structures, or to analyze large structures – including all crosstalk parameters – that could not be handled by other simulation methods. A shortcoming of the physics-based model in the context of the presented approach is that it does not provide the DC value of the network parameters, which is required for the following time domain analysis. However, a good approximation of the DC point can be obtained based on the resistance of the stripline conductor. For comparison, a second DC value was obtained by linear extrapolation of both magnitude and phase of the network parameters calculated for higher frequencies, as described in [5]. Both approaches lead to very similar analysis results.

8.2.3 Statistical Approach for the Time Domain Simulation

To carry out the time domain simulations which are required in the second step of the presented approach, a statistical calculation method [156, 157] is used. A numerical code for the statistical time domain simulation was implemented as part of a Diplomarbeit in [38]. It should be pointed out that like the network parameter calculation, the time domain evaluation is not restricted to a specific method. All approaches which are able to generate an eye diagram are in general feasible. However, the statistical approach has some advantages over conventional methods for the eye diagram calculation. Conventional methods calculate the eye diagram as a superposition of receiver voltages for a certain bit pattern. Sufficiently long bit patterns are required to allow a reliable statement about the eye opening. In the statistical approach, in contrast, the eye diagram is a two-dimensional map showing the probability density of voltage levels at each point in time over the length of two unit intervals (UIs). In this sense, the eye diagram is not the result of a certain bit pattern, but of a generalized signal with given properties (i.e. certain probabilities of the logical states "1" and "0"). Furthermore, the statistical approach allows for the inclusion of both uncorrelated and crosstalk with a known phase offset. Also additional external noise models can be taken into account.

For the evaluation of four design alternatives in Section 8.3, a random non-return-to-zero (NRZ) signal with equiprobable voltage levels V_{min} (corresponding to a logical zero) and V_{max} (corresponding to a logical one) is assumed. V_{min} is always set to zero, while V_{max} corresponds to the variable input voltage swing of the link. For a single bit, a trapezoidal shape with rise and fall time both corresponding to 10 % of the unit interval is assumed at the transmitter output. It should be pointed out that the time domain evaluation is based on the S-parameter description of the PCB link only, and does not take into account an additional impact of packages and sockets. As shown in Fig. 8.2, for a system consisting of L channels, the transmission between transmitter and receiver is given by the entry $S_{i+L,i}$ of the S-parameter matrix. The far-end crosstalk from the next channel is represented by the entry $S_{i+L,i+1}$. Examples for the resulting eye diagrams are shown in Fig. 8.3. For a data rate of 15 Gb/s, the eye diagram of a PCB interconnect is shown without any impact of crosstalk (Fig. 8.3(a)) and including far-end crosstalk from 5 aggressor channels (Fig. 8.3(b)).

8.2.4 Power Evaluation

While the time domain evaluation provides the input voltage swing requirements for the different design alternatives, a more meaningful comparison can be carried out in terms of the total link input power, which is therefore chosen as the main figure of merit as described in Section 8.2.1. Besides the input voltage swing, the calculation of the total link input power requires the (frequency dependent) input impedance of each channel and the power spectral density of the input signal. For the calculation of the input impedances, the simplified link model shown in Fig. 8.2 is applied. The model consists of two termination impedances (one at the transmitter and one at the receiver side) and of the network

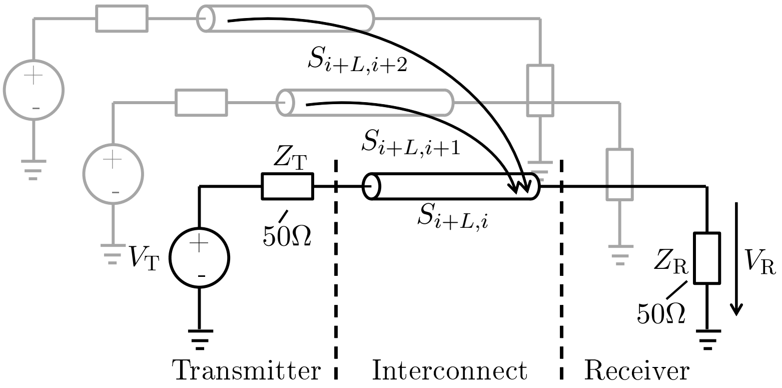

Figure 8.2: Circuit model assumed for the analysis. The time domain analysis calculates the eye diagrams based on the transfer function from beginning to end of the interconnect, including far-end crosstalk from all neighboring channels. The power calculation takes into account losses in the termination impedances at the transmitter and receiver sides. 50 Ω terminations are assumed for the evaluation in Section 8.3 (Figure adapted from [5]).

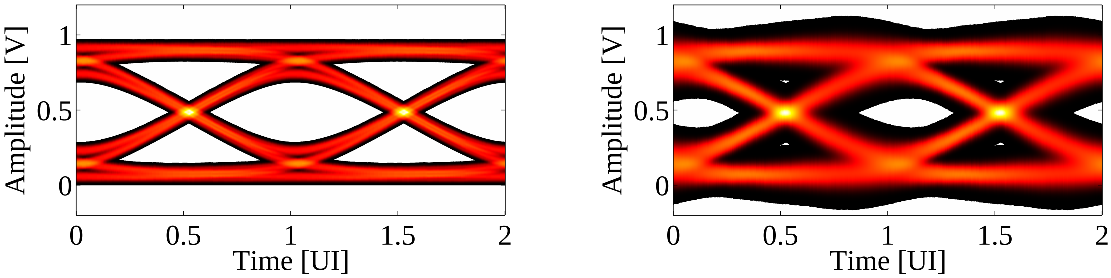

(a) (b)

Figure 8.3: Eye diagrams of a PCB interconnect for a data rate of 15 Gb/s. The eye diagram is shown (a) calculated based on the transmission properties of the interconnect only (Figure from [5]) and (b) including far-end crosstalk from 5 aggressor channels (Figure from [5]). White areas have a probability below the required bit error rate (BER), which has been chosen as 10^{-12} for the example. Otherwise, bright colors indicate high probabilities.

parameters of the interconnect itself. If necessary, the output impedance of the transmitter and the input impedance of the receiver can be included in the termination impedances. For the simplified link model, the input impedance of channel i can be calculated from the network parameter description of the complete link as

$$Z_{\mathrm{in},i}(f) = Z_{\mathrm{T}} + Z_{\mathrm{R}} \cdot \frac{1 + S_{i+L}(f)}{1 - S_{i+L}(f)}, \tag{8.1}$$

with the termination at the transmitter side Z_{T}, the termination at the receiver side Z_{R}, and the S-parameter matrix S of the link, which has been normalized to Z_{R}. The evaluation in Section 8.3 assumes $Z_\mathrm{T} = Z_\mathrm{R} = 50\,\Omega$. For a NRZ signal with voltage levels 0 and V_max and equal probabilities $p = 0.5$ for each level, the power spectral density (unit: V^2/Hz) is given in [158, ch. 11.2] as

$$P_\mathrm{XX}(f) = \frac{|\tilde{F}(f)|^2}{4T_\mathrm{b}} \left(1 + \frac{2\pi}{T_\mathrm{b}} \sum_{n=-\infty}^{\infty} \delta\left(2\pi f - \frac{2\pi n}{T_\mathrm{b}}\right)\right), \tag{8.2}$$

with the bit period T_b and the single bit Fourier transform $\tilde{F}(f)$. The upper voltage level V_max is contained in the single bit Fourier transform $\tilde{F}$, which for a trapezoidal bit shape with 10 % rise and fall time takes the form [159, ch. 12.18]

$$\tilde{F}(f) = V_\mathrm{max} \cdot \mathrm{sinc}(fT_\mathrm{b}) \cdot \mathrm{sinc}(fT_\mathrm{b}/10), \tag{8.3}$$

with the sinc function defined as $\mathrm{sinc}(x) = \sin(\pi x)/(\pi x)$. Based on the results in (8.1), (8.2), (8.3), the input power of channel i can be evaluated as

$$P_i = \int_{-\infty}^{\infty} P_\mathrm{XX}(f) \cdot \mathrm{Re}\left\{\frac{1}{Z_{\mathrm{in},i}(f)}\right\} \mathrm{d}f. \tag{8.4}$$

For the practical evaluation, the integral in (8.4) can be evaluated by numerical integration, using equidistant frequency points with $\Delta f = 100\,\mathrm{MHz}$ for the evaluation of $Z_{\mathrm{in},i}(f)$ and $\tilde{F}(f)$. Due to the simplifications made, the calculation of the total link input power from the given network parameters and input voltage swings is very fast (in the range of seconds to a few minutes) even for links consisting of several thousands of vias.

8.3 Example: Comparison of Four Design Alternatives

In this section, the described approach is applied to evaluate four link design alternatives based on two fundamental design decisions for the via arrays. The design goal is to transmit an aggregate data rate of 1 Tb/s between two surface mounted ICs over a PCB link (compare the initial high speed link example in Fig. 1.1). The general link setup for the study is shown in Fig. 8.4. Two via arrays, each consisting of 32 × 32 vias, are connected by striplines routed on different signal layers. The distance between the via arrays is 5 inch (edge to edge). In comparison to via array 1, the via arrangement in array 2 is mirrored along the vertical figure axis. Each signal via in array 1 is connected to the corresponding (mirrored) via in array 2, so that the exact stripline length depends on the via position. For simplicity, only the highlighted triangular regions are assumed to be connected. The four compared design alternatives are different in the signaling scheme - single-ended transmis-

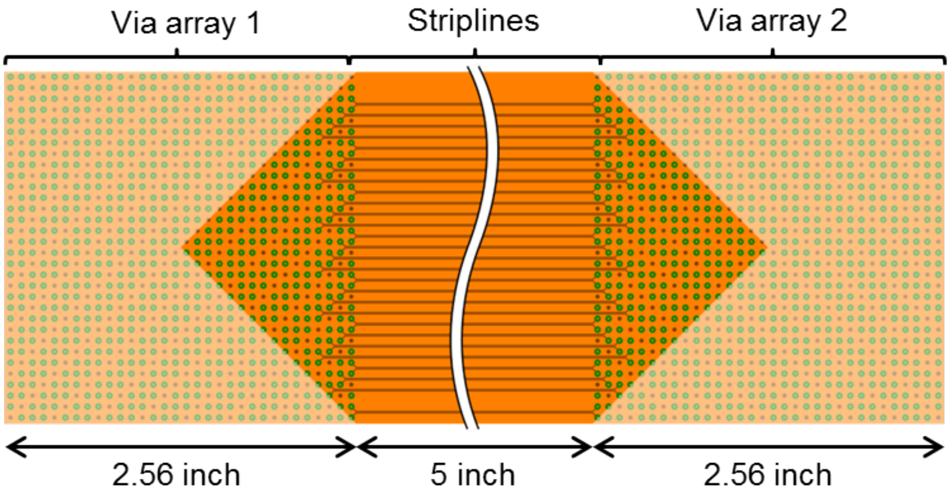

Figure 8.4: General setup for the comparison of link design alternatives (top view): two via arrays are connected over single-ended or differential striplines. The separation between the via arrays is 5 inch (edge to edge). In via array 2, the via arrangement is mirrored along the vertical figure axis in comparison to the arrangement in via array 1. The detailed setups for the individual design scenarios are depicted in Fig. 8.5 (Figure from [5]).

sion is compared to differential transmission - and in the signal-to-ground via ratio, for which values of 2:1 and 1:1 are compared. While the decisions for differential signaling and for a lower signal to ground ratio should both improve the signal integrity properties of the link, they also both reduce the number of available channels – requiring a higher single-channel data rate, which is detrimental to signal integrity. The basic question of the evaluation is how these two opposing effects impact the energy efficiency of the links as measured by the input power necessary to achieve the same aggregate data rate and the same bit error rate for all design alternatives.

The detailed setups of the four design alternatives are given in Fig. 8.5. The via arrays contain diagonals of signal, power and ground vias arranged corresponding to the respective signal to ground ratio. Depending on the design alternative, three or four rows of ground vias can be routed per signal layer. The via rows closest to the edges of the via array are routed on the highest signal layer. With increasing distance from the edges, lower routing layers are assigned. The detailed stripline dimensions for single-ended and differential signaling are shown in Fig. 8.6. The geometry and material parameters used for the test structures are given in Table 8.1, and the stackup is specified in Table 8.2. The stackup contains six signal layers in total, which are necessary for routing in the case SE21. In other cases, lower signal layers remain unused (assuming that they are necessary for other signals routed on the PCB, and not taking into account a possible reduction in layer count in the

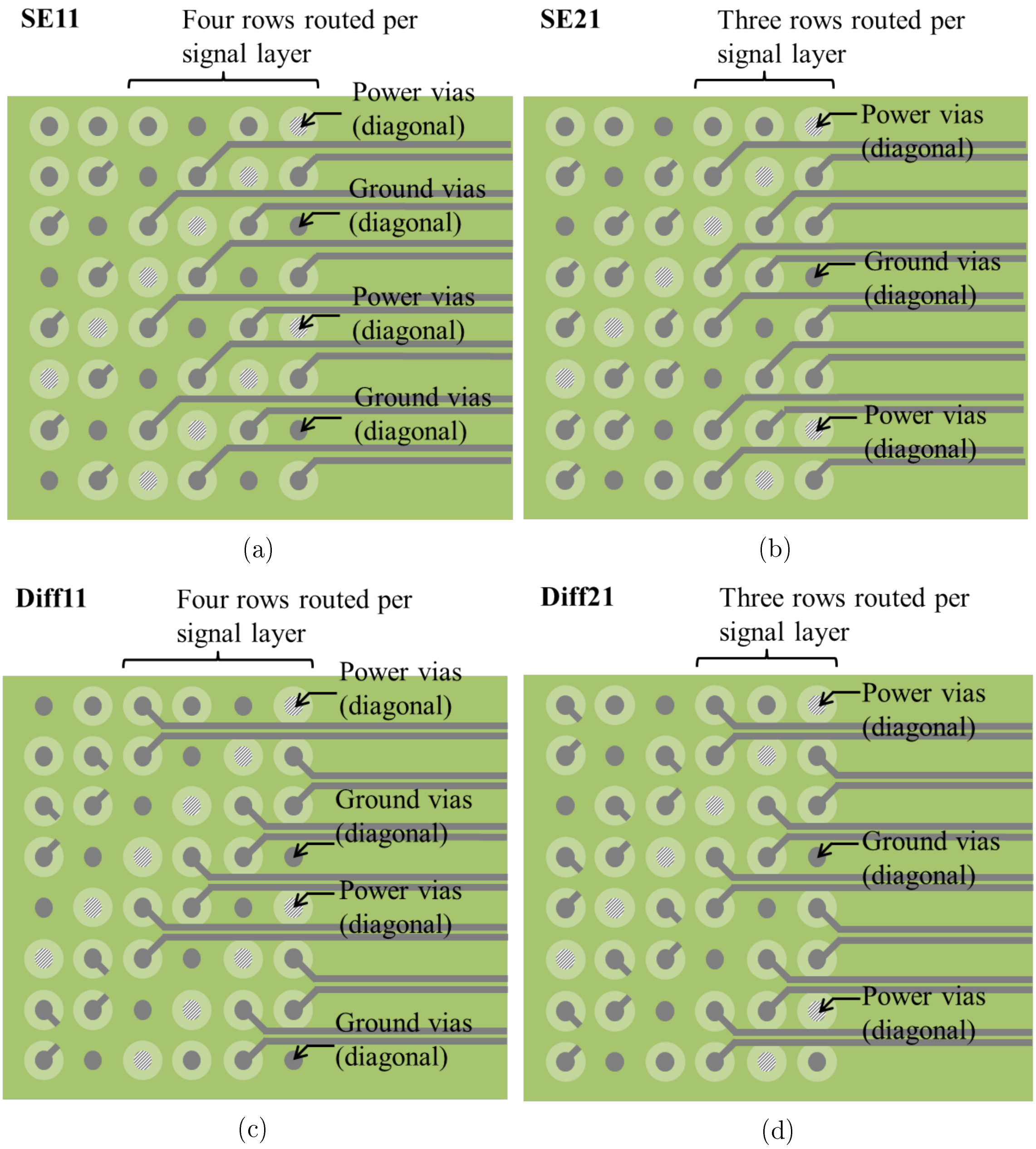

Figure 8.5: Detailed setups for the compared design alternatives (all Figures from [5]). (a) Single-ended transmission with a signal to ground ratio of 1:1 (SE11). Per signal layer, four rows of vias can be routed. (b) Single-ended transmission with a signal to ground ratio of 2:1 (SE21). Per signal layer, three rows of vias can be routed. (c) Differential transmission with a signal to ground ratio of 1:1 (Diff11). Per signal layer, four rows of vias can be routed. (d) Differential transmission with a signal to ground ratio of 2:1 (Diff21). Per signal layer, three rows of vias can be routed.

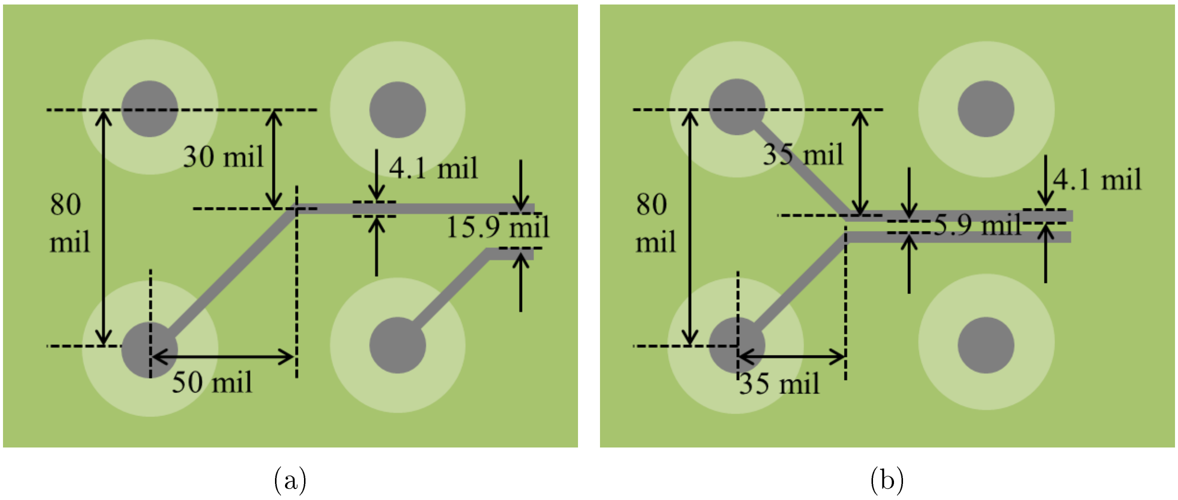

(a) (b)

Figure 8.6: Detailed stripline arrangement for single-ended and differential signaling. The drawings are not to scale. (a) Single-ended case. Two striplines are routed per routing channel between two vias (Figure from [5]). (b) Differential case. One differential stripline is routed per routing channel between two vias (Figure from [5]).

Table 8.1
Parameters of the test structures in this section (Table adapted from [5])

Geometry parameter	**Value**
Via radius r_v	5 mil
Antipad radius r_ap	15 mil
Via pitch	80 mil
Trace width	4.1 mil
Trace separation (single-ended, edge-to-edge)	15.9 mil
Trace separation (differential, edge-to-edge)	5.9 mil
Material parameter	**Value**
Copper conductivity σ_Copper	$5.8 \cdot 10^7\,\mathrm{S/m}$
Dielectric permittivity $\varepsilon_\mathrm{Diel.}$	$3.6 \cdot \varepsilon_0$
Dielectric loss tangent $\tan(\delta_\mathrm{Diel.})$	0.02

evaluation carried out here). Two power planes are contained in the stackup. However, no signals are routed in cavities with adjacent power planes, so that effects of mixed reference planes do not play a role in the analysis.

As described, the approach for a systematic evaluation first requires complete network parameter descriptions of all design alternatives. The simulation times required for an evaluation using the physics-based via model are listed in Table 8.3. Exemplary simulation results for transmission and far-end crosstalk – the relevant functions for the following time

Table 8.2
PCB stackup used for all test cases (Table adapted from [5])

Layer number	Thickness [mil]	Assignment	Layer number	Thickness [mil]	Assignment
1	2.1	Ground	19	0.7	Ground
2	7.5	Substrate	20	3.8	Substrate
3	0.7	Power	21	0.7	Signal 4
4	3.7	Substrate	22	4.4	Substrate
5	0.7	Ground	23	0.7	Ground
6	4.4	Substrate	24	3.8	Substrate
7	0.7	Signal 1	25	0.7	Signal 5
8	3.8	Substrate	26	4.4	Substrate
9	0.7	Ground	27	0.7	Ground
10	4.4	Substrate	28	3.8	Substrate
11	0.7	Signal 2	29	0.7	Signal 6
12	3.8	Substrate	30	4.4	Substrate
13	0.7	Ground	31	0.7	Ground
14	4.4	Substrate	32	3.7	Substrate
15	0.7	Signal 3	33	0.7	Power
16	3.8	Substrate	34	7.5	Substrate
17	0.7	Ground	35	2.1	Ground
18	7.5	Substrate			

Table 8.3
Simulation times for the different scenarios (Table adapted from [5])

	SE11	SE21	Diff11	Diff21
S-parameter sim. (16 cores)	19.7 h	20.5 h	19.2 h	19.7 h
Time domain sim. (8 cores)	16.0 h	20.0 h	7.5 h	10.4 h

domain evaluation – are depicted in Fig. 8.7. Results are shown for a via (or via pair for the differential cases) close to the center of the triangular sections highlighted in Fig. 8.4. The connected striplines are routed on SL2 in the cases SE11 and Diff11, and on SL3 in the cases SE11 and Diff11. It should be noted that vias at other positions in the array will show different properties due to different routing layers and different local environments, especially if they are located close to the edges of the array. Additional S-parameter plots for a vias at the edge of the array and for the reflection can be found in [5]. As described before, an advantage of proposed approach over a comparison in terms of S-parameters is that it does not compare single channels, but provides a figure of merit taking into account the impact of all channels in the link.

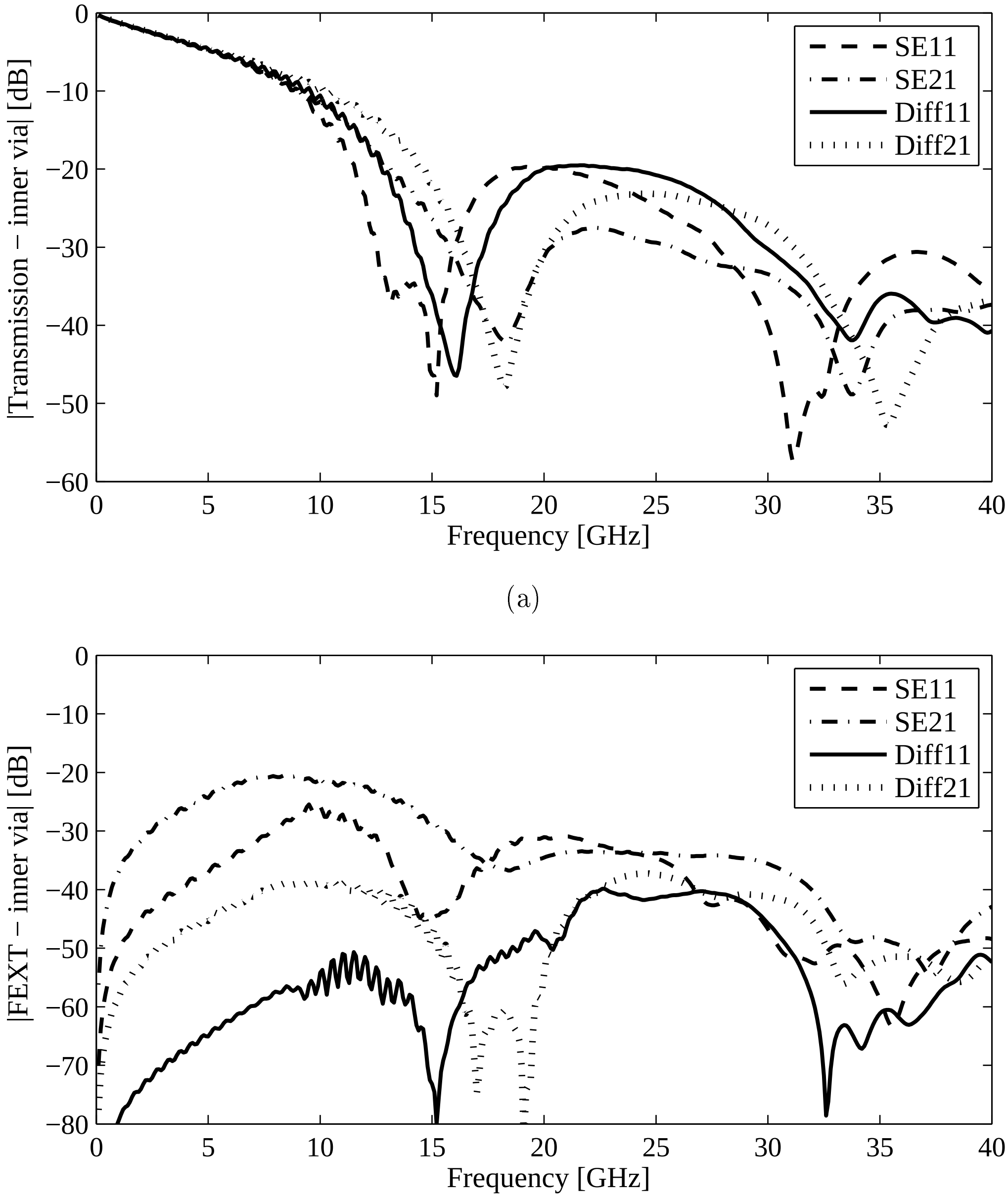

(a)

(b)

Figure 8.7: Comparison of simulated S-parameters for the different design alternatives. All results are shown for a via inside the array. (a) Results for the transmission, showing the impact of the lossy dielectric on the stripline transmission as well as the resonances caused by the via stubs (Figure from [5]). (b) Far-end crosstalk to a neighboring channel. Up to 15 GHz, differential transmission and a lower signal to ground ratio result in a lower crosstalk. About 40 dB difference can be seen between best scenario (Diff11) and worst scenario (SE21). At higher frequencies, the crosstalk behavior becomes more complex (Figure from [5]).

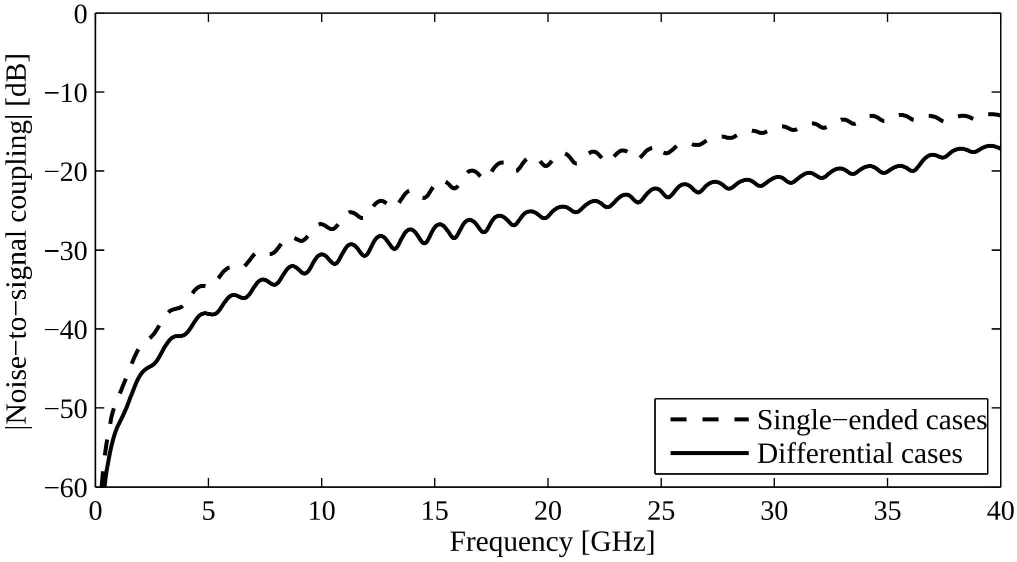

Figure 8.8: Assumed transfer function for noise coupling into signal vias. Different functions are used for single-ended and differential case based on results in [32] (Figure from [5]).

In the next step, the time domain evaluation is carried out with the input signal described in Section 8.2.3. The numbers of channels in the link and the resulting single channel data rates for the time domain evaluation are listed in Table 8.3. Simulations have been carried out for two scenarios: the first series of simulations takes into account far-end crosstalk from all channels in the link, but no external noise. The second series of simulations again takes into account the complete far-end crosstalk from all channels, but additionally includes a model to reflect a possible impact of external noise. The assumed noise model is Gaussian noise with a standard deviation of 100 mV, which is coupled into signal ports over the transfer functions shown in Fig. 8.8. The transfer functions are obtained from simulations carried out in [32], and lead to a noise coupling which is stronger in the single-ended cases than in the differential cases. In the results of the time domain evaluation in Table 8.4, the impact of the external noise can be seen in an increase of the required input voltage swing. To illustrate the outcome of the time domain analysis, the eye diagrams of the different design alternatives are shown for operation with the calculated link input power values in Fig. 8.9. The simulation times required for the time domain evaluation of the different design alternatives – for the cases with external noise – are listed in Table 8.3.

As a final evaluation step, the input power calculation described in Section 8.2.4 is carried out based on the calculated input voltage swings. The resulting values listed in Table 8.4 allow a meaningful comparison of the different design alternatives. The results show that in general, the differential transmission leads to a drastically lower value for the required input

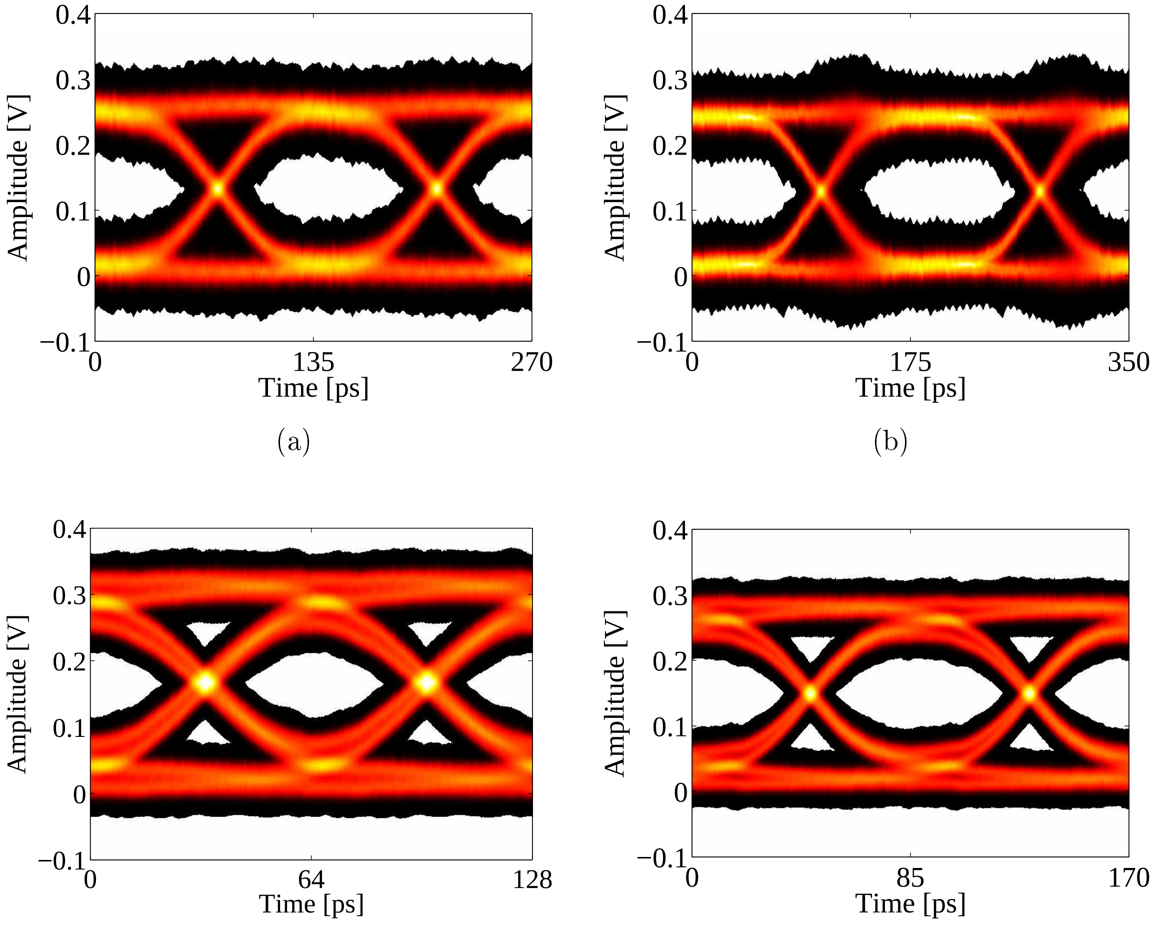

(a) (b)

(c) (d)

Figure 8.9: Eye diagrams for the four compared design alternatives. Each link is operated at the respective data rate and with the voltage swing found in the time domain analysis step, leading to a vertical eye opening of 100 mV (all Figures from [5]): (a) SE11, (b) SE21, (c) Diff11, (d) Diff21.

power - about 50 % or less of the input power calculated for the single-ended cases. While the exact values depend on the assumptions made for the implemented differential signaling scheme, the results confirm that differential signaling may be considerably more efficient for high-speed signaling in spite of the smaller number of available channels. Although the signal to ground ratio shows a smaller impact, the resulting difference in the input power requirement may be even more relevant, since it is the result of only a structural variation, without any change in signaling scheme or other assumptions. The observed difference in the required input power is about 17 % in the single-ended case and about 12 % in the differential case (without the impact of noise). Including the impact of noise, the best

Table 8.4
Comparison of the different design alternatives (Table adapted from [5])

	SE11	**SE21**	**Diff11**	**Diff21**	**Diff21 bd.**
Number of channels	135	175	64	85	85
Single ch. data rate [Gb/s]	7.41	5.71	15.63	11.76	11.76
Without external noise					
Req. voltage swing [mV]	187	181	276	227	230
Total link power [mW]	**23.4**	**28.3**	**12.4**	**10.9**	**10.8**
External noise, $\sigma = 100\,\mathrm{mV}$					
Req. voltage swing [mV]	279	260	337	299	302
Total link power [mW]	**52.3**	**58.3**	**18.5**	**19.0**	**18.6**

design alternative (lowest input power requirement) changes from Diff21 (without noise) to Diff11 (with noise). The impact of noise on the outcome of the evaluation shows the importance of a realistic noise model for practical investigations.

As an additional application of the presented approach, the impact of backdrilling the signal vias is studied for the design alternative Diff21. Vias are assumed to be backdrilled up to the next reference layer below the connected signal layer, so that the open via stub is removed almost completely. An additional network parameter calculation and additional time domain and power evaluations are carried out to determine the impact of the design change on the energy efficiency of the link. The results of the evaluation – listed under "Diff21 bd." in Table 8.4 – show that the impact of backdrilling is very small. In comparison to the case without backdrilling, the input voltage swing is even increased by a few mV. The input power requirement is slightly decreased due to changes in the input impedance values. However, it can be concluded that the impact of backdrilling on the input power requirement is smaller than expected. A detailed evaluation of the analysis results shows the reason: due to the impact of crosstalk, the worst case channel is located close to the center of the array and routed on SL5. Since a via connected to a stripline on SL5 only has a short stub, backdrilling of the stub improves the transmission properties of the channel only at high frequencies, which are not relevant for the studied data rate.

8.4 Summary and Discussion

The approach presented in this chapter allows a systematic, energy aware comparison of different design alternatives. The application to four different link design alternatives shows that under the assumptions made for the evaluation, differential transmission is more energy efficient than single-ended transmission. Furthermore, the choice of an appropriate signal to ground ratio can considerably reduce the input power required for operation of the link. It should be noted that the specific input power values resulting from the presented evaluation depend on many details of the compared structures (such as via geometries, ground via placement and assignment of striplines to different routing layers) as well as on assumptions made for the employed signaling scheme and the external noise model. More important than the specific results is the general conclusion that the presented approach can be applied to compare different design alternatives in a systematic way, showing the impact of design changes. In principle, changes ranging from small geometric variations (e.g. a variation of the antipad size) over global design decisions (such as the variation of the signal to ground ratio presented here) to non-geometric changes such as the signaling scheme can be evaluated.

For future work, several extensions of the presented evaluation are desirable. Important directions for further investigations are the inclusion of more accurate transmitter and receiver models, the inclusion of packages and connectors in the network parameter description of the link, and the consideration of equalization schemes in the proposed approach. While all these extensions are in principle well suited for the presented approach, their actual inclusion will require a considerable implementation effort. At the same time, the application example in this chapter covered only two design decisions. Many more applications of the presented approach are thinkable. Finally, the evaluation of a design scenario with several thousand vias currently still takes more than a day (see calculation times listed in this chapter). The applicability of the presented approach will therefore benefit from further accelerations of both the S-parameter calculation and the time domain evaluation.

9 Conclusion and Outlook

This thesis has studied the application of physics-based via models for an efficient modeling of large via arrays on PCBs. Three main aspects have been addressed: the study and improvement of the modeling accuracy, the study and improvement of the modeling efficiency, and the application of the model in a systematic evaluation of via array design alternatives for high speed links.

With regard to the modeling accuracy, the application of an improved local field model is proposed as a suitable way to improve the model accuracy for the simulation of via arrays, especially at frequencies above 20 GHz. At the same time, the via pitch is found to constitute the main limitation for the application of the physics-based model. Accurate modeling results can only be expected for pitch sizes of 60 mil or larger. For smaller pitch sizes, methods which take into account anisotropic modes have to be applied. An overview of the applicability of different modeling methods depending on via density and upper frequency limit is displayed in Fig. 9.1, including the impact of the improvements suggested in this work.

Different impacts have been studied with regard to the model efficiency, and an efficient algorithm for the evaluation of the physics-based via model has been proposed. Together with additional optimizations, the efficient algorithm leads to a total acceleration factor of about 26 in comparison to a previous implementation of the physics-based via model. This makes it possible to study very large via arrays in multilayer PCBs in a reasonable time —about 40 minutes per frequency point for the simulation of 10,000 vias with the parallel code. For smaller via arrays in multilayer PCBs containing a few 100 vias, the acceleration allows to actually carry out fast design explorations on a standard PC.

The presented approach for a systematic design evaluation integrates the advantages of the efficient physics-based via model in a larger concept. With the approach, a comparison of design alternatives becomes possible that takes into account the impact of the design changes on the complete system, fully including changes of transmission and crosstalk behavior for all channels in a high speed link. Furthermore, the evaluation in terms of link input power allows a quantitative comparison of design alternatives that takes into account both signal integrity and energy efficiency.

As described in the thesis, several possible directions for further work exist. With regard to the modeling accuracy, an inclusion of anisotropic modes at least for the propagating field

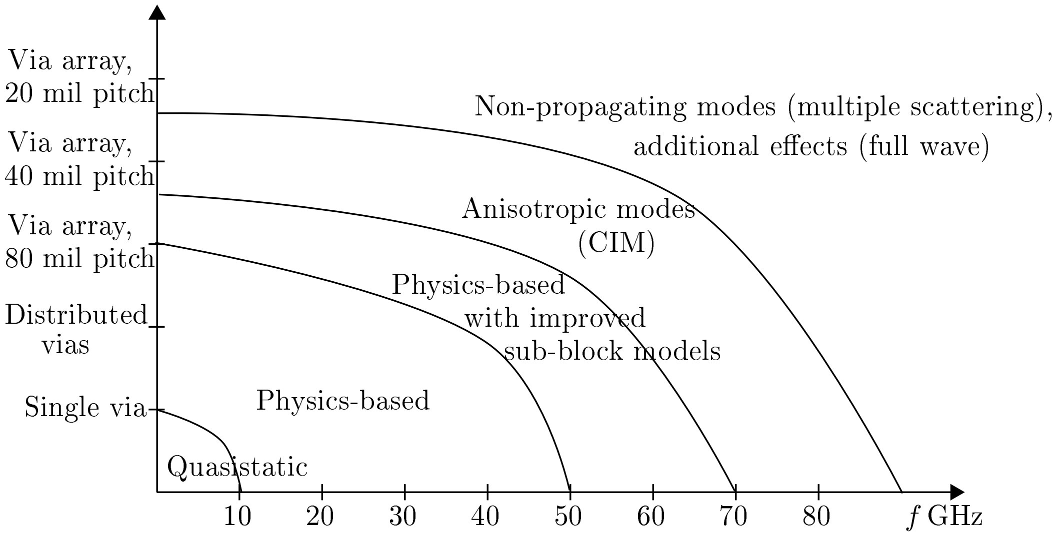

Figure 9.1: Plot illustrating up to which frequency accurate modeling results can be achieved with different modeling approaches. The shown curves represent an estimation based on the investigations that have been carried out rather than strict limits.

model is necessary to simulate via arrays with pitch sizes below 60 mil. A further increase of the modeling efficiency is desirable to further reduce calculation times and memory requirements. The final goal would be to allow the fast evaluation of large via arrays containing 1000 or more vias on a single PC. As described, the application of the adaptive cross approximation for the setup of the propagating field model and of H-matrices for further calculation steps as described in Chapter 5 may provide a step into this direction.

Finally, the presented approach for a systematic design comparison can serve as a basis for several further investigations. As described in Chapter 8, the presented approach may be extended in several ways, e.g. by an inclusion of the effects of equalization on the energy efficiency of links. Furthermore, it can be applied to study a large range of problems beyond the design study carried out in this thesis. In the context of high speed links on PCBs, many design decisions exist that constitute a trade-off between different advantageous and disadvantageous effects. The range of these design decisions does not only include changes of geometric parameters, but also high-level decisions such as the change to a multi-level signaling scheme. A fair assessment of these design changes is only possible if their impact on the complete system is taken into account.

A The Multiple Scattering Approach

In this Appendix, a detailed description of a multiple scattering approach is given based on [81]. The described approach is applicable to standard cases with circular via and antipad geometries, a homogeneous dielectric substrate and infinite reference planes. The formulation is sufficient for all multiple scattering simulations carried out in the context of this thesis. For a description of multiple scattering approaches for more complex scenarios, the reader is referred to the literature listed in Section 2.2.3.

For the application to via modeling problems, the Foldy-Lax equations can be formulated in terms of radial waveguide modes. As described in Section 3.1.1, vertical via currents excite only transverse magnetic TM_{ln}^{z} modes, where l gives the mode order with respect to variations in z-direction and n gives the mode order with respect to φ-direction. In [81], the system of linear equations is set up in terms of exciting field coefficients at the via locations. The exciting field coefficient $w_{ln}^{TM(q)}$ of mode TM_{ln}^{z} at via q is the sum of the incident field at via q represented by the coefficient $a_{ln}^{TM(q)}$ and the scattered fields from all other vias, as expressed in the following equation [81]:

$$w_{ln}^{TM(q)} = a_{ln}^{TM(q)} + \sum_{\substack{p=1 \\ p\neq q}}^{N} \sum_{m=-\infty}^{\infty} H_{n-m}^{(2)}\left(k_{rl}|\vec{\rho_p} - \vec{\rho_q}|\right) \cdot \mathrm{e}^{\mathrm{j}(n-m)\cdot\arg(\vec{\rho_p}-\vec{\rho_q})} T_{lm}^{(p)} w_{lm}^{TM(p)}. \tag{A.1}$$

In (A.1), N is the number of vias in the system, $\vec{\rho_p}$ and $\vec{\rho_q}$ are the positions of vias q and p, k_{rl} is the radial wavenumber as defined in (3.2), and $w_{lm}^{TM(p)}$ is the exciting field coefficient of mode TM_{lm}^{z} at via p. For typical PCB dimensions, the radial wavenumber is imaginary for $l \geq 1$, since the corresponding modes are in cutoff. For the cutoff modes, the negative branch of the square root in the radial wave number has to be chosen in the calculation. The T-matrix coefficient [81]

$$T_{lm}^{(p)} = -\frac{J_m(k_{rl} r_v)}{H_m^{(2)}(k_{\mathrm{rl}} r_{\mathrm{v}})} \tag{A.2}$$

describes the relation between incident field coefficient and scattered field coefficient of the TM_{lm}^{z} mode at the via p with via radius r_{v} (assuming a PEC via barrel).

Like in the physics-based via model, the multiple scattering approach assumes the coaxial TEM mode in the antipad regions as the external excitation to the cavity. For the solution of the multiple scattering problem, the coaxial TEM mode is represented by a magnetic frill current on the interface between antipad region and cavity. The incident field coefficients can then be obtained by solving a 2D surface integral over the interface area. Assuming equal via radii r_v and antipad radii r_ap for all vias, the resulting incident field coefficients for an excitation at the upper via ports are given as [81]

$$\begin{aligned} a_{ln}^{TM(q)} = & \frac{\mathrm{j}k}{2h}\frac{(-1)^{n+l}}{k_{rl}^2} f_l \frac{2\pi V_{qu}}{\ln(r_\mathrm{ap}/r_\mathrm{v})}\delta_{n0}\left[H_0^{(2)}(k_{rl}r_\mathrm{ap}) - H_0^{(2)}(k_{rl}r_\mathrm{v})\right] \\ & + \sum_{p\neq q}^{N} \frac{\mathrm{j}k}{2h}\frac{(-1)^{n+l}}{k_{rl}^2} f_l H_n^{(2)}\left(k_{rl}|\vec{\rho}_q - \vec{\rho}_p|\right) \mathrm{e}^{\mathrm{j}n\cdot\arg(\vec{\rho}_q - \vec{\rho}_p)} \\ & \cdot \left[\frac{2\pi V_{pu}}{\ln(r_\mathrm{ap}/r_\mathrm{v})}\left[J_0(k_{rl}r_\mathrm{ap}) - J_0(k_{rl}r_\mathrm{v})\right]\right], \end{aligned} \tag{A.3}$$

where $f_l = 1/2$ for $l = 0$ and $f_l = 1$ else, h is the thickness of the dielectric substrate, and V_{qu} and V_{pu} are the upper excitation voltages at via q and via p, respectively. Due to symmetry, the calculation has to be carried out only for excitations at upper via ports, as described in more detail at a later point. The Kronecker delta δ_{n0} becomes zero for all anisotropic modes ($n \geq 0$). It represents the fact that the assumed isotropic external excitation, when applied to via q, leads to only isotropic modes in the incident field at via q. With the incident field coefficients known, the Foldy-Lax equations can be solved for the exciting field coefficients. It can be seen in (A.1) that modes with different mode orders l are decoupled, so that a separate system of linear equations can be set up for each l. For a given l, however, a coupling between all modes with different mode orders m (representing anisotropic modes with different azimuthal variation) exists, as described by the second summation in (A.1). For the numerical evaluation, only a finite number of modes can be taken into account. An evaluation of N vias inside a PCB cavity for $l = 0 \ldots L$ and $m = -M \ldots 0 \ldots M$ requires the evaluation of $L + 1$ systems of $N \cdot (2M + 1)$ linear equations. For each l, the system of linear equations takes the form

$$\overline{\overline{F}}_l \overline{w}_l = \overline{a}_l, \tag{A.4}$$

with the vector $\overline{w}_l$ containing the exciting field coefficients for all vias and modes from $-M$ to M, the vector $\overline{a}_l$ containing the corresponding incident field coefficients for the given external excitation, and the matrix $\overline{\overline{F}}_l$ providing the relation described by (A.1).

To calculate the entry Y_{ij} of the Y-parameter matrix describing the cavity, the current at via port i has to be calculated for an excitation voltage at via port j (for the numerical evaluation, an excitation voltage of 1 V can be chosen). For the following considerations, it is assumed that the ports i and j both are upper via ports, with port i being located at via p. To obtain the via current, first (A.4) has to be solved for the exciting field coefficients $\overline{w}_l$ in case of an excitation voltage at port j (the excitation voltage is represented by the corresponding incident field vector $\overline{a}_l$). In total, $L+1$ systems of linear equations have to be solved. The via current at the upper via port i can then be calculated from the exciting field coefficients as [81]

$$I^{(p)\mathrm{uu}} = \sum_{l=0}^{L} w_{l0}^{TM(p)} \frac{4}{\eta H_0^{(2)}(k_{rl} r_{\mathrm{v}})} (-1)^l, \tag{A.5}$$

where the index uu indicates that the current at an upper via port due to an excitation voltage at an upper via port is calculated. It can be seen in (A.5) that only the isotropic modes contributes to the via current, since the integration of the surface current density over the the via barrel circumference, which is employed for the current calculation in [81], leads to zero for all anisotropic modes. By evaluating all n via currents at the upper ports for each of the N excitation voltages at the upper ports, the admittance matrix $\overline{\overline{Y}}^{\mathrm{uu}}$ can be set up which relates upper currents and voltages.

If the port i is located at the bottom of via p, the via current due to an excitation at the upper via port j can be calculated as [81]

$$I^{(p)\mathrm{bu}} = \sum_{l=0}^{L} w_{l0}^{TM(p)} \frac{4}{\eta H_0^{(2)}(k_{rl} r_{\mathrm{v}})}. \tag{A.6}$$

This allows to set up the admittance matrix $\overline{\overline{Y}}^{\mathrm{bu}}$, which relates bottom currents to upper voltages. Due to the symmetry of the system, an evaluation for excitation voltages at the lower via ports is not necessary. The Y-parameter matrix of the complete system can be obtained by assembling the two calculated submatrices as [81]

$$\overline{\overline{Y}} = \begin{bmatrix} \overline{\overline{Y}}^{\mathrm{uu}} & -\overline{\overline{Y}}^{\mathrm{bu}} \\ -\overline{\overline{Y}}^{\mathrm{bu}} & \overline{\overline{Y}}^{\mathrm{uu}} \end{bmatrix}. \tag{A.7}$$

The minus signs in (A.7) result from the current and voltage definitions in [81]. It is interesting to note the difference between (A.7) and the expanded parallel plate admittance in (3.10). As shown by the investigations in Section 4.2.2, (A.7) provides a more accurate solution for cases where via-coupling provided by non-propagating modes exists.

It shall be mentioned that the evaluation of the different entries of the Y-parameter matrix can be nicely summarized using matrix notation. For this purpose, the incident field vector is written as

$$\overline{a}_l = \overline{\overline{E}}_l \overline{V}_u, \tag{A.8}$$

with the vector $\overline{V}_u$ containing the excitation voltages at the upper ports and the matrix $\overline{\overline{E}}_l$ providing the relation described in (A.3). As previously described, (A.4) has to be solved for N excitation voltage vectors to calculate the Y-parameter matrix of the system. Together, these voltage vectors form the identity matrix $\overline{\overline{I}}$, so that the solution to (A.4) can be written as [81]

$$\overline{\overline{P}}_l = \overline{\overline{F}}_l^{-1} \overline{\overline{E}}_l \overline{\overline{I}} = \overline{\overline{F}}_l^{-1} \overline{\overline{E}}_l. \tag{A.9}$$

The exciting field coefficient matrix $\overline{\overline{P}}_l$ can be used to calculate the Y-parameter matrices $\overline{\overline{Y}}^{\mathrm{uu}}$ and $\overline{\overline{Y}}^{\mathrm{bu}}$ as [81]

$$\overline{\overline{Y}}^{\mathrm{uu}} = \sum_{l=0}^{L} B_l \overline{\overline{P}}_l \tag{A.10}$$

and

$$\overline{\overline{Y}}^{\mathrm{bu}} = \sum_{l=0}^{L} D_l \overline{\overline{P}}_l, \tag{A.11}$$

with B_l and D_l defined correspondingly to (A.5) and (A.6) as [81]

$$B_l = \frac{4}{\eta H_0^{(2)}(k_{rl} r_{\mathrm{v}})} (-1)^l \tag{A.12}$$

and

$$D_l = \frac{4}{\eta H_0^{(2)}(k_{rl} r_{\mathrm{v}})}. \tag{A.13}$$

B Formulas for the Williamson Model

In this appendix, the detailed formulas for the elements of the local field model according to Williamson [73] are provided. The formulas refer to the equivalent circuit in Fig. 3.3(a) of this thesis, where the overall topology of the model as well as the labeling of the individual elements are shown. All formulas are given as presented in [73], with adjustments to the nomenclature used in this thesis.

As described in Section 3.2.2, the elements B_a and B_c in the Williamson model correspond to the via barrel-to-plane capacitances that have been used as a simpler local field model without any further elements for example in [59]. Their values are given by

$$B_\mathrm{a} = B_\mathrm{c} = \frac{2\pi}{\eta \ln(r_\mathrm{ap}/r_\mathrm{v})} \left(\frac{1}{\sin(kh)} - \cot(kh) \right) + 4 \sum_{l=1,3,5,\ldots}^{\infty} D_l^\mathrm{c}. \tag{B.1}$$

The summation terms D_l^c in (B.1) are defined as

$$\begin{aligned} D_l^\mathrm{c} = & \frac{2\pi}{\eta k h \ln^2(r_\mathrm{ap}/r_\mathrm{v})} \frac{1}{q_l^2} \frac{K_0(q_l k r_\mathrm{ap})}{K_0(q_l k r_\mathrm{v})} \\ & \cdot \left(I_0(q_l k r_\mathrm{v}) K_0(q_l k r_\mathrm{ap}) - I_0(q_l k r_\mathrm{ap}) K_0(q_l k r_\mathrm{v}) \right), \end{aligned} \tag{B.2}$$

where I_0 is the modified Bessel function of the first kind and order zero, and K_0 is the modified Bessel function of the second kind and order zero. In comparison to the via barrel-to-plane capacitance given in (3.7), the calculation in (B.1) and (B.2) uses the normalized quantity q_l instead of the radial wavenumber k_{rl} defined in (3.2), with

$$q_l = \sqrt{\left(\frac{l\pi}{kh} \right)^2 - 1} = \sqrt{(-1) \left(k - \left(\frac{l\pi}{h} \right)^2 \right)} / k = \mathrm{j} \frac{k_{rl}}{k}. \tag{B.3}$$

As shown in Fig. 3.4(a), the behavior of the elements B_a and B_c is essentially the same as that of the via barrel-to-plane capacitances calculated according to (3.7), with some deviation in the magnitude that increases over frequency. In comparison to the convergence behavior of the via barrel-to-plane capacitance depicted in Fig. 3.4(b), the elements B_a and B_c show a much faster convergence, which is due to the contribution of the constant term in (B.1).

In comparison to the simpler local field model that is based on the via barrel-to-plane capacitances only, the Williamson model contains three additional elements: the admittances B_b and B_3 and an ideal transformer with transformer ratio R. The values of these elements are calculated as

$$B_b = -\frac{2\pi}{\eta \ln(r_\mathrm{ap}/r_\mathrm{v})} \frac{1}{\sin(kh)} + 2 \sum_{m=1}^{\infty} (-1)^l \, D_l^c, \tag{B.4}$$

$$B_3 = \frac{2\pi r_\mathrm{v}}{\eta h} \frac{J_1(kr_\mathrm{v})Y_0(kr_\mathrm{ap}) - J_0(kr_\mathrm{ap})Y_1(kr_\mathrm{v})}{J_0(kr_\mathrm{v})Y_0(kr_\mathrm{ap}) - J_0(kr_\mathrm{ap})Y_0(kr_\mathrm{v})}, \tag{B.5}$$

and

$$R = \frac{2}{\pi} \frac{\ln(r_\mathrm{ap}/r_\mathrm{v})}{J_0(kr_\mathrm{v})Y_0(kr_\mathrm{ap}) - J_0(kr_\mathrm{ap})Y_0(kr_\mathrm{v})}. \tag{B.6}$$

The frequency dependent values of these additional elements and their impact in terms of a modification of the parallel-plate impedance Z^pp are illustrated in Fig. 3.5 of this thesis for an example with typical PCB geometry and material parameters.

C Additional Simulation Results

In this appendix, additional comparisons of simulation results are displayed to support the argumentation with regard to the accuracy of the physics-based via model for the simulation of via arrays in multilayer PCBs in Section 4.4. Unless otherwise indicated, all simulations have been carried out for the 8×8 via array with the via arrangement and port definitions shown in Fig. 4.10(a) and the stackup in Fig. 4.15.

The figures show a phase plot of the transmission between via ports 2 and 5 (Fig. C.1) to supplement the magnitude plots in Section 4.4.1, and additional crosstalk plots for directly adjacent vias (Fig. C.2) and vias in a larger distance from each other (Fig. C.3). Plots illustrating the impact of the coaxial field model on the simulated phase for the transmission through a via are shown for different cumulated thicknesses of the reference planes in Fig. C.4. To further illustrate the impact of the via pitch on the modeling accuracy as studied in Section 4.4.3, plots for the crosstalk are compared for different pitch sizes in Fig. C.5, and plots of the transmission are shown for further pitch sizes in Fig. C.6.

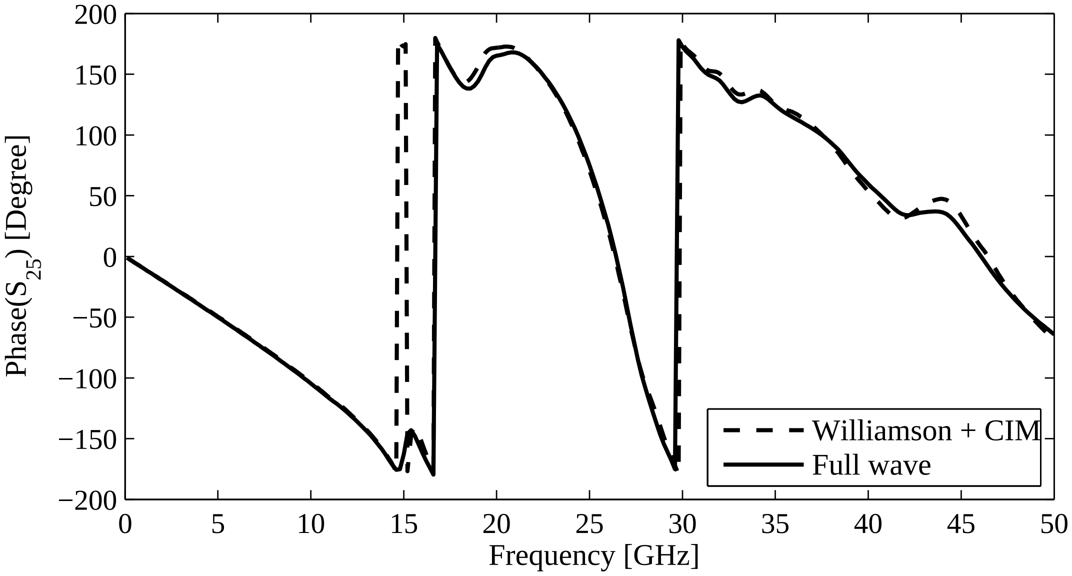

Figure C.1: Phase of the transmission between via ports 2 and 5 for the multilayer stackup. A good agreement between physics-based via model and full-wave result can be observed over the entire frequency range up to 50 GHz. The apparent large deviation around 15 GHz results from a small actual deviation and the phase wrapping applied for the plot.

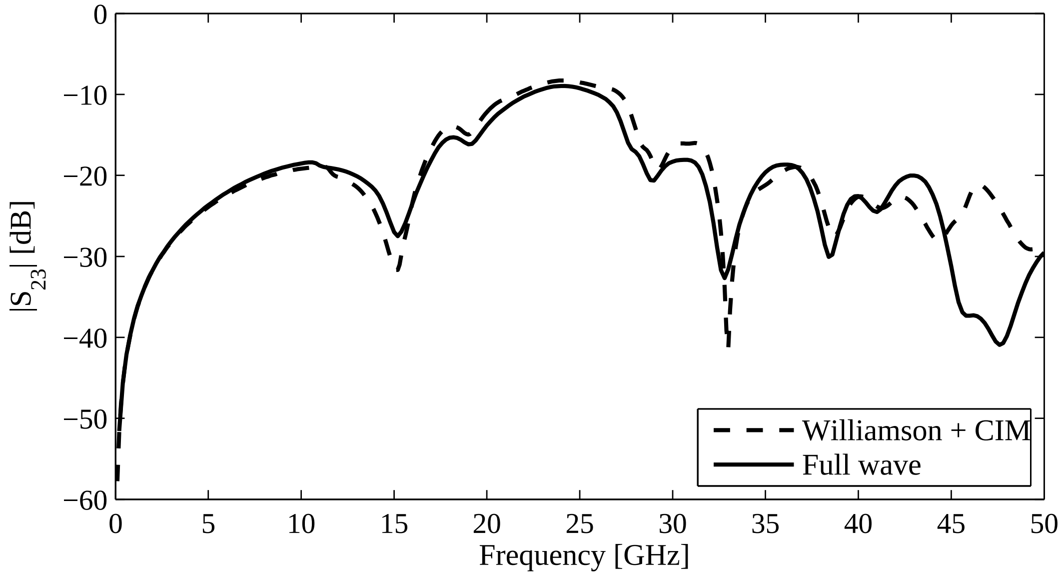

(a)

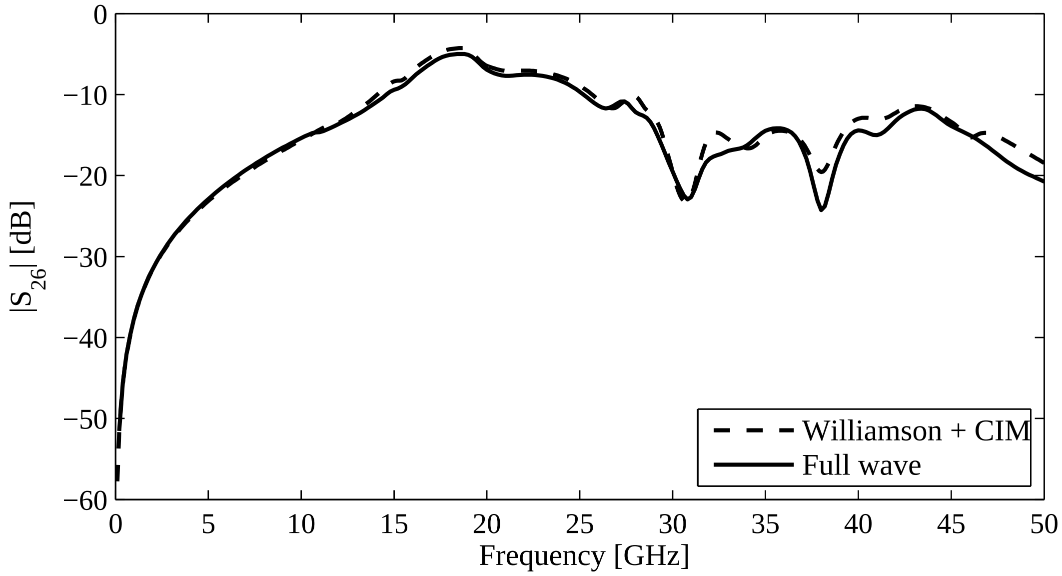

(b)

Figure C.2: Comparison between results obtained with the improved physics-based via model and a full-wave solution for the crosstalk between two directly adjacent vias in the multilayer stackup. (a) Near-end crosstalk between via ports 2 and 3 (Figure adapted from [7]). (b) Far-end crosstalk between via ports 2 and 6. Both near- and far-end crosstalk show a good agreement between physics-based model and full-wave result, with some larger deviations in the near-end crosstalk for frequencies above 40 GHz (Figure adapted from [7]).

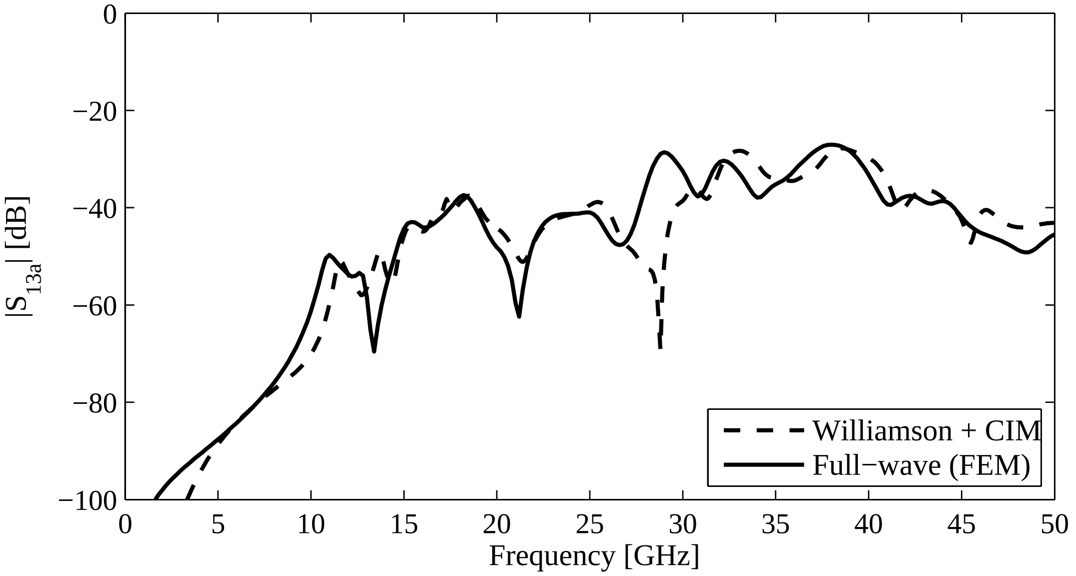

(a)

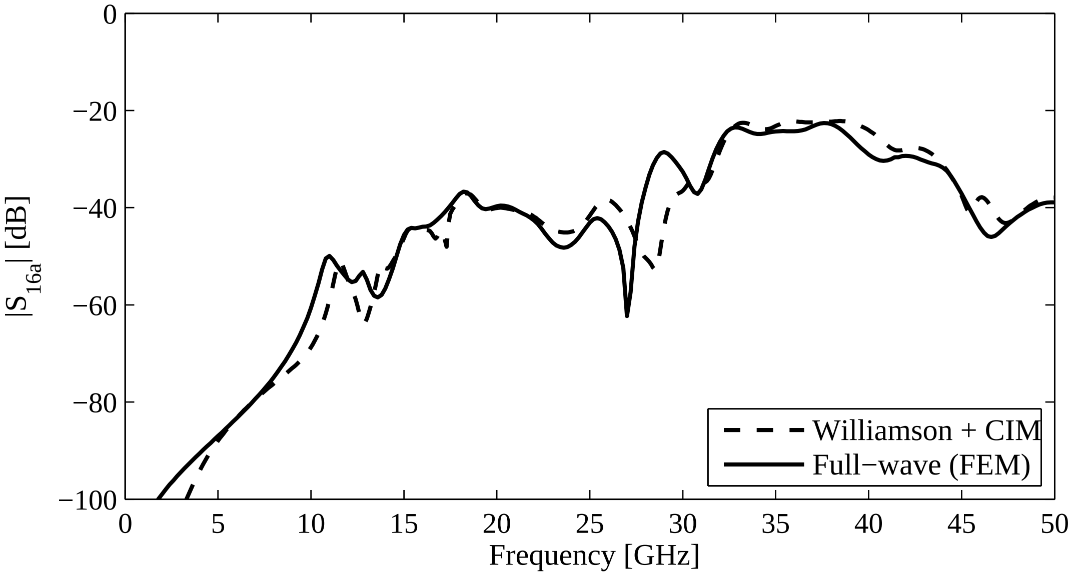

(b)

Figure C.3: Comparison between results obtained with the improved physics-based via model and a full-wave solution for two vias in a larger distance from each other in the multilayer stackup. (a) Near-end crosstalk between via ports 1 and 3a. (b) Far-end crosstalk between via ports 1 and 6a. In comparison to the agreement observed for vias with a smaller separation, some larger deviations can be observed already at lower frequencies. Nevertheless, the physics-based model still provides a good overall approximation of the full-wave result, especially in face of the lower overall crosstalk level.

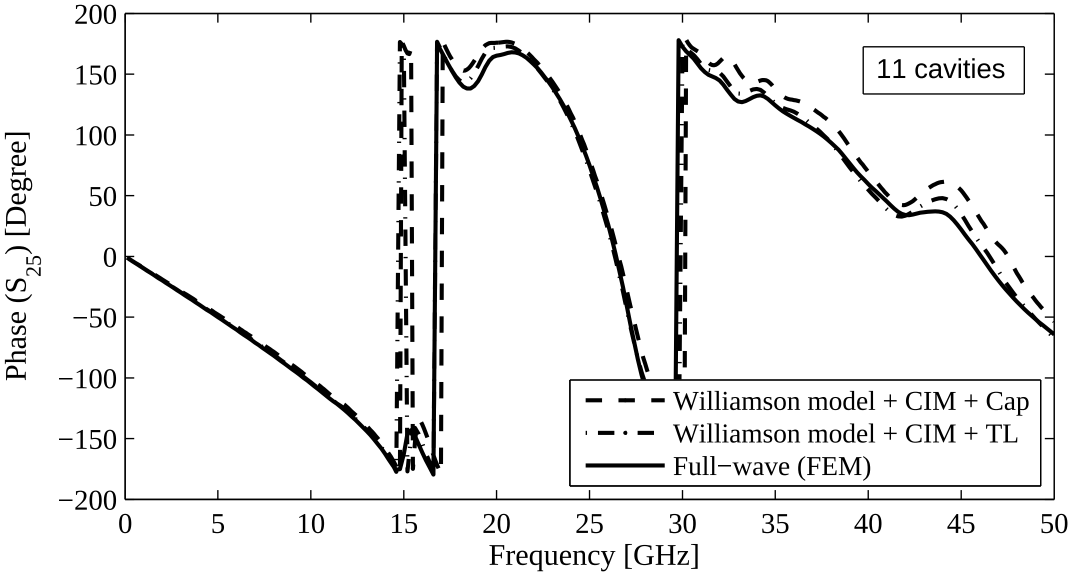

(a)

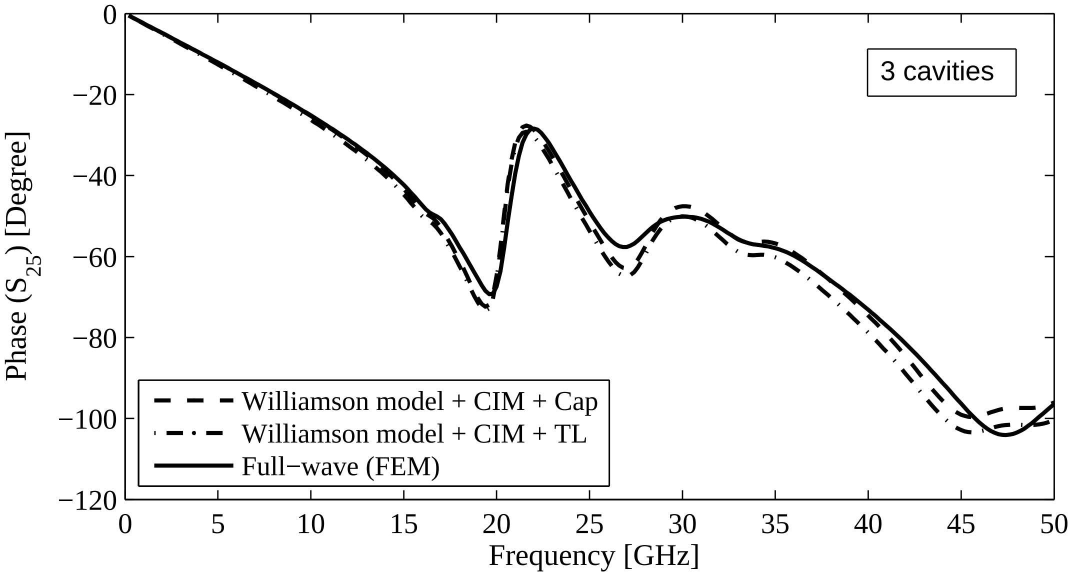

(b)

Figure C.4: Impact of the coaxial field model on the phase of the transmission between via ports 2 and 5. (a) Result for the full stackup with 11 cavities as defined in Fig. 4.15. Above 30 GHz, a deviation of about 15° can be observed if the capacitance model is used instead of the TL model for the coaxial field region. (b) Result with the stackup reduced to the 3 center cavities of the original 11 cavity stackup. Here, the use of the capacitance model instead of the TL model leads to a deviation of less than 5° due to the reduced cumulated thickness of the reference layers. The capacitance model is even closer to the full-wave result at higher frequencies, however, this observation is most probably a coincidence related to the small overall impact of the coaxial field model in this scenario.

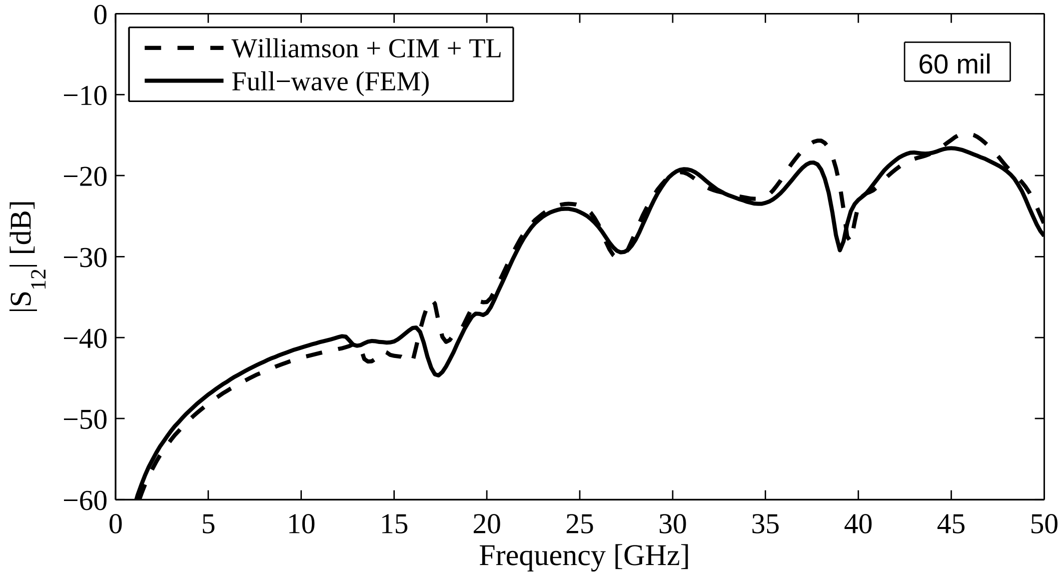

(a)

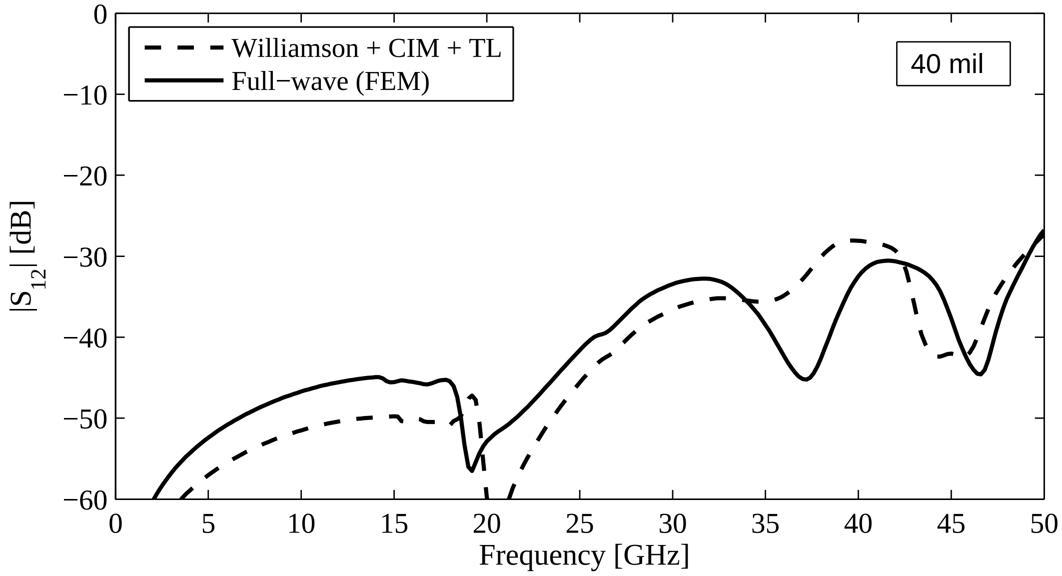

(b)

Figure C.5: Additional plots of the near-end crosstalk between via ports 1 and 2 for the multilayer stackup and smaller pitch sizes. (a) For 60 mil via pitch, the physics-based via model still shows a good agreement to the full-wave result. (b) For 40 mil via pitch, a much larger deviation between physics-based via model and full-wave result can be observed. In particular, a considerable deviation exists already at low frequencies - similar to the observation for the near-end crosstalk in the single cavity scenario in Fig. 4.13(b). All in all, the observed accuracies for the crosstalk are similar to the accuracies observed for the transmission in Fig. 4.19 for the respective pitch sizes.

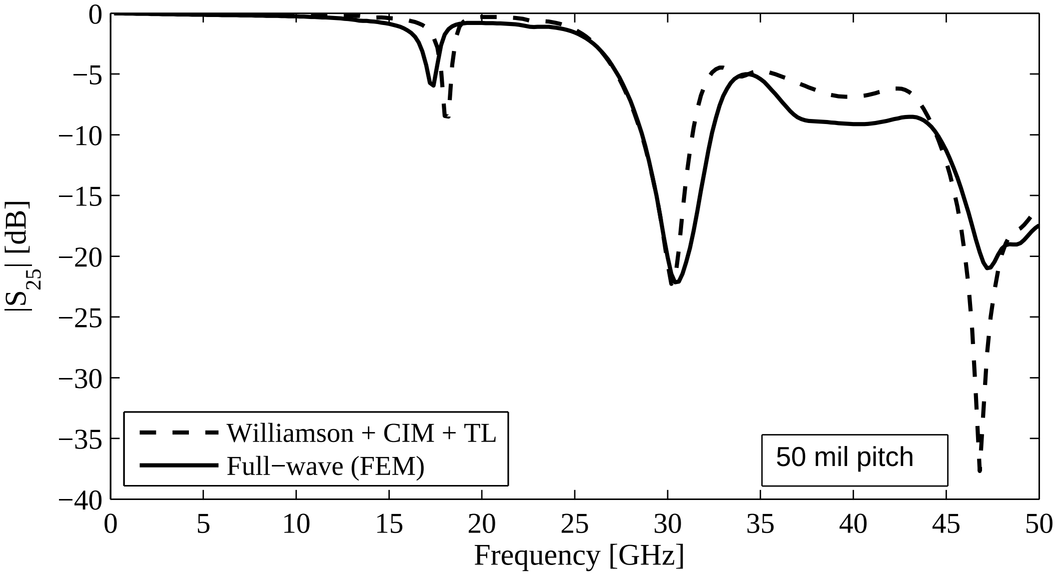

(a)

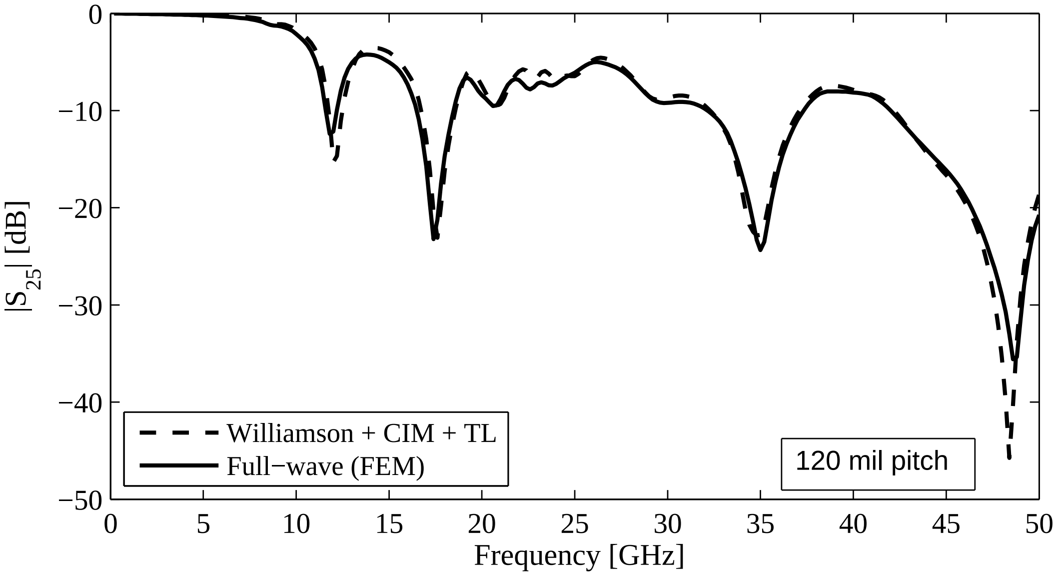

(b)

Figure C.6: Plots showing the transmission between via ports 2 and 5 for the multilayer stackup for additional pitch sizes. (a) For 50 mil via pitch, the physics-based via model still provides a fair agreement to the full-wave result, although increasing deviations can be observed in comparison to the results for 60 mil via pitch. (b) For 120 mil via pitch, a good agreement between physics-based via model and full-wave result exists. The results illustrate that a further increase of the via pitch beyond 80 mil does not lead to accuracy problems.

D Modeling Accuracy for Power Vias

In this appendix, the accuracy of the physics-based via model for the simulation of structures containing power vias is briefly discussed. For this purpose, results obtained with the physics-based via model are compared to full-wave (FEM) results for the test structure in Fig. D.1. The test structure is a 7×6 via array with a regular pattern of signal, power and ground vias. The via arrangement and detailed geometry and material parameters are given in Fig. D.1(a). The stackup, which contains two power planes, is shown in Fig. D.1(b).

Simulation results are shown for the vias indicated in Fig. D.1(a), with ports placed at the upper via ends. The lower via ends remain open. With regard to the reflection at the via port, the physics-based model shows a reduced accuracy for the power via for 80 mil pitch (Fig. D.2) and – even more clearly – 40 mil pitch (Fig. D.3). Nevertheless, accurate results are obtained for the coupling between signal vias (Fig. D.4(a)) and even for the coupling between signal and power vias (Fig. D.4(b)) in case of 80 mil pitch, so that the results of the studies carried out in this thesis are not impaired by the presence of power vias.

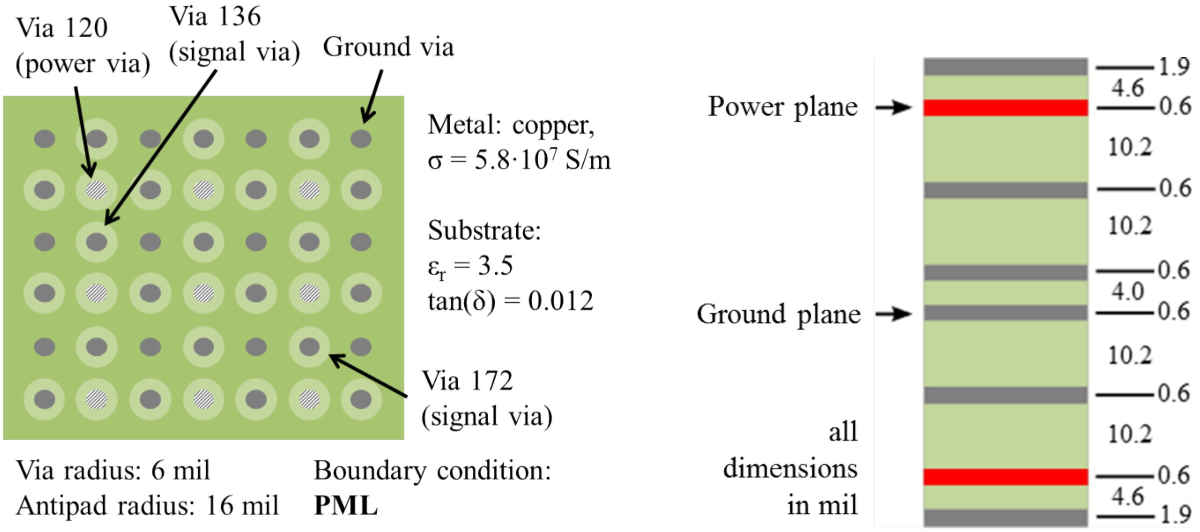

(a) (b)

Figure D.1: Via array structure for the investigation of structures containing power vias. (a) Top view showing the via arrangement and the geometry and material parameters. Simulations with 80 mil and 40 mil via pitch have been carried out, and infinite reference planes have been assumed for the simulations. (b) Stackup of the test structure with two power planes.

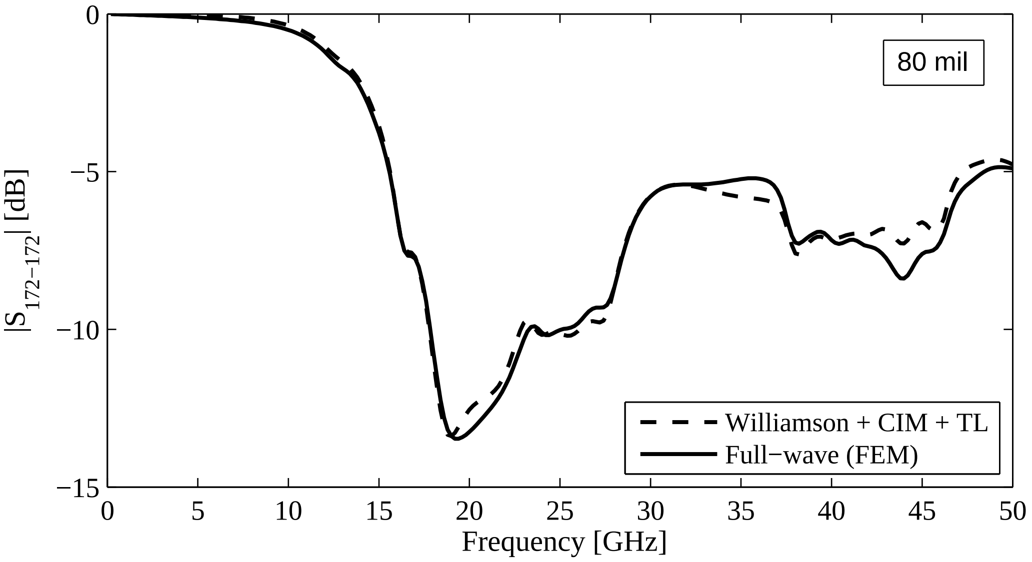

(a)

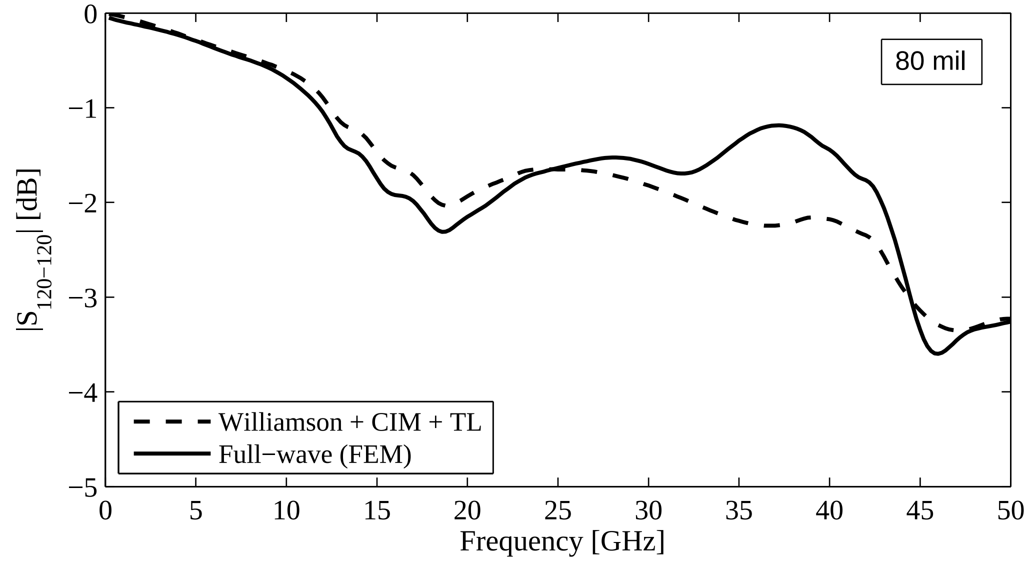

(b)

Figure D.2: Reflections at the upper via ports in case of 80 mil pitch. (a) Reflection at a signal via port (port 172). A good general agreement between physics-based via model and full-wave result can be observed. (b) Reflection at a power via (port 120). In comparison to the results for the signal via, it seems that the physics-based via model captures the characteristic features of the reflection less accurately for the power via.

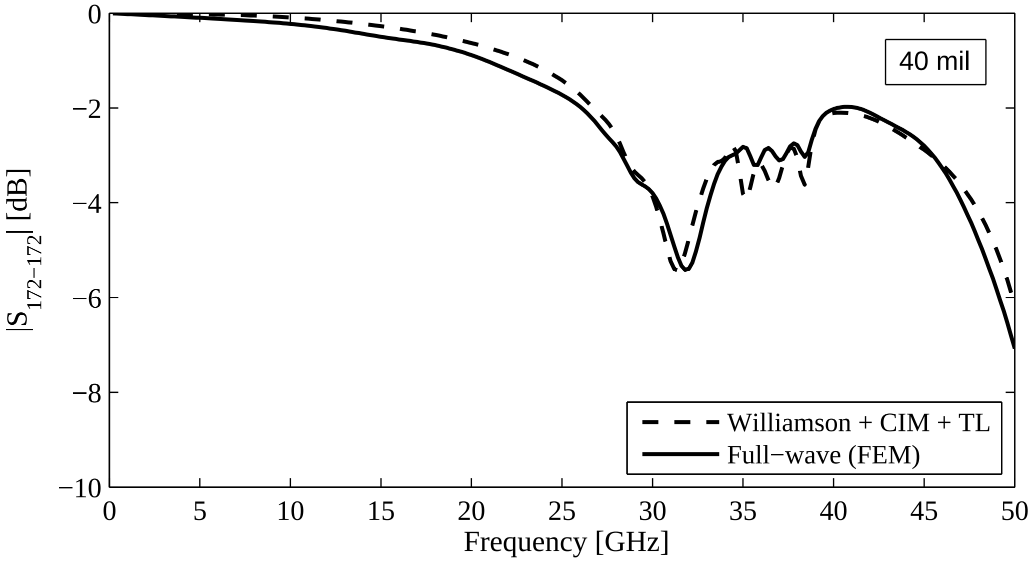

(a)

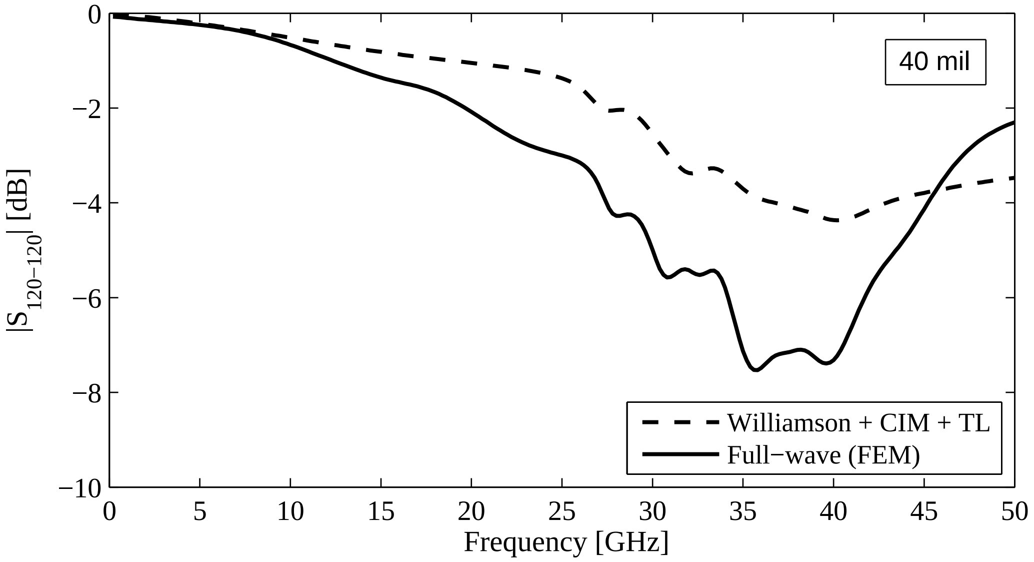

(b)

Figure D.3: Reflections at the upper via ports in case of 40 mil pitch. (a) Reflection at a signal via port. Although at lower frequencies, larger deviations than in the case of 80 mil pitch can be observed, a good overall agreement between physics-based via model and full-wave result is still obtained at the signal via. (b) Reflection at a power via port. The deviation between physics-based via model and full-wave result that exists for frequencies above 10 GHz in the case 80 mil pitch becomes very pronounced in the case of 40 mil pitch. This shows that the inaccuracy is related to the via array environment, and depends on the via pitch. This is also supported by the finding that a very good agreement between physics-based model and full-wave results can be obtained in case of an isolated power via.

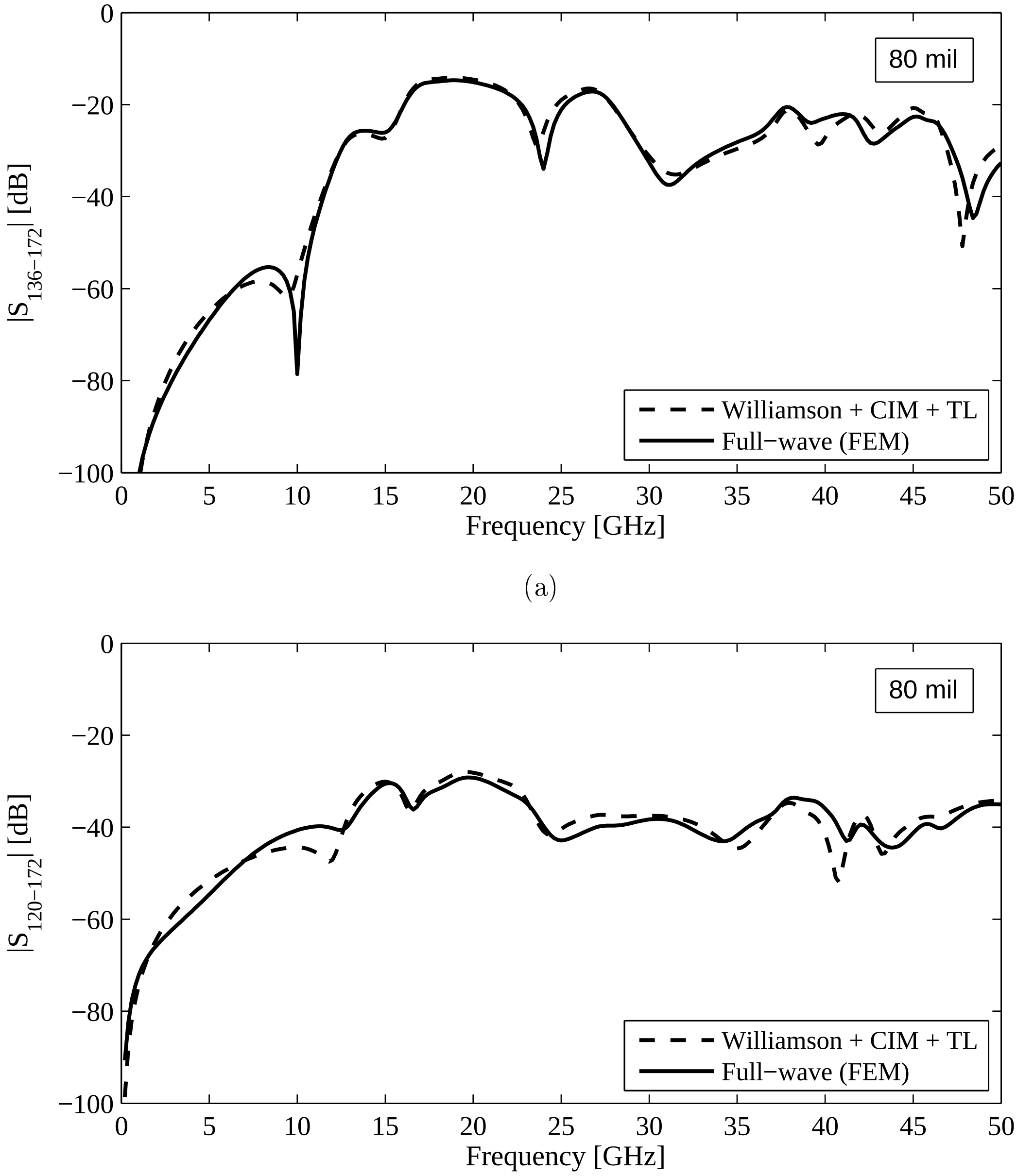

(a)

(b)

Figure D.4: Coupling between upper via ports in case of 80 mil pitch. (a) Coupling between two signal vias. In spite of the inaccuracies observed for the reflection at power via ports, the presence of power vias in the structure does not impair the accuracy of the physics-based via model for the simulation of coupling between signal vias. (b) Coupling between a signal and a power via. Even for the coupling to a power via, the physics-based via model provides a good approximation in the case of 80 mil pitch. It should be noted that in the case of 40 mil pitch, the physics-based via model does not provide accurate results for the coupling between signal vias, as previously observed for structures without power vias in Section 4.4.3. Also for the coupling between a signal and a power via, the physics-based via model is not accurate for 40 mil pitch.

E Additional Measurement Results

In this appendix, additional measured and simulated results for the test structure in Fig. 6.4 are shown to supplement the findings in Section 6.3.1. The main difference to the previously shown results lies in the routing layer of the striplines that provide the connection between the vias inside the array and the respective launch vias. While vias with striplines routed on the highest routing layer (SL3) were analyzed in Section 6.3.1, all results in this appendix have been obtained for vias with striplines routed on the lowest signal layer (SL9). Results are shown for the transmission between via V22 inside the array and the connected launch via L22 in Fig. E.1(a) and for the reflection at the launch via L22 in Fig. E.1(b). For the transmission, the agreement between physics-based via model and measurement is similar to the agreement observed in case of routing on the highest signal layer in Fig. 6.5(a). For the reflection, the deviations between physics-based via model and measurement are – in the frequency range between 5 GHz and 30 GHz – larger than observed for routing on the highest signal layer in Fig. 6.5(b). The larger deviations may be explained by the lower magnitude of the reflection for the lowest routing layer in combination with the previously observed sensitivity of the measured reflection to effects such as the parasitics of the probe launch described in Section 6.2.

The crosstalk is studied for two scenarios: crosstalk along a via array diagonal with one intermediate via and crosstalk along a via array diagonal with three intermediate vias. Results for the first scenario are shown in Fig. E.2. Although it can be observed that the detailed characteristic features of the crosstalk depend on both via location and routing layer of the connected striplines, the agreement between physics-based via model and measurement for vias connected to striplines on the lowest routing layer is similar to the agreement for vias connected to striplines on the highest routing layer in Fig. 6.6. For the second scenario, results are shown in Fig. E.3. Although not all detailed characteristics of the measured results are represented in the results obtained with the physics-based via model, a good general agreement can be observed in the frequency range up to 50 GHz.

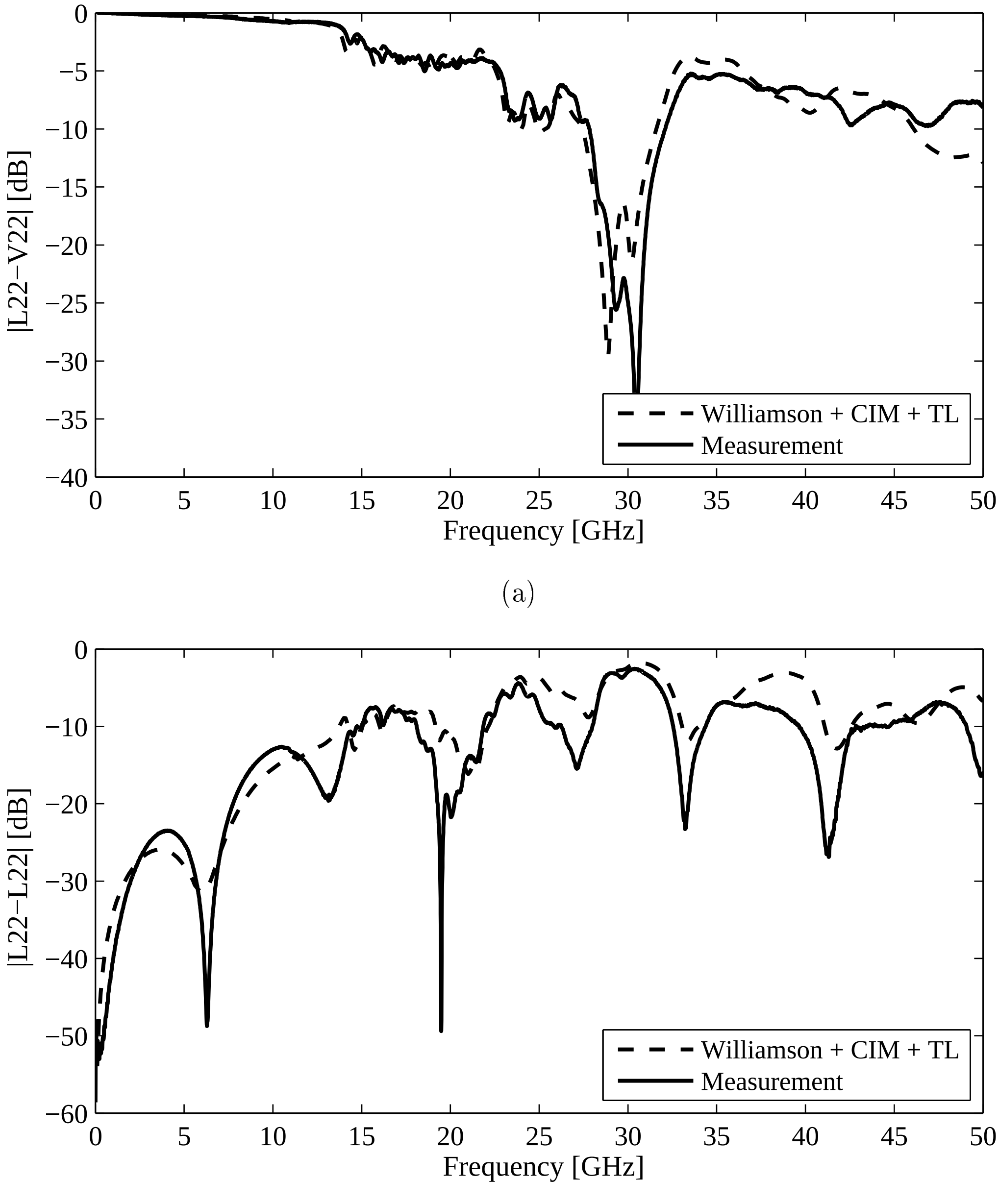

(a)

(b)

Figure E.1: Comparison between physics-based via model and measurement for transmission and reflection of two vias routed on SL9. (a) Transmission between signal via V22 and launch via L22 outside of the array. In comparison to the transmission on the highest signal layer depicted in Fig. 6.5(a), the stub resonance is shifted to higher frequencies due to the shorter via stub. The quality of the agreement between physics-based via and measurement for the transmission is not changed by the different routing layer. (b) Reflection at launch via L22. In the frequency range between 5 GHz and 30 GHz, larger deviations between physics-based via model and measurement exist than for a routing on the highest signal layer. The larger deviations may be related to the lower magnitude of the reflection in this frequency range.

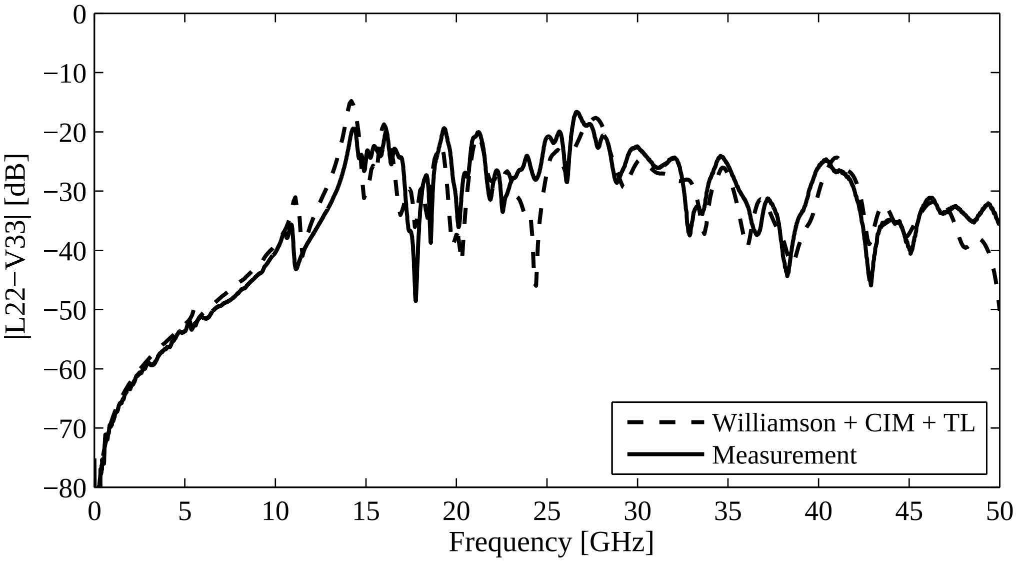

(a)

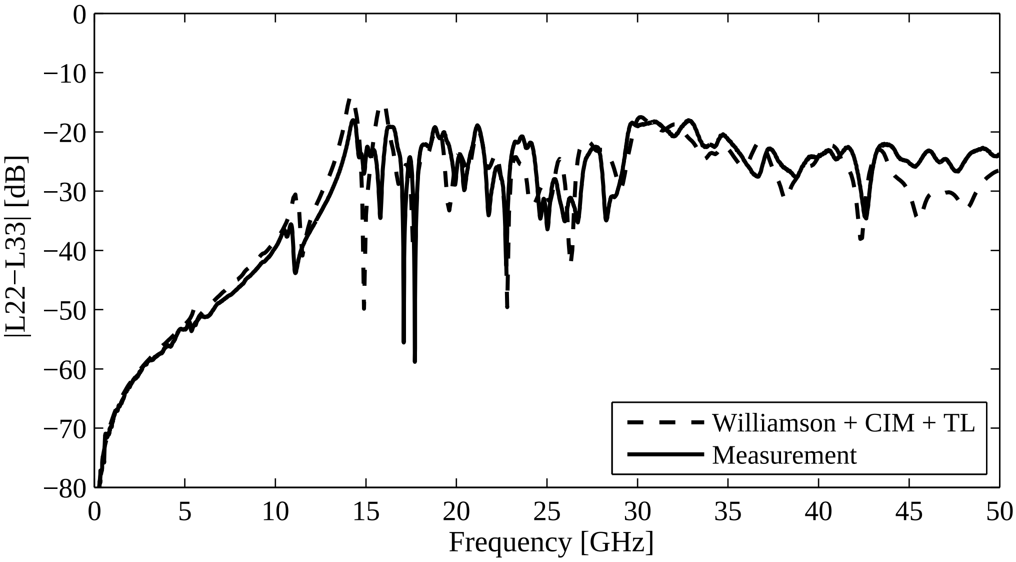

(b)

Figure E.2: Comparison between physics-based via model and measurement for the crosstalk along a diagonal with one intermediate via. (a) Crosstalk between via V33 inside the array and launch via L22 (including the impact of one stripline transmission). (b) Crosstalk between launch via L33 and launch via L22 (including the impact of two stripline transmissions). A good general agreement between physics-based via model and measurement can be observed—similar to the agreement observed for vias connected to striplines routed on the highest signal layer in Fig. 6.6.

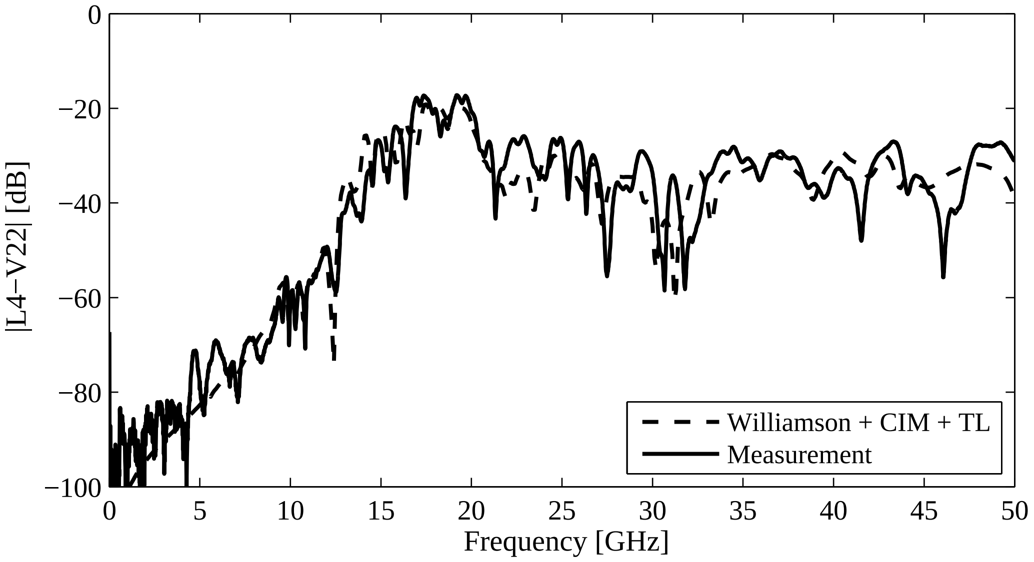

(a)

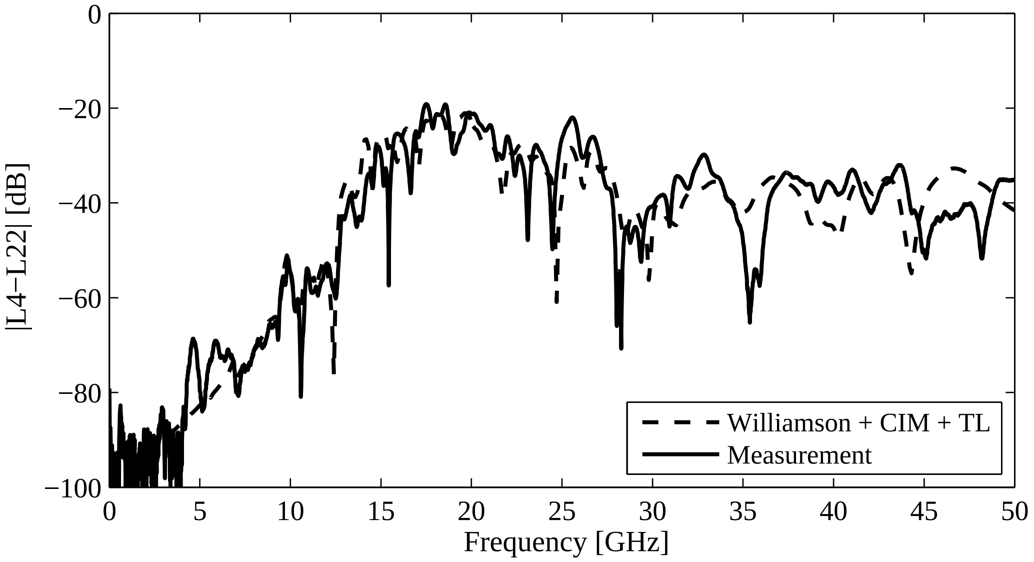

(b)

Figure E.3: Comparison between physics-based via model and measurement for the crosstalk along a diagonal with three intermediate vias. (a) Crosstalk between via V22 inside the array and launch via L4 (including the impact of one stripline transmission). (b) Crosstalk between launch via L4 and launch via L22 (including the impact of two stripline transmissions). Due to the larger separation between the studied vias and the complex characteristics of the measured curves, not all details of the measured results are represented in the results of the physics-based via model. Nevertheless, the modeling results provide a good approximation of the measurement in the frequency range up to 50 GHz.

Bibliography

[1] R. Rimolo-Donadio, “Development, validation, and application of semi-analytical interconnect models for efficient simulation of multilayer substrates,” Dissertation, TUHH, 2011.

[2] V. Stojanovic and M. Horowitz, “Modeling and analysis of high-speed links,” in *Custom Integrated Circuits Conference (CICC)*, San Jose, CA, USA, Sep. 21–24, 2003.

[3] M. Georgas, J. Orcutt, R. J. Ram, and V. Stojanovic, “A monolithically-integrated optical receiver in standard 45-nm SOI,” in *European Solid State Circuits Conference (ESSCIRC)*, Helsinki, Finland, Sep. 12–16, 2011.

[4] S. Müller, X. Duan, and C. Schuster, “Energy-aware analysis of electrically long high speed I/O links,” *Computer Science - Research and Development*, vol. 29, no. 2, pp. 97–102, May 2014.

[5] S. Müller, T. Reuschel, R. Rimolo-Donadio, Y. H. Kwark, H.-D. Brüns, and C. Schuster, “Energy aware signal integrity analysis for high-speed PCB links,” *submitted to IEEE Transactions on Electromagnetic Compatibility*, 2014.

[6] M. Kotzev, R. Frech, H. Harrer, D. Kaller, A. Huber, T.-M. Winkel, H.-D. Brüns, and C. Schuster, “Crosstalk analysis in high density connector via pin fields for digital backplane applications using a 12-port vector network analyzer,” in *Electronic System-Integration Technology Conference (ESTC)*, Berlin, Germany, Sep. 13–16, 2010.

[7] S. Müller, X. Duan, M. Kotzev, Y.-J. Zhang, J. Fan, X. Gu, Y. H. Kwark, R. Rimolo-Donadio, H.-D. Brüns, and C. Schuster, “Accuracy of physics-based via models for simulation of dense via arrays,” *IEEE Transactions on Electromagnetic Compatibility*, vol. 54, no. 5, pp. 1125–1136, Oct. 2012.

[8] X. Duan, R. Rimolo-Donadio, S. Müller, K. J. Han, X. Gu, Y. H. Kwark, H.-D. Brüns, and C. Schuster, “Impact of multiple scattering on passivity of equivalent-circuit via models,” in *IEEE Electrical Design of Advanced Packaging and Systems Symposium (EDAPS)*, Hangzhou, China, Dec. 12–14, 2011.

[9] L. Shan, T. Dickson, Y. Kwark, C. Baks, D. Becker, R. Krabbenhoft, T. Chainer, S. Müller, M. Hoshino, J. Kodemura, M. Hashimoto, T. Jimbo, and C. Blatt, “Realization of ultra-low power I/O,” in *IEEE Electronic Components and Technology Conference (ECTC)*, Las Vegas, NV, USA, May 28–31, 2013.

[10] PCI-SIG, “PCI-SIG Delivers PCI Express 2.0 Specification,” Jan. 2007. [Online]. Available: https://www.pcisig.com/news_room/PCIe2_0_Spec_Release_FINAL2.pdf

[11] PCI-SIG, “PCI-SIG Announces PCI Express 4.0 Evolution to 16GT/s, Twice the Throughput of PCI Express 3.0 Technology,” Nov. 2011. [Online]. Available: https://www.pcisig.com/news_room/Press_Releases/PCIe_4_0_BitRate_Release_11_29_11.pdf

[12] Optical Internetworking Forum, “Common Electrical I/O (CEI) - Electrical and Jitter Interoperability agreements for 6G+ bps and 11G+ bps I/O,” Feb. 2005. [Online]. Available: http://www.oiforum.com/public/documents/OIF_CEI_02.0.pdf

[13] Optical Internetworking Forum, “Common Electrical I/O (CEI) - Electrical and Jitter Interoperability agreements for 6G+ bps, 11G+ bps and 25G+ bps I/O,” Sep. 2011. [Online]. Available: http://www.oiforum.com/public/documents/OIF_CEI_03.0.pdf

[14] M. Poess and R. O. Nambiar, “Energy cost, the key challenge of today’s data centers: a power consumption analysis of TPC-C results,” *Proceedings of the VLDB Endowment*, vol. 1, no. 2, pp. 1229–1240, Aug. 2008.

[15] U.S. Environmental Protection Agency ENERGY STAR Program, “Report to congress on server and data center energy efficiency - public law 109-431,” 8.2007. [Online]. Available: http://www.energystar.gov/ia/partners/prod_development/downloads/EPA_Datacenter_Report_Congress_Final1.pdf

[16] Parliamentary Office of Science and Technology, “ICT and CO2 emissions,” 12.2008. [Online]. Available: http://www.parliament.uk/documents/post/postpn319.pdf

[17] S. Müller, R. Rimolo-Donadio, H.-D. Brüns, and C. Schuster, “Schnelle Simulation verlustbehafteter Verbindungsstrukturen auf Leiterplatten auf der Grundlage quasi-analytischer Via-Modelle und der Leitungstheorie,” in *Internationale Fachmesse und Kongress für elektromagnetische Verträglichkeit (EMV Düsseldorf)*, Düsseldorf, Germany, Mar. 09–11, 2010.

[18] S. Müller, R. Rimolo-Donadio, M. Kotzev, H.-D. Brüns, and C. Schuster, "Effect of mixed-reference planes on single-ended and differential links in multilayer substrates," in *IEEE Workshop on Signal Propagation on Interconnects*, Hildesheim, Germany, May 09–12, 2010.

[19] S. Müller, X. Duan, R. Rimolo-Donadio, H.-D. Brüns, and C. Schuster, "Non-uniform currents on vias and their effects in a parallel-plate environment," in *IEEE Electrical Design of Advanced Packaging and Systems Symposium (EDAPS)*, Singapore, Dec. 7–9, 2010.

[20] S. Müller, X. Duan, R. Rimolo-Donadio, H.-D. Brüns, and C. Schuster, "Recent developments of via and return current path modeling," in *International Conference on Electromagnetics in Advanced Applications (ICEAA)*, Torino, Italy, Sep. 12–16, 2011.

[21] S. Müller, R. Rimolo-Donadio, H.-D. Brüns, and C. Schuster, "Anwendung quasianalytischer Via-Modelle zur schnellen Simulation dichter Via-Arrays," in *Internationale Fachmesse und Kongress für elektromagnetische Verträglichkeit (EMV Düsseldorf)*, Düsseldorf, Germany, Feb. 07–09, 2012.

[22] S. Müller, R. Rimolo-Donadio, X. Duan, H.-D. Brüns, and C. Schuster, "Analytical calculation of conduction and displacement current contributions in PCB return current paths," in *Asia-Pacific Symposium on Electromagnetic Compatibility (APEMC)*, Singapore, May 21–24, 2012.

[23] S. Müller, A. Hardock, R. Rimolo-Donadio, H.-D. Brüns, and C. Schuster, "Analytical extraction of via near-field coupling using a multiple scattering approach," in *IEEE Workshop on Signal and Power Integrity (SPI)*, Paris, France, May 12–15, 2013.

[24] S. Müller, H.-D. Brüns, and C. Schuster, "Einfluss der Routinglage in Via-Arrays auf die Signalqualität bei hohen Datenraten," in *Internationale Fachmesse und Kongress für elektromagnetische Verträglichkeit (EMV Düsseldorf)*, Düsseldorf, Germany, Mar. 11-13, 2014.

[25] S. Müller, X. Duan, and C. Schuster, "Erratum to: Energy-aware analysis of electrically long high speed I/O links," *Computer Science - Research and Development*, vol. 29, no. 2, p. 103, May 2014.

[26] S. Müller, F. Happ, X. Duan, R. Rimolo-Donadio, H.-D. Brüns, and C. Schuster, "Complete modeling of large via constellations in multilayer printed circuit boards," *IEEE Transactions on Components, Packaging and Manufacturing Technology*, vol. 3, no. 3, pp. 489–499, Mar. 2013.

[27] S. Müller, "Correction to 'Complete modeling of large via constellations in multilayer printed circuit boards' [Mar 13, pp. 489-499]," *IEEE Transactions on Components, Packaging and Manufacturing Technology*, vol. 4, no. 4, p. 748, Apr. 2014.

[28] X. Gu, Y. H. Kwark, Y.-J. Zhang, J. Fan, A. Ruehli, M. Kotzev, S. Müller, R. Rimolo-Donadio, C. Schuster, and B. Archambeault, "Validation and application of physics-based via models to dense via arrays," in *IEC DesignCon Conference*, Santa Clara, CA, USA, Jan. 31–Feb. 02, 2011.

[29] X. Gu, Y. Kwark, D. Liu, Y. Zhang, J. Fan, R. Rimolo-Donadio, S. Müller, C. Schuster, and F. d. Paulis, "Backplane channel design optimization: recasting a 3Gb/s link to operate at 25Gb/s and above," in *UBM DesignCon Conference*, Santa Clara, CA, USA, Jan. 30–Feb. 02, 2012.

[30] R. Rimolo-Donadio, S. Müller, X. Duan, M. Kotzev, H.-D. Brüns, and C. Schuster, "Signal integrity: Efficient, physics-based via modeling: Principles and methods," *IEEE Electromagnetic Compatibility Magazine*, vol. 1, no. 1, pp. 55–61, 2012.

[31] A. Hardock, S. Müller, X. Duan, H.-D. Brüns, and C. Schuster, "Minimizing displacement return currents in multilayer via structures," in *IEEE Conference on Electrical Performance of Electronic Packaging and Systems (EPEPS)*, Tempe, AZ, USA, Oct. 21–24, 2012.

[32] R. Rimolo-Donadio, X. Duan, Y. H. Kwark, X. Gu, C. Baks, S. Müller, T.-M. Winkel, T. Strach, L. Shan, H. Harrer, and C. Schuster, "Signal and power integrity (SPI) co-analysis for high-speed communication channels," in *UBM DesignCon Conference*, Santa Clara, CA, USA, Jan. 28–31, 2013.

[33] T. Reuschel, S. Müller, H.-D. Brüns, and C. Schuster, "Investigation of long range differential crosstalk on printed circuit boards," in *IEEE Workshop on Signal and Power Integrity (SPI)*, Ghent, Belgium, May 11–14, 2014.

[34] Y. H. Kwark, R. Rimolo-Donadio, C. Baks, S. Müller, and C. Schuster, "Proximity effects between striplines and vias," in *IEEE International Conference on Signal and Power Integrity (SIPI)*, Raleigh, NC, USA, Aug. 4–8, 2014.

[35] F. Happ, "Machbarkeit der Simulation von großen Via-Arrays unter Einsatz paralleler Algorithmen," Diplomarbeit, TUHH, 2011.

[36] A. Heine, "Analysis of coupling effects between vias and striplines in printed circuit boards," Bachelorarbeit, TUHH, 2012.

[37] H. Färber, “Segmentierte Modellierung gekoppelter Mehrfachstreifenleitungen auf Leiterplatten,” Bachelorarbeit, TUHH, 2011.

[38] D. Timmermann, “Combined signal and power integrity time domain simulation of high-speed data links,” Diplomarbeit, TUHH, 2012.

[39] G. Edlund, Y. H. Kwark, C. Schuster, and L. Shan, “Developing a working model for vias,” in *IEC DesignCon Conference*, Santa Clara, CA, USA, Feb. 2–5, 2004.

[40] C. Schuster, Y. H. Kwark, G. Selli, and P. Muthana, “Developing a ’physical’ model for vias,” in *IEC DesignCon Conference*, Santa Clara, CA, USA, Feb. 6–9, 2006.

[41] X. Duan, “Extension of the contour integral method for the electrical design of planar structures in digital systems,” Dissertation, TUHH, 2012.

[42] T. Wang, R. F. Harrington, and J. R. Mautz, “Quasi-static analysis of a microstrip via through a hole in a ground plane,” *IEEE Transactions on Microwave Theory and Techniques*, vol. 36, no. 6, pp. 1008–1013, Jun. 1988.

[43] P. Kok and D. de Zutter, “Capacitance of a circular symmetric model of a via hole including finite ground plane thickness,” *IEEE Transactions on Microwave Theory and Techniques*, vol. 39, no. 7, pp. 1229–1234, Jul. 1991.

[44] K. S. Oh, J. E. Schutt-Aine, R. Mittra, and B. Wang, “Computation of the equivalent capacitance of a via in a multilayered board using the closed-form green’s function,” *IEEE Transactions on Microwave Theory and Techniques*, vol. 44, no. 2, pp. 347–349, Feb. 1996.

[45] P. A. Kok and D. de Zutter, “Scalar magnetostatic potential approach to the prediction of the excess inductance of grounded via’s and via’s through a hole in a ground plane,” *IEEE Transactions on Microwave Theory and Techniques*, vol. 42, no. 7, pp. 1229–1237, Feb. 1994.

[46] E. Pillai, F. Rostan, and W. Wiesbeck, “Derivation of equivalent circuits for via holes from full wave models,” *Electronics Letters*, vol. 29, no. 11, p. 1026, May 1993.

[47] T. Wang, J. R. Mautz, and R. F. Harrington, “The excess capacitance of a microstrip via in a dielectric substrate,” *IEEE Transactions on Computer-Aided Design of Integrated Circuits and Systems*, vol. 9, no. 1, pp. 48–56, Jan. 1990.

[48] P. A. Kok and D. de Zutter, “Prediction of the excess capacitance of a via-hole through a multilayered board including the effect of connecting microstrips or

striplines," *IEEE Transactions on Microwave Theory and Techniques*, vol. 42, no. 12, pp. 2270–2276, Dec. 1994.

[49] E. Laermans, J. de Geest, D. de Zutter, F. Olyslager, S. Sercu, and D. Morlion, "Modeling differential via holes," *IEEE Transactions on Advanced Packaging*, vol. 24, no. 3, pp. 357–363, Aug. 2001.

[50] E. Laermans, J. de Geest, D. de Zutter, F. Olyslager, S. Sercu, and D. Morlion, "Modeling complex via hole structures," *IEEE Transactions on Advanced Packaging*, vol. 25, no. 2, pp. 206–214, May 2002.

[51] H. Johnson, *High-Speed Signal Propagation: Advanced Black Magic.* Prentice Hall, Upper Saddle River, 2003.

[52] "High frequency structure simulator (HFSS TM), ver. 14," Canonsburg, PA, USA, 2014. [Online]. Available: http://www.ansys.com

[53] R. Abhari, G. V. Eleftheriades, and E. van Deventer-Perkins, "Physics-based cad models for the analysis of vias in parallel-plate environments," *IEEE Transactions on Microwave Theory and Techniques*, vol. 49, no. 10, pp. 1697–1707, Jan. 2001.

[54] G. Selli, C. Schuster, and Y. Kwark, "Model-to-hardware correlation of physics based via models with the parallel plate impedance included," in *IEEE International Symposium on Electromagnetic Compatibility (EMC)*, Portland, OR, USA, Aug. 14–18, 2006.

[55] C. Schuster, G. Selli, Y. H. Kwark, M. Ritter, and J. L. Drewniak, "Accuracy and application of physics-based circuit models for vias," in *International Symposium on Microelectronics (IMAPS)*, San Diego, CA, USA, Oct. 8–12, 2006.

[56] C. Schuster, G. Selli, Y. H. Kwark, M. B. Ritter, and J. L. Drewniak, "Progress in representation and validation of physics-based via models," in *IEEE Workshop on Signal Propagation on Interconnects (SPI)*, Genova, Italy, May 13–16, 2007.

[57] G. Selli, C. Schuster, Y. H. Kwark, M. Ritter, and J. L. Drewniak, "Developing a physical model for vias - part II: coupled and ground return vias," in *UBM DesignCon Conference*, Santa Clara, CA, USA, Jan. 29 – Feb. 01, 2007.

[58] R. Rimolo-Donadio, A. J. Stepan, H.-D. Brüns, J. L. Drewniak, and C. Schuster, "Simulation of via interconnects using physics-based models and microwave network parameters," in *IEEE Workshop on Signal Propagation on Interconnects (SPI)*, Avignon, France, May 12–15, 2008.

[59] R. Rimolo-Donadio, X. Gu, Y. Kwark, M. Ritter, B. Archambeault, F. de Paulis, Y. Zhang, J. Fan, H.-D. Brüns, and C. Schuster, "Physics-based via and trace models for efficient link simulation on multilayer structures up to 40 GHz," *IEEE Transactions on Microwave Theory and Techniques*, vol. 57, no. 8, pp. 2072–2083, Aug. 2009.

[60] F. de Paulis, Y.-J. Zhang, and J. Fan, "Signal/power integrity analysis for multilayer printed circuit boards using cascaded S-Parameters, pages = 1008–1018, volume = 52, number = 4, issn = 0018-9375, journal = IEEE Transactions on Electromagnetic Compatibility, doi = 10.1109/TEMC.2010.2072784," Nov. 2010.

[61] Z. Z. Oo, E.-X. Liu, X. C. Wei, Y. Zhang, and E.-P. Li, "Cascaded microwave network approach for power and signal integrity analysis of multilayer electronic packages," *IEEE Transactions on Components, Packaging and Manufacturing Technology*, vol. 1, no. 9, pp. 1428–1437, Aug. 2011.

[62] S. Ramo, J. R. Whinnery, and T. van Duzer, *Fields and Waves in Communication Electronics*. New York: John Wiley & Sons, 1993.

[63] J. Parker, "Via coupling within parallel rectangular planes," *IEEE Transactions on Electromagnetic Compatibility*, vol. 39, no. 1, pp. 17–23, Feb. 1997.

[64] T. Okoshi, *Planar Circuits for Microwaves and Lightwaves*, ser. Springer Series in Electrophysics. Berlin and Heidelberg: Springer, 1985, vol. 18.

[65] G.-T. Lei, R. Techentin, P. Hayes, D. Schwab, and B. Gilbert, "Wave model solution to the ground/power plane noise problem," *IEEE Transactions on Instrumentation and Measurement*, vol. 44, no. 2, pp. 300–303, Apr. 1995.

[66] R. Chadha and K. C. Gupta, "Green's functions for triangular segments in planar microwave circuits," *IEEE Transactions on Microwave Theory and Techniques*, vol. 28, no. 10, pp. 1139–1143, Oct. 1980.

[67] X.-C. Wei, E.-P. Li, E.-X. Liu, and X. Cui, "Efficient modeling of rerouted return currents in multilayered power-ground planes by using integral equation," *IEEE Transactions on Electromagnetic Compatibility*, vol. 50, no. 3, pp. 740–743, Oct. 2008.

[68] M. Stumpf and M. Leone, "Efficient 2-D integral equation approach for the analysis of power bus structures with arbitrary shape," *IEEE Transactions on Electromagnetic Compatibility*, vol. 51, no. 1, pp. 38–45, Feb. 2009.

[69] W. Hoefer, "The transmission-line matrix method–theory and applications," *IEEE Transactions on Microwave Theory and Techniques*, vol. 33, no. 10, pp. 882–893, Oct. 1985.

[70] J. Park, H. Kim, Y. Jeong, J. Kim, J. S. Pak, and D. G. Kam, “Modeling and measurement of simultaneous switching noise coupling through signal via transition,” *IEEE Transactions on Advanced Packaging*, vol. 29, no. 3, pp. 548–559, Aug. 2006.

[71] Y. Zhang, J. Fan, G. Selli, M. Cocchini, and F. de Paulis, “Analytical evaluation of via-plate capacitance for multilayer printed circuit boards and packages,” *IEEE Transactions on Microwave Theory and Techniques*, vol. 56, no. 9, pp. 2118–2128, Sep. 2008.

[72] M. Friedrich, C. Bednarz, and M. Leone, “Improved expression for the via-plate capacitance based on the magnetic-frill model,” *IEEE Transactions on Electromagnetic Compatibility*, pp. 1362–1364, Dec. 2013.

[73] A. G. Williamson, “Radial-line/coaxial-line junctions: analysis and equivalent circuits,” *International Journal of Electronics*, vol. 58, no. 1, pp. 91–104, Jan. 1985.

[74] Q. Gu, Y. E. Yang, and M. A. Tassoudji, “Modeling and analysis of vias in multilayered integrated circuits,” *IEEE Transactions on Microwave Theory and Techniques*, vol. 41, no. 2, pp. 206–214, Feb. 1993.

[75] Q. Gu, M. A. Tassoudji, S. Y. Poh, R. T. Shin, and J. A. Kong, “Coupled noise analysis for adjacent vias in multilayered digital circuits,” *IEEE Transactions on Circuits and Systems I: Fundamental Theory and Applications*, vol. 41, no. 12, pp. 796–804, Dec. 1994.

[76] Y.-J. Zhang and J. Fan, “An intrinsic circuit model for multiple vias in an irregular plate pair through rigorous electromagnetic analysis,” *IEEE Transactions on Microwave Theory and Techniques*, vol. 58, no. 8, pp. 2251–2265, Aug. 2010.

[77] K. C. Gupta and M. D. Abouzahra, Eds., *Analysis and Design of Planar Microwave Components.* New York: IEEE Press, 1994.

[78] L. L. Foldy, “The multiple scattering of waves,” *Physical Review*, vol. 67, no. 3-4, pp. 107–119, Feb. 1945.

[79] M. Lax, “Multiple scattering of waves,” *Reviews of Modern Physics*, vol. 23, no. 4, pp. 287–310, Aug. 1951.

[80] M. Lax, “Multiple scattering of waves. II. The effective field in dense systems,” *Physical Review*, vol. 85, no. 4, pp. 621–629, Feb. 1952.

[81] L. Tsang, H. Chen, C.-C. Huang, and V. Jandhyala, “Modeling of multiple scattering among vias in planar waveguides using foldy-lax equations,” *Microwave and Optical Technology Letters*, vol. 31, no. 3, pp. 201–208, Sep. 2001.

[82] Z. Z. Oo, E.-X. Liu, E.-P. Li, X. Wei, Y. Zhang, M. Tan, L.-W. J. Li, and R. Vahldieck, “A semi-analytical approach for system-level electrical modeling of electronic packages with large number of vias,” *IEEE Transactions on Advanced Packaging*, vol. 31, no. 2, pp. 267–274, May 2008.

[83] B. Wu and L. Tsang, “Signal integrity analysis of package and printed circuit board with multiple vias in substrate of layered dielectrics,” *IEEE Transactions on Advanced Packaging*, vol. 33, no. 2, pp. 510–516, May 2010.

[84] B. Wu and L. Tsang, “Modeling multiple vias with arbitrary shape of antipads and pads in high speed interconnect circuits,” *IEEE Microwave and Wireless Components Letters*, vol. 19, no. 1, pp. 12–14, Jan. 2009.

[85] L. Tsang and X. Chang, “Modeling of vias sharing the same antipad in planar waveguide with boundary integral equation and group T-matrix method,” *IEEE Transactions on Components, Packaging and Manufacturing Technology*, vol. 3, no. 2, pp. 315–327, Feb. 2013.

[86] E.-X. Liu, X. Wei, Z. Z. Oo, E.-P. Li, and L.-W. Li, “Modeling of advanced multilayered packages with multiple vias and finite ground planes,” in *IEEE Electrical Performance of Electronic Packaging (EPEP)*, Atlanta, GA, USA, 2007.

[87] Y.-J. Zhang and J. Fan, “A generalized multiple scattering method for dense vias with axially anisotropic modes in an arbitrarily shaped plate pair,” *IEEE Transactions on Microwave Theory and Techniques*, vol. 60, no. 7, pp. 2035–2045, Jul. 2012.

[88] J. Jin, *The Finite Element Method in Electromagnetics*, 2nd ed. New York: Wiley, 2002.

[89] K. S. Yee, “Numerical solution of initial boundary value problems involving maxwell’s equations in isotropic media,” *IEEE Transactions on Antennas and Propagation*, vol. 14, no. 3, pp. 302–307, May 1966.

[90] A. Taflove and S. C. Hagness, *Computational Electrodynamics: The Finite-Difference Time-Domain Method*, 3rd ed. Boston: Artech House, 2005.

[91] T. Weiland, “Eine Methode zur Lösung der Maxwellschen Gleichungen für sechskomponentige Felder auf diskreter Basis,” *AEÜ*, vol. 31, no. 3, pp. 116–120, 1977.

[92] R. F. Harrington, *Field Computation by Moment Methods.* Piscataway: IEEE Press, 1993.

[93] X. Duan, A. Vogt, H. Dietrich Brüns, and C. Schuster, "Progress towards a combined CIM/MoM approach for EMI analysis of electronic systems," in *International Symposium on Electromagnetic Compatibility (EMC Europe)*, Rome, Italy, Sep. 17–21, 2012.

[94] A. E. Engin, K. Bharath, and M. Swaminathan, "Multilayered finite-difference method (MFDM) for modeling of package and printed circuit board planes," *IEEE Transactions on Electromagnetic Compatibility*, vol. 49, no. 2, pp. 441–447, May 2007.

[95] K. Bharathy, J. Y. Choi, and M. Swaminathan, "Use of the finite element method for the modeling of multi-layered power/ground planes with small features," in *IEEE Electronic Components and Technology Conference (ECTC)*, San Diego, CA, USA, May 26–29, 2009.

[96] C. A. Balanis, *Advanced Engineering Electromagnitics.* New York: John Wiley & Sons, 1989.

[97] CST Corporation, "CST Microwave Studio (MWS TM)," Darmstadt and Germany, Mar. 2011. [Online]. Available: http://www.cst.com

[98] A. R. Chada, Y. Zhang, G. Feng, J. L. Drewniak, and J. Fan, "Impedance of an infinitely large parallel-plane pair and its applications in engineering modeling," in *2009 IEEE International Symposium on Electromagnetic Compatibility (EMC)*, Austin, TX, USA, Aug. 17–21, 2009.

[99] X. Duan, R. Rimolo-Donadio, H.-D. Brüns, and C. Schuster, "Circular ports in parallel-plate waveguide analysis with isotropic excitations," *IEEE Transactions on Electromagnetic Compatibility*, vol. 54, no. 3, pp. 603–612, Jun. 2012.

[100] R. Rimolo-Donadio, H.-D. Brüns, and C. Schuster, "Hybrid approach for efficient calculation of the parallel-plate impedance of lossy power/ground planes," *Microwave and Optical Technology Letters*, vol. 51, no. 9, pp. 2051–2056, Sep. 2009.

[101] Z. Wang, O. Wada, Y. Toyota, and R. Koga, "Convergence acceleration and accuracy improvement in power bus impedance calculation with a fast algorithm using cavity modes," *IEEE Transactions on Electromagnetic Compatibility*, vol. 47, no. 1, pp. 2–9, Feb. 2005.

[102] M. Hampe, V. A. Palanisamy, and S. Dickmann, "Single summation expression for the impedance of rectangular pcb power-bus structures loaded with multiple lumped elements," *IEEE Transactions on Electromagnetic Compatibility*, vol. 49, no. 1, pp. 58–67, Feb. 2007.

[103] Z. L. Wang, O. Wada, Y. Toyota, and R. Koga, "Application of segmentation method to analysis of power/ground plane resonance in multilayer PCBs," in *International Symposium on Electromagnetic Compatibility*, May 21–24, 2002, pp. 775–778.

[104] D.-B. Lin, C.-T. Wu, K.-C. Hung, and F.-N. Wu, "Single summation expression in combination with modified segmentation method for calculating transfer impedance of an arbitrary shaped power bus," in *IEEE Electrical Design of Advanced Packaging and Systems Symposium (EDAPS)*, Hong Kong, China, Dec. 2–4, 2009.

[105] H.-G. Unger, *Elektromagnetische Wellen auf Leitungen*, 3rd ed. Heidelberg: Hüthig, 1996.

[106] A. E. Engin, W. John, G. Sommer, W. Mathis, and H. Reichl, "Modeling of striplines between a power and a ground plane," *IEEE Transactions on Advanced Packaging*, vol. 29, no. 3, pp. 415–426, Aug. 2006.

[107] C. R. Paul, *Analysis of Multiconductor Transmission Lines*, 2nd ed. Hoboken: Wiley-Interscience and IEEE Press, 2008.

[108] S. Müller, "Including multiconductor transmission lines in a quasi-analytical model for multilayer structures," Diplomarbeit, TUHH, 2009.

[109] B. C. Wadell, *Transmission Line Design Handbook.* Norwood: Artech House, 1991.

[110] "High frequency structure simulator (HFSS TM), ver. 12.1," Canonsburg, PA, USA, 2010. [Online]. Available: http://www.ansoft.com

[111] S. Maeda, T. Kashiwa, and I. Fukai, "Full wave analysis of propagation characteristics of a through hole using the finite-difference time-domain method," *IEEE Transactions on Microwave Theory and Techniques*, vol. 39, no. 12, pp. 2154–2159, Dec. 1991.

[112] "High frequency structure simulator (HFSS TM), ver. 13," Canonsburg, PA, USA. [Online]. Available: http://www.ansys.com

[113] X. Duan, R. Rimolo-Donadio, H.-D. Brüns, and C. Schuster, "Extension of the contour integral method to anisotropic modes on circular ports," *IEEE Transactions on*

Components, Packaging and Manufacturing Technology, vol. 2, no. 2, pp. 321–331, Feb. 2012.

[114] J. Gipprich and D. Stevens, "A new via fence structure for crosstalk reduction in high density stripline packages," in *IEEE MTT-S International Microwave Symposium Digest*, Phoenix, AZ, USA, May 20–24, 2001.

[115] G. E. Ponchak, D. Chen, and J.-G. Yook, "Characterization of plated via hole fences for isolation between stripline circuits in ltcc packages," in *IEEE MTT-S International Microwave Symposium Digest*, Baltimore, MD, USA, Jun. 7–12, 1998.

[116] G. E. Ponchak, D. Chun, J.-G. Yook, and L. Katehi, "The use of metal filled via holes for improving isolation in LTCC RF and wireless multichip packages," *IEEE Transactions on Advanced Packaging*, vol. 23, no. 1, pp. 88–99, Feb. 2000.

[117] M. Merzer, "Influence of via rows on coupling between PCB striplines - experiment vs simple formula," in *IEEE International Symposium on Electromagnetic Compatibility (EMC)*, Istanbul, Turkey, May 11–16, 2003.

[118] D. Guckenberger, C. Schuster, Y. Kwark, and K. Kornegay, "On-chip crosstalk mitigation for densely packed differential striplines using via fence enclosures," *Electronics Letters*, vol. 41, no. 7, p. 412, Mar. 2005.

[119] G. Blando, J. Miller, I. Novak, J. DeLap, and C. Preston, "Attenuation in PCB traces due to periodic discontinuities," in *IEC DesignCon Conference*, Santa Clara, CA, USA, Feb. 6–9, 2006.

[120] "Q3D Extractor TM, ver. 11," Canonsburg and PA and USA, 2014. [Online]. Available: http://www.ansys.com

[121] G. H. Golub and van Loan, C. F., *Matrix Computations.* London: The Johns Hopkins University Press, 1996.

[122] University of Tennessee, "MPI: A message-passing interface standard," 2008. [Online]. Available: http://www.mpi-forum.org

[123] W. Gropp, E. Lusk, and A. Skjellum, *Using MPI Portable Parallel Programming with the Message-Passing Interface.* MIT Press, 1995.

[124] L. S. Blackford, J. Choi, A. Cleary, E. d'Azevedo, J. Demmel, I. Dhillon, J. Dongarra, S. Hammarling, G. Henry, A. Petitet, K. Stanley, D. Walker, and R. C. Whaley, "ScaLAPACK users' guide," 1997. [Online]. Available: http://www.netlib.org/scalapack/slug/

[125] H. Chen, Q. Li, L. Tsang, H. C.-C., and V. Jandhyala, “Analysis of a large number of vias and differential signaling in multilayered structures,” *IEEE Transactions on Microwave Theory and Techniques*, vol. 51, no. 3, pp. 818–829, Apr. 2003.

[126] C.-C. Huang, L. Tsang, C. Chan, and K.-H. Ding, “Multiple scattering among vias in planar waveguides using preconditioned SMCG method,” *IEEE Transactions on Microwave Theory and Techniques*, vol. 52, no. 1, pp. 20–28, Jan. 2004.

[127] M. Bebendorf, “Approximation of boundary element matrices,” *Numerische Mathematik*, vol. 86, no. 4, pp. 565–589, Oct. 2000.

[128] W. Hackbusch, “A sparse matrix arithmetic based on H-matrices. Part I: Introduction to H-matrices,” *Computing*, vol. 62, no. 2, pp. 89–108, Apr. 1999.

[129] W. Hackbusch and B. N. Khoromskij, “A sparse H-matrix arithmetic. Part II: Application to multi-dimensional problems,” *Computing*, vol. 64, no. 1, pp. 21–47, Feb. 2000.

[130] M. Kotzev and C. Schuster, “Custom-made calibration standards for measurements of multilayer substrates,” in *German Microwave Conference (GeMiC)*, Darmstadt, Germany, Mar. 14–16, 2011.

[131] M. A. Kotzev, “Probing and fixturing techniques for wideband multiport measurements in digital packaging,” Dissertation, TUHH, 2013.

[132] Agilent Technologies, Inc., 2014. [Online]. Available: http://www.home.agilent.com

[133] W. L. Gore & Associates, Inc., 2014. [Online]. Available: http://www.gore.com

[134] GGB Industries, 2014. [Online]. Available: www.ggb.com

[135] W. Kruppa and K. F. Sodomsky, “An explicit solution for the scattering parameters of a linear two-port measured with an imperfect test set (correspondence),” *IEEE Transactions on Microwave Theory and Techniques*, vol. 19, no. 1, pp. 122–123, Jan. 1971.

[136] R. Rimolo-Donadio, C. Schuster, X. Gu, Y. H. Kwark, and M. B. Ritter, “Analysis and optimization of the recessed probe launch for high frequency measurements of PCB interconnects,” in *Design, Automation and Test in Europe*, Munich, Germany, Mar. 10–14, 2008.

[137] Y. Kwark, C. Schuster, L. Shan, C. Baks, and J. Trewhella, “The recessed probe launch—a new signal launch for high frequency characterization of board level packaging,” in *IEC DesignCon Conference*, Santa Clara, CA, USA, Jan. 31 – Feb. 3, 2005.

[138] M. Kotzev, R. Rimolo-Donadio, C. Schuster, X. Gu, Y. H. Kwark, and M. B. Ritter, “Bandwidth study of recessed probe launch variations for broadband measurement of embedded pcb structures,” in *German Microwave Conference (GeMIC)*, Munich, Germany, Mar. 16–18, 2009.

[139] M. Kotzev, R. Rimolo-Donadio, Y. H. Kwark, C. W. Baks, X. Gu, and C. Schuster, “Electrical performance of the recessed probe launch technique for measurement of embedded multilayer structures,” *IEEE Transactions on Instrumentation and Measurement*, vol. 61, no. 12, pp. 3198–3206, Dec. 2012.

[140] “High frequency structure simulator (HFSS TM), ver. 12,” Pittsburg and PA and USA, 2009. [Online]. Available: http://www.ansoft.com

[141] T. Kushta, K. Narita, T. Kaneko, T. Saeki, and H. Tohya, “Resonance stub effect in a transition from a through via hole to a stripline in multilayer PCBs,” *IEEE Microwave and Wireless Components Letters*, vol. 13, no. 5, pp. 169–171, May 2003.

[142] S. Deng, J. Mao, T. H. Hubing, J. L. Drewniak, J. Fan, J. L. Knighten, N. W. Smith, and R. Alexander, in *International Symposium on Electromagnetic Compatibility*, Santa Clara, CA, USA, Aug. 9–13, 2004, pp. 1017–1022.

[143] J. Shin and T. Michalka, “Comprehensive design guidance for PTH via stub in board-level high speed differential interconnects,” in *Electronic Components and Technology Conference (ECTC)*, Las Vegas, NV, USA, Jun. 1–4, 2010.

[144] C.-L. Yeh, Y.-C. Tsai, C.-M. Hsu, L.-S. Liu, S.-H. Tsai, Y. H. Kao, and G.-H. Shiue, “Influence of via stubs with different terminations on time-domain transmission waveform and eye diagram in multilayer PCBs,” in *IEEE Electrical Design of Advanced Packaging and Systems Symposium (EDAPS)*, Taipei, Taiwan, Dec. 9–11, 2012.

[145] T. V. Kalyan, M. Mutyam, and P. V. S. Rao, “Exploiting variable cycle transmission for energy-efficient on-chip interconnect design,” in *International Conference on VLSI Design (VLSID)*, Hyderabad, India, Jan. 4–8, 2008.

[146] Bo Fu, D. Wolpert, and P. Ampadu, “Lookahead-based adaptive voltage scheme for energy-efficient on-chip interconnect links,” in *ACM/IEEE International Symposium on Networks-on-Chip*, San Diego, CA, USA, May 10–13, 2009.

[147] E. Nigussie, S. Tuuna, J. Plosila, J. Isoaho, and H. Tenhunen, “Semi-serial on-chip link implementation for energy efficiency and high throughput,” *IEEE Transactions on Very Large Scale Integration (VLSI) Systems*, vol. 20, no. 12, pp. 2265–2277, Dec. 2012.

[148] K. Jung, Y. Lu, and E. Alon, “Power analysis and optimization for high-speed I/O transceivers,” in *IEEE International Midwest Symposium on Circuits and Systems (MWSCAS)*, Seoul, South Korea, Aug. 7–10, 2011.

[149] B. Kim and V. Stojanovic, “Equalized interconnects for on-chip networks: modeling and optimization framework,” in *IEEE/ACM International Conference on Computer-Aided Design*, San Jose, CA, USA, Nov. 4–8, 2007.

[150] H. Hatamkhani, F. Lambrecht, V. Stojanovic, and C.-K. K. Yang, “Power-centric design of high-speed I/Os,” in *Design Automation Conference*, San Francisco, CA, USA, Jul. 24–28, 2006.

[151] C. Svensson, “Optimum voltage swing on on-chip and off-chip interconnect,” *IEEE Journal of Solid-State Circuits*, vol. 36, no. 7, pp. 1108–1112, Jul. 2001.

[152] Gang Huang, A. Naeemi, and J. Meindl, “Minimizing energy-per-bit for on-board LC transmission lines,” in *IEEE 2005 International Interconnect Technology Conference*, Jun. 6–8, 2005, pp. 77–79.

[153] H. Hatamkhani and C.-K. K. Yang, “A study of the optimal data rate for minimum power of I/Os,” *IEEE Transactions on Circuits and Systems II: Express Briefs*, vol. 53, no. 11, pp. 1230–1234, Nov. 2006.

[154] W. Beyene, “A study of optimal data rates of high-speed channels,” in *IEC DesignCon Conference*, Santa Clara, CA, USA, Jan. 31 – Feb. 3, 2011.

[155] K. J. Han, X. Gu, Y. H. Kwark, L. Shan, and M. B. Ritter, “Modeling on-board via stubs and traces in high-speed channels for achieving higher data bandwidth,” *IEEE Transactions on Components, Packaging and Manufacturing Technology*, vol. 4, no. 2, pp. 268–278, Feb. 2014.

[156] A. Sanders, “Statistical simulation of physical transmission media,” *IEEE Transactions on Advanced Packaging*, vol. 32, no. 2, pp. 260–267, May 2009.

[157] D. Timmermann, R. Rimolo-Donadio, Y. H. Kwark, T.-M. Winkel, C. Siviero, H. Harrer, and C. Schuster, “Methods for calculation of eye diagrams for digital links with multiple aggressors having unknown time offsets,” in *IEEE Workshop on Signal and Power Integrity (SPI)*, Sorrento, Italy, May 13–16, 2012.

[158] B. P. Lathi, *Modern Digital and Analog Communication Systems*, 3rd ed. New York: Oxford University Press, 1998.

[159] K. L. Kaiser, *Electromagnetic Compatibility Handbook*. Boca Raton: CRC, 2005.